

DISS ETH NO. 26215

**Novel synthesis routes to colloidal nanocrystals of  
semiconductive metal pnictides and metal halides**

*A thesis submitted to attain the degree of*

DOCTOR OF SCIENCES of ETH ZURICH

(Dr. Sc. ETH Zurich)

*presented by*

GEORGIAN NEDELICU

MSc. in Chemistry of Advanced Materials

MSc. in Science of Conservation/Restoration of Patrimony Works through Physical and  
Chemical Methods

University of Bucharest, Romania

Born on 09.11.1989

Citizen of Romania

*Accepted on the recommendation of*

Prof. Dr. Maksym V. Kovalenko, examiner

Prof. Dr. Chih-Jen Shih, co-examiner

**ETH**

Eidgenössische Technische Hochschule Zürich  
Swiss Federal Institute of Technology Zurich

*Department of Chemistry and Applied Biosciences*

Laboratory of Inorganic Chemistry

2019



*“There’s plenty of room at the bottom...  
and even more on top”*

Richard Feynman – Maksym Kovalenko



## Declaration

I hereby confirm that I am the sole author of the written work herein enclosed and that I have compiled it in my own words. Parts excepted are corrections of form and content by the supervisor.

### **Title of work:**

*Novel synthesis routes to colloidal nanocrystals of semiconductive metal pnictides and metal halides*

With my signature, I confirm:

1. I have committed none of the forms of plagiarism.
2. I have documented all methods, data, and processes truthfully.
3. I have not manipulated any data.
4. I have mentioned all persons who were significant contributors to this work, as described below.
5. I obtained copyright permissions from the journal for reproducing the text and Figures in this thesis, where needed.
6. I am aware that the work may be screened electronically for plagiarism.

Place, date

Signature(s)

Dr. E. Schrader and Prof. Dr. H. Grützmacher (ETH Zürich) provided all the acylphosphine compounds involved in the experiments presented in Chapter 3.

Dr. M. Rigo, S. Schutte, and Prof. Dr. M. Driess provided the  $\text{Al}^{(\text{Mes})\text{BAAs}}_3$  used for the synthesis of metal arsenide QDs presented in Chapter 4.

Dr. F. Krumeich (ETH Zürich), Dr. K. Kravchick and Dr. M. Walter (EMPA) helped with the EDX measurements and analysis presented in Chapter 5.

M. Becker, Dr. G. Raino, Dr. T. Stöferle, Dr. R. F. Mahrt (IBM Zürich), and Dr. V. I. Klimov (Los Alamos National Laboratory) helped with the single dot spectroscopy measurements and analysis of the data presented in Chapter 6.

Dr. S. Kumar and Prof. Dr. C.-J. Shih (ETH Zürich) helped with the characterization and analysis of the LED data presented in Chapter 6.

M. Wagner and Prof. Dr. Richard Schaller (Northwestern University and Los Alamos National Laboratory) helped with the ultrafast spectroscopy measurements and data analysis presented in Chapter 6.

---



## Acknowledgments

First and foremost, I would like to thank Prof. Dr. Maksym V. Kovalenko for the exceptional opportunity to join his group and work in the exciting field of quantum dots. His guidance, support, and encouragement when the projects were not working exactly as planned, as well as that he pushed every day my limits, were extremely valuable.

I thank Prof. Dr. Chih-Jen Shih for his kind willingness to co-examine this dissertation.

I thank Dr. Loredana Protesescu, who taught me most experimental skills ranging from the synthesis of monodisperse colloidal quantum dots to their characterization, as well as for being my friend and supporting me all these years. Also, I want to thank Dr. Maryna Bodnarchuk and Dr. Dmitry Dirin for helping me when I had difficulties in my projects, as well as Dr. Michael Wörle for his help whenever was needed with the XRD measurements and data analysis.

I want to thank Dr. Olga Nazarenko, Romain J.-C. Dubey, Dr. Marc Walter, Dr. Christoph Guntlin, Dr. Yusuf Kelestemur, and Franziska Krieg for their continuous support, for listening to my complaints about my projects and for their friendship.

I want to express my gratitude to all Kovalenko group members for their support and their contribution to a harmonious working environment. Also, I want to thank my former semester students for their dedication and contribution to some of my projects.

I want to thank all my extraordinary collaborators all over the world that I had the chance to work with and to learn from.

Special thanks go to Claudia for her unlimited support in all administrative matters.

Last and most importantly, special thanks to my parents for their unconditional support, for believing in me and for giving me the freedom to chose my path. As well, many thanks to all my friends for supporting me and always having joyful and relaxing moments.

Zürich, 14<sup>th</sup> of August

---





---

## Table of Contents

Summary .....	i
Zusammenfassung.....	v
Chapter 1. Introduction .....	1
1.1. Fundamentals, history, and development of colloidal semiconductor nanocrystals (quantum dots).....	1
1.2. Semiconductor nanocrystals: between molecules and bulk .....	19
1.3. Optical properties of colloidal semiconductor nanocrystals .....	22
1.4 Metal pnictide nanocrystals.....	29
1.5 Cesium lead halide (CsPbX <sub>3</sub> , X = Cl, Br, I) perovskite nanocrystals .....	36
1.6 Applications of semiconductor nanocrystals.....	51
1.7 Scope and outline of the doctoral thesis .....	57
Chapter 2. Methods and techniques .....	61
2.1. Synthesis of ligand-stabilized colloidal semiconductor nanocrystals .....	61
2.2 Anion exchange.....	61
2.2. Characterization methods and techniques .....	62
Chapter 3. Acylphosphines – a new class of phosphorus compounds for the facile synthesis of metal-phosphide quantum dots .....	66
3.1. Introduction .....	66
3.1. Experimental section .....	69
3.3. Results and discussion.....	73
3.4. Conclusions .....	78
Chapter 4. Aluminum-tris(bismesitoylarsine), Al( <sup>Mes</sup> BAAs) <sub>3</sub> – inexpensive, air-stable, and versatile arsenic-precursor for the synthesis of metal-arsenide semiconductor quantum dots 66	
4.1. Introduction .....	80
4.2. Experimental section .....	81
4.3. Results and discussion.....	86
4.4. Conclusions .....	97
Chapter 5. Fast anion-exchange in highly luminescent nanocrystals of cesium lead halide perovskites (CsPbX <sub>3</sub> , X = Cl, Br, I).....	98
5.1. Introduction .....	98
5.2. Experimental section .....	100
5.3. Results and discussion.....	103
5.4. Conclusions .....	109

---

Chapter 6. Cesium lead bromide nanoplatelets (CsPbBr <sub>3</sub> NPLs) with stable emission at 492 nm .....	111
6.1. Introduction .....	111
6.2. Experimental section .....	113
6.3. Results and discussion.....	116
6.4. Conclusions .....	135
Chapter 7. Conclusions and Outlook .....	136
7.1. Conclusions .....	136
7.2 Outlook.....	138
Bibliography .....	140
Annex A. List of abbreviations .....	166
Annex B. Curriculum Vitae .....	167
Annex C. List of publications .....	169
Annex D. List of presentations .....	173

---

## Summary

Since the discovery of size-dependent optical properties more than three decades ago, colloidal semiconductor nanocrystals (NCs) have drawn enormous research interest, both fundamentally and practically. Semiconductor NCs are miniscule crystallites of nanometric size, formed by hundreds to thousands of atoms and an outer layer of organic surfactant molecules (stabilizing ligands), and are also known as “quantum dots” (QDs) or “artificial atoms.” These small, inorganic NCs approach the lower limit of achievable particle size and thus have opened new directions for fundamental research due to their unique excitonic structure and hence optical properties, all being affected and hence eventually engineerable by the size, composition, shape, and surface state. Moreover, semiconductor NCs have already been shown as efficient and versatile photoluminescent and electroluminescent light emitters for LED and LCD TV displays, or biological imaging, as well as promising light-harvesters for photodetectors and solar cells. The photoluminescence (PL) quantum yields (QYs) of the QDs, can approach unity (100%) upon adequate surface engineering, as thus far achieved for visible-emissive II-VI NCs (i.e., CdSe), III-V NCs (i.e., InP), and metal halide perovskite NCs (i. e. CsPbX<sub>3</sub>, with X being halide). This dissertation presents novel synthesis approaches in both directions: (i) conventional metal pnictide III-V QDs, where new precursors have been shown to yield high-quality In(Zn)P and InAs QDs with PL emission spanning into the visible and IR spectral domains; and (ii) presents synthetic advancements in the newcomer lead halide perovskite NCs, for which the anion exchange has been shown for the first time while tunability in lower dimensions enable access to highly stable blue-emitting materials, very much demanded in the LED field.

The III-V semiconductor NCs started to present research interest about a decade later after the more traditional II-VI and IV-VI semiconductor NCs, receiving more considerable attention with the growing importance of the Restrictions of Hazardous Substances (RoHS) for the electric and electronic equipment. III-V semiconductor NCs are characterized by direct band gaps, low exciton binding energies, and bulk band gap values that cover a wide spectral range from ultraviolet to infrared region, being environmentally benign NCs when compared to II-VI and IV-VI NCs. Compared to most of the II-VI and IV-VI NCs, the III-V compounds have a stronger covalent character which requires higher reaction temperatures, longer reaction

times, and highly reactive precursors for their synthesis, all factors which hinder the precise control of the size and size distribution of the NCs. Additionally, the III-V semiconductor NCs, (e.g., InP or InAs), are much more air-sensitive than their II-VI or IV-VI counterparts (e.g., CdSe or PbS) and air-free conditions are necessary for their synthesis. Moreover, because of the low electron affinity of group V elements, difficulties arise in finding the appropriate precursors, for instance, the usual group V precursors involved in the synthesis of III-V semiconductor NCs involve highly electropositive elements such as H, Na or Si (e.g.,  $AH_3$ ,  $ANa_3$ ,  $A(SiMe_3)_3$ ,  $A(N(SiMe_3)_2)_3$ ,  $A(NMe_2)_3$ , where  $A = P, As$ ). Therefore, one of the most critical tasks, when designing a new approach targeting the synthesis of highly monodisperse NCs, is the selection of the molecular precursors. These have to fulfill multiple requirements, such as good solubility in non-polar organic solvents, stability at room temperature, sufficiently reactive at elevated temperatures, selective reactivity, and to yield the desired product in highly pure form. Also, it is preferable that the precursors are commercially available, or their production is accurately documented and available.

Two of the projects presented in this dissertation have focussed on exploring safer and inexpensive alternative pnictide precursors to enable the facile synthesis of highly luminescent metal pnictide semiconductor QDs, in particular, In(Zn)P and InAs QDs.

A new type of efficient and safer-to-handle phosphorous precursors have been chosen from the class of acylphosphine compounds and used in the synthesis of In(Zn)P QDs. The reactivity of the precursors was verified in two different synthetic approaches: (i) the acetate approach, and (ii) the halide approach, following both the heat-up and hot-injection methods. Advancements such as the synthesis of luminescent cores of In(Zn)P QDs at relatively low temperatures (200 °C) were possible by using  $^{Ph}BAPH$  as the phosphorous precursor in the acetate method. Tunability of the PL emission is demonstrated for each of the new acylphosphines involved in the synthesis of these QDs and QYs, reaching values higher than 70% after efficient surface passivation with a GaP/ZnS double-shell. Good performance was also achieved for the  $^{Ph}TAP$  precursor that enabled the synthesis of emissive In(Zn)P QDs with enhanced PL QYs after overgrowing a ZnS shell. Moreover, in the case of  $^{Me}TAP$  precursor, tunability of the PL spectra could be attained by varying the ratio between In and P precursors. The performance of the acylphosphines in the synthesis of In(Zn)P QDs demonstrates that these compounds have a high potential also for the synthesis of other metal phosphide NCs, opening new avenues for fundamental studies but also for practical applications such as LEDs or LCD TV displays.

---

The synthesis of InAs was explored as well, and it has been demonstrated that the air-stable  $\text{Al}(\text{MesBAAs})_3$  can afford monodisperse InAs QDs by reacting quickly at various temperatures (90 – 270 °C) with  $\text{In}(\text{OAc})_3$  and myristic acid in octadecene. The synthesized InAs QDs are characterized by PL emission tunable from 700 nm up to 1000 nm by varying the reaction temperature. It was found that by introducing  $\text{Zn}(\text{OAc})_2$  into the synthesis of InAs QDs, as already reported for InP QDs, the quality of the PL spectra would improve, which means that the synthesized QDs are less surface defective. Moreover, the PL QYs of the monodisperse InAs cores could be increased from 1-2% up to 20% after overcoating the cores with a ZnS shell. Additionally, by using the synthetic protocol developed for InAs QDs, other metal arsenide QDs could be efficiently achieved, such as  $\text{Cd}_3\text{As}_2$ , GaAs, or  $\text{Zn}_3\text{As}_2$ . Remarkably, luminescent  $\text{Cd}_3\text{As}_2$  QDs could also be obtained after very short reaction time (5 minutes) by using  $\text{Al}(\text{MesBAAs})_3$  in the generalized synthetic protocol. The PL emission can be tuned either by varying the reaction temperature or by using reducing agents in a modified procedure. GaAs and  $\text{Zn}_3\text{As}_2$  QDs were obtained as well using  $\text{Al}(\text{MesBAAs})_3$  as an As-source, but no PL emission was recorded for those.

Colloidally stabilized  $\text{CsPbX}_3$  (X = Cl, Br, I) perovskite NCs, characterized by tunable luminescence over the UV-Vis spectral range, narrow emission line widths and high PL QYs, were introduced by the same research group in 2015. Apart from their exceptional properties, the synthesis of the blue-emitting  $\text{CsPbCl}_3$  and red-emitting  $\text{CsPbI}_3$  NCs proved to be more challenging regarding their size distribution. In order to overcome this inconvenience, a post-synthetic anion-exchange process was developed for the perovskite  $\text{CsPbX}_3$  NCs which enabled the obtaining of highly monodisperse NCs for all three halide compositions. It was observed that the anion-exchange is remarkably fast and efficient in  $\text{CsPbX}_3$  perovskite NCs, in contrast to all known studies that describe the anion-exchange process as prolonged and inefficient in metal chalcogenide NCs. Overall, the behavior of perovskite halides with respect to anion-exchange is orthogonal to common metal chalcogenide NCs, namely since the cationic sub-lattice is substantially rigid and the singly-charged halide ions are highly mobile. In metal chalcogenides, ion-exchange has been observed with such ease only for cations. Semiconducting properties of lead halide perovskites are highly defect-tolerant, maintaining bright excitonic emission throughout and upon completion of the anion-exchange. Of practical note, the herein demonstrated fine-tuning of the spectrally narrow and bright PL of anion-exchanged  $\text{CsPbX}_3$  NCs over the entire visible spectral region can be conveniently accomplished from numerous halide sources at low temperatures. Also, fast anion-exchange between  $\text{CsPbX}_3$  NCs of different compositions can be readily achieved. Future investigations

---

of halide-exchange reactions in other nanoscale metal halide systems are warranted, as high ionic conductivity may not be strictly necessary due to the short diffusion paths within the NCs and the low charges of halide ions.

By varying different parameters in the synthetic protocol, such as reaction temperature, ligand ratio or using long- and short-alkyl chain ligands, the shape and size of the CsPbBr<sub>3</sub> NCs can be altered to zero-dimensional QDs, one-dimensional nanowires, and two-dimensional nanoplatelets (NPLs) and nanosheets. Despite the easiness of synthesis of all these morphologies of CsPbBr<sub>3</sub> perovskite semiconductors, they often have limited stability towards purification and processability, which makes their use in various applications difficult if not impossible. In this last project, the synthesis of highly stable (more than two years) and monodisperse CsPbBr<sub>3</sub> NPLs is achieved, with PL emission in blue spectral regime (492 nm). These CsPbBr<sub>3</sub> NPLs are characterized by high PL QYs up to 75% retained in deposited films, a prerequisite for efficient light-emitting devices employing NPLs as the active medium. The synthesis of thinner NPLs has been tested successfully by lowering the injection temperature, but they proved limited stability. Since the tunability of the thickness of NPLs is limited via direct synthesis and hence is not a viable option for modulating the optical properties, anion-exchange was used to tune the PL emission by altering the halide composition. As expected from previous experience, the optical features could be tuned (from 492 nm to 398 nm in the violet-blue region, and 632 nm in the red region) by fast-anion exchange performed at room temperature in air, while the size and shape of the parent NPLs were preserved. In addition to the synthesis of these highly stable blue-emitting CsPbBr<sub>3</sub> NPLs, a comprehensive optical characterization, and their performance in a blue LED containing these NPLs as an emissive layer are presented. Ultrafast spectroscopy (transient absorption and time-resolved PL) unveiled the exciton dynamics with the specific Auger relaxation time and exciton radiative decay. Single NPL spectroscopy performed at cryogenic and RT attest single NPLs emit a stream of single photons, making them a good candidate for single-photon LEDs. A light-emitting diode architecture that contains blue-emissive (492 nm) CsPbBr<sub>3</sub> NPLs as the emissive layer was realized and the preliminary results have shown a maximum luminance of 22.1 cd m<sup>-2</sup> and high external quantum efficiency (EQE) of 0.19%.

This dissertation encompasses significant progress for two major classes of semiconductor NCs; one is focusing more on the chemical insights and mechanistic processes while the second revolves around maximizing the optoelectronic properties, bringing these QDs closer to daily usage.

## Zusammenfassung

Seit der Entdeckung größenabhängiger optischer Eigenschaften vor mehr als drei Jahrzehnten haben kolloidale Halbleiter-Nanokristalle (NKs) sowohl in der Grundlagenforschung als auch praktisch grosses Interesse geweckt. Halbleiter-NKs sind winzige Kristallite nanometrischer Größe, gebildet durch hunderte bis tausende von Atomen und eine äußere Schicht organischer Tensidmoleküle (stabilisierende Liganden), und sind auch als "quantum dots" (QDs) oder "künstliche Atome" bekannt. Diese kleinen, anorganischen NKs nähern sich der unteren Grenze der erreichbaren Partikelgröße und haben -dank ihrer einzigartigen excitonischen Struktur und den damit verbundenen optischen Eigenschaften, die alle durch Größe, Zusammensetzung, Form und Oberflächenzustand verändert und so angepasst werden können- neue Wege für die Grundlagenforschung eröffnet. Darüber hinaus wurden Halbleiter-NKs bereits als effiziente und vielseitige photolumineszente und elektrolumineszente Lichtquellen für LED- und LCD-TV-Bildschirme oder biologische Bildgebung sowie vielversprechende Solarkonzentratoren für Solarzellen und Photodetektoren gezeigt. Die Quantenausbeuten (QYs) der Photolumineszenz (PL) dieser QDs kann sich bei ausreichender Oberflächenpassivierung der Einheit nähern (100%); diese wurde bisher im bei im Sichtbaren emittierenden II-VI-NKs (zB. CdSe), III-V-NKs (zB. InP) und Metallhalogenidperovskit-NKs (zB. CsPbX<sub>3</sub>, wobei X ein Halogenid ist) erreicht. Diese Dissertation stellt neuartige Syntheseansätze in beide Richtungen vor: (i) konventionelle Metallpnictide III-V QDs, bei denen aus neuen Ausgangsstoffen hochwertige In(Zn)P- und InAs QDs mit PL-Emission in den sichtbaren- und IR-Spektraldomänen entstehen; und (ii) synthetische Fortschritte im Bereich der neuauftkommenden Bleihalogenid-Perovskit-NKs, für die der Anionenaustausch zum ersten Mal nachgewiesen wurde, während die Herstellung niedrigdimensionaler CsPbBr<sub>3</sub> NKs den Zugang zu hochstabilen blauemittieren Materialien ermöglicht, die in der LED-Branche sehr gefragt sind.

Die III-V-Halbleiter-NKs begannen etwa ein Jahrzehnt später Forschungsinteresse zu wecken, nach den traditionellen II-VI- und IV-VI-Halbleiter-NKs, wobei sie angesichts der wachsenden Bedeutung der Beschränkungen gefährlicher Stoffe (RoHS) für elektrische und elektronische Geräte eine immer grössere Aufmerksamkeit geniessen. III-V Halbleiter-NKs zeichnen sich durch eine direkte Bandlücke und eine niedrige exzitonische Bindungsenergie

aus. Dazu besitzen sie Festkörperbandaufspaltungen, die einen weiten Spektralbereich von Ultraviolett bis hin zu Infrarot abdecken und sind umweltschonend, verglichen mit II-VI- und IV-VI-NKs. Im Vergleich zu den meisten II-VI- und IV-VI-NKs haben die III-V-Verbindungen einen stärkeren kovalenten Charakter, der höhere Reaktionstemperaturen, längere Reaktionszeiten und hochreaktive Ausgangsstoffe für ihre Synthese erfordern; alles Faktoren, die eine genaue Kontrolle der Größe und Größenverteilung der NKs behindern. Darüber hinaus sind die III-V-Halbleiter-NKs (z.B. InP oder InAs) viel luftempfindlicher als ihre II-VI- oder IV-VI-Gegenstücke (z.B. CdSe oder PbS) und inerte Bedingungen sind für ihre Synthese notwendig. Darüber hinaus ergeben sich aufgrund der geringen Elektronenaffinität von Elementen der Gruppe V Schwierigkeiten bei der Suche nach geeigneten Ausgangsstoffen; z. B. sind die üblichen Vorstufen der Gruppe V, die an der Synthese von III-V-Halbleiter-NKs beteiligt sind, elektropositive Elemente wie H, Na oder Si (z.B.  $AH_3$ ,  $ANa_3$ ,  $A(SiMe_3)_3$ ,  $A(N(SiMe_3)_2)_3$ ,  $A(NMe_2)_3$ , wobei  $A = P, As$ ). Daher ist die Auswahl der molekularen Vorstufen eine der wichtigsten Aufgaben bei der Entwicklung eines neuen Syntheseweg hochmonodisperser NKs. Diese müssen mehrere Anforderungen, wie gute Löslichkeit in apolaren organischen Lösungsmitteln, Stabilität bei Raumtemperatur, ausreichende Reaktivität bei erhöhten Temperaturen und selektive Reaktivität erfüllen sowie das gewünschte Produkt mit einem hohen Reinheitsgrad ergeben. Außerdem ist es von Vorteil, wenn die Ausgangsstoffe im Handel erhältlich sind oder ihre Herstellung genau dokumentiert und verfügbar ist.

Bei zwei der in dieser Dissertation vorgestellten Projekte lag der Schwerpunkt in der Erforschung sichererer und kostengünstiger alternativer Pnictid-Vorstufen, um eine einfache Synthese von hochlumineszenten Metallpnictid-Halbleiter-QDs, insbesondere In(Zn)P und InAs QDs, zu ermöglichen.

Aus der Klasse der Acylphosphinverbindungen wurde eine neue Art von effizienten und sicher zu handhabenden Phosphorquellen ausgewählt, die bei der Synthese von In(Zn)P QDs verwendet wurden. Die Reaktivität dieser Vorstufen wurde in zwei verschiedenen Ansätzen überprüft: (i) dem Acetatansatz und (ii) dem Halidansatz, beide sowohl nach der Aufheiz- als auch der sogenannten "hot-injection"-Methode. Fortschritte wie die Synthese von lumineszenten In(Zn)P QDs bei relativ niedrigen Temperaturen (200 °C) wurden durch die Verwendung von  $^{Ph}BAPH$  als Phosphorquelle bei der Acetatmethode erzielt. Die Abstimmbarkeit der PL-Emission wird für jedes der neuen Acylphosphine demonstriert, die an der Synthese dieser QDs beteiligt sind. Dazu konnten nach effizienter Oberflächenpassivierung



---

mit einer GaP/ZnS-Doppelschale QY Werte von mehr als 70 % erreicht werden. Gute Resultate wurden auch für die <sup>Ph</sup>TAP Vorstufe erreicht, die die Synthese von emittierenden In(Zn)P QDs mit verbesserten PL QYs ermöglichte, nachdem sie mit einer ZnS-Schale geschützt worden waren. Darüber hinaus konnte im Fall des <sup>Me</sup>TAP-Vorläufers eine gute Abstimbarkeit der PL-Spektren durch eine Variation des Verhältnisses zwischen den In- und P-Quellen erreicht werden. Die Resultate, die mit den Acylphosphinen bei der Synthese von In(Zn)P QDs erreicht wurden zeigen, dass diese Verbindungen auch für die Synthese anderer Metallphosphid-NKs ein hohes Potenzial haben. Sie eröffnen neue Wege, nicht nur für Grundlagenstudien, sondern auch für praktische Anwendungen wie LEDs oder LCD-TV-Bildschirme.

Die Synthese von InAs wurde ebenfalls untersucht, dabei hat sich gezeigt, dass das Luft stabile  $\text{Al}(\text{MesBAAs})_3$  mit  $\text{In}(\text{OAc})_3$  und Myristinsäure in Octadecen bei Temperaturen zwischen 90 und 270°C in einer schnellen Reaktion, monodisperse InAs QDs bildet. Dabei kann die Emissionswellenlänge der QDs, je nach Reaktionstemperatur, zwischen 700 und 1000 nm variiert werden. Durch die Einführung von  $\text{Zn}(\text{OAc})_2$  in die Synthese kann die optische Qualität der InAs QDs verbessert werden, dies steht in engem Zusammenhang mit der Präsenz von Oberflächendefekten, die durch  $\text{Zn}(\text{OAc})_2$  passiviert werden. Dieses Verfahren hat sich bereits bei der Passivierung von InP QDs als nützlich erwiesen. Nachdem eine ZnS Schale um die monodispersen InAs Kerne gebildet worden war, konnte der PLQY von 1-2% auf 20% verbessert werden. Dasselbe Syntheseverfahren konnte erfolgreich für die Produktion von  $\text{Cd}_3\text{As}_2$ , GaAs, or  $\text{Zn}_3\text{As}_2$  angepasst werden. In kurzen Reaktionszeiten von 5 Minuten konnten  $\text{Cd}_3\text{As}_2$  QDs von bemerkenswerter Lumineszenz geformt werden, unter Verwendung von  $\text{Al}(\text{MesBAAs})_3$ . Dabei konnte die Emissionswellenlänge einerseits durch die Reaktionstemperatur und andererseits durch die Beigabe eines Reduktionsmittels kontrolliert werden. Die Arsenquelle  $\text{Al}(\text{MesBAAs})_3$  konnte auch erfolgreich für die Bildung von GaAs und  $\text{Zn}_3\text{As}_2$  QDs verwendet werden. In diesen Systemen wurde jedoch keine Lumineszenz beobachtet.

Kolloidale  $\text{CsPbX}_3$  (X = Cl, Br, I) Perovskit NKs wurden in 2015 erstmals durch unsere Gruppe vorgeschlagen. Sie zeichnen sich vor Allem durch schmale, effiziente Emissionslinien aus, deren Maximum auf jede Wellenlänge im ganzen Wellenlängenbereich des sichtbaren Lichts eingestellt werden kann. Ungeachtet derer ausnehmend positiven optischen Eigenschaften, hat es sich als schwierig erwiesen monodisperse  $\text{CsPbCl}_3$  oder  $\text{CsPbI}_3$  NKs herzustellen. Diese Unannehmlichkeit konnte jedoch durch Anionenaustausch ausgehend von monodispersen  $\text{CsPbBr}_3$  NKs behoben werden. Damit konnten alle Halidzusammensetzungen

in monodispersen Ensembles gebildet werden. Es wurde festgestellt, dass der Anionenaustausch in Halidperovskiten bemerkenswert schnell und effizient ist im Gegensatz zu Metalchalkogenid Nanokristallen, wo der Prozess mühsam und langwierig ist, wenn er denn stattfindet. Im Grossen und Ganzen ist der Ionenaustausch in Perovskitnanokristallen orthogonal zu demselben in Metalchalkogeniden. In Metallchalkogeniden ist der anionische Teil des Gitters rigide während die kleineren Kationen mobil sind, in Perovskiten hingegen sind die weniger geladenen Anionen um Grössenordnungen mobiler als die zweifach geladenen (Blei) oder grossen (Cäsium) Kationen. Die Halbleitereigenschaften von Bleihalidperovskiten sind defekttolerant, so dass die hell leuchtende Emission während des Anionenaustausches und auch nach seiner Komplettierung erhalten bleibt. Daher kann jede Wellenlänge des sichtbaren Lichts ausgehend von monodispersen CsPbBr<sub>3</sub> NKs praktisch unter Verwendung verschiedenster Halogenidquellen bei Raumtemperatur durch Anionenaustausch erreicht werden. Auch tauschen Cäsiumbleihalidkristalle verschiedener Halidzusammensetzung innert kurzer Zeit Halogenide aus, sodass eine homogene Verteilung entsteht. Es ist naheliegend, dass solche Halogenidaustausche auch in nanometrischen Verbindungen anderer Metallhalide statt findet, da gute Anionenleitfähigkeit durch die kurzen Diffusionswege nicht unbedingt nötig ist.

Durch Variation der Synthesebedingungen, speziell Reaktionstemperatur, Ligandenverhältnis oder Alkylkettenlänge der Liganden, können null-, ein- (Stäbchen) oder zweidimensionale (Plättchen) Nanokristalle geformt werden. Trotz der einfachen Herstellung dieser Formvielfalt, sind nicht-würfelförmige Kristalle oft nicht stabil gegen Isolation, Aufreinigung und anderweitige Verarbeitung, was deren praktische Anwendung in optoelektronischen Geräten erschwert wenn nicht verunmöglicht. In diesem letzten Projekt wurde die Synthese von langzeit stabilen (2 Jahre), monodispersen CsPbBr<sub>3</sub> Nanoplättchen (NPLs) vorgeschlagen, welche blaues Licht (492 nm) emittieren. Diese zeichnen sich durch einen hohen QY von 75% aus, der selbst in kompakten Filmen erhalten bleibt, eine Notwendigkeit für die Herstellung von effizienten, blauen LEDs. Auch dünnere NPLs können hergestellt werden, dazu müssen tiefere Synthesetemperaturen verwendet werden, jedoch nimmt mit der Plättchendicke auch die Stabilität ab. Da dadurch die Variation der Emissionswellenlänge limitiert ist, wurde die Emissionswellenlängenvariabilität durch Anionenaustausch erreicht, so konnte die Wellenlänge von ursprünglich 492 nm nach 398 nm blau- oder 632 nm rotverschoben werden. Dabei blieb die Form, Form- und Grössenverteilung der NPLs erhalten. Zusätzlich wurden die so erhaltenen NPLs mit Picosekunden-Spektroskopie optisch charakterisiert. Sowohl, Emissions-, als auch Absorptionstransienten wurden dazu analysiert

---

und identifizierten eine Excitondymanik, welche sich durch charakteristische Augerrelaxationszeiten und radiative Lumineszenzzerfälle auszeichnen. Emissionsspektren von einzelnen NPLs bei Raumtemperatur sowie unter cryogenen Bedingungen zeigen, dass solche NPLs ein photon aufs Mal ausstossen, was sie zu guten Kandidaten für Ein-Photon-LEDs macht. Ebenso wurden blaue LEDs hergestellt, die CsPbBr<sub>3</sub> NPLs als optischaktives Material verwenden. Dabei wurde eine Luminanz von 22.1 cd m<sup>-2</sup> und eine externe Quanteneffizienz von 0.19% erreicht.

Diese Dissertation beinhaltet signifikante Fortschritte in den zwei Hauptklassen von Halbleiternanokristallen. Im ersten Teil liegt der Fokus auf chemischen und mechanistischen Einsichten, während im zweiten Teil die Maximierung der optoelektronischen Eigenschaften, mit dem Ziel einer baldigen Markteinführung im Vordergrund steht.

## Chapter 1. Introduction

### 1.1. Fundamentals, history, and development of colloidal semiconductor nanocrystals (quantum dots)

The general term *nanoparticle* (NP) refers to small inorganic particles that have at least one dimension smaller than 100 nanometers and consists of a few hundred to a few thousand atoms. Typically, when an NP consists of atoms with a crystalline or polycrystalline arrangement, the NP should be referred to as *nanocrystal* (NC). It is generally accepted that when the size of the semiconductor NC is reduced in the range of 1 – 20 nm in all three spatial dimensions – zero-dimensional (0D) – the adequate terminology is *quantum dot* (QD). Due to the considerable decreased size, the QDs do not have a band-like energetic structure, characteristic to bulk semiconductors, but instead have discrete energy levels. These discrete levels generate the *quantum confinement effect*, which is explained by the quantum mechanical particle-in-a-box model.<sup>1-2</sup>

Terms like *colloidal NCs* or *colloidal QDs* mean that the semiconductor NC (or QD) is stabilized by an organic layer of surfactant molecules which serve as ligands. The ligands provide sufficient repulsion between the NCs preventing their aggregation in solution.

Historically, applications of nanomaterials can be tracked as far back as Rome in the IV<sup>th</sup> century when artisans used colloidal gold and silver in the glass in the Lycurgus cup (**Figure 1.1a**) or later, in the VI<sup>th</sup> century, when gold and metal oxides NPs were used in the stained glass windows of Notre Dame Cathedral (**Figure 1.1b**).<sup>3-6</sup> In the late 1850s, Michael Faraday discovered accidentally that his “ruby red solution” has light scattering properties.<sup>7</sup> The “ruby red solution” consisted of colloidal gold, known as *Faraday’s sols*, and represents the first scientifically documented synthesis of a colloidal NP. The nano-field was publicly launched in the late 1950s by Richard Feynman when he challenged the auditorium at Caltech with his talk *“There’s Plenty of Room at the Bottom: An Invitation to Enter a New Field of Physics.”*<sup>8</sup>

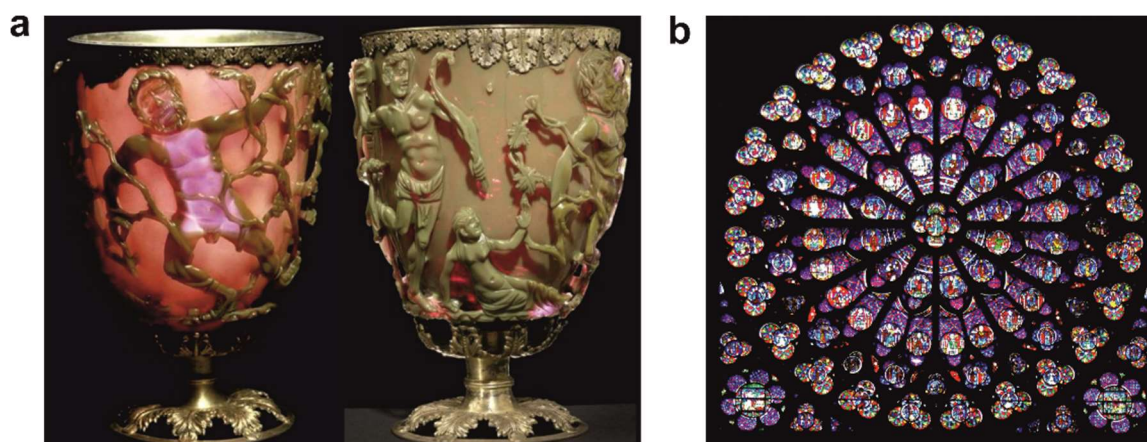


**Figure 1.1.** Images of (a) Lycurgus Cup (© Trustees of the British Museum) illuminated from inside (red) and in daylight (green), and (b) the South window of Notre Dame Cathedral (source: [www.pinterest.ch](http://www.pinterest.ch)).

Later, in the early 1980s, the quantum-size-effects were discovered and explained independently by A. I. Ekimov and A. Efros in the USSR in copper halide doped glasses, and by L. Brus in the USA in colloidal cadmium sulfide.<sup>9-12</sup> The discovery of quantum-size-effects stirred imagination towards new degrees of freedom in tuning the optical properties of semiconductor NCs. For a given NC, for instance, CdSe, the bandgap energy and, therefore, the material's color and its photoluminescence (PL) emission can be adjusted by the size of the NC. Additionally, if the QDs are synthesized in a colloidal manner, this would open a plethora of other possibilities such as mixing with other materials, facile deposition as thin films for energy-oriented applications or functionalizing their surface for bio-medical applications. Since QDs proved to have strongly size-dependent properties, which is also related to their size-dispersity, a major challenge was to develop synthetic methods to facilitate obtaining of NCs with uniform and tunable sizes, as well as tunable morphologies. Murray, Norris, and Bawendi have accomplished the challenge in the early 1990s by developing a novel method, namely the hot-injection method, to synthesize colloidal QDs of cadmium chalcogenides (CdE, E = S, Se, Te) with low size-dispersity.<sup>13</sup> Since then, the research on colloidal QDs expanded, and variations of the hot-injection method have been used in order to synthesize a large variety of colloidal semiconductors such as II-VI (CdS, CdSe, CdTe), III-V (InP, InAs, InSb), and IV-VI (PbS, PbSe, PbTe) compounds.<sup>13-29</sup> Besides colloidal QDs, other morphologies such as nanowires,<sup>30</sup> nanodisks,<sup>31-32</sup> tetrapods<sup>33</sup> or nanoplatelets, and nanosheets were reported.<sup>34-35</sup>

Many other synthetic methods were designated for the synthesis of NPs. These methods have been divided into *top-down* and *bottom-up* approaches. In a typical *top-down* approach, the engineering of the nanomaterials occurs via mechanical (e.g., ball-milling) or/and chemical

(e.g., lithography, exfoliation, etching) fragmentation and (re)structuring of macroscopic solids. In the case of the *bottom-up* approaches, they start with molecules, atoms, and ions, and proceed via gas- or liquid-phase chemical reactions, aggregations, and crystallization. The liquid-phase synthesis in aqueous (e.g., co-precipitation, hydrolysis, hydrothermal, etc.) or non-aqueous (surfactant-assisted) solutions proved to be convenient methods for the successful generation of NPs. The surfactant-assisted methods have earned the highest appreciation among all the synthetic methods. By enabling the possibility of modulating various reaction parameters (e.g., temperature, solvents, ligands, etc.), the size and shape of the final colloidal nanostructures (QDs, NCs, NPs) can be precisely controlled. Further on, the focus will be on the surfactant-assisted colloidal synthesis of NCs/QDs, as this method was used in all the projects that are presented in the following chapters.

These methods were designed following the *classical nucleation theory* (CNT), which uses a thermodynamic analysis of atomic or molecular clusters as a function of size in order to identify the rate-limiting step in nucleation. Therefore, the total expected time for the cluster to grow to a large size is assumed to be approximately equivalent to the expected time for the rate-limiting step to occur.

As depicted in **Figure 1.2**, in a typical surfactant-assisted synthesis of NCs, suitable molecular precursors are introduced into a reaction mixture where they undergo a chemical reaction generating the “monomers” (phase I) for the homogeneous nucleation of the NCs (phase II).

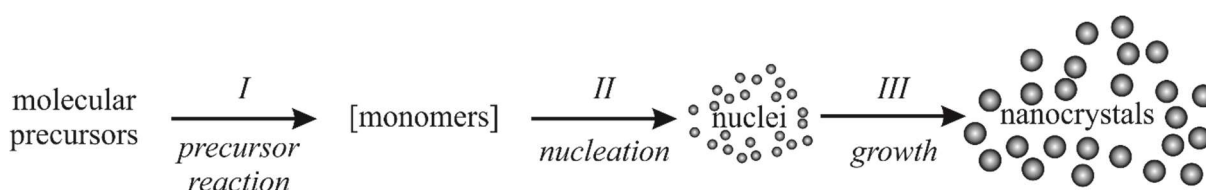


**Figure 1.2** Schematic representation of the three phases in the synthesis of colloidal NCs.

The continuous flux of monomers into the reaction mixture determines the growth of the nanocrystals (phase III). Further growth of the NCs is possible and may occur after depletion of the monomers via the Ostwald ripening process when the smaller NCs are dissolved, and the matter supplies the growth of the larger NCs (Kelvin effect). The presence of the surfactants, molecules that contain long alkyl chains and at least one functional group in their composition (e.g., trioctylphosphine oxide, oleate, oleylamine), in the reaction mixture can significantly influence all these phases. They have a critical role contributing to the formation

of the NCs, their shape, size, and size distribution. The surfactants must provide sufficient steric repulsion to ensure colloidal stability to the NCs and prevent their aggregation in the medium.

Classical studies of LaMer and Dinegar predict that in order to obtain colloidal solutions of NCs with narrow size distribution, it is necessary to temporarily separate the nucleation and growth steps. (**Figure 1.3**).<sup>36</sup>

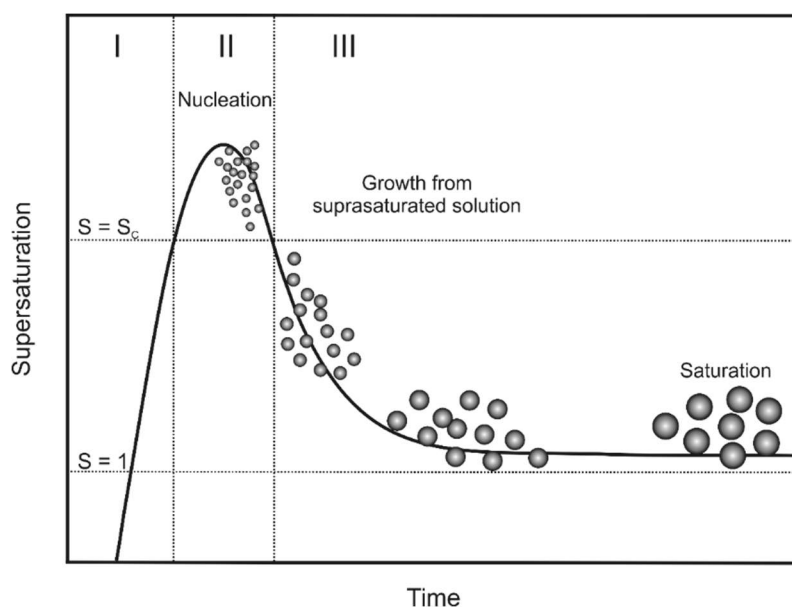


**Figure 1.3.** Mechanism of NC formation according to LaMer model. The model describes three phases, namely supersaturation (I), nucleation (II), and growth (III) of the NCs. The precursor conversion reactions limit the crystallization dictating the temporal evolution of monomer concentration as well as the steady-state supersaturation during the growth phase.

According to the LaMer model depicted in **Figure 1.3**, in phase I, the concentration of monomers is continuously increasing by external addition of precursors or by producing the monomers in situ within the reaction medium. At this stage, even in supersaturated solutions ( $S > 1$ ), no nucleation occurs due to the high energy barrier for spontaneous nucleation. In phase II, when a higher degree of supersaturation is attained ( $S > S_c$ ), the energy barrier for the spontaneous homogeneous nucleation is exceeded followed by the nucleation burst and finalized with the formation of stable nuclei. Next, due to the nucleation and growth processes, the rate of monomer consumption will exceed the rate of monomer supply, and hence, the supersaturation decreases below  $S_c$ . Therefore, the nucleation becomes zero. In phase III, the growth of the formed nanoparticles continues under further monomer consumption as long as the system is in the supersaturated regime. In order to increase the mean NC size without

altering the narrow size distribution, subsequent injections of precursors can be carried out in order to keep the system in the critical supersaturation  $S_c$  regime.

*Nucleation* can be either heterogeneous or homogeneous. As summarized by Reiss *et al.*,<sup>37</sup> the *heterogeneous nucleation* can be achieved by using the method of “seeded growth.” In this method, the seeds are separately formed, isolated and later injected in the reaction mixture which contains the appropriate precursors and stabilizers for the growth in a concentration regime which does not induce further nucleation of seeds.<sup>38</sup> Heterogeneous nucleation requires lower activation energy than that of homogeneous nucleation and occurs at preferential sites of seed surfaces. These characteristics empowered the “seeded growth” method for the synthesis of spherical core/elongated shell semiconductor heterostructures, giving unprecedented control over the tunability of the diameter and length in the CdSe/CdS NCs or over the growth direction as for InP and InAs nanorods synthesized using Au NPs.<sup>39-41</sup> In the case of *homogeneous nucleation*, as mentioned above and depicted in **Figure 1.2**, the monomer formation precedes the nucleation and growth phases. In this case, the precursor transformation into monomers is often irreversible, and the conversion rate is not affected by the concentration of monomers or NCs.

Classical nucleation theory considers the nucleus as a sphere of a condensed phase having a radius  $r$  and free energy of the formation  $\Delta G_{(r)}$  – Eq. 1.1. According to Eq. 1.1, the free formation energy  $\Delta G_{(r)}$  is the sum of the surface energy (positive value described by  $4\pi r^2\gamma$ ) and the free energy of the bulk crystal formation  $\Delta G_V$  (volume energy; negative values for supersaturation  $S > 1$ ).

$$\Delta G_{(r)} = 4\pi r^2\gamma + \frac{4}{3}\pi r^3\Delta G_V \quad (1.1)$$

where  $\gamma$  is the surface tension and  $\Delta G_V = -\frac{RT \ln S}{V_m}$ , ( $R$  is the gas constant,  $T$  is the absolute temperature,  $V_m$  is the molar volume of the monomer in the crystal, and  $S$  is the supersaturation defined as the ratio between the monomer concentration and the solubility of the bulk material).

For the case of small particles, the free formation energy  $\Delta G_{(r)}$  has positive values due to the positive contribution of surface energy. Differentiation of  $\frac{d\Delta G_{(r)}}{dr}$  yields the critical radius that a particle needs to have in order to not be dissolved in the solution, but instead to grow, expressed as:

$$r_C = \frac{2\gamma V_m}{RT \ln S} \quad (1.2)$$



From Eq. 1.2, it can be deduced that high temperature and high supersaturation are necessary for obtaining small nuclei. Furthermore, by introducing 1.2 in 1.1 the expression for the critical free energy of nucleation,  $\Delta G_N$ , corresponding to the formation of stable nuclei, what is obtained is:

$$\Delta G_N = \frac{16\pi\gamma^3 V_m^2}{3(RT \ln S)^2} \quad (1.3)$$

The nucleation rate,  $dN/dt$ , can be interpreted as the rate of increasing the particle number  $N$ , and can be described using the Arrhenius equation, where  $A$  is a pre-exponential factor and  $k_B$  is Boltzmann constant – Eq. 1.4:

$$\frac{dN}{dt} = A e^{-\frac{\Delta G_N}{k_B T}} = A e^{-\frac{16\pi\gamma^3 V_m^2}{3k_B^3 T^3 (\ln S)^2}} \quad (1.4)$$

Based on Eq. 1.4, the degree of supersaturation  $S$  can be rewritten, and the critical supersaturation level  $S_c$  can be expressed as follows – Eq. 1.5:

$$\ln S_c = \sqrt{\frac{16\pi\gamma^3 V_m^2}{3k_B^3 T^3 \ln\left(\frac{A}{N}\right)}} \quad (1.5)$$

These equations are the mathematical translation of the prerequisite for the homogeneous nucleation to occur. The nucleation burst has to be as short as possible and not generate new nuclei in the later phases of particle growth. According to Eq. 1.2,  $S$  should be sufficiently high so that  $r_c$  can be adequately small. As translated from Eq. 1.5,  $dN/dt$  should be high in order to equilibrate or to surpass the redissolution rate of the particles, which will afford the accumulation and growth of the nuclei.  $S_c$  can be considered to be the threshold concentration at which the formation and accumulation of nuclei exceed their dissolutions, and the best way of achieving a high  $S$  is by using highly reactive precursors.

*Growth.* As described by Kwon and Hyeon,<sup>42</sup> the growth of each particle can be treated independently if the distance between particles is sufficiently large. Fick law expresses the diffusion of the monomers through the surface of the particle – Eq 1.6:

$$J = 4\pi x^2 D \frac{dC}{dx} \quad (1.6)$$

where  $J$  is the flux of monomers that diffuse through the surface of the particle,  $D$  is the diffusion coefficient,  $x$  is the distance to the center of the particle, and  $C$  is the concentration of monomers at distance  $x$  (**Figure 1.4**). If the concentration gradient is considered, then the Eq. 1.6 can be rewritten as – Eq. 1.7:

$$J=4\pi D \frac{r(r+\delta)}{\delta} (C_b - C_s) \quad (1.7)$$

where  $C_b$  is the bulk concentration of monomers at the distance of  $(r + \delta)$  and  $C_s$  is the monomer concentration at the surface of the nanoparticle. At a given  $r \ll \delta$  and  $(r + \delta) \approx \delta$ , then  $J$  is written as – Eq. 1.8:

$$J=4\pi r D (C_b - C_s) \quad (1.8)$$

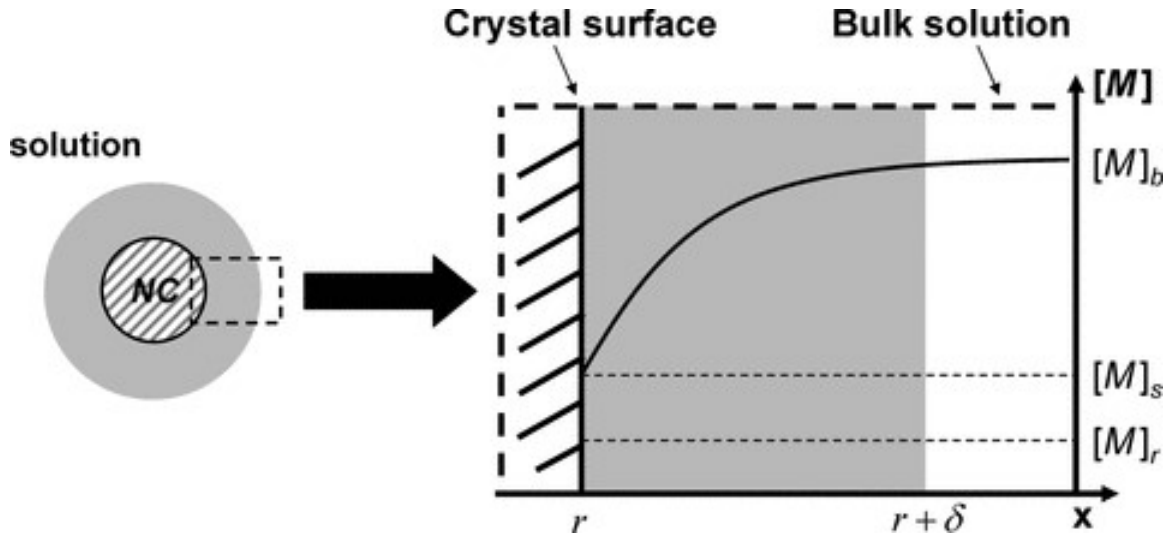


**Figure 1.4.** Schematic representation of the diffusion layer (gray area) at the nanocrystal surface (left), and graphical representation of monomer concentration as a function of distance  $x$  (right). Reprinted with permission from “Formation Mechanisms of Uniform Nanocrystals via Hot-Injection and Heat-Up Methods” by Kwon, S.G., Hyeon, T., *Small* 2011, 7, 2685-2702. © 2011 WILEY-VCH Verlag GmbH & Co. KGaA, Weinheim.<sup>42</sup>

If the limiting factor is the reaction at the surface, then  $J$  gets a new expression:

$$J=4\pi r^2 k (C_s - C_r) \quad (1.9)$$

where  $k$  is the reaction constant and is independent of particle size, and  $C_r$  is the solubility of a nanoparticle characterized by radius  $r$ .

Based on Eq. 1.7, 1.8, and 1.9, the growth rate  $dr/dt$  can be calculated as a function of the limiting factor (diffusion – Eq. 1.10; or surface reaction – Eq. 1.11; or none – Eq. 1.12):

$$\frac{dr}{dt} = (C_b - C_r) \frac{V_m D}{r} \quad (1.10)$$

$$\frac{dr}{dt} = (C_b - C_r) k V_m \quad (1.11)$$

$$\frac{dr}{dt} = (C_b - C_r) \frac{V_m D}{r + D/k} \quad (1.12)$$

According to the Gibbs-Thomson effect, the solubility of a spherical particle with radius  $r$  is affected by its size. This because of the extra characteristic chemical potential ( $\Delta\mu = \frac{2\gamma V_m}{r}$ ). Therefore, the solubility  $C_r$  of the particle of radius  $r$  can be calculated according to – Eq. 1.13:

$$C_r = C_b e^{\frac{2\gamma V_m}{rRT}} \quad (1.13)$$

By replacing  $C_r$  (Eq. 1.13) in Eq. 1.12, a general expression of the particle growth can be obtained – Eq. 1.14:

$$\frac{dr^*}{dt} = \frac{S - e^{r^*}}{r^* + K} \quad (1.14)$$

where the  $r^*$  is the dimensionless radius ( $r^* = \frac{RT}{2\gamma V_m} r$ , 1.15),  $K$  is the Damköhler number ( $K = \frac{RT}{2\gamma V_m} \frac{D}{k}$ , 1.16) and is an indicator of diffusion- or reaction-controlled system. When  $K < 0.01$ , the overall growth rate is dominated by the rate of mass transfer, and the growth is called *diffusion-controlled growth*. When  $K > 10$ , the growth rate is mainly determined by the surface reaction rate, and is called *reaction-controlled growth* (Figure 1.5).

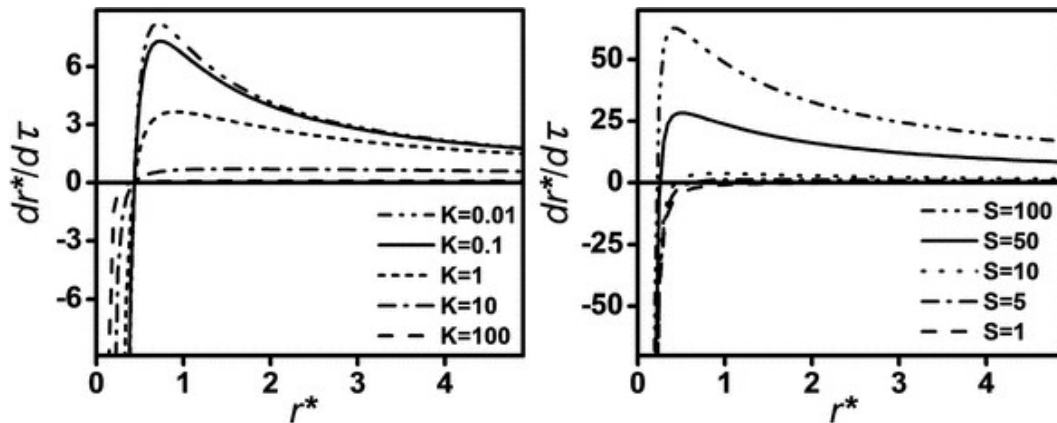


**Figure 1.5.** Graphical representation of the growth rate of a particle as a function of  $K$  (left) and  $S$  (right), for various values of  $K$  and  $S$ . Reprinted with permission from “Formation Mechanisms of Uniform Nanocrystals via Hot-Injection and Heat-Up Methods” by Kwon, S.G., Hyeon, T., *Small* 2011, 7, 2685-2702. © 2011 WILEY-VCH Verlag GmbH & Co. KGaA, Weinheim.<sup>42</sup>

**Figure 1.5** depicts how the growth of an individual particle is affected by mass transport and by the competing dissolving process. According to Eq. 1.10, the mass transport process enables the smaller particles to grow faster than the larger ones, and according to the Gibbs-Thomson effect, the smaller particles dissolve faster than larger ones because they are less thermodynamically stable (Eq. 1.13). At the point of zero growth rate  $dr^*/d\tau = 0$ , and by multiplying  $r_c$  in Eq. 1.2 and  $r^*$  in its describing expression, the dimensionless critical radius is

found to be  $r_C^* = \frac{l}{\ln S}$ . When  $r^* < r_C^*$ , the Gibbs-Thomson effect is powerful and would cause the complete solvation of the particles. In the case of  $r^* > r_C^*$ , the particles grow steadily, and the curve exhibits a negative slope (**Figure 1.5**). In conclusion, as can be noticed in **Figure 1.5**, a lower value of  $K$  and a higher value of  $S$  favor the surface reaction rate and make the growth process rather diffusion-controlled, as indicated by the left shift of  $r_C^*$  and steeper negative slope.

As described by Kwon and Hyeon,<sup>42</sup> the growth rate,  $dr/dt$ , of a particle can be calculated in the case of diffusion-controlled mode by combining Eq. **1.10**, **1.13**, and **1.15** and considering the Gibbs-Thomson effect – Eq. **1.17**:

$$\frac{dr}{dt} = \frac{K_D}{r} \left( \frac{1}{r^*} - \frac{1}{r} \right) \quad (1.17)$$

where  $K_D$  is given by the expression  $K_D = \frac{2\gamma D V_m^2 C_b}{kT}$ . In order to study the relationship between particle radius  $r$  and its dimensionless critical radius  $r_C^*$  in a size-focussing or defocusing system, the dimensionless radius can be substituted with the critical dimensionless radius  $r_C^*$ , and Eq. **1.17** becomes:

$$\frac{dr}{dt} = \frac{K_D}{r} \left( \frac{1}{r_C^*} - \frac{1}{r} \right) \quad (1.18)$$

In the case of reaction-controlled mode, the growth rate  $dr/dt$  of a particle is expressed by the Eq. **1.19**, obtained by combining the Eq. **1.11**, **1.13**, and **1.15** and substituting the  $r$  with  $r_C^*$ :

$$\frac{dr}{dt} = K_R \left( \frac{1}{r_C^*} - \frac{1}{r} \right) \quad (1.19)$$

where  $K_R = \frac{2\gamma D V_m^2 C_b}{RT}$ .

The derivative of  $dr/dt$  in Eq. **1.18** and **1.19** is described as the change in growth rate with radius  $r$  (expressed as  $d\Delta r/dr$ ) and takes the following form for the case of diffusion-controlled mode (Eq. **1.20**) and reaction-controlled mode (Eq. **1.21**):

$$\frac{d\Delta r}{dt} = \frac{K_D}{r^2} \left( \frac{2}{r} - \frac{1}{r_C^*} \right) \quad (1.20)$$

$$\frac{d\Delta r}{dt} = \frac{K_R}{r^2} \quad (1.21)$$

Considering the  $r_C^* = \frac{l}{\ln S}$ , Eq. **1.20** takes the following form:

$$\frac{d\Delta r}{dt} = \frac{K_D}{r^2} \left( \frac{2}{r} - \ln S \right) \quad (1.22)$$

Based on the Eq. 1.22 – diffusion-controlled mode, it can be determined whether the system is size-focusing (when  $(\frac{2}{r}-\ln S) < 0$  the  $dAr/dr$  is negative) or size-defocussing (if  $dAr/dr$  is positive). At a high level of supersaturation the  $(\frac{2}{r}-\ln S)$  is more likely to be negative, which is translated in a decrease of growth rate as  $r$  increases and size-focusing of the system. When the supersaturation level is low, the  $(\frac{2}{r}-\ln S)$  tends to be positive, which means that the system will be in a size-defocussing mode. In the case of a fixed level of supersaturation, where  $r$  is small, the  $(\frac{2}{r}-\ln S)$  tends to be positive indicating an increasing growth rate at small sizes, as suggested by the positive slope of  $dr^*/dt$  represented in **Figure 1.5**. If  $r$  further increases then  $(\frac{2}{r}-\ln S)$  tends to be negative as suggested by the negative slope of  $dr^*/dt$  (**Figure 1.5**) leading to a decreasing growth rate when the particles become large. In the case of reaction-controlled mode (Eq. 1.21),  $\frac{K_R}{r^2}$  always has positive values due to the Gibbs-Thomson effect, which means that the growth of larger particles is gaining momentum and the evolution of size distribution is thereby always a self-defocusing process.

As mentioned above, the nucleation and growth phase must be temporarily separated in order to achieve monodisperse NCs. As is already known, two ligand-assisted methods have been developed to produce highly monodisperse NCs: the *hot-injection (HI)* and *heating-up (HU) method*. In the case of the HI method, the separation of phases can be achieved by the rapid injection of the precursors into the hot solvent, which raises the concentration in the reaction mixture above the nucleation threshold. The nucleation burst is rapidly quenched by two factors: (i) the fast cooling of the reaction mixture (the injected solution is at room temperature); (ii) the decreased supersaturation due to the conversion of precursors into monomers and their consumption during nucleation. In a recent review, van Embden, Chesman, and Jasieniak summarized the differences between the HU and HI methods.<sup>43</sup> In the case of the HU method, the nucleation phase is much longer than in the HI method. The extended nucleation phase in the HU method is assured by the gradual monomer generation, which is accelerated during the temperature increase and subsequent heating stage. Hence, even after the nucleation is triggered, a high supersaturation is maintained for an extended period, overlapping with the growth phase, which leads to a broadened size distribution. In the same time, the size distribution broadening can be avoided while favoring size focusing if the supersaturation is high enough with respect to the solubility of the particles of the mean size. The essential factors in the HU method are the heating rate and the selection of the precursors

and ligands. For instance, increasing the heating rate leads to a decrease in the mean NC size and an increase of the NC concentration.

In the last couple of years, many studies reported discordant results in comparison with those predicted by the classical nucleation theory. For many nanoscale systems, the formation of ordered phases seems to involve nonclassical nucleation and growth processes. In recent years, extensive experimental and computational studies have reported the occurrence of metastable phases, multistep nucleation, and intermediate-mediated self-assembly, all of which affect the outcome of these reactions.<sup>44-45</sup> Although various nonclassical nucleation models have been developed in order to explain the deviations from CNT, they are united by the fact that during the reaction, intermediates containing multiple monomer units increase in concentration and their subsequent reactivity impact the later course of the crystallization process (**Figure 1.6**).<sup>46</sup>

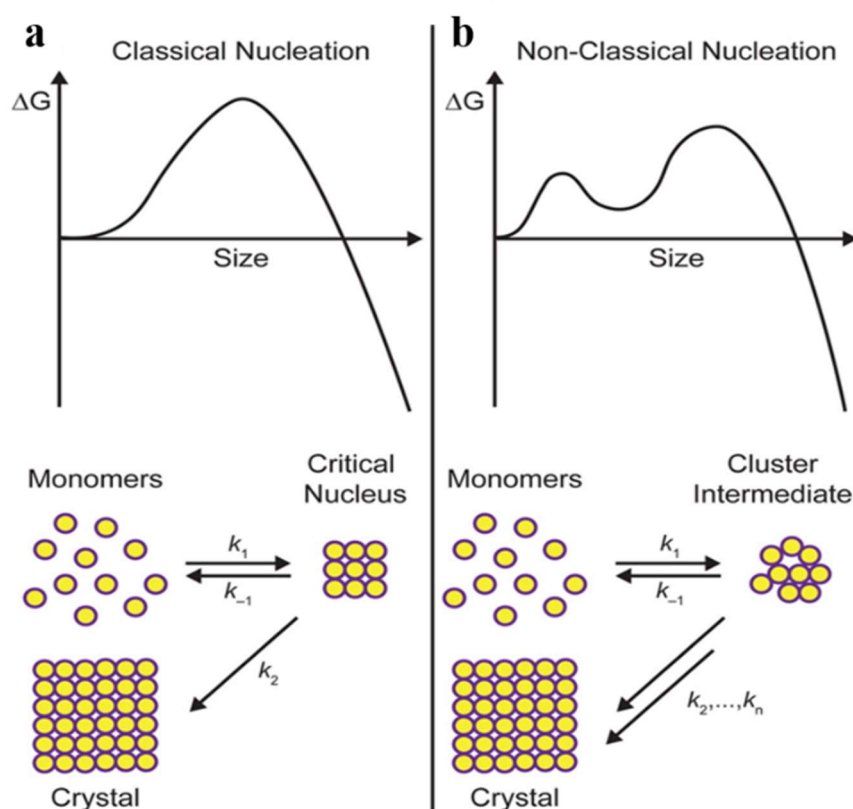


**Figure 1.6.** Plots of free energy change as a function of particle size and schematic representation of crystallization for classical (a) and nonclassical (b) nucleation models. In the classical model, the formation of the critical nucleus is rate determining and subsequent growth occurs continuously from monomers in solution while in nonclassical models, cluster intermediates form (often prenucleation) and then must transform (in a series of steps that can be slow) before crystal formation. Adapted with permission from Brandi M. Cossairt, *Chem. Mater.* 2016, 28 (20) 7181-7189. ©2016, American Chemical Society.

The CNT model proved to be reasonably accurate in helping scientists design new synthetic paths and understand the formation mechanisms for colloidal II-VI and IV-VI semiconductor QDs, but often showed deviations in the case of III-V semiconductor QDs. For instance, the nucleation of InP QDs involves the formation of magic-sized clusters (MSCs) which result either from low-energy electronic structures or favorable ligand coordination and are not accounted for in CNT.<sup>47-52</sup> In a recent study, Wall *et al.* proposed a new thermodynamic framework designed for a deeper understanding and demonstrated its utility for the case of InP QDs and Au NPs. The new model is called reaction-driven nucleation theory (RDNT) and makes use of CNT to which adds new terms in order to make more precise quantitative predictions. In the holistic approach of the RDNT model, the free energy of cluster formation and the free energy contribution from the chemical reaction system as a whole are considered. Also, the best available computational tools, such as density functional theory (DFT), are used to estimate more precisely the free energy of clusters.<sup>53</sup> Therefore, this new nucleation theory, in addition to phase transformation considered by the CNT, quantitatively counts the chemical thermodynamics for the role of chemical reactions (**Figure 1.7**). The work of cluster formation (**1.23**) can be written by multiplying the average (e.g., geometric mean) change in bulk free energy per generated crystalline monomer,  $kT \ln(\overline{Q}_{bulk}/K_{eq})$ , by the number of crystalline monomers in the cluster,  $n$ , then adding the excess free energy term,  $\Phi(n, \zeta, \xi)$ . The excess free energy of a cluster with  $n$  units characterized by the structural arrangement of cluster growth units,  $\zeta$ , and its reaction coordinates,  $\xi$ , is given when the cluster reaction has the same stoichiometry as the bulk crystallization reaction by the energy of the cluster with  $n$  units minus the bulk energy of  $n$  units.<sup>53</sup>

$$W(n) = nkT \ln(\overline{Q}_{bulk}/K_{eq}) + \Phi(n, \zeta, \xi) \quad (1.23)$$

The equation **1.23** is the central equation that enables thermodynamic simplification of the complex nucleation system, and expresses the required work to be put in a nucleation system in order to generate a cluster of  $n$  atoms from the reactants involved in the nucleation reaction. The first term has bulk stoichiometry and can be determined experimentally (e.g., UV-Vis absorbance spectroscopy) while the second term can be determined by computational approaches (e.g., DFT).<sup>54</sup>

**Figure 1.7** depicts a comparison between the work of cluster formation, according to CNT and RDNT. It can be observed that in the case of classical work of cluster formation, the first term depends only on the concentration,  $C$ , and the solubility,  $C_{eq}$ , of solvated growth

units, while the second term is expressed by a simplified form of  $\Phi(n, \zeta, \xi)$ . This simplified form treats clusters as having the same structural properties as a larger crystal and typically assumes that they are perfectly spherical.

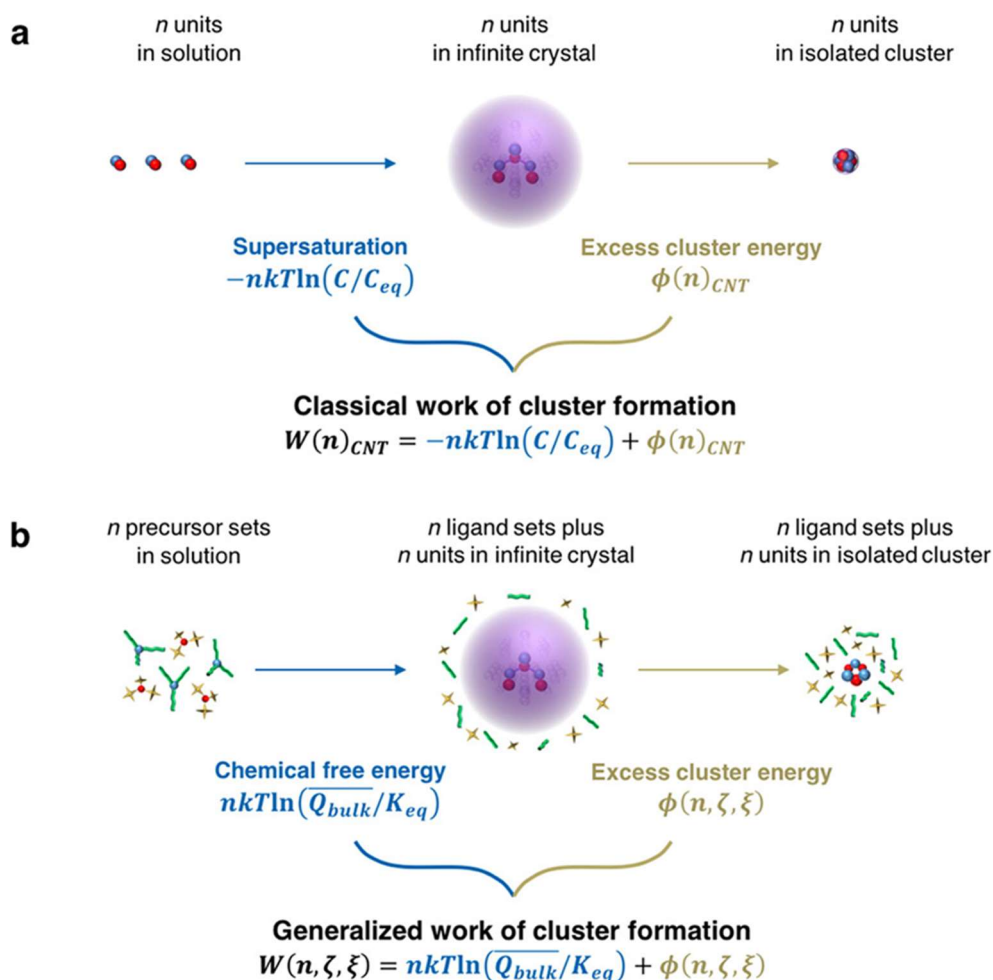


**Figure 1.7.** Comparison between the classical nucleation theory and reaction-driven nucleation theory for the work of cluster formation, which is given by two terms. The first term is defined by the difference in free energy between  $n$  units inside of a large crystal (e.g., bulk) and  $n$  dissolved units, while the second term is a correction factor defined by the difference in free energy between the cluster of  $n$  units and the  $n$  units inside of an infinite crystal. **(a)** In the case of CNT, the free energy difference between the dissolved and crystalline states depends only on the excess concentration of dissolved growth units,  $C/C_{eq}$ , and the correction factor is approximated as a simple function of the surface area of a hypothetical spherical cluster with the bulk crystal structure. **(b)** In the case of RDNT, the free energy difference of the dissolved precursors and crystalline state is a function of the entire nucleation reaction system,  $\overline{Q}_{bulk}/K_{eq}$ . The correction factor employed in RDNT is an exact correction and not a spherical, bulk approximation. Adapted with permission from Wall *et al.*, *J. Phys. Chem. C* 2018, 122, 9671-9679. ©2018, American Chemical Society.

As reported by Wall *et al.*, the quantitative predictions of RDNT are in line with the experimental observations of InP QD nucleation and can be useful for quantitative analyses and predictions of nucleation systems.



The surface chemistry of colloidal semiconductor NCs plays an essential role in many physical and chemical processes, such as solubility or photoluminescence, and may generate completely new effects (e.g., surface plasmon resonance, size-dependent catalytic activity, etc.).<sup>55-57</sup> A colloidal semiconductor NC (**Figure 1.8a**) is composed in general from an inorganic semiconducting nanosized core and an outer organic layer of surfactant molecules which serve as ligands, having various essential roles.<sup>58</sup> The inorganic core can have a binary (e.g., InP, InAs, GaP, GaAs, Cd<sub>3</sub>As<sub>2</sub>, Zn<sub>3</sub>As<sub>2</sub>), ternary (e.g., InAsP, GaInP<sub>2</sub>, (Cd<sub>x</sub>Zn<sub>1-x</sub>)<sub>3</sub>As<sub>2</sub>, CsPbX<sub>3</sub>, X = Cl, Br, I) or even quaternary (Cu<sub>2</sub>ZnSn(S,Se)<sub>4</sub>, CuIn<sub>1-x</sub>Ga<sub>x</sub>Se<sub>2</sub>, CsPbCl<sub>x</sub>Br<sub>3-x</sub>, ZnAgInSe) composition.<sup>19, 59-65</sup> Besides the multi-element composition, the core can be more complex by combining multiple semiconductor domains, generating heterostructures.<sup>66</sup> Such examples are (i) Janus NCs, where the NC consist of two separate semiconductor domains (**Figure 1.8b**); (ii) gradient alloys, in which the composition of the NC gradually changes from the inside to the surface or from one side to the other; (iii) or core/shell heterostructures, where one semiconductor is overcoated by at least one different semiconductor (**Figure 1.8c**).<sup>67-69</sup> Although its semiconductor crystal structure can describe the inorganic core, the whole NC's structure is much more complicated. Due to their small size, spherical NCs are not perfectly spheric, but rather truncated exposing different “facets”, as can be observed in **Figure 1.8a**.

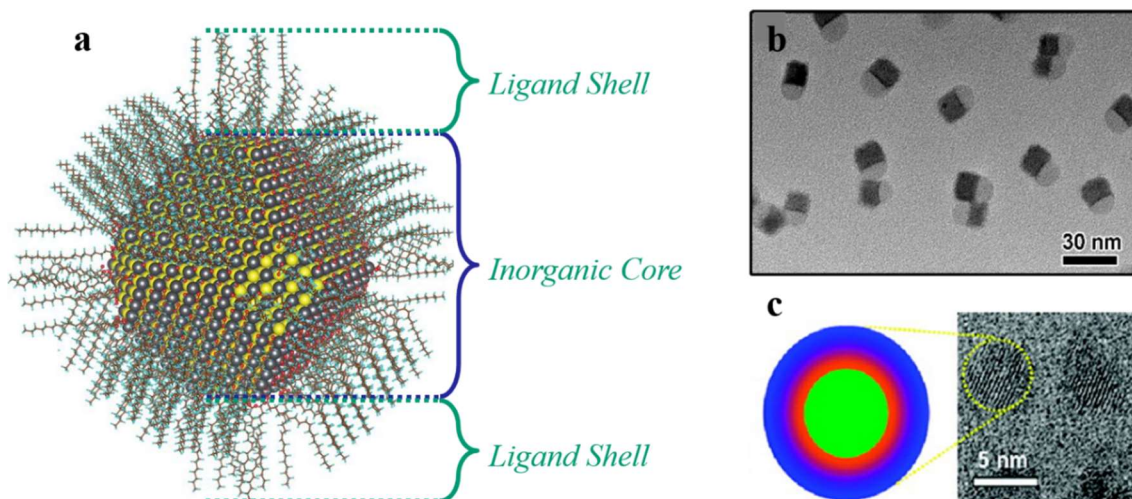


**Figure 1.8.** (a) Illustration of a calculated atomic structure of a 5 nm PbS NC core capped by an organic layer of ligands (Adapted with permission from *Science*, 2014, 344, 1380-1384. ©2014, American Association for the Advancement of Science).<sup>70</sup> (b) TEM image displaying CsPbBr<sub>3</sub>/SiO<sub>2</sub> Janus-type NCs (Adapted with permission from *J. Am. Chem. Soc.* 2018, 140, 406-412. © 2018, American Chemical Society).<sup>67</sup> (c) Graphical representation of a InP QD core (green) overcoated by a double-gradient shell of ZnSeS (ZnSe – red color, ZnS – blue color, and the transition purple color represents the gradient interpretation of the two protective shells), depicting the structure of the QD marked in the HR-TEM image. Adapted with permission from *Chem. Matter.* 2011, 23, 4459-4463. © 2011, American Chemical Society.<sup>68</sup>

The ligands that form the outer organic shell contribute, from the beginning of the reaction, to the transformation of the starting chemicals into molecular precursors, which light-emitting into monomers. They assure the growth of NCs at elevated temperatures by preventing the uncontrolled aggregation of the monomers and formed nuclei in solution. Another critical role of the ligands is that they enable the control of size and morphology of the final NCs by regulating the nucleation and growth kinetics. By providing appropriate repulsion forces of steric or electrostatic nature, they stabilize the NCs in the colloidal form once the reaction is finished. Also, ligands have a significant role in passivating the surface of NCs by completing the coordination sphere of the surface atoms, ideally preventing the formation of deep trap states which are detrimental for luminescence properties. In most of the cases, two or more ligands are applied simultaneously (e.g., use of myristic acid, for the synthesis of InP QDs, or oleic acid (OA) and oleylamine (OLAH) for the synthesis of CsPbX<sub>3</sub> perovskite NCs, X = Cl, Br, I) in order to fulfill all the mentioned requirements. For syntheses in organic solvents, the ligands are generally of surfactant type and consist of a polar headgroup (e.g., carboxylic or phosphonic acid, amine, thiol) that shows an affinity for the NC surface, and one or several alkyl chains with an affinity for the medium (solvent). In some cases, the ligands play a dual role: ligand and solvent, and are classified as a coordinating solvent. Trioctylphosphine oxide (TOPO), OA and OLA are among the most popular coordinating solvents used in the synthesis of monodisperse colloidal NCs.<sup>13, 70-72</sup>

Interaction between the NC core and ligand headgroup can be rationalized by employing the *classification of covalent bonds*, proposed initially for metal coordination complexes and adapted for NCs by Owen and co-workers (**Figure 1.9**).<sup>73-74</sup> This classification is based on the possible bonding functions, and the ligands are divided into *X*-, *L*-, and *Z*-type, based on the number of electrons involved and the identity of the electron donor and acceptor groups. *X*-type ligands are ligands that have a single occupied orbital and requires one electron from the element center in order to form a two-electron covalent bond. In practice, *M-X* bonds often cleave heterolytically generating ionic, closed-shell fragments. *X*-type ligands can be neutral radicals binding neutral surface sites (each with an unpaired electron) or monovalent ions binding oppositely charged sites at the NC surface. Such examples of *X*-type ligands include carboxylates (RCOO<sup>-</sup>), thiolates (RS<sup>-</sup>), and phosphonates (RPO(OH)O<sup>-</sup>), as well as inorganic ions (e.g., Cl<sup>-</sup>, InCl<sub>4</sub><sup>-</sup>, AsS<sub>3</sub><sup>3-</sup>) or bound ion pairs (e.g., NEt<sub>4</sub><sup>+</sup>I<sup>-</sup>) in a nonpolar solvent.

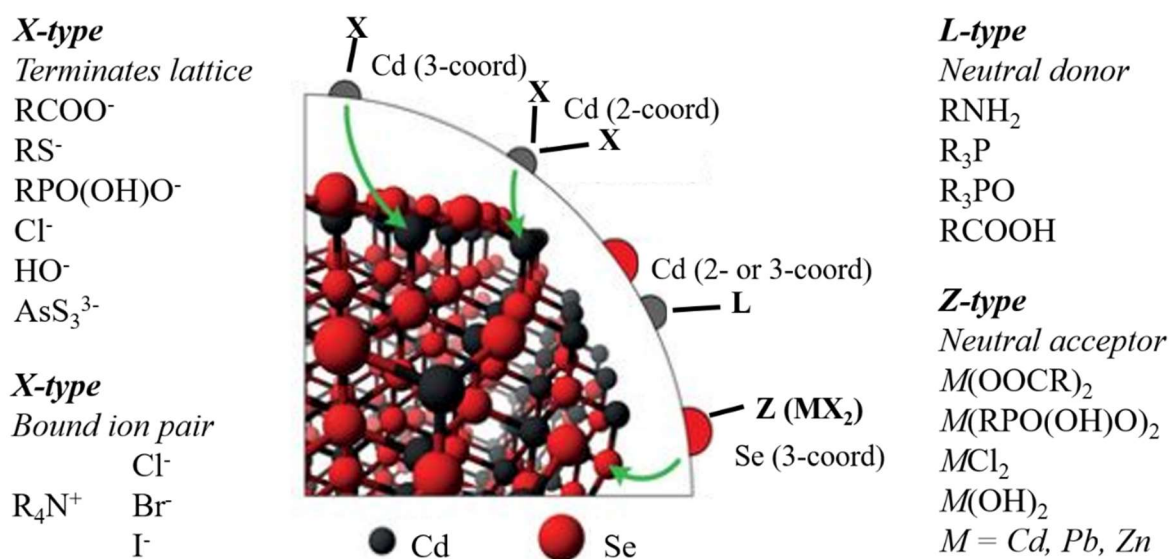


**Figure 1.9.** Classification of ligand binding motifs at the surface of a CdSe NC. Anionic X-type ligands bind to surface cations imparting electroneutrality to metal-rich NC facets. Neutral L-type electron donor ligands attach to electrophilic metal sites on stoichiometric NC facets; Neutral Z-type electron acceptor ligands bind to electron-rich undercoordinated metal atoms. Green arrows indicate examples of such atoms at the surface of the CdSe NC model. Adapted with permission from *Nature Materials* 2016, 15, 141–153. © 2016 Macmillan Publishers Limited.<sup>75</sup>

L-type ligands are neutral two-electron donors with a lone electron pair that datively coordinates surface metal atoms — such examples of L-type ligands are amines (RNH<sub>2</sub>), phosphines (R<sub>3</sub>P), and phosphine oxides (R<sub>3</sub>PO). Z-type ligands are characterized by an empty orbital that receives an electron pair from the metal — such as Pb(OOCR)<sub>2</sub> or CdCl<sub>2</sub>. The Z-type ligands can interact with the surface of metal chalcogenides, oxides and other NCs that expose electron-rich Lewis basic sites, while the nucleophilic (electron-rich) X- and L-type ligands bind to electron-deficient (electrophilic) surface sites with pronounced Lewis acidity, such as undercoordinated metal ions at the NC surface.

This classification is useful for expressing the composition and surface chemistry of NCs. For instance, for the above example presented in **Figure 1.9**, the CdSe NCs are capped by a combination of X- and L-type ligands and can be expressed as (CdSe)<sub>m</sub>(Cd<sub>n</sub>X<sub>p</sub>L<sub>q</sub>), where *m* relates to the size of the NC core and *n*, *p*, and *q* describe the ligand shell composition. For more details about this topic, the reader is kindly invited to consult Boles *et al.*<sup>75</sup>

Stabilizing ligands can directly influence the optical, electrical, magnetic, and catalytic properties of NCs. In a QD, the valence and conduction bands are split into discrete, quantum-confined states that generate size-dependent luminescence colors.<sup>10</sup> In general, undercoordinated surface atoms with dangling bonds contribute a set of electronic states with

energies localized between the highest occupied and lowest unoccupied orbitals of the QD (**Figure 1.10**). These localized states behave as traps for electrons and holes, generating the quenching of the photoluminescence and affecting the performance of NC-based devices.

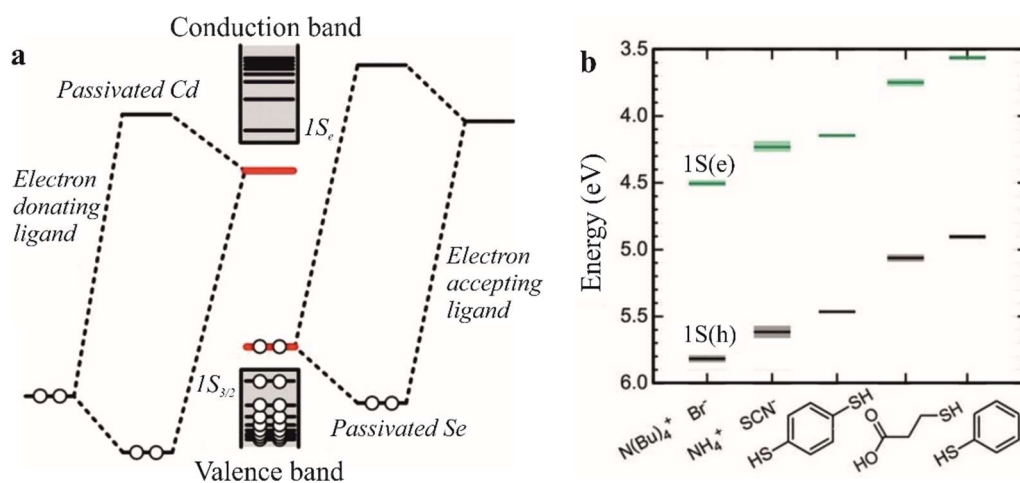


**Figure 1.10.** Influence of ligands on NC surface states and within the NC core. **(a)** Simplified molecular orbital diagram of a CdSe QD showing that the energies of Cd and Se surface electronic states (red levels) are pushed outside the bandgap upon ligand binding. **(b)** Graphical representation of the influence of surface ligands upon the energy of highest occupied, 1S(h), and lowest unoccupied, 1S(e), states of PbS QDs measured by ultraviolet photoelectron spectroscopy for representative organic and inorganic ligands – bromide, thiocyanate, benzenedithiol, 3-mercaptopropionic acid, and benzenethiol. Adapted with permission from *Nature Materials* 2016, 15, 141–153. © 2016 Macmillan Publishers Limited.<sup>75</sup>

As can be observed in **Figure 1.10a**, a new set of molecular orbitals with bonding ( $\sigma$ ) and antibonding ( $\sigma^*$ ) character are formed by the interaction of the ligand with the surface atoms of the NC. The bonding orbitals are localized while the antibonding orbitals are delocalized with respect to the energies of the non-interacting surface atom and ligand. The energies of  $\sigma$  and  $\sigma^*$  orbitals are shifted outside the bandgap by the formation of a strong covalent bond between the surface atom and ligand, eliminating the trap states from the bandgap. However, even if surface passivation upon ligand binding is common practice it is not always the best approach because some types of ligands may quench the photoluminescence, such as alkanethiols for CdSe QDs by fast hole trapping.<sup>76</sup> Ligands may also alter the absolute energy of QDs electronic states. For instance, for the case of PbS QDs ( $\sim 3.5$  nm), as can be noticed in **Figure 1.10b**, the energies of 1S(h) and 1S(e) states were measured by ultraviolet photoelectron spectroscopy (UPS) when different types of ligands stabilized the NCs, and a variation of band energies ( $\sim 0.9$  eV) could be observed across various ligand choices.<sup>77</sup> When ligands like alkyl carboxylates, phosphonates or amines stabilize the QDs, the electronic transitions are assumed to take place only within the inorganic core. The

effect of surface ligands and oscillator strength of the surface atom-ligand interactions are assumed to be negligible because the ligand frontier orbital energies are far from QD core states, maintaining strong ligand character even when bound to the QD surface. In contrast, ligands characterized by a redox potential comparable to the QD electron affinity and ionization potential favor the mixing of states between ligands and the inorganic core. For instance, when phenyldithiocarbamate ligands exchange oleate ligands on CdSe QDs surface, the former can reduce the optical bandgap of CdSe QDs by up to  $\sim 0.2$  eV by delocalizing the exciton hole via mixing with QD states in the proximity of the valence band edge.<sup>78</sup>

Despite enabling effective control over the kinetics of NC nucleation and growth, design of shape, or colloidal stability in various solvents, the long-chain insulating organic ligands must be replaced by other surface-binding species better suited for the end application. This process facilitates the integration of NCs into solids with tunable electronic properties, as required for NC-based solar cells, light-emitting diodes, photodetectors, thermoelectrics, transistors, and integrated electronic circuits.<sup>79</sup> It has been demonstrated that by exchanging the organic ligands with smaller inorganic species, such as metal chalcogenide complexes, oxo- and polyoxometallates, and metal-free ions ( $S^{2-}$ ,  $HS^-$ ,  $Se^{2-}$ ,  $OH^-$ ,  $SCN^-$ , etc.), the charge transport in NC solids are improved while the integrity, size-tunable optical properties, and solution-processability of NCs are preserved.<sup>79-88</sup> Such an example of ligand exchange is summarized in **Figure 1.11**, which describes a general methodology for solution-phase ligand exchange applied to a variety of inorganic NCs, such as InP, PbS, CdSe, CdS, etc., where, according to Dirin *et al.*, the halometallate ligands passivate the surface of the NCs efficiently improving the excitonic photoluminescence.<sup>79</sup>

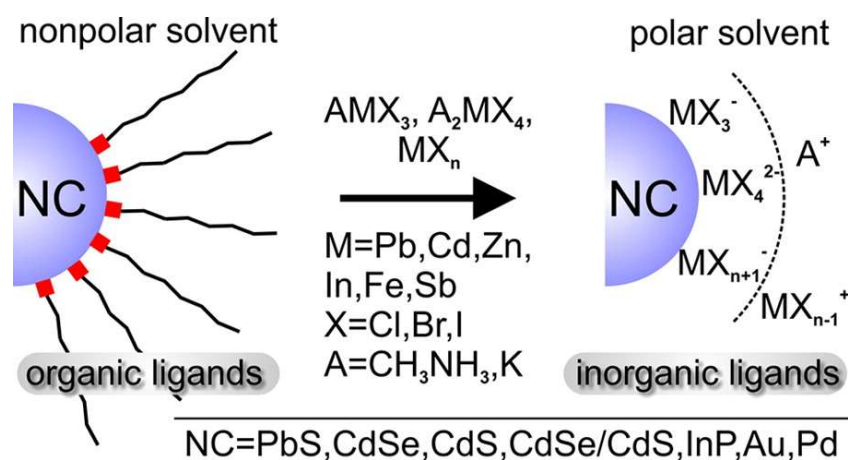


**Figure 1.11.** Schematic representation of the solution-phase ligand exchange methodology for obtaining halometallate-capped colloidal NCs. Adapted with permission from *J. Am. Chem. Soc.* 2014, 136, 6550–6553. © 2014 American Chemical Society.<sup>79</sup>

## 1.2. Semiconductor NCs: between molecules and bulk

*Quantum confinement effect* is one of the essential characteristics of semiconductor NCs and is responsible for various properties, such as optical and electronic properties. As summarized by Ashrafi, quantum confinement effect can be observed once the dimensions of a particle are considerably reduced to the nano-size.<sup>89</sup> At the nanoscale, as the confining dimension decreases to certain limits (which is characteristic to each material), the energy spectrum becomes discrete in contrast to the bulk, which is characterized by continuous energy states (**Figure 1.12**). As an effect of the confinement, the bandgap of the nanostructures becomes size and shape dependent, resulting in a blue shift in the optical response, as discussed in greater detail in the next section.

In order to understand the quantum confinement effect, one would need to know the basics of quantum mechanics, more precisely the role of a *particle-in-a-box*. The energy in a box can be quantitatively described as it follows:

$$E_n = \frac{n^2 \hbar^2}{8mL^2} \quad (1.24)$$

where  $n$  is the quantum number,  $\hbar$  is the Planck's constant,  $m$  is the mass, and  $L$  is the size of a particle. This means that the bandgap energy of a semiconductor NC increases, starting from the corresponding value of the bulk, as its size decreases. As depicted in **Figure 1.12**, at the nanoscale, the energy-level separation increases generating discrete levels in bulk solids, however, the energy levels are closely spaced as quasi-continuous bands.

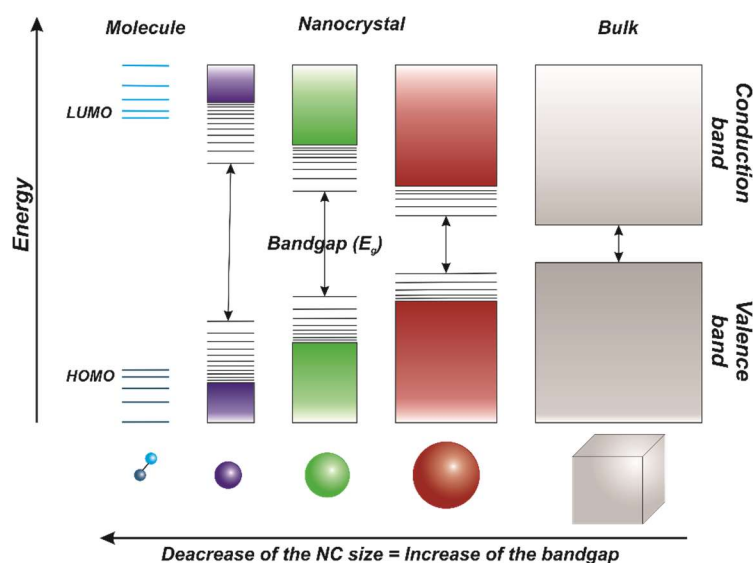


**Figure 1.12.** *Quantum confinement effect and depiction of the evolution of band structure. Comparison of a molecule case, NCs, and bulk systems, showing the size-dependent bandgap of NCs and formation of the discrete states near the band edge.*

The onset of quantum confinement is dependent on a series of parameters, such as the dielectric constant of the semiconductor and effective mass of the charge carriers, but calculations have shown that most nanomaterials show quantum confinement effects at sizes below 10 nm. Therefore, the quantum confinement effect occurs when nanomaterial dimensions are considerably reduced, approaching the size of an exciton in bulk crystal, called the Bohr exciton radius, defined by:

$$a_B = \frac{\hbar}{m_e c \alpha} \quad (1.25)$$

where  $\hbar$  is the Planck's constant,  $m_e$  is the electron rest mass,  $c$  is the speed of light, and  $\alpha$  is the fine structure constant. In other words, when the quantum confinement effect is present, that means that the excitons are trapped in a very small area.

As depicted in **Figure 1.12**, when an NC is found in strong quantum confinement, that it is very small size. Thus, the behavior of the exciton ensembles more like an atom as its surrounding space shortens, being similar to the case of the 3D model of a particle in a box, and is expressed as it follows:

$$\Psi_{n_x, n_y, n_z} = \sqrt{\frac{8}{L_x L_y L_z}} \sin\left(\frac{n_x \pi x}{L_x}\right) \sin\left(\frac{n_y \pi y}{L_y}\right) \sin\left(\frac{n_z \pi z}{L_z}\right) \quad (1.25)$$

Furthermore, the energy level in the quantum level of materials/atoms takes the following form:

$$E_{n_x, n_y, n_z} = \frac{n^2 \pi^2}{2m} \left[ \left(\frac{n_x}{L_x}\right)^2 + \left(\frac{n_y}{L_y}\right)^2 + \left(\frac{n_z}{L_z}\right)^2 \right] \quad (1.27)$$

Moreover, due to the 1D confinement, the expression of the electron energy levels for an infinitely deep potential well (Eq. **1.28**) can be found from the solution of the Schrodinger equation:

$$E_n = \frac{\hbar^2 \pi^2}{2\mu L^2} n^2, \quad n=1, 2, 3, \dots \quad (1.28)$$

where  $\mu$  is the effective mass of the electron and the dependence of the energy levels on  $L^2$  is the quantum size effect. The dispersion relation for the conduction band can be written (for confinement in the  $z$ -direction) as:

$$E(k) = E_c + E_{nz} + \frac{\hbar^2 (k_x^2 + k_y^2)}{2\mu} \quad (1.29)$$

where  $E_c$  is the energy of the bottom of the conduction band, and  $E_{nz}$  is given by Eq. **1.28**. For the conduction band, the density of states per unit area in a 2D quantum well system in the subbands can be expressed as (for energies higher than  $E_c + E_{nz}$ ):

$$g(E) = \frac{\mu^2}{\pi \hbar^2} \quad (1.30)$$

Thus, for each quantum number  $nz$ , the density of states is constant and the overall density of states is the sum of these for all values of  $nz$ , which results in a staircase-type distribution with a step height given by the  $g(E)$  (**Figure 1.13**).

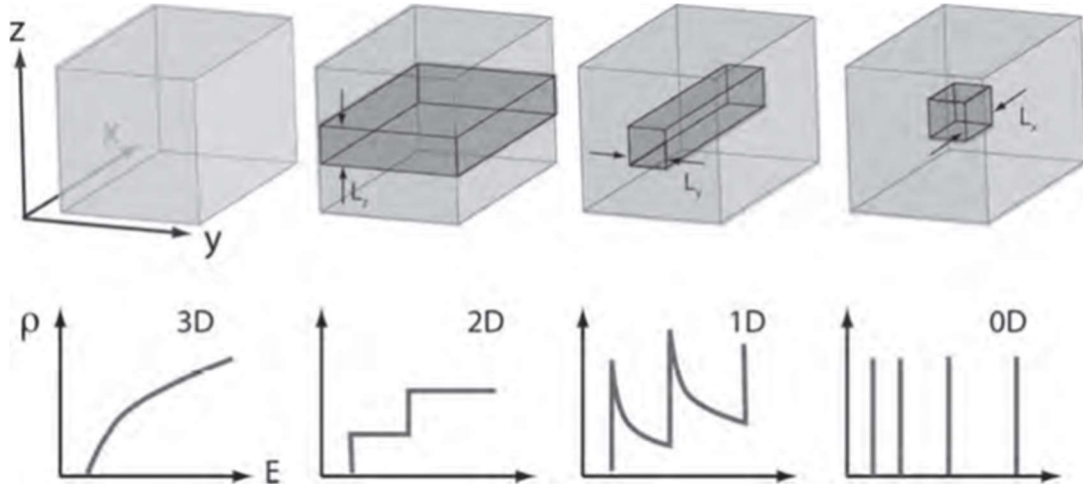


**Figure 1.13.** Graphical representation of the density of states as a function of energy in bulk – 3D, quantum wells – 2D, quantum wires – 1D, and quantum dots – 0D. Adapted with permission from *Encyclopedia of Semiconductor Nanotechnology, Vol. 5, 2011*. © 2011 American Scientific Publishers.<sup>89</sup>

In a 1D quantum well, the case of nanowires under confinement regime, the carriers are confined in two directions,  $z$  and  $x$ , and the dispersion relation for the conduction band has the following expression:

$$E(k) = E_c + E_{nz} + E_{nx} + \frac{\hbar^2 k_y^2}{2\mu} \quad (1.31)$$

In each of the sub-bands, the density of states can be described as a function of energy by:

$$g_e(E) \approx E^{-\frac{1}{2}} \quad (1.32)$$

In the case of a quantum dot system, 0D, the carriers are confined in all three directions, and the relation for the conduction band can be expressed as:

$$E(k) = E_c + E_{nz} + E_{nx} + E_{ny} \quad (1.33)$$

Therefore, for each of the situations: (i) 3D – bulk systems with continuous bands, (ii) 2D – quantum wells (nanoplatelets) strongly confined in only one direction, (iii) 1D – quantum wells (nanowires) manifesting strong confinement in two directions, and (iv) 0D – quantum dots with strong confinement on all three directions; the density of states is described by a set of discrete  $\delta$ -functions, as depicted in **Figure 1.13**.



### 1.3. Optical properties of colloidal semiconductor nanocrystals

*Absorption* of a photon by an NC will occur if photon's energy is exceeding the band gap energy of the NC. By decreasing the NC's size, a blue shift of the absorption onset is observed due to quantum confinement.<sup>90</sup> An absorption feature near the absorption onset, which corresponds to the excitonic peak, is positioned at specific wavelengths depending on the bandgap of the NC and its size, while the shape and width are influenced by the size distribution and the morphology of the NCs (**Figure 1.14**).<sup>91</sup> Therefore, samples consisting of polydisperse NCs typically exhibit more a shoulder-like absorption feature at the position of the excitonic transition. In general, it can be stated that the larger the number of such spectral features and the more distinctly they are resolved in the absorption spectrum, the smaller is the size dispersion of the NCs.

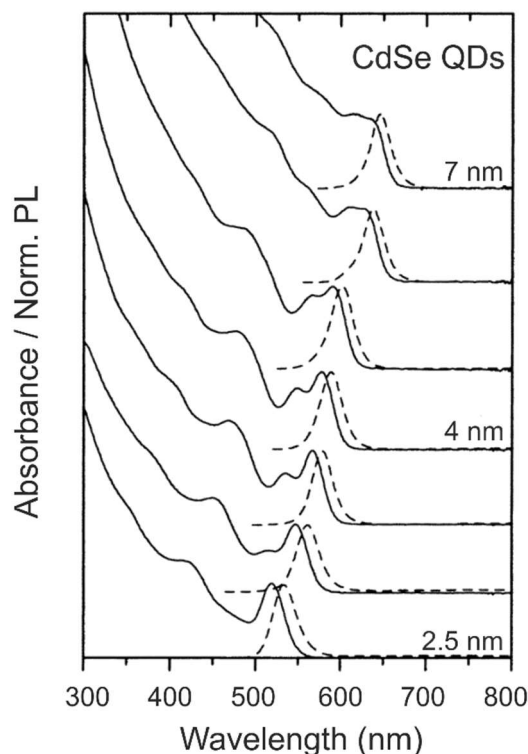


**Figure 1.14.** Room-temperature absorption and emission spectra of CdSe NCs are showing the dependence between the size of the NC and optical properties. Adapted with permission from *Nano Lett.* 2001, 1, 207–211. © 2001 American Chemical Society.<sup>91</sup>

*Photoluminescence* (PL) is the generation of luminescence as a result of the excitation by photons, and is classified in fluorescence and phosphorescence, depending upon the electronic configuration of the excited state and emission pathway. Fluorescence occurs when a semiconductor NC absorbs photons with a higher energy  $h\nu_e$  than its band gap and emits light

of a higher wavelength (lower energy  $h\nu_f$ ) after a short interval, called the fluorescence lifetime (Figure 1.15).

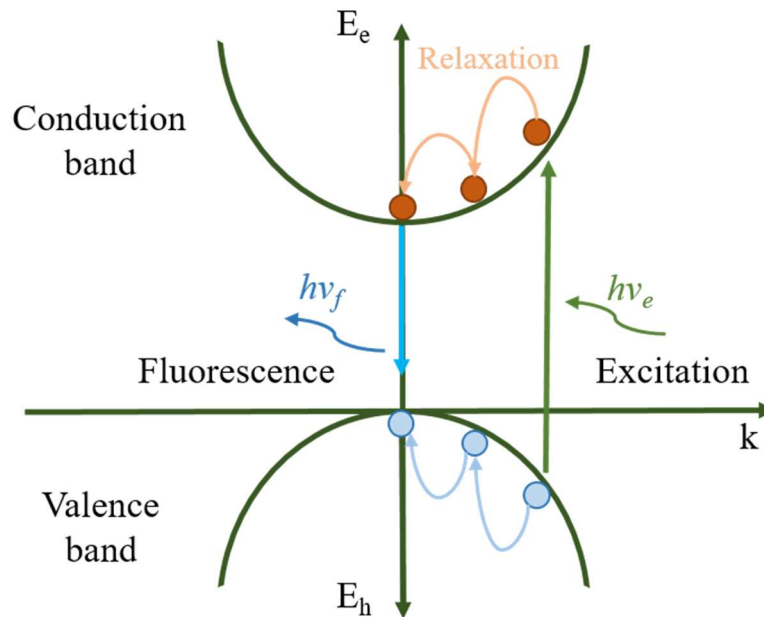


**Figure 1.15.** Graphical representation of the fluorescence phenomenon in bulk semiconductors. Adapted with permission from SpringerWienNewYork: *Semiconductor Nanocrystal Quantum Dots. Synthesis, Assembly, Spectroscopy and Applications* by Andrey L. Rogach ©2008 Springer-Verlag/Wien (2008).<sup>92</sup>

Phosphorescence occurs similarly but due to the symmetry of state it shows a considerably longer excited state lifetime. The energy of the emitted photons corresponds to the band gap of the NC and, as a consequence, the emission wavelength can be tuned by adjusting the size of the NC. It should be stressed that for an efficient band edge emission, the NCs must have a well-passivated surface. If the NC's surface is not efficiently passivated, the charge carriers will be trapped in the surface states, enhancing non-radiative recombination. As can be noticed in Figure 1.14, the PL peak maxima are approximately 10-20 nm red-shifted in comparison with the excitonic peak in the absorption spectra. This red-shift is generated by the particular structure of the exciton energy levels inside the NC and is called generic Stokes-shift. As reported earlier, in bulk wurtzite CdSe, the exciton band edge state ( $1S_{3/2} 1S_e$ ) is eight-fold degenerate, while in CdSe NCs, the degeneracy is partially lifted and the band edge state is split into five states.<sup>93-94</sup> The degeneracy is reduced to five states in the case of CdSe NCs due to the internal crystal field and the electron-hole exchange interaction, which is strongly enhanced by the quantum confinement.

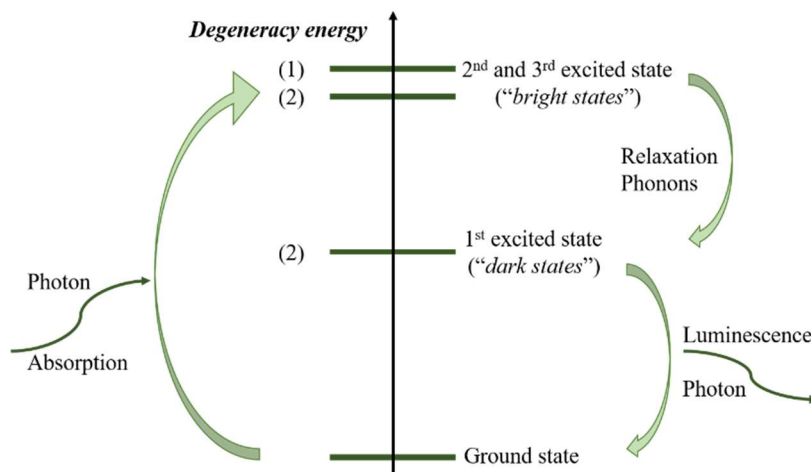


**Figure 1.16** Schematic representation of the exciton states of CdSe NCs involved in absorption and emission processes. Adapted with permission from SpringerWienNewYork: *Semiconductor Nanocrystal Quantum Dots. Synthesis, Assembly, Spectroscopy and Applications* by Andrey L. Rogach ©2008 Springer-Verlag/Wien (2008).<sup>92</sup>

As depicted in **Figure 1.16**, only three states are optically active. Because of symmetry reasons, two of the five states (one singlet and one doublet) are optically inactive. The energetic level of the optically active states depends on the size and shape of the NC. In the case of weak excitation of a given state, the absorption of the photon depends on the oscillator strength of the given state. Because the bright states (second and third) have a much higher oscillator strength than that of the dark state (first), the excitation occurs at the bright states. Due to the relaxation of the bright states, a substantial population on the dark state is created, enabling the radiative recombination. Thus, photoluminescence occurs as it depends on the product of oscillator strength and the population of the respective state.

*Photoluminescence quantum yield.* The photoluminescence quantum yield (PL QY) is the ratio between the number of absorbed photons and the number of emitted photons. The theoretical value of 1 for QY is challenging to achieve, and this is mainly attributed to the quality of the NC surface. QY values can be enhanced by improving the passivation of the NC surface by involving different procedures such as growing a shell, ligand exchange, or surface treatment with acids. For instance, it was reported that for the case of III-V semiconductor QDs, an enhancement of the PL QY of InP QDs from an initial value of about 1% up to 25-40% is possible upon treatment with HF.<sup>95-96</sup>

*Core/shell structures.* An essential strategy for improving the optical properties and robustness of the NCs is to overgrow an appropriate shell of a second semiconductor, generating a core/shell heterostructure.<sup>66, 97</sup> An essential criterion to take into account when

choosing a semiconductor material to serve as a shell is the band gap and how this aligns with the band gap of the core NC. According to Reiss and co-workers, **Figure 1.17** gives an overview of the band alignment of some of the most interesting III-V and II-VI semiconductor materials which are mostly used in NC synthesis.<sup>98</sup>

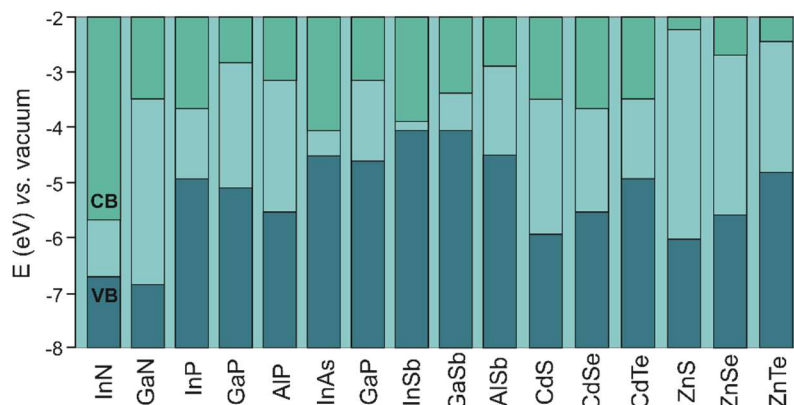


**Figure 1.17.** Schematic representation of electronic energy levels of some III-V and II-VI semiconductors based on their valence band offsets as reported by Wei *et al.* (VB = valence band, CB = conduction band). Adapted with permission from Small 2009, 5, 154-168. ©2009 Wiley-VCH Verlag GmbH & Co. KGaA, Weinheim.<sup>98</sup>

The shell can have different functions in core/shell NCs depending on the band gaps and the relative position of electronic energy levels of the involved semiconductors. According to Cossairt and co-workers, based on the band alignment of the core and shell materials, three most common situations of core/shell systems can be identified: type I, type II and advanced gradient or multi-shell heterostructures (**Figure 1.18**).

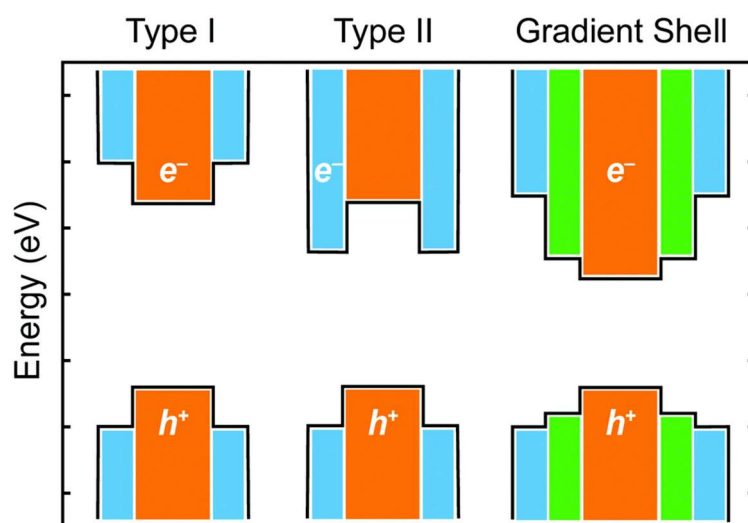


**Figure 1.18.** Graphical representation of energy diagram of type I, type II, and representative gradient core-multishell NC heterostructures. Adapted with permission from Chem. Commun. 2018, 54, 7109–7122. ©2018 The Royal Society of Chemistry.<sup>66</sup>

*Type I* band alignment entails when the band gap of the shell material is larger than that of the core material, and both electrons and holes are confined in the core. In a *type II* band alignment situation, either the valence band edge or the conduction band edge of the shell material is located in the band gap of the core. This band alignment leads, upon excitation of the core/shell heterostructure NC, to a spatial separation of the hole and the electron in different regions of the core/shell structure. The third most common type of heterostructures is the *gradient or multishell type* used to overcome the lattice mismatch between the core and the shell material to afford the overgrowing a shell with significant thickness without deteriorating the PL properties.

In type I core/shell heterostructure systems, the primary role of the shell is to passivate the surface of the core and to enhance its optical properties. The shell's purpose in this situation is more a protective one, by physically separating the optically active core and its surface from the surrounding medium. Therefore, the NCs become more robust, and their optical properties are less affected by changes that occur in the surrounding environment that are induced, for instance, by the presence of oxygen or water molecules. Also, the growth of the shell reduces the number of surface dangling bonds, which are known to act as trap states for charge carriers, reducing the PL QY. For example, in the case of InP cores characterized by no PL properties, 50% and 60% PL QY was attained by growing a shell of ZnSe and ZnS, respectively.<sup>72</sup> Usually, shell growth in case of type I core/shell system is accompanied by a small redshift of the excitons peak in the UV-Vis absorption and PL spectra, which is attributed to a partial leakage of the excitons into the shell material.

In type II core/shell heterostructure systems, overgrowth of the shell is typically accompanied by a large redshift of the PL spectrum. The primary role in this situation is to tune the optical properties. They allow the tuning of the PL emission towards spectral ranges that are challenging to reach by tuning the core dimensions or with other materials and is attained by modulating the thickness of the shell. Type II core/shell heterostructures have been developed in particular to cover the near infrared spectral range by designing, for instance, CdTe/CdSe, CdSe/ZnTe or CdS/CdTe core/shell NCs for bioimaging applications.<sup>99-100</sup> The resulting type II core/shell heterostructures show prolonged PL decay times compared to with the type I core/shell heterostructures, due to the lower overlap of the electron and hole wavefunctions. The PL QYs of the type II heterostructures can be enhanced by the overgrowth of an outer shell of appropriate material in the same manner as in the type I systems.

According to Reiss and co-workers, one of the motivations for overgrowing a gradient shell or multiple shells onto NCs is the difficulty in satisfying the requirements of appropriate electronic (bandgap, band alignment) and structural (lattice mismatch) parameters simultaneously for most binary core/shell systems.<sup>97</sup> In most cases, the lattice mismatch between the core and the shell material limits the overgrowth of a shell with considerable thickness without deteriorating the photoluminescence properties. In order to reduce the strain between the core and the outer shell, two approaches can be used: (i) the overgrowth of a gradient shell, typically type I (e.g., InP/ZnSeS, InAs/ZnCdS), or (ii) multiple shells (e.g., InP/GaP/ZnS, InP/ZnSe/ZnS, InAs/CdSe/ZnS, InAs/CdSe/CdS).<sup>68, 101-106</sup> In both cases, in order to reduce the lattice-strain between the core and shell, a semiconductor material characterized by band offsets located between those of the core and outer shell is used to act as a “lattice-adaptor.”<sup>97</sup> These two cases are quite distinctive despite the similarity of their working principle. For instance, such approaches are very beneficial for InP and InAs QDs, which are a greener alternative for more toxic conventional semiconductor Cd- and Pb-based chalcogenides. The optoelectronic properties of InP and InAs ODs cover a broad spectral range, from UV to IR domain, but are characterized by low PL QYs (~1-2%). Thus, the overgrowth of a protective shell is imperative for maximizing their properties. Because InP and InAs QDs have a stronger covalent character, which is translated as a need of highly reactive precursors and higher reaction temperatures for their synthesis, the overgrowth of a shell is more demanding in contrast to Cd- and Pb-based chalcogenides. Therefore, using a “lattice-adaptor” shell may improve the overall result.

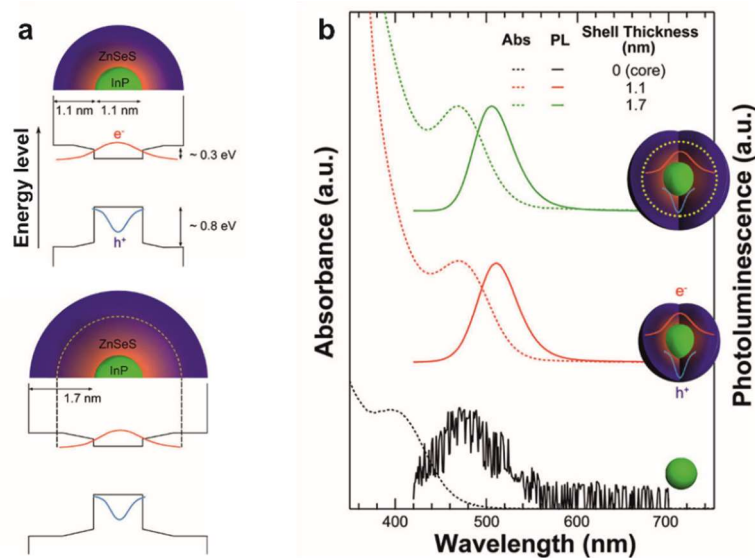


**Figure 1.19.** (a) Illustration of the band structure of InP/ZnSeS QDs with 1.1 nm shell thickness (up) and 1.7 nm shell thickness (below). While the hole wave functions are mostly confined in the InP core

phase, the electron wave functions are delocalized to the shell phase (~1.1 nm shell thickness). A dashed line on the lower scheme denotes a confinement region of electron wave functions. **(b)** Absorption (dashed lines) and photoluminescence (solid lines) spectra of InP core (black), InP/ZnSeS QDs with 1.1 nm shell thickness (red) and 1.7 nm shell thickness (green), respectively. Adapted with permission from *ACS Nano* 2013, 7, 9019–9026. ©2013 American Chemical Society.<sup>106</sup>

For example, Lim *et al.* demonstrated that by overgrowing a gradient shell of ZnSeS onto InP QD cores, a maximum of PL QY of 81% could be attained (**Figure 1.19**). This was possible because of the minimized lattice mismatch (e.g., 3.4% for ZnSe and 7.7% for ZnS) between the InP core and the outer ZnS shell, achieved by a ZnSe shell acting as a buffer. It was explained that Se is dominantly located near the InP core (smaller lattice mismatch and higher reactivity of TOP-Se), whereas S increases in the radial direction of the shell.<sup>68, 106</sup> Another example of maximized PL QYs is the case of core/shell/shell InP/GaP/ZnS QDs for which Kim *et al.* attained a maximum PL QY of 85% (**Figure 1.20**).<sup>103</sup> In this case, a type I heterostructure is formed, consisting of an inner GaP shell that mitigates the effect of lattice mismatch between the InP core and ZnS outer shell (**Figure 1.20a**). Despite the significant lattice mismatch between InP and GaP of ~6.82%, the overgrowth of GaP shell onto the InP core is facilitated due to their common zinc-blende structures of similar lattice parameters (InP, 5.86 Å; GaP, 5.45 Å), and similar ionic radii ( $\text{In}^{3+} = 0.81 \text{ \AA}$  and  $\text{Ga}^{3+} = 0.75 \text{ \AA}$ ).<sup>103</sup> Two hypotheses were proposed to explain the overgrowth of GaP shell onto the InP core: (i) either by the adsorption of  $\text{Ga}^{3+}$  ion on the InP cores, or (ii) partial cation exchange between  $\text{In}^{3+}$  and  $\text{Ga}^{3+}$  (**Figure 1.20b**), the second being the most probable option and also in line with the experimental results. Thus, a successful replacement of the  $\text{In}^{3+}$  by  $\text{Ga}^{3+}$  ions near the surface generated a structurally congruent InP/GaP core/shell structure and further facilitated the overgrowth of the outer shell of ZnS making possible a performant PL QY of 85%, superior thermal stability and water-dispersibility via ligand exchange (**Figure 1.20c**).<sup>103</sup>

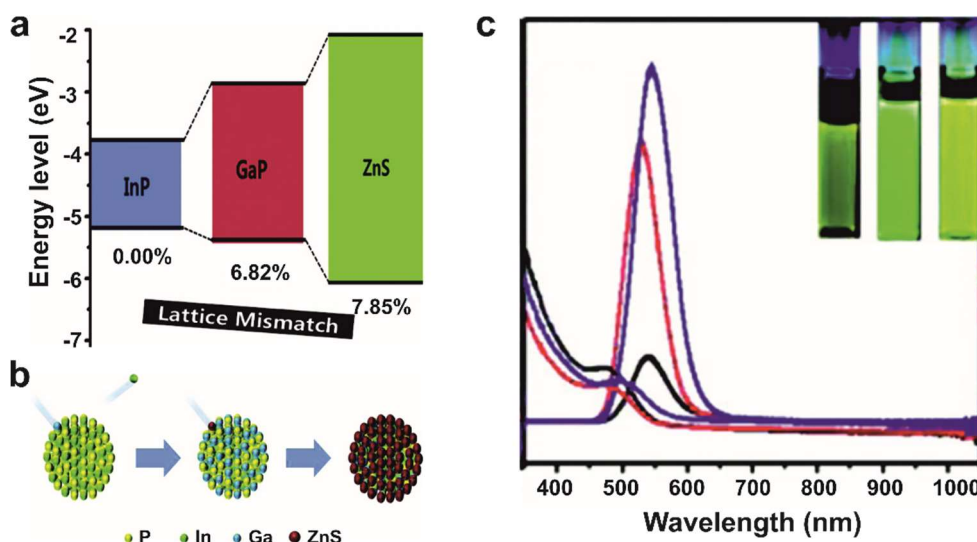


**Figure 1.20** (a) Representation of the energy diagram showing the band offsets and lattice mismatch of InP, GaP, and ZnS core/shell/shell materials. (b) Illustration of the substitution of In<sup>3+</sup> cations by Ga<sup>3+</sup> cations at the InP core surface, followed by the overgrowth of the ZnS outer shell. (c) Absorption and photoluminescence spectra of InP core (black), InP/GaP core/shell (red), and InP/GaP/ZnS core/shell/shell (blue). Inset: Photograph of InP (left), InP/GaP (middle), and InP/GaP/ZnS (right). Adapted with permission from *J. Am. Chem. Soc.* 2012, 134, 3804–3809. ©2012 American Chemical Society.<sup>103</sup>

## 1.4 Metal pnictide nanocrystals

Metal pnictides NCs, especially III-V semiconductor NCs, have drawn significant research interest due to their unique properties such as high electron mobility, direct band gap, low exciton binding energy, and bulk band gap values that cover a wide spectral range from ultraviolet to infrared region.<sup>37, 92</sup> The III-V semiconductor NCs are often referred to as “greener” NCs when compared to II-VI and IV-VI NCs, due to group IIIA elements like In and Ga which are less toxic and more environmentally friendly than Cd, Pb or Hg.<sup>37, 107-108</sup> Despite that the III-V semiconductor NCs are very potent surrogates for the II-VI and IV-VI NCs; the studies and applications regarding these greener NCs are rather sparse mainly because of the challenges regarding their synthesis. Compared to most of the II-VI and IV-VI NCs, the III-V compounds have a stronger covalent character which leads to the necessity of higher reaction temperatures, longer reaction times, and highly reactive precursors for their synthesis.<sup>109</sup> These conditions hinder the precise control of the size and size distribution of the NCs and also favor the Ostwald ripening process, which leads, to the broader size distribution of the NCs.

Additionally, the III-V semiconductor NCs (e.g., InP or InAs), are much more air-sensitive than their II-VI or IV-VI counterparts (e.g., CdSe or PbS) and air-free conditions are



necessary for the synthesis. Moreover, because of the low electron affinity of group V elements, difficulties arise in finding the appropriate precursors, for instance, the usual group V precursors used for the synthesis of III-V semiconductor NCs involve highly electropositive elements such as H, Na or Si (e.g.,  $AH_3$ ,  $ANa_3$ ,  $A(SiMe_3)_3$ ,  $A(N(SiMe_3)_2)_3$ ,  $A(NMe_2)_3$ , where  $A = P, As, Sb$ ).<sup>18-19, 24, 26, 110-115</sup>

Most of the studies regarding III-V semiconductor NCs concern the synthesis of InP QDs followed by InAs QDs. These two direct bandgap semiconductors are the most attractive III-V compounds due to their size-dependent optoelectronic properties over the visible and near-infrared spectral range, showing the enormous potential of being “greener” surrogates for Cd and Pb chalcogenide NCs.

**Table 1.2.** Characteristic physical properties of some III-V semiconductor compounds\*

III-V semiconductor	$\epsilon^{116}$	$\mu_e(m_0)^{117}$	$\mu_h(m_0)^{117}$	$E_g$ (eV) <sup>92</sup>	Exciton Bohr radius (nm) <sup>37</sup>	Exciton binding energy (meV) <sup>37</sup>
<i>InN</i>	5.5	0.12	0.5	0.8	3.0	43.5
<i>InP</i>	12	0.077	0.6	1.35	9.3	6.44
<i>InAs</i>	12.3	0.022	0.4	0.35	31.2	1.87
<i>InSb</i>	15.6	0.014	0.4	0.23	60.9	0.75
<i>GaN</i>	5.8	0.18	0.54	3.44	2.3	54.5
<i>GaP</i>	8.5	0.35	0.5	2.27(i)	2.2	38.7
<i>GaAs</i>	10.9	0.067	0.5	1.42	12.9	3.87
<i>GaSb</i>	14.4	0.041	0.28	0.75	21.3	2.34

\*all reported values are calculated at room temperature (300 K).

Except for a few examples (e.g., BN, BP, AIP, AlAs, GaP), most of the III-V compounds are direct bandgap semiconductors, and some of their basic properties are summarized in **Table 1.2**. Based on the calculated exciton Bohr radius and exciton binding energy, one can estimate how much they deviate in nano-regime from the bulk, and if their optoelectronic properties are size-dependent. The exciton Bohr radius can be calculated by applying the formula:

$$r_B = \frac{\epsilon m_0}{\mu} a_0 \quad (1.34)$$

where  $a_0 = 4\pi\epsilon_0\hbar^2/m_0$ ,  $\epsilon$  is the dielectric constant,  $\epsilon_0$  is the vacuum permittivity,  $\hbar = h/2\pi$ ,  $m_0$  is the free electron mass, and  $\mu$  is the effective mass.

Since the dielectric constant is frequency-dependent, the reported values in **Table 1.2** have been used high frequency optical dielectric constants ( $\epsilon_\alpha$ ) in order to have a qualitative idea

regarding the quantum confinement and binding energies of the presented compounds. The following Eq. **1.35** has been used for the calculation of exciton binding energy:

$$E_{Bind} = \frac{\mu}{m_0 \epsilon^2} R_y \quad (1.35)$$

where  $R_y$  is Rydberg constant (13.6 eV).<sup>37</sup>

Based on the calculated values of exciton Bohr radius, it can be noted that GaSb, InAs, and InSb can exhibit quantum size effects in a broader range of sizes, whereas GaN, GaAs, and InN NCs have to be very small in order to exhibit quantum confinement effects. Therefore, extremely small particles have to be synthesized to observe quantum confinement effects within these class of compounds. Further on, InP and InAs QDs will be addressed in greater detail, as these are of interest in this thesis.

*Indium Phosphide QDs* are a direct and environmentally friendly alternative for replacing CdSe QDs in various applications due to their tunable PL emission which can be tuned over a wide spectral range, from blue to near-infrared (NIR), by varying the NC size (~2 – 6 nm) due to the quantum confinement effect (**Figure 1.21**).<sup>110</sup>

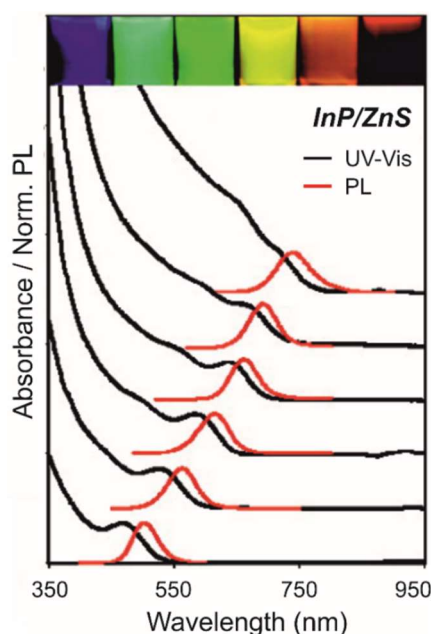


**Figure 1.21.** Absorbance (a) and normalized photoluminescence (b) spectra of InP/ZnS core/shell system showing tunability of optical properties over a broad spectral range. Inset: Images of colloidal solutions of InP/ZnS QDs under UV light. Adapted with permission from *J. Am. Chem. Soc.* 129, 50, 15432-15433; © 2007 American Chemical Society.<sup>110</sup>

Recent reviews dedicated to InP QDs summarize and describe the developed synthetic methods, identifying three predominant types of approaches: (i)  $\text{InX}_3 + \text{P}(\text{SiMe}_3)_3$  (X = halide

or carboxylate), (ii)  $\text{In}(0) + \text{P}(0)$ , and (iii)  $\text{InX}_3 + \text{P}(\text{NR}_2)_3$  ( $X = \text{halide}$ ,  $R = \text{Me, Et}$ ).<sup>37, 46, 118</sup> The first studies reporting the synthesis of colloiddally stabilized InP QDs appeared in the mid-1990s by Micic *et al.*<sup>17</sup> The InP QDs were obtained by the reaction of chloroindium oxalate and highly reactive tris(trimethylsilyl) phosphine ( $\text{P}(\text{SiMe}_3)_3$ ) in trioctylphosphine oxide (TOPO) at 270 °C for several days. The polydisperse QDs showed an average size of 2.5 nm and no PL emission. Later on, Wells *et al.* reported a new synthetic method based on the dehalosilylation reaction involving the use of  $\text{InX}_3$  ( $X = \text{Cl, Br, I}$ ) and  $\text{P}(\text{SiMe}_3)_3$  obtaining colored powders of NPs with average sizes of 4 nm (for  $\text{InCl}_3$  and  $\text{InBr}_3$  cases) and 2.5 nm (for  $\text{InI}_3$ ).<sup>60</sup> Similarly, the approaches reported by Micic *et al.* and Wells *et al.*, Guzelian *et al.* developed a new approach reporting size tunability (1.9 – 4.3 nm) and size-dependent PL emission for InP QDs. All of these were achieved by adding dodecylamine to stabilize the QDs and running the reaction for almost one week at 270 – 360 °C.<sup>18</sup> Starting with these first reports, InP QDs have drawn a tremendous interest, and many researchers have started to address the challenges of synthesizing these QDs. An essential characteristic of these first procedures is that they are based on the use of ionic precursors with equal and opposite charge ( $\text{In}^{3+}$  and  $\text{P}^{3-}$ ) eliminating the need of redox chemistry in order to form InP. The second category of approaches involves  $\text{In}(0)$  particles and zero-valent sources of P (e.g.,  $\text{P}_4$ ), and amorphous or hollow InP particles, via Kirkendall effect, are obtained. The reaction implies the deposition of  $\text{P}(0)$  on the surface of  $\text{In}(0)$  particles and intercalation via a surface-mediated diffusion mechanism.<sup>46, 119-120</sup> The third and most recent class of synthetic approaches is making use of  $\text{InX}_3$  and less hazardous tris(dialkylamino)phosphine (where the alkyl is either methyl or ethyl), often in the presence of a  $\text{Zn}^{2+}$  source and a primary amine (e.g., oleylamine).<sup>72, 121</sup> The formation of InP QDs is based on the involvement of the amine and  $\text{P}(\text{III/V})$  redox couple and facilitates size tuning based on the selection of  $\text{InX}_3$ .<sup>72</sup> Most of these synthetic methods have been designed based on the CNT and LaMer model, but over the years, it has been identified that the nucleation and growth of InP QDs undergoes a two-step nucleation model via magic-size cluster intermediates.<sup>47, 122</sup> Revising the CNT based on these new findings, and making use of the best computational methods, a new model – Reaction-Driven Nucleation Theory – has been designed and tested successfully by Wall *et al.* for the case of InP QDs and Au NPs as briefly summarized above.<sup>123</sup>

Improvements concerning the size distribution and optical properties of the QDs have been made by applying postsynthetic treatments. By applying size-selective washing, the size-distribution improved. Furthermore, by treating the QDs with HF or  $\text{NH}_4\text{F}$ , the PL QY

increased up to 30% from the initial value of about 1%.<sup>18, 96, 124</sup> The PL QY has been further improved by applying the HF treatment under UV irradiation, achieving 40%.<sup>125</sup>

Since the III-V semiconductor NCs are even more prone to oxidation than the II-VI or IV-VI NCs, the idea of overgrowing a protective inorganic shell has also been addressed in order to improve the PL QY as well as the chemical and photo-stability.<sup>97</sup> Micic *et al.* synthesized lattice-matched InP/ZnCdSe core/shell QDs, achieving a PL QY of 5-10%.<sup>126</sup> Following this work, many others tried to overgrow various shells, such as ZnS, ZnSe, GaP or gradient ZnSeS, reaching today PL QY values of 81% for a gradient shell of ZnSeS and 85% for a double shell of GaP/ZnS.<sup>68, 103, 106, 127</sup>

Advancements on the synthesis of the III-V QDs have also been made. The coordinating solvents like TOPO have been replaced with noncoordinating ones, such as 1-octadecene (ODE), in combination with fatty acids (e.g., lauric, myristic, palmitic or stearic acid).<sup>19, 21, 110, 118</sup> Better control over the size and size distribution of the QDs has been achieved in shorter reaction time (minutes to hours) at lower temperatures (178-188 °C).<sup>19, 21, 110</sup> Recently, it has been proved that by using a source of zinc ions (zinc acetate or halide) at the beginning of the synthesis of the cores will improve not only the PL QY of the cores, but will also improve the surface passivation and can help for growing a Zn-based shell.<sup>69, 103, 128-129</sup> Moreover, despite the remarkable progress achieved by employing P(SiMe<sub>3</sub>)<sub>3</sub> as P-source, more recent studies explore less hazardous and more inexpensive compounds as alternative P-precursors. The motivation arises from overcoming the main drawbacks of P(SiMe<sub>3</sub>)<sub>3</sub>, namely its pyrophoric nature, high cost, commercial availability, hazardous reagents, and by-products associated with its production. Another motivation is the difficulty to attain larger QDs (>4nm) by using P(SiMe<sub>3</sub>)<sub>3</sub> because of its rapid depletion.<sup>118, 130</sup> Therefore, less reactive precursors like tris(trimethylgermyl)phosphine (P(GeMe<sub>3</sub>)<sub>3</sub>) or tris(trimethylstannyl)phosphine (P(SnMe<sub>3</sub>)<sub>3</sub>) have been tested but did not prove to be very successful.<sup>131</sup> Few recent studies have indicated that tris(dialkylamine)phosphine (alkyl = methyl, ethyl; P(NMe<sub>2</sub>)<sub>3</sub>, P(NEt<sub>2</sub>)<sub>3</sub>) is a very potent P-precursor.<sup>71-72, 121</sup> Initially, the P(NMe<sub>2</sub>)<sub>3</sub> was tested in the generally used synthesis based on In-carboxylate in ODE and showed an inferior performance. Later it was reacted with InCl<sub>3</sub> in oleylamine in the presence of ZnCl<sub>2</sub> and produced non-luminescent InP QDs which became luminescent after overcoating with ZnS, displaying PL QYs of 51 – 53% and emission line widths of 60 – 64 nm, comparable to those synthesized using P(SiMe<sub>3</sub>)<sub>3</sub>.<sup>71</sup> The method was further improved by Tessier *et al.* and higher PL QYs (up to 60%) and narrower emission line widths (46 – 63 nm) were achieved.<sup>72</sup> Further investigations of the employment of P(NMe<sub>2</sub>)<sub>3</sub>

into the synthesis of InP QDs led to InP/ZnSeS/ZnS QDs with PL QY of 82%, comparable with the InP/GaP/ZnS QDs synthesized with  $P(\text{SiMe}_3)_3$  (PL QY 85%).<sup>103, 132</sup>

*Indium Arsenide QDs* have a smaller band gap than InP QDs (**Table 1.2.**) and are an alternative for applications for the near-infrared spectral range, more precisely in the range of 700-1400 nm. The development of InAs QDs followed the development of InP QDs closely, and, in most of the cases, were synthesized by adapting the methods and approaches developed for the synthesis of InP QDs. The first study to address the synthesis of colloiddally stabilized InAs QDs was shortly reported after the first reports of InP QDs in the mid-1990s by Guzelian *et al.*<sup>24</sup> The InAs QDs were prepared based on the dehalosilylation reaction developed by Wells *et al.*, by reacting  $\text{InCl}_3$  and tris(trimethylsilyl)arsine ( $\text{As}(\text{SiMe}_3)_3$ ) in TOP at elevated temperatures (240 – 265 °C). The size of the QDs was in the range of 2.5 to 6 nm and showed a relatively narrow size distribution of 10 – 15% by involving the post-synthetic size-selective precipitation. In parallel with the progress observed for InP QDs, the synthesis of InAs QDs was adjusted by replacing the solvent with non-coordinating ODE, allowing the observation of excitonic peaks in the spectral region of 650 – 800 nm.<sup>19</sup> Additionally by using ODE as solvent enabled the observation of excited states at higher energies which indicate a narrow size distribution of nanoparticles. Similar to  $P(\text{SiMe}_3)_3$ ,  $\text{As}(\text{SiMe}_3)_3$  is highly reactive and decomposes fast in the initial stages of the reaction, enabling the Ostwald ripening to predominate the growth mechanisms and so limiting the size tuning in a very narrow range. A way to achieve size-focusing is by maintaining a high monomer concentration via a second slow-injection of the precursor, which proved to afford an improvement of the size distribution from the initial 20% to 8.7%.<sup>105, 133-134</sup> Another approach for achieving monodisperse QDs is the concept of “self-focusing”, where a high particle concentration is maintained in order to force the diffusion spheres of adjacent NCs overlap.<sup>135-136</sup> Due to the concentration gradient, the slightly higher concentration near the surface of the smaller NCs should move to the surface of the larger ones, forcing the complete dissolution of the smaller, and relatively slow growth of the larger NCs. By applying this concept, Xie *et al.* optimized the concentration and the reaction temperature of the initially formed InAs nanoclusters and synthesized InAs QDs (1-3 nm) showing PL emission in the range of 700-1400 nm (**Figure 1.22**).<sup>135</sup> Moreover, the PL QY could be tremendously improved from 1% up to 90%, by overgrowing a shell of CdSe.<sup>135</sup> Previous studies reported the investigation of various shell materials for InAs core QDs, including both III-V (InP and GaAs) and II-VI (CdSe, ZnSe, and ZnS) semiconductors,

reporting improvements of the PL QY up to 8% for InAs/ZnS, and 20% for InAs/ZnSe or InAs/CdSe.<sup>137</sup>

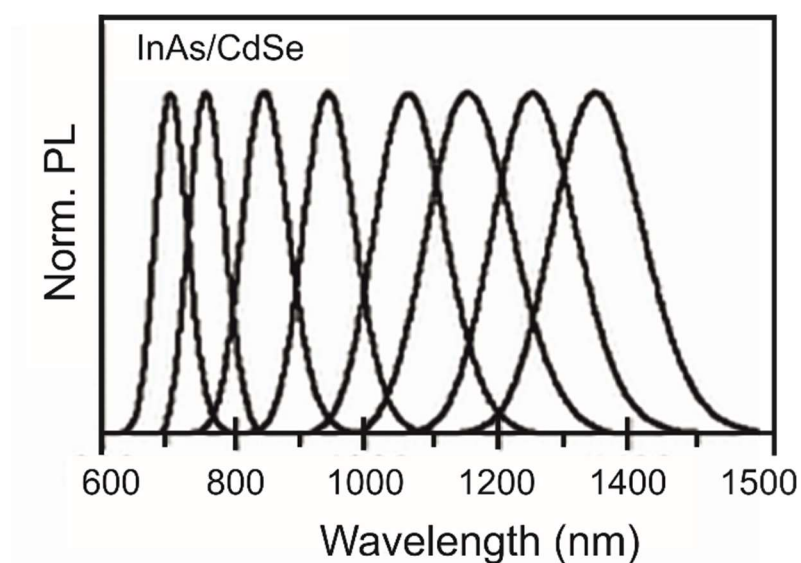


**Figure 1.22.** Normalized photoluminescent spectra of InAs/CdSe core/shell system showing a broad coverage of the spectral region from 600 to 1400 nm. Adapted with permission from *Angew. Chem. Int. Ed.* 2008, 47, 7677–7680; © 2008 Wiley-VCH Verlag GmbH & Co. KGaA, Weinheim<sup>135</sup>

Recent studies have reported hexaalkylarsenic triamide ( $\text{As}(\text{NR}_2)_3$ ,  $\text{R} = \text{Me}, \text{Et}$ ) as a commercially available and less expensive arsenic precursor for the synthesis of InAs QDs.<sup>138</sup> It has been reported for both precursors,  $\text{As}(\text{NMe}_2)_3$  and  $\text{As}(\text{NEt}_2)_3$ , that they undergo a transamination reaction with oleylamine, where it is used as solvent and ligand in order to stabilize the newly formed InAs QDs, generating three equivalents of flammable and corrosive dialkylamines in order to provide trioyleylaminearsenide,  $\text{As}(\text{OLA})_3$ , for the reaction. Moreover, subsequent addition of a reducing agent is necessary in order to obtain InAs from the reaction of  $\text{InX}_3$  ( $\text{X} = \text{Cl}, \text{Br}, \text{I}$ ) with  $\text{As}(\text{OLA})_3$ . Typically, diisobutylaluminum hydride (DIBAL-H)<sup>138</sup> is used, but nowadays, are also used *N,N*-dimethylethylamine complex ( $\text{DMEA-AlH}_3$ )<sup>25</sup> and trioyleylphosphine ( $\text{P}(\text{OLA})_3$ )<sup>139</sup>. More recently, tri(pyrazolyl)arsine,  $\text{As}(\text{Pyr})_3$ , has been reported as a less toxic and much safer precursor for the synthesis of InAs QDs.<sup>140</sup> Despite that, this compound is available on a gram-scale synthesis, and it is safer to work with. However, it has the inconvenience of being needed to first prepare a stock solution of  $\text{As}(\text{OLA})_3$  by reacting the  $\text{As}(\text{pyr})_3$  with oleylamine (OLA), which would make it inconvenient for the scale-up synthesis. Also, in this situation, the addition of a reducing agent is needed in order to react  $\text{As}(\text{OLA})_3$  with  $\text{InX}_3$ .<sup>25</sup>

## 1.5 Cesium lead halide ( $\text{CsPbX}_3$ , $X = \text{Cl, Br, I}$ ) perovskite NCs

*History.* Cesium lead trihalide compounds were reported for the first time in the 1890s in various compositions and stoichiometries:  $\text{CsPbX}_3$  ( $X = \text{Cl, Br, I}$ ),  $\text{CsPb}_2\text{X}_5$ , and  $\text{Cs}_2\text{PbX}_6$  ( $X = \text{Cl, Br}$ ).<sup>141</sup> A few decades later, in the late 1950s, it had been reported for  $\text{CsPbX}_3$  compounds that they crystallize in a perovskite-like crystal structure with temperature-dependent phase transitions, and exhibit photoconductivity.<sup>142-143</sup> Later, in the 1990s, the  $\text{CsPbX}_3$  perovskites were identified as isolated quantum dots in a single crystal of  $\text{CsX}$  ( $X = \text{Cl, Br}$ ) matrix and their quantum size effects were investigated.<sup>144</sup>

Although  $\text{CsPbX}_3$  perovskite compounds had been known for many years, they have been ignored until recent breakthroughs in the field of photovoltaics using lead halide perovskites as light-absorbers. A tremendous number of studies addressing various aspects of this class of materials have burst since the first reported study in early 2015 by Protesescu *et al.* on the synthesis and investigation of the optical properties of colloiddally stabilized  $\text{CsPbX}_3$  NCs. (Figure 1.23).<sup>145</sup>

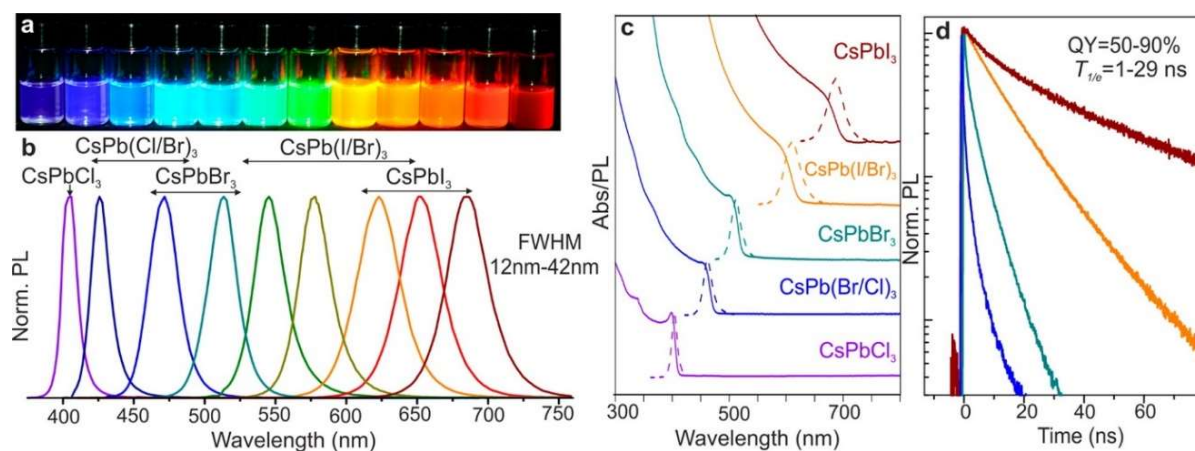


**Figure 1.23.** Colloidal perovskite  $\text{CsPbX}_3$  NCs ( $X = \text{Cl, Br, I}$ ) exhibit size- and composition-tunable bandgap energies covering the entire visible spectral region with narrow and bright emission: (a) colloidal solutions in toluene under UV lamp ( $\lambda = 365 \text{ nm}$ ); (b) representative PL spectra ( $\lambda_{\text{exc}} = 400 \text{ nm}$  for all but  $350 \text{ nm}$  for  $\text{CsPbCl}_3$  samples); (c) typical optical absorption and PL spectra; (d) time-resolved PL decays for all samples shown in (c) except  $\text{CsPbCl}_3$ . Adapted with permission from *Nano Lett.*, **2015**, *15* (6), pp 3692–3696. © 2015 American Chemical Society.

Employing the HI method, a solution of cesium oleate (Cs-oleate) is swiftly injected into a solution of  $\text{PbX}_2$  solubilized with oleic acid (OA) and oleylamine (OLA), which act as stabilizers, in ODE at a relatively high temperature ( $140 - 200^\circ\text{C}$ ). The reaction is stopped after a few seconds by immersing the reaction flask in a water-ice bath. The obtained monodisperse

colloidal NCs have a cuboidal shape and exhibit tunable absorption and photoluminescence (PL) with remarkable high PL QYs (up to 90%), narrow full widths at half maximum (12 – 42 nm), and short radiative lifetimes of 1 – 29 ns (**Figure 1.23**), without applying any additional postsynthetic surface treatments or passivation by a protective shell as necessary for more traditional semiconductor QDs. The tuning of the PL emission can be easily achieved over the entire visible spectral range by merely altering the halide composition.

*Structural insights – Goldschmidt tolerance factor and octahedral factor.* The CsPbX<sub>3</sub> NCs were found to have a three-dimensional (3D) perovskite structure, formed by the three primary ions with an ABX<sub>3</sub> stoichiometry, and predominantly ionic character in comparison with more traditional II-VI or III-V semiconductor QDs. In general, for fully-inorganic halide perovskites, the monovalent A-cation is cesium, the bivalent B-cation is lead, tin or germanium, and X is chlorine, bromine or iodine, or a combination of the three.<sup>146</sup> In the case of mixed organic-inorganic halide perovskite, the monovalent A-cation is either methylammonium (MA) or formamidinium (FA).<sup>147</sup> The B-cation is coordinated with six halide anions forming 3D interconnected [PbX<sub>6</sub>]<sup>4-</sup> octahedra, hosting the A-cation in the large voids by the [PbX<sub>6</sub>]<sup>4-</sup> octahedra. The A-cation is coordinated with twelve halide anions and forms cuboctahedral configurations. The [PbX<sub>6</sub>]<sup>4-</sup> octahedra can be assembled into an ideal cubic lattice (**Figure 1.24a**; typical for bulk FAPbBr<sub>3</sub> and FAPbI<sub>3</sub> at RT) or a distorted version, such as 3D orthorhombic phase (**Figure 1.24b**, typical for CsPbBr<sub>3</sub> at RT) or 3D tetragonal phase (typical for MAPbI<sub>3</sub> at RT, not shown here).<sup>148</sup> The stability of these 3D polymorphs – cubic, orthorhombic and tetragonal – and of the 3D polymorphs generated by their phase transformation into lower-dimensional, and hence, wider-bandgap structures such as the 1D hexagonal or 1D-orthorhombic depicted in **Figures 1.24c** and **1.24d**, are of paramount importance for the practical use of perovskites in any solid-state device. For instance, in the case of iodine, several challenges have been encountered. Bulk CsPbI<sub>3</sub> is found at RT exclusively in the yellow, orthorhombic 1D phase, which can be converted to the desired 3D polymorph (band gap at 710 nm) only above 315°C.<sup>148</sup>

Recent studies have shown that potential perovskite compositions can be predicted by computational means and it is vital to take into account two factors, namely the *Goldschmidt tolerance factor* and *octahedral factor* (**Figure 1.24e**).<sup>148-150</sup>



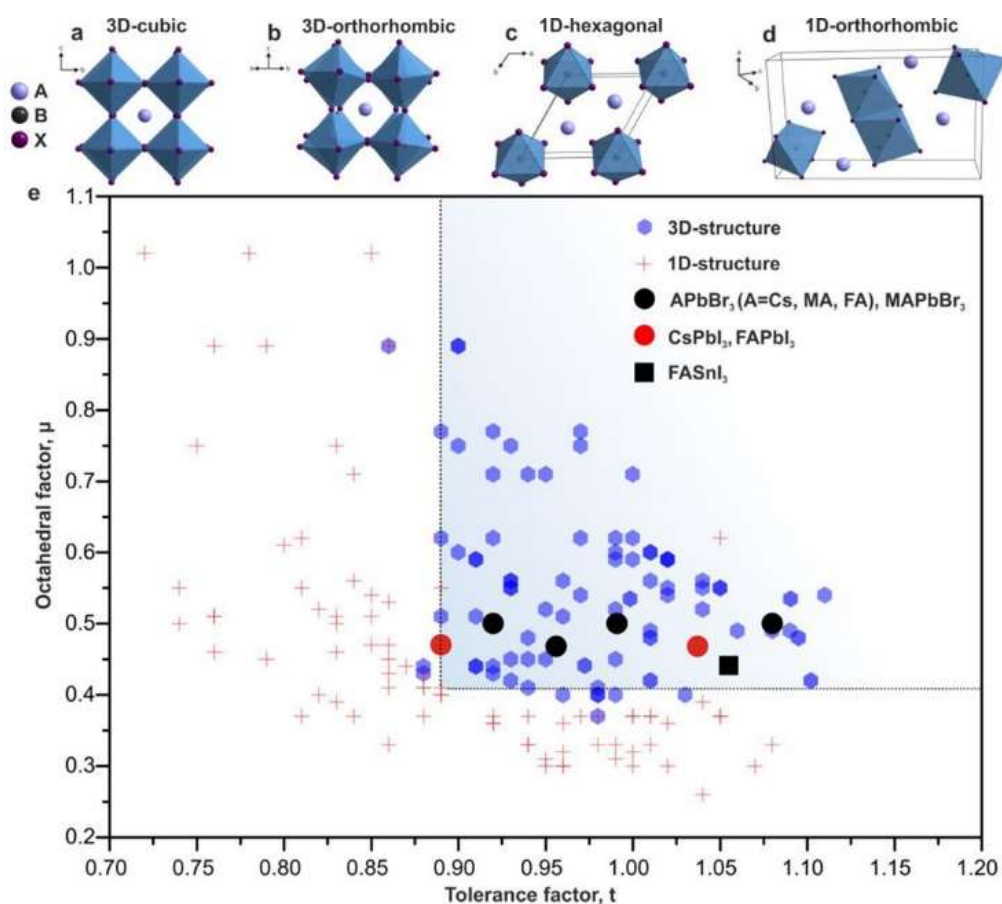


**Figure 1.24.** Schematic representation of (a) ideal 3D cubic interconnection of  $PbX_6$  octahedra, as observed in  $\alpha$ -FAPbI<sub>3</sub>; (b) orthorhombically distorted 3D polymorph, which is commonly reported for CsPbBr<sub>3</sub>; (c) 1D hexagonal lattice found in the yellow FAPbI<sub>3</sub>; and (d) 1D orthorhombic lattice found in the yellow CsPbI<sub>3</sub>. (e) Survey of the reported formabilities of the 3D and 1D polymorphs of nearly all known inorganic and hybrid ABX<sub>3</sub> compounds, where A is either an alkali metal, organic cation (Ma or FA), or another single-charged metal ion ( $Ag^+$ ,  $Tl^+$ , or  $Cu^+$ ); B = Pb, Sn, Mg, Ca, Sr, Ba, Ti, V, Cd, Hg, Mn, Cu, Co, Zn, Tm, Dy, or Yb; and X = F, Cl, Br, or I. The light blue squared represents the area of possible, stable compounds. Adapted with permission from ACS Nano, 2017, 11, 3119–3134. © 2017 American Chemical Society.<sup>148</sup>

The Goldschmidt tolerance factor,  $t$ , addresses the close packing of ions and has been used to predict the stability of perovskite structures of ABX<sub>3</sub>-type.<sup>149</sup> The tolerance factor is calculated based on the ionic radii,  $r_i$ , of the constituent ions (A, B, X) as described by the Eq. 1.36, and should take values within 0.76-1.13 range in order for a 3D perovskite structure to be stable. If  $t$  has lower or higher values outside the mentioned range then the formation of a different polymorph of a lower dimensionality (0D, 1D or 2D) is promoted.<sup>151</sup>

$$t = \frac{r_A + r_X}{\sqrt{2}(r_B + r_X)} \quad (1.36)$$

Such situations occur when the A-cation is either too small ( $Na^+$ ,  $K^+$ , and  $Rb^+$ ) or too large (imidazolium, ethylammonium, and guanidinium).<sup>152</sup> Perovskite compositions that are at the edge of the tolerance factor requirement, such as CsPbI<sub>3</sub> ( $t \sim 0.8$ ) or FAPbI<sub>3</sub> ( $t \sim 1$ ), present

high instability at room temperature and undergo a phase transition preferring more stable phases like orthorhombic or hexagonal. Another requirement that has to be fulfilled for the formation of a perovskite structure is the octahedral factor –  $\mu$ , which addresses the stability of the  $BX_6^{2-}$  octahedra. The octahedral factor takes into account the ionic radii of both B and X ions, according to equation (1.37), and should be between 0.442 and 0.895.<sup>150</sup>

$$\mu = \frac{r_B}{r_X} \quad (1.37)$$

*Defect tolerance.* In contrast to conventional metal chalcogenide (e.g., CdSe) or pnictide (e.g., InP), CsPbX<sub>3</sub> NCs, exhibit exceptional optical properties (e.g., nearly unity PL QYs, narrow emission line widths, broad coverage of the color gamut) without any electronic surface passivation due to their high tolerance towards defects. The *defect tolerance* means that their optical and electronic properties function like there are no electronic traps or excessive doping present despite the indication of various structural defects identified using structural and other characterization methods.<sup>153</sup> This behavior indicates that the structural defects reside either in the valence band (VB) or conduction band (CB) and do not affect the bandgap.<sup>154</sup>

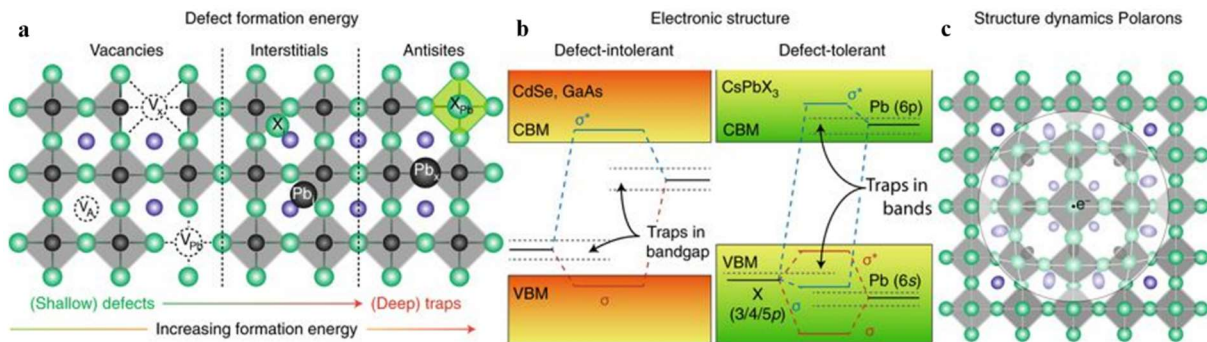


**Figure 1.25.** Overview of the factors contributing to the defect-tolerant behavior of lead halide perovskites. **(a)** Graphical representation of typical point defects in lead halide perovskites: vacancies, interstitial and antisite atoms; **(b)** Schematic representation of electronic band structure of typical defect-intolerant semiconductors (e.g., CdSe, GaAs) and defect-tolerant lead halide perovskites (e.g., CsPbX<sub>3</sub>); **(c)** Schematic representation of polaron formation by the combination of a local structural deformation of Pb-Br framework with a charge carrier (electron or hole). Reprinted with permission from *Nat. Mater.* 2018, 17, 394-405. © 2018 Springer Nature.

Recent theoretical studies addressed the defect tolerance of various perovskite compounds, demonstrating that point defects or grain boundaries in the bulk perovskite, as well as the surface defects are either resonant with the VB and CB states or they form shallow trap states (**Figure 1.25**).<sup>155-158</sup> So far, it has been demonstrated that the defect tolerance is a consequence of a few factors favorably combined. One such factor is the formation of vacancies only, out of a variety of conceivable point defects, among interstitial and antisite

defects (**Figure 1.25a**). The vacancies are characterized by low formation energy and generate only shallow trap states located near or in the VB and CB (**Figure 1.25b**). In contrast, the formation of interstitial and antisite defects would generate deep trap states in the band gap. Because their formation would implicate the misplace of the ions within the crystal lattice, which is energetically demanding, the interstitial and antisite defects are mostly absent.<sup>153, 155, 159-160</sup> Another contributing factor is the antibonding character of the VB, resulting from the coupling of halide 3/4/5p orbitals with the lead 6s orbitals, which, combined with the spin-orbit effects in the CB (which has a predominant Pb 6p character), favor the shallow character of the vacancy-related states. These lead to the opening of the bandgap between two antibonding bands, which means that structural defects may arise either from halide or other A<sup>+</sup>-type vacancies and their energy levels fall preferably within the VB and CB instead of the bandgap itself. Furthermore, the surface of the NC can be considered a plane of vacancies, so it should exhibit similarly mild behavior as vacancies. This assumption would explain the near-unity PL QYs manifested by the lead halide perovskite NCs without any surface treatments. However, the reported PL QY values of 80-95 % in the green region and 10-20 % near 400 nm (for CsPbCl<sub>3</sub> NCs), convey that these lead halide perovskite NCs are not entirely defect-free. Nevertheless, the PL QYs exhibited by these perovskite NCs exceed any other non-passivated QDs emitting in the same wavelength range. More than this, recent studies focused on finding accessible post-synthetic ligand treatments, such as thiocyanates, PbBr<sub>2</sub> + didodecylammonium bromide (DDAB), or trioctylphosphine-PbI<sub>2</sub>, boost the PL QYs close to 100%.<sup>161-162</sup> A third factor that is responsible for the defect tolerance of these perovskite NCs is the soft and dynamic nature of the perovskite lattice, which seems to protect its carriers from trapping and scattering.<sup>163</sup> Combined with the highly ionic bonding character, the intense structural dynamics of Pb-X lattices at room temperature lead to the formation of polarons, which are the result of the coupling of electrons and holes with ionic displacements (**Figure 1.25c**). The formed polarons have been proposed to screen the Coulombic potential and reduce trapping, and carrier scattering.<sup>163-164</sup>

*Synthetic approaches.* After the initial study of Protesescu *et al.*, a tremendous number of studies addressing different aspects such as synthetic strategies exploring better control of NC size or morphology, a more profound understanding of their structure or the optoelectronic capabilities at the ensemble and single dot level, or testing the performance in different applications have emerged.<sup>64, 145, 157-158, 165-169</sup> To date, a significant number of methods have

been developed for the synthesis of perovskite NCs, and they can be classified either as top-down or bottom-up approaches (**Figure 1.26**).<sup>170-192</sup>

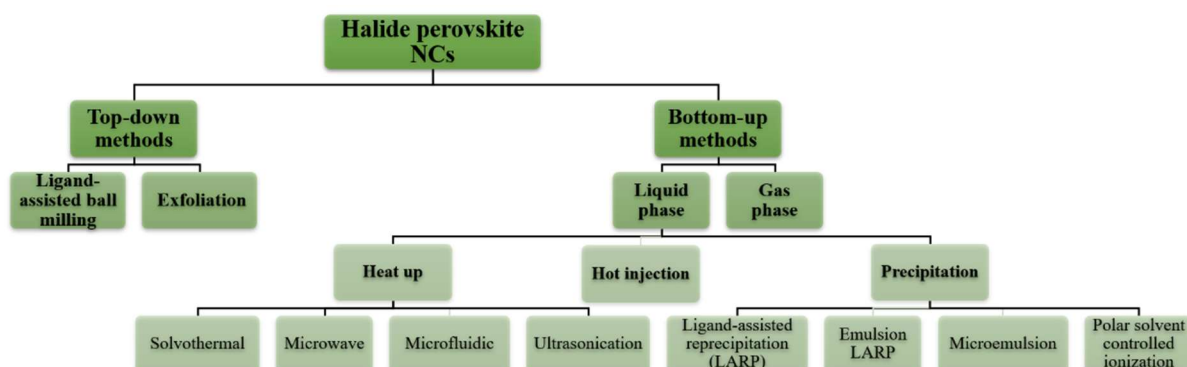


**Figure 1.26.** Classification of various methods employed for the synthesis of halide perovskite NCs.

As reported early in 2015, Protesescu *et al.* adapted the ligand-assisted hot injection method for the synthesis of  $\text{CsPbX}_3$  ( $X = \text{Cl}, \text{Br}, \text{I}$ ) NCs.<sup>145</sup> The  $\text{CsPbX}_3$  NCs were synthesized by injecting a preheated solution of Cs-oleate swiftly into a hot ( $140 - 200$  °C) solution containing the  $\text{PbX}_2$  precursor solubilized with oleic acid and oleylamine in ODE. The reaction was stopped after a few seconds by immersing the flask into a water-ice bath, affording highly emissive colloiddally stabilized perovskite NCs. It was observed that equal amounts of acids and amines are necessary to afford monodisperse NCs with cuboidal shape in this situation. It was also observed that, as in the case of conventional semiconductor NCs, the size of NCs could be adjusted by varying the reaction temperature. Also, by simply adjusting the lead halide ratios ( $\text{PbCl}_2/\text{PbBr}_2$  or  $\text{PbBr}_2/\text{PbI}_2$ ), homogeneously-mixed compositions could be obtained exhibiting a tunable PL emission over the entire visible spectral range ( $410 - 700$  nm). Subsequently, by adjusting the synthetic protocol developed by Protesescu *et al.*, it was possible to synthesize hybrid perovskite NCs, such as  $\text{MAPbX}_3$  ( $X = \text{Br}, \text{I}$ ), or so-called “perovskite-related” lead halide based materials, such as  $\text{Cs}_4\text{PbX}_6$  ( $\text{Cl}, \text{Br}, \text{I}$ ).

By employing a droplet-based microfluidic platform, Lignos *et al.* studied the growth kinetics of  $\text{CsPbX}_3$  NCs.<sup>165</sup> It was found that these NCs have high-speed kinetics, which was observed by in situ monitorization of the evolution of absorption and PL spectra. It was found that the nucleation and growth take place in the first 1-5 seconds of the reaction.

Despite that these NCs can be produced with high quality quite quickly, they have some drawbacks. One such drawback is that they are highly soluble in polar solvents which leads to reduced stability under atmospheric conditions (variable humidity, heat, light) and drops of

their PL QYs. In a recent study, Woo *et al.* addressed the stability problem by synthesizing the NCs under halide-rich conditions. Woo and co-workers found that by using  $\text{ZnBr}_2$  as an extra Br-source, the resulting NCs have a more halide-rich composition, and this helped in increasing their stability without a significant drop in the PL QY.<sup>193</sup> Another drawback is the use of metal halide salts as both a cation and an anion precursor which limits the possibility of working with the desired ion stoichiometry.<sup>145, 194</sup> In order to overcome such restrictions, recently, a “three-precursor” HI approach has been developed for the synthesis of  $\text{CsPbX}_3$  NCs.<sup>195</sup> In their approach, Liu *et al.* used  $\text{NH}_4\text{X}$  ( $\text{X} = \text{Cl}, \text{Br}, \text{I}$ ) and  $\text{PbO}$  as sources of halide and lead ions separately, affording high contents of halide in the final NC composition. Subsequently, later studies from Imran *et al.* and Creutz *et al.* overcome the shortcomings of the initial “three-precursor” HI approach by introducing the use of highly reactive halide precursors.<sup>171, 196</sup> By employing benzoyl halides, Imran *et al.* demonstrated a reasonable control over the size distribution, and phase purity was achieved for the entire family of all-inorganic and hybrid lead halide perovskite NCs.<sup>196</sup> Moreover, besides the freedom of working with desired cation/anion ratios in a halide-rich environment, it was demonstrated for the  $\text{CsPbCl}_3$  NCs that their PL QY could be boosted up to 65% when synthesized in excess of benzoyl chloride.

The control over the size and morphology of the  $\text{CsPbX}_3$  perovskite nanostructures is possible using the HI method by varying the ligand combinations (long and short alkyl-chain) and ratios, as well as the reaction temperature (**Figure 1.27**). For instance, it was proved that by lowering the reaction temperature in the range of 90-130 °C and using equal ratios of OA and OLA leads to the formation of quasi 2D geometries referred to as *nanoplatelets (NPLs)*.<sup>197</sup> On the other hand, by letting the reaction to run for long periods at relatively high temperatures (170 – 200 °C) the formation of *nanowires (NWs)* is favored.<sup>198</sup> In other studies, the effects of the ligands upon the morphology of the  $\text{CsPbBr}_3$  NCs have been investigated; for instance, Pan *et al.* studied the influence of the length of the alkylamine and carboxylic acids by systematically varying one of them while the second was maintained constant, as well as their behavior at different reaction temperatures.<sup>199</sup> Furthermore, atomically thin  $\text{CsPbBr}_3$  *nanosheets (NSs)* with a thickness of 3.3 nm and an edge length of about 1  $\mu\text{m}$  could be synthesized by employing a prolonged reaction time (up to 3 hours) and a combination of dodecylamine and OA.<sup>200</sup> Another variation of NSs with tunable lateral dimensions from 200 nm up to a few micrometers with a constant thickness of a few unit cells, was obtained by employing short-chain octylamine and octanoic acid in addition to OA and OLA.<sup>201</sup> Many other studies have focused their attention on finding a synthetic approach by employing various

ligand combinations or even different methods (e.g., solvothermal, ultrasonication, microwave), which would afford better control over the dimensions of these various morphologies and assure their stability towards postsynthetic processing.<sup>165, 173-176, 178-179, 202-206</sup> Despite achieving precise control over the dimensions of the synthesized morphologies, all the reported studies failed to find a synthetic procedure that would assure more robustness for these nanostructures.

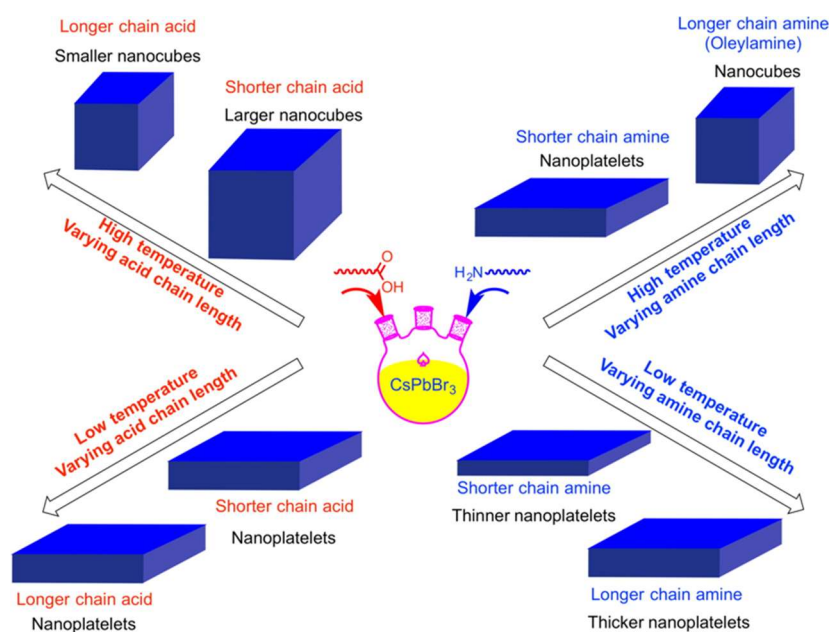


**Figure 1.27.** Graphical overview of morphology control by applying various synthetic conditions. Reprinted with permission from *ACS Nano* 2016, 10, 7943–7954. © 2016 American Chemical Society.

Later, it was proved that the formation of  $\text{CsPbX}_3$  perovskite NCs is possible even at room temperature by employing the ligand-assisted reprecipitation (LARP) method.<sup>181</sup> This is possible due to the highly ionic character of the chemical bonding in these NCs, in contrast to the conventional QDs that necessitates high reaction temperatures because of the highly covalent character of their chemical bonds. LARP method appears to be an “easy-to-use” alternative method that does not require advanced instrumentation and techniques, as in the case of the hot injection method, and can afford gram-scale production of perovskite nanostructures. LARP method consists of simply dropping the solution formed by solubilizing the precursor salts in a “good” solvent (e.g., dimethylformamide, dimethylsulfoxide) into a “bad” solvent (e.g., toluene, hexane) containing the ligands. By mixing the “bad” and “good” solvents, the instantaneous supersaturation is achieved triggering the nucleation and the growth of perovskite NCs. This method was tested back in 2012, before the first report of colloidal inorganic perovskites, for the hybrid perovskites facilitating the synthesis of NCs with

dimensions in the range of 30-160 nm and much more intense PL emissions than expected from the bulk counterparts.<sup>207</sup> The development of this method was slow, and it took a few years until the procedure was perfected for the synthesis of hybrid MAPbX<sub>3</sub> perovskite NCs, and later extended to ABX<sub>3</sub> NC systems (A = MA, FA, Cs; B = Pb, Sn, Bi, Sb; X = Cl, Br, I), as well as CsPb<sub>2</sub>Br<sub>5</sub> and Cs<sub>4</sub>PbX<sub>6</sub>.<sup>208-217</sup> Although it facilitates the direct synthesis of various perovskite systems at RT under air conditions, the LARP method has some drawbacks as well. For example, the method is based on polar solvents (e.g., DMF, DMSO) which can quickly degrade or dissolve the formed perovskite NCs.<sup>181, 208, 218</sup> Moreover, it was reported that the precursor-polar solvent interactions play an essential role in the formation of defective perovskite NCs containing residual solvent molecules on the surface and iodine vacancies in the bulk.<sup>187</sup>

Most of the alternative synthetic methods, such as emulsion LARP or reverse microemulsion, were first developed for the synthesis of hybrid perovskite NCs and later adapted for the synthesis of all-inorganic perovskite NCs in order to overcome the main drawbacks of HI method (air-free conditions for performing the synthesis and difficulties to scale up the synthesis for large-scale production).<sup>188-190, 219-226</sup> Additionally, by employing either the heat-up or precipitation method, perovskite NCs can be produced on a gram scale even under air atmosphere, but with a more precarious control over the size and morphology of the NCs, which leads to extra work to overcome these drawbacks.<sup>173-174, 176, 178, 180, 203</sup>

*The surface of lead halide perovskite NCs* is characterized by highly dynamic binding between the surface capping ligands, typically a pair consisting of an anion (halide or oleate) and a cation (cesium or alkylammonium), and the oppositely charged NC surface ions.<sup>227-228</sup> The ligand shell rapidly desorbs upon isolation and purification of colloids, causing the loss of colloidal stability and eventually also the loss of structural integrity, leading to the sintering of NCs into bulk polycrystalline materials. As recently described by Bodnarchuk *et al.*, the surface modifications can extend beyond the ligand shell, denoted outer shell {AX'}, to the surface regions of the NCs, the inner shell (PbX<sub>2</sub>), altering the surface stoichiometry and damaging the PbX<sub>6</sub> octahedra (**Figure 1.28**). Therefore, the whole CsPbX<sub>3</sub> NC can modify its crystal structure, partially or fully converting to, for instance, CsX, CsPb<sub>2</sub>X<sub>5</sub>, PbX<sub>2</sub>, or Cs<sub>4</sub>PbX<sub>6</sub> phases, or even fully disintegrate upon the action of various solvents or complexing agents. In the recent study from Bodnarchuk *et al.*, density functional theory (DFT) is used to model an atomistic structure of colloidal CsPbX<sub>3</sub> (X = Cl, Br, I) NCs for various degrees of surface damage. Based on the model of CsPbBr<sub>3</sub> NC, it is rationalized that the formation of the trap states occurs as a

consequence of postsynthetic processing of perovskite NCs (ligands exchange, solvent effect, aging), corroborated by DFT simulations and validated by the experimental data.<sup>227</sup> According to Bodnarchuk and coworkers, the “healing” of the surface trap states requires restoration of all damaged  $\text{PbX}_6$  octahedra and establishing of a stable outer  $\text{AX}'$  shell with cationic (A) and anionic ( $\text{X}'$ ) ligands forming a core-inner shell-outer shell NC structure depicted as  $[\text{CsPbX}_3](\text{PbX}_2)\{\text{AX}'\}$  (**Figure 1.28**).<sup>227</sup> Such NCs are halogen-rich when  $\text{X}'$  is largely made of X ions, and halogen-poor when other anions assume the positions of  $\text{X}'$ . Restoration of such a structure was attained by using a postsynthetic treatment with  $\text{PbBr}_2$  and didodecylammonium bromide (DDAB). After this treatment, an enhancement of the PL QYs to 90-100% was recorded. Moreover, this combined treatment with  $\text{PbBr}_2$  and DDAB improves the colloidal stability of NCs, retaining their high PL QYs after three to four cycles of precipitation and redispersion.

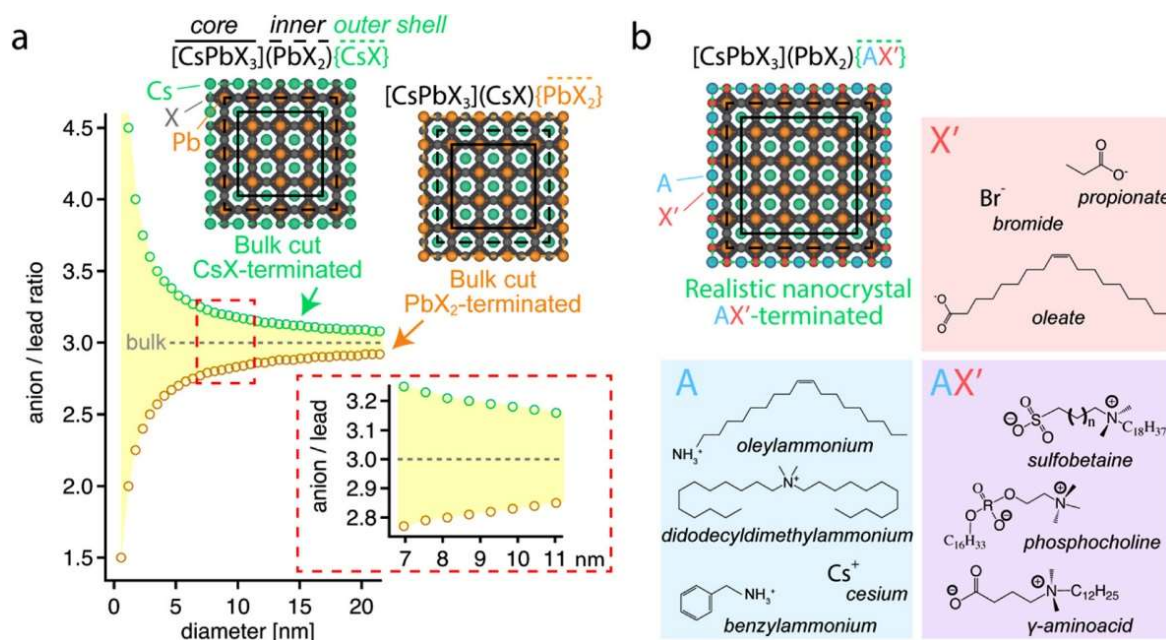


**Figure 1.28.** (a) Size-dependent anion/lead ratio ( $X/\text{Pb}$ ) of cubic  $\text{CsPbX}_3$  NCs, where Cs, Pb, and X (=halide) atoms are depicted by green, orange, and gray spheres, respectively. Unlike in bulk, in an NC the anion/lead ratio deviates from three, with the upper bound (green circles) and lower bound (orange circles) given by  $\text{CsX}$  and  $\text{PbX}_2$  termination, respectively. The inset shows commonly found experimental sizes, for which the anion/lead ratio should vary only between about 2.8 and 3.2, indicated by the yellow shaded area. (b) Arbitrarily structuring of the NC into core, inner, and outer shell. For a realistic NC requiring colloidal stability, the outermost layer is commonly replaced either by ligand pairs  $\{\text{AX}'\}$ , where A = cationic ligand (e.g., oleylammonium) and  $\text{X}'$  = anionic ligand (e.g., bromide, oleate), respectively, or more recently also with zwitterionic ligands  $\{\text{AX}'\}$ , e.g., sulfobetaines. In either case, the anion/lead ratio (now  $[X + \text{X}']/\text{Pb}$ ) still falls within the yellow shaded area depicted in (a), and green circles correspond to full capping by the  $\{\text{AX}'\}$  ligand shell. Reprinted with permission from ACS Energy Lett. 2019, 4, 63–74. © 2018 American Chemical Society.<sup>227</sup>



*Ion exchange* reactions have proved to be an efficient synthetic alternative for ionic NCs that demonstrated to be challenging to synthesize or not accessible by conventional methods such as HI method.<sup>229</sup> The ion exchange approach makes use of an existing ionic crystal lattice and by replacing one ion with another, allows the syntheses of crystal phases or novel heterostructures while preserving the size and morphology of the initial template NC.<sup>229-233</sup> Ion exchange reactions are divided into cation and anion exchange reactions, depending on the exchanged species.

*Cation exchange* (CE) reactions have been reported to be very useful for various I-VI, II-VI, IV-VI, and III-V semiconductor NCs but not so efficient in the case of perovskite NCs. It has been reported that in the case of conventional semiconductors, that have a more covalent character, the CE process generates rapidly new compositions with new optical properties by entirely exchanging the constituent cations.<sup>29, 32, 232, 234-240</sup> In the case of (some) perovskite materials, which are characterized by a strongly ionic character, the CE process is rather challenging and in most of the situations alter the crystal structure.<sup>64, 151</sup> In principle, both the A- and B-cations can be partially or entirely exchanged through CE reactions.<sup>148, 241-243</sup> In the first study on ion exchange reactions in lead halide perovskite NCs, was reported that various attempts to exchange either the Cs<sup>+</sup> cations (with Rb<sup>+</sup>, Ag<sup>+</sup>, Cu<sup>+</sup>, Ba<sup>2+</sup>) or Pb<sup>2+</sup> cations (with Sn<sup>2+</sup>, Ge<sup>2+</sup> or Bi<sup>3+</sup>), in the CsPbX<sub>3</sub> NCs have led to the decomposition of the parent NCs.<sup>64</sup> Later on, it was reported that the CE in CsPbX<sub>3</sub> NCs is possible when organic A-cations are used. The nature of A-cation has a significant influence in establishing the symmetry of the crystal structure. For instance, the organic cations (e.g., MA, FA) are more dynamic and able to bind to [PbX<sub>6</sub>]<sup>4-</sup> octahedra through hydrogen bonds whereas the inorganic ones (e.g., Cs) are not. Therefore, replacement of the inorganic cations with organic ones will induce symmetrical changes which ultimately lead to alterations of the vibrational modes into the perovskite NC structure.<sup>151</sup> Also, exchanging the A-cation in the lead halide perovskite can modify (i) the tolerance factor further affecting the stability of NCs, (ii) the tilting of the B-X-B bond further affecting the emission peak position and lifetime, and ultimately (iii) the dimensionality. For instance, FA<sup>+</sup> cations can replace partially or entirely Cs<sup>+</sup> cation into the structure of CsPbI<sub>3</sub> NCs generating more stable NCs with emission in the near-IR spectral region.<sup>148</sup> Replacement of B-cation through postsynthetic CE reactions is more challenging than exchanging the A-cation, because of its structural position – it is forming [PbX<sub>6</sub>]<sup>4-</sup> octahedra which are enclosed by 8 A-cations. Despite these, partial CE of B-cation has been reported for CsPbBr<sub>3</sub> perovskite NCs contrary to the first negative observation. By mixing a solution of CsPbBr<sub>3</sub> NCs, with a

solution of  $MBr_2$  ( $M = Sn, Zn$  or  $Cd$ ) an alloyed  $CsPb_{1-x}M_xBr_3$  structure is formed (**Figure 1.29a**). A blue shift of the emission PL maxima was observed for the new NCs while the typical high PL QY and narrow emission linewidths of the parent NCs were preserved.<sup>241</sup> The blue shift was explained as being a consequence of the lattice contraction induced by the guest  $[MBr_6]^{4-}$  octahedra, which are electronically decoupled from the  $PbBr_6$  framework. Furthermore, the contraction of  $PbBr_6$  octahedra leads to shorter  $Pb - Br$  bonds, which means that the interactions between  $Pb$  and  $Br$  orbitals are stronger than before exchanging  $Pb^{2+}$  cations with other  $M^{2+}$  ones. This stronger interaction further influences the CB, which is composed of antibonding combinations of  $Pb(6p)$  and  $Br(4p)$  orbitals, by shifting it to higher energies which in turn widens the band gap. It has been theorized that the CE process is facilitated by the presence of halide vacancies in the parent  $CsPbBr_3$  NCs, where the  $Pb^{2+}$  cations are exchanged through a halide vacancy-assisted migration.<sup>241</sup> This means that the OLA molecules present in the solution strip the  $Br^-$  anions from the NC's surface followed by the removal of  $PbBr_2$  units, leaving behind halide vacancies (**Figure 1.29b**). The formed vacancies are occupied by the introduced  $MBr_2$  species which diffuse inside the lattice.<sup>241</sup>

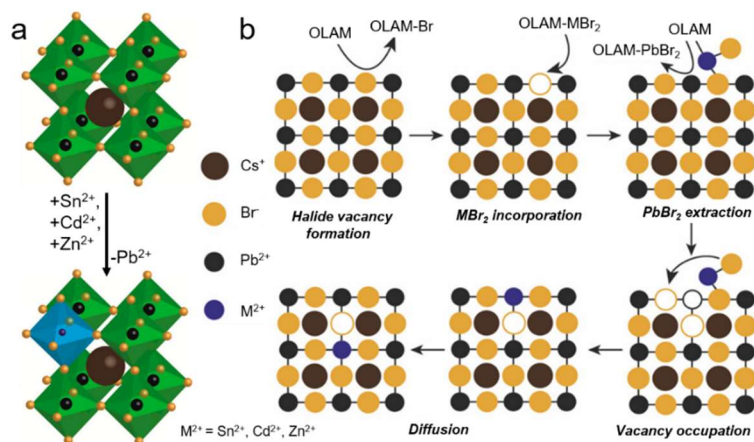


**Figure 1.29.** An overview of the cation exchange processes in lead halide perovskites; **(a)** Schematic representation of  $Pb^{2+}$  replacement by  $Sn^{2+}$ ,  $Cd^{2+}$ , or  $Zn^{2+}$  in the lead halide perovskite lattice; **(b)** Representation of the proposed mechanism for cation exchange within the lead halide perovskite according to van der Stam et al.<sup>241</sup> Reprinted with permission from *Chem. Rev.* 2019, 119, 3296-3348. © 2019 American Chemical Society.

Recent studies have shown that CE reactions can be used as an alternative approach to obtain alloyed  $CsPb_xMn_{1-x}Cl_3$  perovskite NCs while preserving the morphology and crystal structure of the parent  $CsPbCl_3$  NCs.<sup>244-245</sup> Moreover, it has been proved that the exchange between  $Pb^{2+}$  and  $Mn^{2+}$  is almost fully reversible when  $CsMnCl_3$  is treated with a solution of  $PbCl_2$  in OA-OLA-ODE. The complete replacement of  $Mn^{2+}$  by  $Pb^{2+}$  in the synthesized

CsMnCl<sub>3</sub> NCs is most likely prevented by the balance between the inward diffusion of Pb<sup>2+</sup> and the outward diffusion of Mn<sup>2+</sup>.<sup>244</sup> The newly synthesized alloyed perovskite NCs are characterized by poor stability towards photooxidation and thermodegradation. In order to overcome this inconvenience, a one-step procedure involving a dual ion exchange was applied. CsPbBr<sub>3</sub> NCs in toluene (or hexane) were selected as parent NCs, and they were mixed with MnCl<sub>2</sub> and KCl salts. The MnCl<sub>2</sub> was used as a single source for both cation and anion exchange. The quick replacement of Br<sup>-</sup> anions by Cl<sup>-</sup> ones facilitated the Pb<sup>2+</sup> substitution with Mn<sup>2+</sup> cations by opening the surrounding rigid halide octahedron. After the completion of ion exchange, the newly formed alloyed NCs were embedded into the KCl matrix which offered robust protection from photooxidation and thermodegradation, producing PL QYs of 60%.<sup>245</sup> The dual ion exchange is characterized by long reaction times (e.g., 40 hours) due to the slow diffusion of Mn<sup>2+</sup> and Cl<sup>-</sup> ions from the surface to the core of the NCs. During these processes, triple emissions bands could be observed using optical measurements, suggesting the formation of intermediate core-shell structures. Other studies reported homogeneous Cs(Pb<sub>x</sub>M<sub>1-x</sub>)(Cl<sub>y</sub>Br<sub>1-y</sub>)<sub>3</sub> NCs obtained via a postsynthetic cation-anion co-substitution reaction as a result of mixing colloidal CsPbBr<sub>3</sub> and CsPb<sub>1-x</sub>Mn<sub>x</sub>Cl<sub>3</sub> NCs in hexane.<sup>246</sup> Furthermore, based on the idea of co-substitution, a more complex, white light emitting Cs(Pb<sub>1-x-z</sub>Zn<sub>z</sub>)(Cl<sub>y</sub>Br<sub>1-y</sub>)<sub>3</sub>:xMn<sup>2+</sup> NCs could be obtained by controlling the mixing of CsPb<sub>1-x</sub>Mn<sub>x</sub>Cl<sub>3</sub> NCs with a solution of ZnBr<sub>2</sub> (in OLA/hexane).<sup>247</sup>

*Anion exchange* (AE) reactions, in contradistinction to the CE, were found to be more challenging or even impossible for the case of conventional semiconductor QDs, while for lead halide perovskite NCs, proved to be very fast and facile. On one hand, for II-VI, III-V or IV-VI semiconductor QDs, the AE proved to be a more elusive process where the extraction and replacement of the anions are more difficult resulting in a partial exchange or limited to a few surface atomic layers.<sup>100, 231, 248-251</sup> Only a few examples of such anion exchange reactions are reported for the more traditional semiconductor QDs, thus reflecting both the typical difficulties encountered (e.g., reordering of the crystal structure or fracturing) and the challenging reaction conditions necessary (e.g., high reaction temperatures of 160-450 °C for ZnO to ZnS(Se) conversions).<sup>231, 248</sup> On the other hand, in the case of lead halide perovskites, which are characterized by high ionic conductivities, the AE process proved to be extremely fast and completely reversible (**Figure 1.30**).<sup>64, 252-258</sup> Since the halide orbitals are significant contributors to the VB, a fine-tuning of the optical properties can be achieved by systematic

halide variation ( $\text{Cl} \rightarrow \text{Br} \rightarrow \text{I}$  or  $\text{I} \rightarrow \text{Br} \rightarrow \text{Cl}$ ), while preserving the size, morphology and crystal structure of the parent NC.<sup>64, 182, 252-253, 258-260</sup>

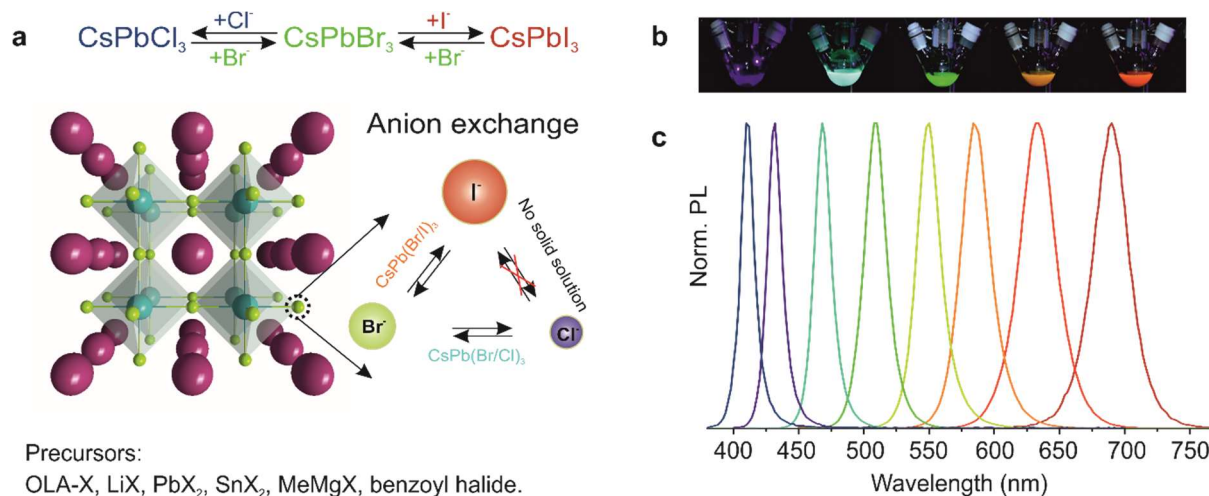


**Figure 1.30.** (a) Schematic representation of anion exchange in lead halide perovskites depicting its versatility; (b) Photos of anion-exchanged colloidal CsPbX<sub>3</sub> (X = Cl, Br, I, and mixed Cl/Br and Br/I respectively) perovskite NCs under UV light ( $\lambda = 365$  nm); (c) Photoluminescence spectra of CsPbX<sub>3</sub> NCs prepared via anion exchange. Reprinted with permission from *Nano Lett.* 2015, 15, 5635-5640. © 2015 American Chemical Society.

In general, in both hybrid and all-inorganic perovskite lattices, the A-cations and halide anions are characterized by high mobility which gives rise to a broad spectrum of lattice domains.<sup>261-262</sup> It has been found that the mobility of halide anions is affected by the high intrinsic concentration of halide vacancies, and is also responsible for the hysteresis in the current-voltage curves from films of these materials.<sup>263-264</sup> Among the various ions and defects, the halides and halide vacancies are the fastest migrating species, having activation energies for their migration in the range of  $\sim 0.1$  eV to  $\sim 0.6$  eV.<sup>265-268</sup> These two factors (the fast ion/defect motion and the low defect formation energy) facilitate the halide exchange reactions in lead halide perovskite NCs. Therefore, a fine-tuning of the optical properties can be easily achieved via postsynthetic AE by simply exposing the NCs to precisely selected amounts of the desired halide precursor.<sup>146, 166, 269-270</sup> Moreover, the fast, deliberately partial or complete AE can be performed at low reaction temperatures in the cases of  $\text{Cl} \rightarrow \text{Br}$ ,  $\text{Br} \rightarrow \text{Cl}$ ,  $\text{Br} \rightarrow \text{I}$ , and  $\text{I} \rightarrow \text{Br}$  via homogeneous solid solutions. Because of the large difference in ionic radii between Cl<sup>-</sup> and I<sup>-</sup>, homogeneous solid solutions of mixed Cl-I compositions were not afforded. When the blue-emissive CsPbCl<sub>3</sub> NCs were exposed to I<sup>-</sup>, the perovskite solution lost its blue emission and started to show a red emission a few seconds later ( $>30$  sec) without showing any emission corresponding to a stable mixed CsPb(Cl/I)<sub>3</sub> composition; the same behavior could

be observed in the reverse situation of CsPbI<sub>3</sub> NCs + Cl<sup>-</sup>.<sup>64</sup> Various halide sources having different reactivities, such as OLA-X, LiX, PbX<sub>2</sub>, SnX<sub>2</sub>, benzoyl halides, or MeMgX, can be used for performing the AE on presynthesized CsPbX<sub>3</sub> NCs.<sup>64, 196, 252, 271-272</sup> It has been found that the AE can be performed in an even more simple manner. By simply mixing solutions of presynthesized CsPbX<sub>3</sub> NCs, for instance, CsPbCl<sub>3</sub> and CsPbBr<sub>3</sub>, a homogeneous mixed-halide composition (CsPb(Cl/Br)<sub>3</sub> or CsPb(Br/I)<sub>3</sub>) can be obtained.<sup>64</sup> Recent studies, based on optical and quantitative X-ray photoelectron spectroscopy analyses, claim that the intermediate compositions (e.g., CsPb(Br/I)<sub>3</sub>) have radial-gradient compositions, and the halide concentration is higher at the surface of the NCs.<sup>271, 273</sup>

Another way of performing the AE reactions is via a reductive dissociation of the solvent molecules. In this case, the CsPbX<sub>3</sub> (X = Cl or Br) NCs are dispersed in dihalomethane, and the AE process is ignited by a photoinduced electron transfer from the perovskite NCs to the solvent molecules, producing halide ions via a reductive dissociation.<sup>256</sup> The in situ generated halide ions drive the AE reaction efficiently as far as the CsPbX<sub>3</sub> NCs are photoexcited above their bandgap. The reaction can be controlled by adjusting either the photon dose or the wavelength of the excitation light which self-limits the reaction when the light becomes off-resonant with the absorption of the NCs.<sup>256</sup>

The AE reactions can also take place in a solid state or at the solid/gas interface. It has been demonstrated that by adding fine powders of KX (X = Cl, Br, I) into solutions of lead halide NCs (in hexane), and subsequent evaporation of the solvent, the AE takes place entirely in the solid state.<sup>253</sup> Furthermore, the AE can take place even when the NCs are sintered in thin films and submerged in a heated PbX<sub>2</sub> solution.<sup>274</sup> Even more, the AE can occur in a controllable manner even at the solid/gas interface, and it has been demonstrated for the case of CsPbX<sub>3</sub> (X = Br, I) NWs which were exposed to volatile halide precursors (such as methylammonium halides or butylammonium halides) that can evaporate slowly under mild conditions (~100 °C).<sup>275</sup>

High and precise control of the AE reaction has been demonstrated in the fabrication of multicolor CsPbX<sub>3</sub> (X = Cl, Br, I or alloy of two halides) NWs heterojunctions having a pixel size down to 500 nm and a PL emission that is tunable over the entire visible spectral range.<sup>255</sup> In order to achieve such control, a CsPbBr<sub>3</sub> NW was transferred onto a SiO<sub>2</sub>/Si substrate and covered with a thin layer of poly(methyl methacrylate) (PMMA) by spin-casting. A selected area of the PMMA film was removed by e-beam lithography exposing in this way a specific

segment of the NW which was later dipped into an OLA-X (X = Cl, I) solution for the AE reaction, resulting in a nanoheterostructure capable of showing distinctive emission at different wavelengths.

Despite being a beneficial method that enables the excellent control of the optical properties of lead halide perovskite NCs, the AE is sometimes an undesired process. Advances in this direction have been recently published, showing that the AE can be suppressed by passivating the NCs with PbSO<sub>4</sub>-oleate.<sup>276</sup> This type of control could be very beneficial for the deposition of different compositions as tandem layers to engineer efficient harvesting of light.

## 1.6 Applications of semiconductor nanocrystals

Nanomaterials have been used since ancient times either for artistic and aesthetic purposes (e.g., Lycurgus cup, the windows of Notre Dame Cathedral) or more functional ones, such as reinforcement of different materials (e.g., ceramic reinforcement by adding natural asbestos nanofibers to their composition) and therapeutic properties (use of “soluble gold” to cure various diseases like heart and venereal problems, dysentery, epilepsy, and tumors).<sup>3-4, 6</sup> Nowadays, due to the enormous progress made, nanomaterials are being used in an extensive range of applications, such as photovoltaics and light-emitting devices, sensors and detectors, waveguides and laser technology, security and anti-terrorism, cosmetics and biomedical industry, aviation and aerospace and so on.

Colloidal semiconductor NCs are a particular class of nanomaterials which by combining their colloidal state with their optoelectronic capabilities, can excel in many various fields. Their colloidal state enables them to be soluble in suitable solvents, which favor the easy fabrication of thin film electronic devices by employing well-established coating and printing techniques. Advancements in the synthesis of colloidal QDs were made such that inexpensive, more environmentally friendly and scalable, wet-chemical synthetic procedures afford high-quality materials, promoting their use in electronic devices in contrast to the expensive manufacturing methods and procedures, such as chemical vapor deposition or molecular beam epitaxy.

The significant progress made in the last two decades toward the synthesis of colloidal InP and InAs QDs using inexpensive and less hazardous precursors has brought their optical properties to a quality comparable to more conventional II-VI and IV-VI QDs. The integration

of QDs into commercial optoelectronic devices started in 2013 when Sony commercialized the first TV, under the trademark *Triluminos*, using CdSe QDs to produce a greater variety of colors and more natural shades and hues.<sup>277</sup> Later, other TV display manufacturers, such as Samsung Electronics, LG Electronics, and TCL Corporation, adopted the use of QDs in developing their technologies and presented their products in 2015 at Consumer Electronics Show (**Figure 1.31**).<sup>278</sup>



**Figure 1.31.** LED-LCD TV displays depicting their evolution from the first Quantum Dot TV with CdSe/CdZnS QDs from Sony (2013) to cadmium-free technology used by Samsung for their InP/ZnS QDs-based SUHD TV (2015) and QLED TV (2017). Source: Samsung Newsroom.

Because of the Directive on the restriction of the use of certain hazardous substances in electrical and electronic equipment, known as Restriction of Hazardous Substances (RoHS), manufacturers had to orient towards more environmentally friendly materials.<sup>279</sup> InP QDs are very potent substitutes for CdSe QDs, and the recent progress on their synthesis affords different core/shell heterostructures characterized by PL QYs up to 85% and reasonable narrow emission lines of 35 nm for blue emission (PL 488nm), 37 nm for green emission (PL 533 nm), and 39 nm for red emission (PL 625 nm).<sup>68, 103, 106, 280-281</sup> Due to such optical capabilities, these various InP-based heterostructures were tested in white light emitting devices (LEDs) as down-conversion phosphor and in the framework of electroluminescence devices.<sup>106, 281-285</sup> For instance, Kim *et al.* reported the design of electroluminescence LEDs (QLEDs) using highly luminescent InP/GaP/ZnS core/shell/shell QDs (PL<sub>555nm</sub> QY = 85%).<sup>103</sup> He observed the direct formation of excitons within QDs and an efficient radiative exciton recombination reporting a luminous efficiency of 54.71 lm/W, Ra of 80.56, and CCT of 7864 K at the color coordinate

(0.3034, 0.2881).<sup>106</sup> Remarkable results were reported as well for green emitting QLEDs by Lim *et al.*<sup>106</sup> The resulting green QLEDs record 3.46% of external quantum efficiency and 3900  $\text{cd m}^{-2}$  of maximum brightness, which represent a 10-fold increase in device efficiency and a 5-fold increase in brightness compared with previous reports.<sup>106</sup> These remarkable results were achieved by the direct exciton formation within InP/ZnSeS heterostructured QDs, facilitated by the insertion of a thin conjugated polyelectrolyte layer – poly[(9,9-bis(3'-(*N,N*-dimethylamino)propyl)-2,7-fluorene)-*alt*-2,7-(9,9-dioctylfluorene)], PFN. The PFN layer has a critical role in the reduction of the electron injection barrier between cathode and QDs via vacuum level shift, and promotes the charge balance within QDs (**Figure 1.32a**). More recent studies reported a considerable enhancement of the brightness ( $>10.000 \text{ cd m}^{-2}$ ), record external quantum efficiency of 6.6% for red, and suppression of the Förster resonant energy and Auger recombination.<sup>284, 286</sup> Wang *et al.* attained these records by using red-emitting InP/ZnSeS/ZnS QDs and an improved electron transporting layer of ZnMgO.<sup>284</sup> Cao *et al.* obtained the same results by overgrowing a thick external shell of ZnS on InP/ZnSe QDs, obtaining at the end InP/ZnSe/ZnS QDs with red emission and dimensions of  $\sim 15 \text{ nm}$  (**Figure 1.32b**).<sup>286</sup> Also, substituting the red, green, and blue (RGB) color filters with narrow-band green and red emitting InP/ZnSeS/ZnS QD films in color-by-blue QD-emissive liquid-crystal displays (LCDs) afforded a 1.49 times improvement in the relative luminance levels and 2.42 times in the EQE values in contrast to conventional color filter (CF)-LCD.<sup>287-288</sup> These latest reports prove that there is still plenty of room for improvement and optimization, and advancements in the synthesis in the metal-phosphide QDs will increase the performance of optoelectronic devices.<sup>288</sup>

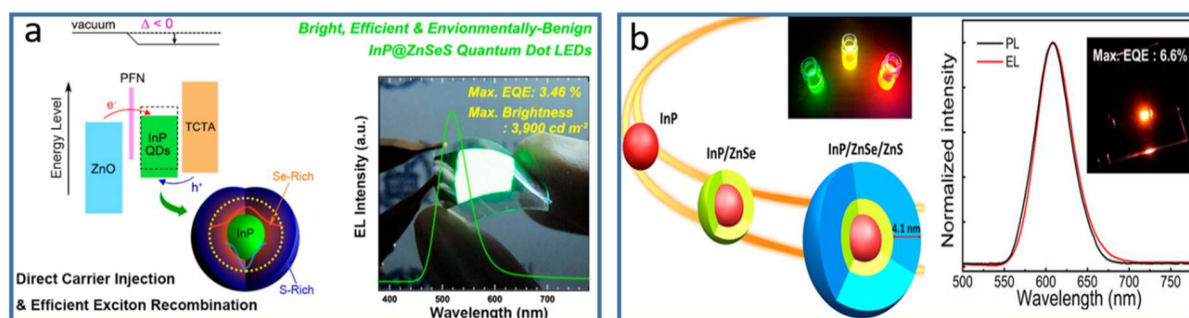


**Figure 1.32.** (a) Schematic representation of the band energy level diagrams of QLEDs illustrating the reduction in electron injection barrier between ZnO and QDs due to the presence of the PFN layer (left), and Normalized EL spectra of InP/ZnSeS (1.7 nm shell thickness) QLEDs (right). Inset: Photograph of large-area and flexible InP/ZnSeS QLED on a polyethersulfone substrate; pixel size = 1.2 cm  $\times$  1.2 cm. Reprinted with permission from ACS Nano 2013, 7, 10, 9019-9026. © 2013 American Chemical Society.<sup>106</sup> (b) Schematic of the synthetic procedure of InP/ZnSe/ZnS core/shell/shell QDs



and photograph of the fluorescent QDs under UV light illumination (left), and normalized electroluminescence (EL) and photoluminescence (PL) spectra of the device; inset: image of QLED operating at 7 V, yielding a bright emission at  $\sim 700$   $\text{cd/m}^2$ . Reprinted with permission from *Chem Matter*. 2018, 30, 8002-8007. © 2018 American Chemical Society.<sup>286</sup>

Recent studies reported advancements into the synthesis of monodisperse InAs QDs using less hazardous and less expensive arsenic precursors, such as tris(dialkylamino)arsine (alkyl = methyl, ethyl) or tripyrazolylarsine.<sup>25, 140</sup> For example, Franke *et al.* reported a continuous injection synthesis that affords monodisperse InAs QDs with tunable PL emission (700-1200 nm) and narrow FWHM ( $<135$  meV) without employing any size-selective purification approaches. Based on these InAs QD cores, a core/shell/shell heterostructured InAs/CdSe/CdS QDs with PL emission that covers the entire sensitivity range of modern short-wavelength infrared (SWIR) cameras (900-1600 nm, <http://www.princetoninstruments.com/products/imcam/nirvana/>), enhanced stability (under laser irradiance and long-term storage), and QYs up to 82%.<sup>105</sup> Moreover, it was demonstrated that these QDs are very good SWIR fluorophores, showing more than six times higher brightness compared with previously reported InAs-based QD systems. Additionally, it has been demonstrated that these heterostructures exhibit two-three order of magnitude higher QYs, compared to carbon nanotubes, across the entire sensitivity range of SWIR cameras and successfully used in non-invasive through-skull fluorescence imaging in mice (**Figure 1.33**).<sup>105, 289-290</sup> Also, these improved capabilities of InAs-based QD systems were suggested as possible use in other applications such as SWIR LEDs, lasers, photovoltaics, photodetectors, and photon upconversion devices.<sup>105, 291-293</sup>

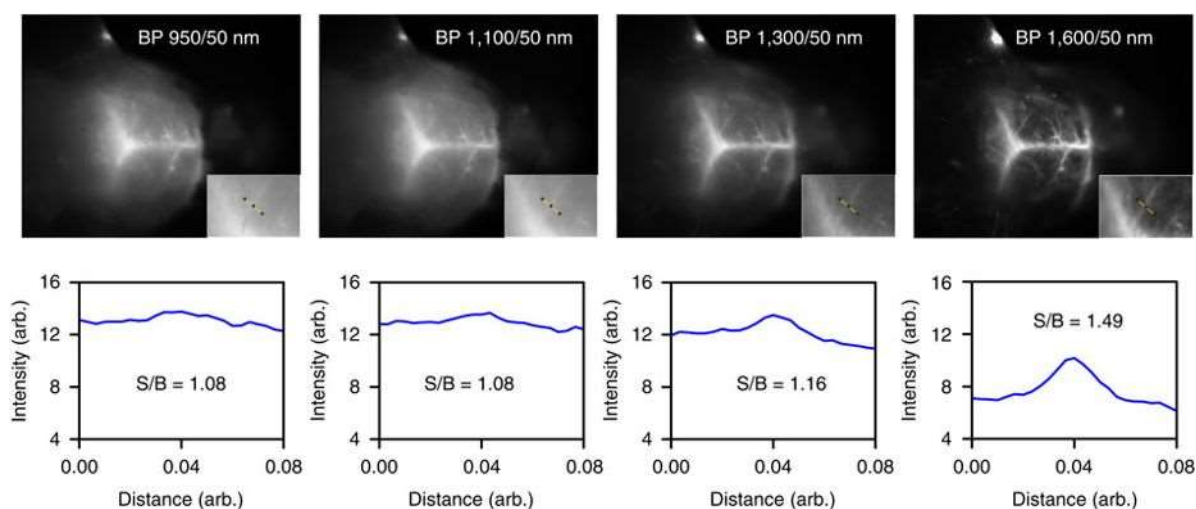


**Figure 1.33.** Fluorescence imaging of mouse brain vasculature through intact skin and skull using a mixture of SWIR InAs/CdSe/CdS heterostructured QDs. The four images were collected using four

bandpass filters (50 nm spectral width) centered at 950, 1,100, 1,300 and 1,600 nm with integration times of 150, 50, 100 and 5,000 ms, respectively. The images show that longer imaging wavelengths enhance the spatial resolution of fine vascular brain structures by significantly improving the signal to background (S/B) ratio in the region of interest, which stresses the need for SWIR emitters with high QYs and narrow emission at the red edge of SWIR detectors. Reprinted with permission from *Nature Communications* 2016, 7, 12749.<sup>105</sup>

Colloidal CsPbX<sub>3</sub> perovskite NCs are highly luminescent nanomaterials with optoelectronic properties tunable over a broad spectral range (400-700 nm) characterized by high PL QYs, narrow emission linewidths, and high defect tolerance, which are beneficial for applications, such as LEDs, LCD TV displays, solar cells, photodetectors, or lasers (**Figure 1.34**).<sup>157-158, 169</sup>

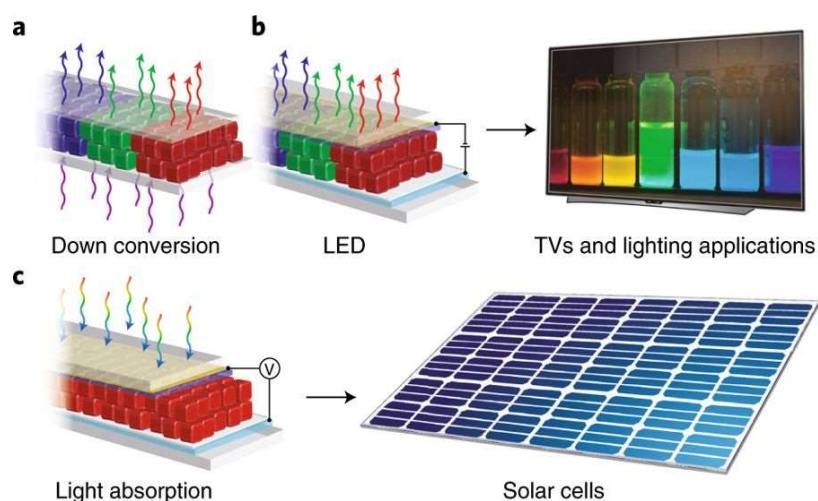


**Figure 1.34.** Optoelectronic applications of LHP NCs. *a–c*, Owing to high PL QYs, narrow PL FWHM and tunability over the entire visible spectral range, lead halide perovskite NCs can find applications in PL down conversion, such as LCDs and lighting (*a*); in electroluminescent devices, such as LEDs (*b*); and in solar cells (*c*). Reprinted with permission from *Nature Materials* 2018, 17, 394-405. © 2018 Macmillan Publishers Limited, part of Springer Nature.<sup>157</sup>

For instance, shortly after the first report on the colloidal CsPbX<sub>3</sub> perovskite NCs, a photoconversion efficiency (PCE) of 10.77% for a solar cell based on phase-stable  $\alpha$ -CsPbI<sub>3</sub> QDs, and later an increase of PCE up to 13.43% after an A-site cation treatment was reported.<sup>294-295</sup> Additionally, the CsPbX<sub>3</sub>-based solar cells, in contrast to the organic metal halide perovskite ones, have shown higher thermal stability (more than 150 hours at 100 °C) and stable performance (up to two weeks) under constant illumination.<sup>296-297</sup> Successful attempts were reported as well for the case of using CsPbX<sub>3</sub> perovskite NCs as emitting layers in LEDs. In a first study, the external quantum efficiency (EQE) of a CsPbBr<sub>3</sub>-based LED was reported to be 0.12%, and in a later study, the reported EQE increased up to 8.7% due to the

careful purification of the NCs with an ester solvent in order to control the ligand density and balance the surface passivation and carrier injection.<sup>192, 298-299</sup> CsPbX<sub>3</sub>-based photodetectors have been prepared as well, and, for instance, an on/off photocurrent ratio of 10<sup>5</sup> and rise and decay times of 24 and 29 ms, respectively, were reported when CsPbI<sub>3</sub> NCs were used as the main component (Figure 1.35).<sup>300</sup>

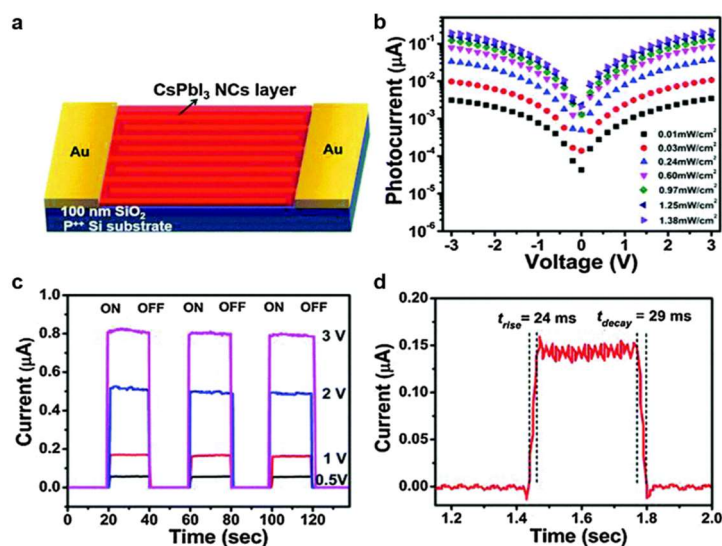


**Figure 1.35.** (a) Schematic of the CsPbI<sub>3</sub> NCs photodetector ( $L = 3 \mu\text{m}$ ,  $W = 7800 \mu\text{m}$ ). (b)  $I$ - $V$  characteristics of close-packed CsPbI<sub>3</sub> NC films as a function of incident light intensity. (c) Photocurrent-time ( $I_{\text{ph}}-t$ ) response measured in the dark and under illumination using a laser diode at 405 nm as a function of applied bias at a fixed light intensity ( $P_{\text{in}} = 1.98 \text{ mW cm}^{-2}$ ). (d) Rise and decay time of the photodetector device. Reprinted with permission from *Chem. Commun.*, 2016, 52, 2067-2070 ©The Royal Society of Chemistry 2016.<sup>300</sup>

CsPbX<sub>3</sub> NCs have proved to be suitable lasing materials due to their extraordinary optoelectronic capabilities. It was possible to realize multicolor and low-threshold lasing with high values of mode line-width (0.14-0.15 nm). Despite all these achievements in all these various fields, the stability of CsPbX<sub>3</sub> perovskite NCs is still limited, and efforts are being made in this direction.<sup>301-303</sup> Further details about the application of perovskite NCs are discussed in greater detail in some recent reviews by Akkerman *et al.*, Zhang *et al.*, Shamsi *et al.*, and Fu *et al.*<sup>157-158, 169, 304</sup>

Both classes of semiconductor NCs, III-V pnictides QDs and CsPbX<sub>3</sub> perovskite NCs, are very sturdy materials and characterized by exceptional properties. Even though some of these nanomaterials are already employed in the production of different electronic devices, active investigations are currently done in order to eliminate the drawbacks of the materials and to maximize their capabilities.

## 1.7 Scope and outline of the thesis

**In summary, this Ph.D. project focused on the exploration of new, low-cost, and non-hazardous synthetic strategies towards obtaining metal-pnictide and metal-halide colloidal NCs with enhanced stability and tunable optoelectronic properties over UV-Vis and NIR spectral regions.** The project was divided into two separate directions summing four independent studies focused on the synthesis of the targeted materials. One of these directions explored new potential phosphorous and arsenic precursors for the synthesis of metal-phosphide and -arsenide QDs, in particular, InP and InAs QDs. The second direction of this project focused on CsPbX<sub>3</sub> (X = Cl, Br, I) perovskite NCs and explored the tunability of their optical properties by compositional and morphological modulations via anion exchange and direct synthesis.

This first Chapter provides background information related to each of the studies and justifies the targeted scientific problems. In Chapter 2, a brief description of the experimental methods and techniques is offered. The actual results are reported in the following four chapters (Chapter 3-6), which correspond to first-author studies, one published and one in preparation, by the candidate (G. Nedelcu). The Outlook Chapter summarizes the thesis and provides an outlook on future directions. It is worth mentioning that the candidate had been involved in a variety of collaborative projects in which some of the developed materials were provided for various, mostly photophysical studies. The results of these collaborative studies are not discussed in this thesis but are discussed in detail in more than 15 co-authored papers which can be found in the publication list in *Appendix C*.

**Acylphosphines – a new class of phosphorus compounds for the facile synthesis of metal-phosphide quantum dots (Chapter 3).** The interest in synthesizing high-quality metal-phosphide QDs, especially InP QDs, increased tremendously in the last couple of years as QDs started to be used in TV display technology. Initially, Cd-based QDs were used in a quantum dot enhancement film (QDEF) in order to improve the LED backlighting in LCD TV. However, because of the toxicity of Cd and the EU's restrictions regarding the use of toxic elements in consumer optoelectronic devices, InP QDs are the best option at the moment for being employed in the fabrication of optoelectronic devices. Despite the current progress towards the use of safer, environmentally friendly, and less expensive phosphorus precursors for the synthesis of high-quality InP QDs, still, the best optoelectronic properties are given by those QDs synthesized by using the highly toxic, pyrophoric and expensive P(SiMe<sub>3</sub>)<sub>3</sub>. Recently, few

studies have demonstrated the use of new types of phosphorous compounds, both commercially available ones, such as  $P(NMe_2)_3$  or  $P(NEt_2)_3$ , or unavailable ones, such as  $P(Pyr)_3$ , as precursors for the synthesis of InP QDs. While these new entries are safer to use and less expensive, their performance is not better, usually worse, than  $P(SiMe_3)_3$ . Therefore, it remains necessary to find safer and more environmentally friendly P-precursors to afford the design of faster and inexpensive synthetic procedures for the synthesis of high-quality InP and other metal-phosphide QDs. In this chapter, acylphosphines are introduced as a new class of potential phosphorous precursors for the synthesis of high-quality InP QDs, and the preliminary results from their testing are summarized and reported. Acylphosphines are used to produce acylphosphine oxides which have an essential role in the manufacture of consumer goods, such as automotive coatings, adhesives, latex composition kits, and orthodontic materials, where they are used as photoinitiators for radical-initiated polymerization reactions.<sup>305-306</sup> The potential of several bis- and tris-acylphosphines were tested for the synthesis of InP QDs by using two different approaches, the acetate and the halide approach, following the models of heating-up and hot-injection methods. Each of the tested acylphosphines proved to be efficient and reactive enough to generate the necessary phosphorous species for the facile synthesis of InP QDs. Breakthroughs, such as the synthesis of luminescent InP QDs without a passivating shell were recorded, in contrast with existing studies which still report that adequate surface passivation is imperative in order to achieve PL emission in these QDs. Tunability of the optical properties was proved as well for each of the precursors involved in the study and PL QYs as high as 70 % were revealed after surface passivation of the QDs with a ZnS shell. Based on these findings, it is safe to speculate that these precursors can be a very efficient phosphorous source for the synthesis of other metal phosphide NCs, such as GaP, AlP, or InGaP.

**Aluminum-tris(bismesitoylarsine),  $Al(MesBAAs)_3$  – inexpensive, air-stable, and versatile arsenic-precursor for the synthesis of metal-arsenide quantum dots (Chapter 4).** Metal-arsenide semiconductor QDs that absorb and emit in the infrared (IR) are of interest for a broad range of applications, such as telecommunications, bioimaging, photovoltaics, photodetectors, and lasers.<sup>31, 61, 105, 291-292, 307-313</sup> Their use in any of these applications, and of course in devices targeting commercialization, is conditioned by the quality of the QDs yielded by the employed synthetic method. Despite recent improvements in the PL QYs, narrow full-width at half-maximum (FWHM), and photostability of arsenide-based QDs, serious drawbacks still exist when it comes to the synthetic procedures and the available precursors for their synthesis. Recent studies have reported synthetic protocols of metal-arsenide NCs using

less hazardous arsenic precursors, such as aminoarsines ( $\text{As}(\text{NMe}_2)_3$  or  $\text{As}(\text{NEt}_2)_3$ ), triphenylarsine ( $\text{AsPh}_3$ ) or tripyrazolylarsine ( $\text{As}(\text{Pyr})_3$ ), but these results do not outperform the performances obtained with  $\text{As}(\text{SiMe}_3)_3$ , and more investigations are needed.<sup>25, 105, 140, 314</sup> In this chapter, a general synthetic protocol, plus some additional synthetic procedures, are designed for the synthesis of InAs, GaAs,  $\text{Cd}_3\text{As}_2$ , and  $\text{Zn}_3\text{As}_2$  QDs using  $\text{Al}(\text{MesBAAs})_3$  as the arsenic source. The presented results prove that the  $\text{Al}(\text{MesBAAs})_3$  precursor can produce luminescent InAs and  $\text{Cd}_3\text{As}_2$  QDs without the involvement of additional procedures, such as overgrowing a shell or applying post-synthetic treatments. Very mild reaction conditions, such as relatively low reaction temperature (90 °C for InAs QDs), short reaction time (5 minutes for  $\text{Cd}_3\text{As}_2$  QDs and 30 minutes for InAs QDs), and optional use of reducing agents, are used in order to obtain QDs. In a preliminary attempt of improving the QY for the InAs QDs, a boost from 1-2 % up to 20 % was achieved by overgrowing a shell of ZnS onto the cores. This initial effort is promising, and the QYs can be further increased by a more detailed investigation of the optimal conditions for growing a protective shell. GaAs and  $\text{Zn}_3\text{As}_2$  QDs were obtained as well using  $\text{Al}(\text{MesBAAs})_3$  as an As-source with somewhat less remarkable properties, demonstrating the generalizability of the  $\text{Al}(\text{MesBAAs})_3$  as a precursor for As-based QD synthesis.

**Fast anion-exchange in highly luminescent nanocrystals of cesium lead halide perovskites ( $\text{CsPbX}_3$ , X = Cl, Br, I; Chapter 5).** Postsynthetic chemical transformations of colloidal nanocrystals, such as ion-exchange reactions, provide an avenue to compositional fine-tuning or to otherwise inaccessible materials and morphologies. While cation-exchange is facile and commonplace, anion-exchange reactions have not received substantial deployment. In this chapter, the fast, low-temperature, deliberately partial, or complete anion-exchange in highly luminescent semiconductor nanocrystals of cesium lead halide perovskites ( $\text{CsPbX}_3$ , X = Cl, Br, I) is presented. By adjusting the halide ratios in the colloidal nanocrystal solution, the bright photoluminescence can be tuned over the entire visible spectral region (410–700 nm) while maintaining high quantum yields of 20–80% and narrow emission line widths of 10–40 nm (from blue to red). Furthermore, fast internanocrystal anion-exchange is demonstrated, leading to uniform  $\text{CsPb}(\text{Cl}/\text{Br})_3$  or  $\text{CsPb}(\text{Br}/\text{I})_3$  compositions simply by mixing  $\text{CsPbCl}_3$ ,  $\text{CsPbBr}_3$ , and  $\text{CsPbI}_3$  nanocrystals in appropriate ratios.

**Cesium lead bromide nanoplatelets ( $\text{CsPbBr}_3$  NPLs) with stable emission at 492 nm (Chapter 6).** In this chapter, the fast and inexpensive synthesis of a few units cell thick colloidal  $\text{CsPbBr}_3$  NPLs is presented. They are characterized by a highly stable PL emission in

---

the blue regime (492 nm), and a sharp absorption band edge. By varying the injection temperature, the thickness of the NPL can be controlled, leading to the tuning of optical properties in the blue spectral range. Moreover, the PL emission and absorption peak can be fine-tuned over a broad spectral range (398 nm – 632 nm) via fast and efficient anion exchange while preserving the size, shape and particular self-assembled superstructure of the 492 nm emissive CsPbBr<sub>3</sub> NPLs. By transient photoluminescence and ultrafast transient absorption spectroscopy, the ultrafast radiative decay ( $3.334 \pm 0.0066$  ns), intraband relaxation lifetime ( $188.2 \pm 13.3$  fs) and Auger recombination lifetime ( $10.7 \pm 2.15$  ps) were investigated. Micro-photoluminescence measurements on single CsPbBr<sub>3</sub> NPLs were performed at room temperature (RT) and cryogenic temperatures ( $T = 5$  K). Low-temperature results show long-time optical stability, blinking-free emission, photon anti-bunching in the second order correlation function, and ultrafast radiative decay (200 ps). At RT, despite PL blinking still affects the emission properties, NPLs show enhanced photo-stability in PMMA polymer compared to cubic NCs. Improved optical stability, and high PL quantum yields (>75%) allow the realization of a first-kind blue light emitting device employing CsPbBr<sub>3</sub> perovskite NPLs as an emissive layer. The maximum luminance of  $22.1 \text{ cd m}^{-2}$  and external quantum efficiency of about 0.2% were recorded in the preliminary investigations. This work demonstrated the potential of NPLs in novel and efficient blue light emitting devices.

---

## Chapter 2. Methods and techniques

### 2.1. Synthesis of ligand-stabilized colloidal semiconductor nanocrystals

The metal-pnictide semiconductor QDs and perovskite NCs were synthesized in air-free conditions by using the HI method, apart from In(Zn)P where the HU method was used as well. The detailed procedures are described in each chapter. Briefly, one of the precursors (for instance, indium acetate for the synthesis of InP and InAs QDs) was loaded into a 25 mL 3-neck flask along with the solvent (e.g., ODE) and ligand(s), and were degassed for 1-2 hours under vigorous stirring and vacuum at a specific temperature (most of the cases 125 °C). After the degassing was finished, the entire reaction system was switched on N<sub>2</sub> gas and either (i) heated up to the desired injection temperature (case of HI method) or (ii) cooled down to the room temperature (case of the HU method for In(Zn)P QDs presented in Chapter 3). After the injection of the second precursor previously prepared, either on Schlenk line (case of perovskite NCs) or inside the glovebox (case of metal-pnictide QDs), the reaction was either immediately stopped or let it run for the desired time – case of the HI method; or, for the case of the HU method, the reaction temperature was raised at the desired value and stopped after a precise time. After the synthesis, the colloiddally stabilized NCs were purified by using different couples of solvent-antisolvent, for dispersion and precipitation of the NCs, and also centrifugation in order to separate the precipitate easily from the undesired byproducts and reaction medium.

### 2.2 Anion exchange

The anion exchange reactions are applied for CsPbX<sub>3</sub> (X = Cl, Br, I) NCs<sup>64</sup> and NPLs, respectively, and a shift of the status quo is presented in Chapters 5 and 6. The halide anions are extracted and replaced extremely fast in the metal halide semiconductor nanostructure. Due to their single ionic charge, the rigid structure of the cationic sublattice which serves as a template, and the efficient vacancy-assisted diffusion mechanism, the anion exchange was effective even at room temperature showing the preservation of the initial morphology while changing the composition and the optical properties. In Chapter 5 the anion exchange reactions



were done at 40 °C under N<sub>2</sub> atmosphere for the simple reason of having controllable conditions, and in Chapter 6, the anion exchange reaction was performed under air at room temperature. The exact procedures and details are described in each corresponding chapter.

### 2.3. Characterization methods and techniques

**Transmission Electron Microscopy (TEM)** is a powerful and vital investigation tool in nanoscience research comprising a complete repertoire of imaging, diffraction and analysis techniques. The first transmission electron microscope was built in the early 1930s by E. Ruska and M. Knoll by using the working principle of a visible-light microscope. As shown in **Figure 2.1**, a transmission electron microscope is using a coherent beam of electrons in order to visualize with sub-atomic resolutions the specimen. The electrons are generated by an electron source which can be thermionic (W or LaB<sub>6</sub>), or a field-emission gun. The emitted electrons are accelerated, and a coherent beam is formed by the condenser lens and condenser apertures (condenser lens system), in front of the objective lens. The objective lens, which consists of two parts and is called pole pieces, is focussing the electron beam to the specimen plane which is located in between the pole pieces. The objective aperture, located in the back focal plane of the objective lens and used mainly for bright- and dark-imaging, along with the selected area aperture, placed in the first focal plane and used for selected area diffraction, are directing the wave of electrons into the projector lenses system with role in magnifying the beam. Depending on the configuration, an image or a diffraction pattern is formed on the fluorescent screen or the recording medium (charge coupled device cameras in most of the cases).

The TEM images presented in this thesis were recorded on different microscopes. In each chapter, the details regarding the type of used microscope and technique are specified. In some cases, Dr. Frank Krumeich or Dr. Maryna Bodnarchuck helped with the acquisition of HRTEM and when the case it will be specified in the Acknowledgements section of the chapter.

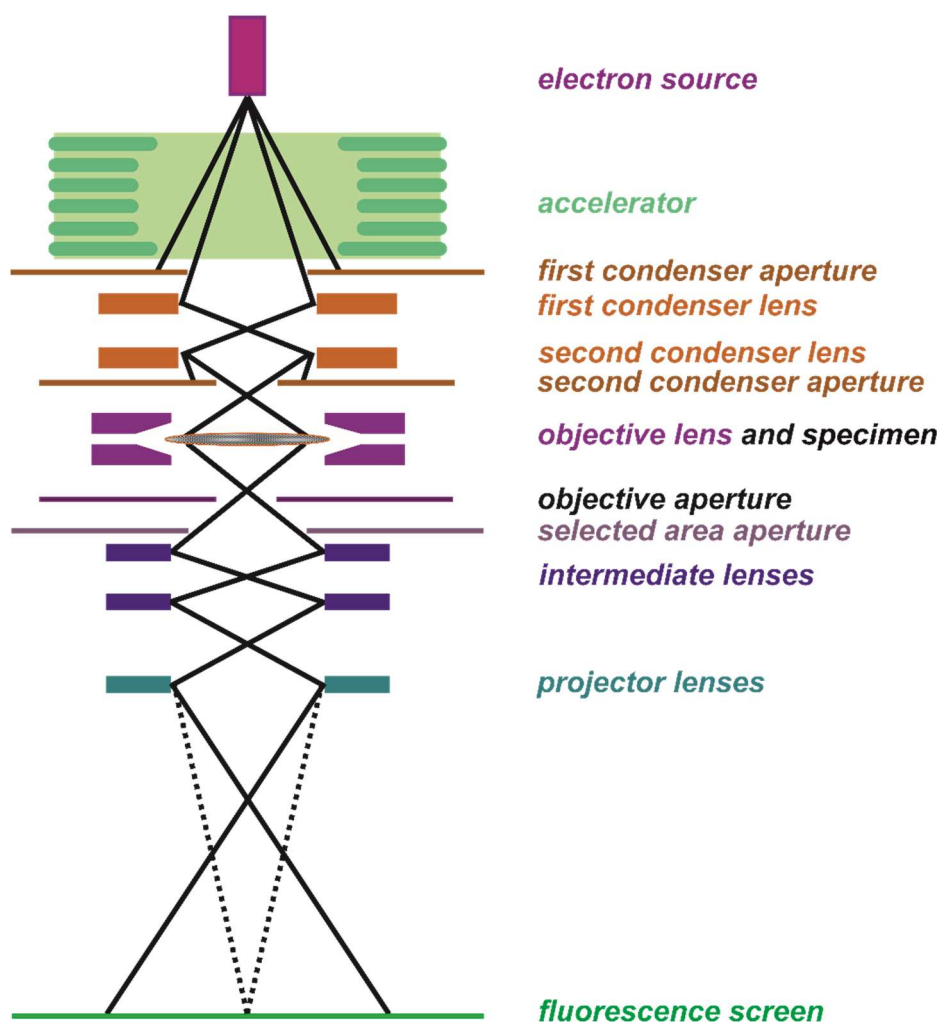


**Figure 2.1.** General representation of a transmission electron microscope and its general working principle. The projector lenses form either an image (solid black line) or a diffraction pattern (dashed black line) on the screen.

### Optical characterizations

**Absorbance.** UV-VIS and NIR absorption spectra were collected using a Jasco V670 spectrometer in transmission mode. The NPs were dispersed in appropriate solvents such as toluene (for UV-VIS spectral regime) or tetrachloroethylene (for NIR spectral regime), filtered and measured using standard cuvettes appropriate for each spectral regime, glass or quartz, respectively. All technical details are provided in each chapter in the **Experimental Section**.

**Photoluminescence (PL)** measurements were done using a Fluorolog iHR 320 Horiba Jobin Yvon spectrofluorimeter equipped with a PMT detector – for UV-VIS spectral regime – and an InGaAs detector – for NIR spectral regime. The samples – solutions or films of NPs -

were excited using a halogen lamp equipped with a monochromator or a laser diode (808 nm, up to 1W power).

For the case of InAs QDs (Chapter 5), the PL spectra were measured using a CCD fiber spectrometer LR1 type (Aseq Instruments). The excitation source was a double-frequency continuous wave Nd:YAG diode-pumped solid-state laser exciting at 532 nm. Photoluminescence emission of the samples was passed through a long-pass optical filter with an edge at 550 nm in order to reject the excitation laser line.

All technical details specific to each material are provided in the **Experimental Section** of the respective chapter.

**In-situ photoluminescence measurements** were performed in Chapter 3 in order to monitor in-situ the anion exchange. The perovskite NPs were excited directly in the reaction flask during the anion exchange process by a CW laser ( $\lambda=405$  nm,  $P= 300$  mW) through one branch of a Y-shaped fiber optic bundle. The PL emission was collected with the second branch of the fiber optic bundle and was recorded with a compact CCD spectrometer (LR1, Aseq-Instruments).

**PL quantum yields (QYs).** The absolute PL QY is defined as a number ratio of emitted to absorbed photons and was measured at room temperature by two different procedures that will be specified in the **Experimental Section** of the specific chapter. One of the procedures involved a standard procedure for the estimation of the PL QY involving appropriate dye molecules for blue, green, and red spectral regions (coumarin 343, fluorescein, and rhodamine 6G).<sup>315</sup> In the second case, the PL QY was estimated automatically by measuring the samples on a Quantaaurus QY (C11347-11, Hamamatsu) equipped with an integrated sphere.

**Powder X-ray diffraction (XRD) patterns** were collected using an STOE STADI P powder diffractometer operating in transmission mode and equipped with a curved Ge(111) monochromator ( $\text{CuK}\alpha_1 = 1.54056 \text{ \AA}$ ), and a silicon strip Mythen detector (Fa. DECTRIS). The samples were prepared by sandwiching the powder of NPs between two Mylar foils or by depositing a film of NPs from a concentrated solution on a Mylar foil and covering it with a second one after evaporation of the solvent.

**Chemical Analysis** was conducted in Chapter 3 in order to verify if the perovskite composition after the anion exchange matches with the predicted composition. For this, two

independent techniques were used: **Energy dispersive X-ray (EDX)** and **Rutherford Backscattering Spectrometry (RBS)**. **EDX** is a localized chemical analysis technique associated with scanning electron microscopy and makes use of the X-ray spectrum recorded from a solid sample bombarded by a focused beam of electrons. The measurements were performed with two scanning electron microscopes (Zeiss Gemini 1530 and Hitachi, S-4800). **RBS** is a non-destructive nuclear analytical technique which allows determining both the atomic mass and concentration of the constituent elements. The sample is irradiated, in most of the cases, with light ions of  $\text{He}^+$  or, rarely,  $\text{H}^+$  (2-3 MeV) and the backscattered projectiles at large angles are detected. The mass of the irradiated atoms can be identified from the energy of the backscattered projectiles which are detected by Si (Au) detectors. Measurements were conducted using a 2 MeV  $^4\text{He}$  beam and a silicon PIN diode detector under an angle of  $168^\circ$ . The collected RBS data was analyzed using simulations by the RUMP code.<sup>316</sup>

## Chapter 3. Acylphosphines – a new class of phosphorus compounds for the facile synthesis of metal-phosphide quantum dots

### 3.1. Introduction

Colloidal quantum dots (QDs) have proven to be a very promising technology for applications such as light emitting devices, display technology, photovoltaics and biomedical imaging.<sup>102, 105, 284, 287-288, 317-319</sup> However, most of the high-performance quantum dots are based on cadmium, lead, or mercury chalcogenides, and are not well-suited for most of these applications because of their high toxicity towards living organisms. For instance, in bio-imaging, both *in vivo* and *in vitro* techniques require materials with low cytotoxicity, which makes the development of an alternative to highly toxic II-VI quantum dots desirable. Applications in consumer products such as photoluminescence barcoding in anti-counterfeiting would also require heavy-metal-free quantum dots in order to comply with the European Restriction on the use of certain Hazardous Substances (RoHS).<sup>320</sup> Indium phosphide emerged as an excellent alternative semiconductor due to its direct bandgap (band gap of 1.34 eV at 300 K) and low toxicity of both indium and phosphorous compared to cadmium, which is classified as highly cytotoxic and carcinogenic.<sup>321</sup> Assessment studies of the toxicity of InP nanoparticles with a ZnS shell show that they are reasonably benign towards single cells and living organisms.<sup>322-323</sup>

In contrast to conventional II-VI semiconductors, III-V materials exhibit a more covalent bonding character, which increases the stability of the bonds and therefore of the QDs as a whole, and reduces their toxicity. Despite this positive feature, the increased stability also leads to a higher occurrence of structural defects, which explains why the photoluminescence (PL) quantum yields (QY) of III-V-based QDs is usually very low (< 1%) compared to what is readily achievable for II-VI quantum dots (QDs). Therefore, surface treatment or core-shell architectures are necessary in order to achieve excellent PL properties. Another essential characteristic of III-V semiconductors is their far larger exciton Bohr radius (10.6 nm for InP

as compared to 2.9 nm for CdS), which leads to a far stronger size effect on optical properties and makes III-V quantum dots more tunable than their II-VI cousins.<sup>324</sup>

Despite the great interest in InP QDs over in the past decades, efficient synthesis of highly monodisperse QDs with high QYs and narrow emission linewidths remains much more challenging than for the conventional II-VI semiconductors. As an example, PL emission in the range of 460-650 nm characterized by QYs of 50 % and linewidths of 40 nm FWHM is easily attainable with core-shell CdSe/ZnS QDs.<sup>325</sup> Meanwhile, core-shell InP/ZnE (E = S, Se) QDs exhibit a broader tunability of the PL emission (470-750 nm ) with lower PL QYs in the 20-40 % range and the corresponding FWHM is higher (50-70 nm typically).<sup>118</sup> Recent studies have reported that high PL QYs can be attained as well for InP/ZnE heterostructures but by involving more tedious and multistep procedures. For instance, a PL QY of 81% but with a relatively broad emission spectrum ( FWHM ~ 50 nm) was obtained when the InP cores were protected by a gradient shell of ZnSeS or even 85% for a double shell of GaP/ZnS (FWHM not reported).<sup>68, 103, 106</sup> A more recent study reported In(Zn)P/ZnSe/ZnS QD heterostructures characterized by narrower PL spectra with FWHM of 35-36 nm for emission at 488 nm and 516 nm, but characterized by lower PL QYs of 44% and 67%, respectively.<sup>281</sup> Despite the tremendous improvement in the PL QY and color purity, the synthesis of such high performance InP QDs is still very much challenging and involves the very expensive, toxic, and pyrophoric tris(trimethylsilyl)phosphine ( $P(\text{SiMe}_3)_3$ ). In order to overcome the disadvantages of using the highly reactive  $P(\text{SiMe}_3)_3$  which cannot afford InP QDs larger than 4 nm because of its rapid depletion, researchers have focused their attention on finding a better substitute for  $P(\text{SiMe}_3)_3$ .<sup>118, 130</sup> Less reactive precursors, such as tris(trimethylgermyl)phosphine ( $P(\text{GeMe}_3)_3$ ) or tris(trimethylstannyl)phosphine ( $P(\text{SnMe}_3)_3$ ), have been tested but did not prove to be very efficient.<sup>131</sup> Recent studies have indicated the tris(dialkylamine)phosphine (alkyl = methyl, ethyl;  $P(\text{NMe}_2)_3$ ,  $P(\text{NEt}_2)_3$ ) as very potent P-precursors.<sup>71-72, 121</sup> Initially, the  $P(\text{NMe}_2)_3$  was tested in the generally used procedure based on In-carboxylate in ODE and showed an inferior performance. Later it was reacted with  $\text{InCl}_3$  in oleylamine (OLA) in the presence of  $\text{ZnCl}_2$  and produced non-luminescent InP QDs which became luminescent after overcoating with ZnS, displaying PL QYs of 51-53% and emission line widths of 60-64 nm, comparable to those synthesized using  $P(\text{SiMe}_3)_3$ .<sup>71</sup> Tessier *et al.* further improved the method and higher PL QYs (up to 60%) and narrower emission line widths (46-63 nm) were achieved.<sup>72</sup> Further investigations of the employment of  $P(\text{NMe}_2)_3$  into the synthesis of InP QDs led to InP/ZnSeS/ZnS QDs with PL QY of 82%, comparable

with the InP/GaP/ZnS QDs synthesized with  $P(\text{SiMe}_3)_3$  (PL QY 85%).<sup>103, 132</sup> Despite these positive outcomes using these commercially available tris(dialkylamine)phosphines as P-source, there are still drawbacks to overcome. For instance, three equivalents of flammable and corrosive alkylamine are released as a result of transamination reaction that the precursor undergoes with the oleylamine in order to produce InP QDs. More recently, tri(pyrazolyl)phosphane,  $P(\text{pyr})_3$ , was reported as a less toxic and much safer to handle P-building block for the direct synthesis of InP QDs. This  $P(\text{pyr})_3$  should be reacted with OLA in order to generate a stock solution of the phosphorus precursor –  $P(\text{OLA})_3$  – and to recover the pyrazole for further use.<sup>326</sup> The obtained non-emissive InP QDs were overcoated with a protective ZnS shell (4h at 260 °C), and the generated core/shell heterostructures showed PL emission covering a relatively limited spectral range (535-620 nm) with PL QYs in the range of 33-62% and FWHM of 59-90 nm, depending on the selected reaction path.<sup>326</sup>

While these P-precursors are safer to use and less expensive in comparison to  $P(\text{SiMe}_3)_3$ , the performance of the synthesized InP QDs has not matched that of those synthesized with the expensive, highly toxic and pyrophoric  $P(\text{SiMe}_3)_3$ . Therefore, remains necessary to find safer and more environmentally friendly P-precursors to afford faster and inexpensive synthetic procedures for the large-scale synthesis of high-quality InP and other metal-phosphide QDs.

In this chapter, acylphosphines are introduced and evaluated as a new class of potential phosphorous precursors for the synthesis of high-quality InP QDs. In general, acylphosphines are used to produce acylphosphine oxides, which play essential roles in the manufacture of consumer goods such as automotive coatings, adhesives, latex composition kits, and orthodontic materials, which are used as photoinitiators for radical-initiated polymerization reactions.<sup>305-306</sup> The tested acylphosphines, presented in **Figure 3.1**, were synthesized by Erik Schrader, then a Ph.D. student in Group of Prof. H. Grützmacher at ETH Zürich, and their synthesis and characterization are fully described in his Ph.D. Thesis.<sup>306</sup>

Each of the precursors was tested in two different synthetic approaches, named (i) the acetate approach, and (ii) the halide approach. In the acetate approach, indium acetate along with zinc acetate and myristic acid in ODE were degassed under vacuum, after which the reaction mixture is switched to an  $\text{N}_2$  atmosphere. The injection of the P-precursor was performed either at low temperature, according to the heat-up method, or at high temperature, according to the hot-injection method. In the case of halide approach, indium chloride along with zinc chloride in OLAH were used, and the procedural steps described above for the acetate

method were followed with minor modifications. Each of the precursors proved to be very efficient in a generate phosphorus species reactive enough to generate InP QDs, but only the results from the three most successful will be described in detail.

## 3.2. Experimental section

**Materials and chemicals.** Indium acetate ( $\text{In}(\text{OAc})_3$ , Aldrich, 99.99%), indium chloride anhydrous ( $\text{InCl}_3$ , ABCR, 99.99%), gallium chloride ( $\text{GaCl}_3$ , ABCR, 99.999%) oleylamine (OLAH, Acros Organics, 80-90), zinc chloride anhydrous ( $\text{ZnCl}_2$ , ABCR, 99.99%) hexane anhydrous (Sigma-Aldrich, 95%), acetone extra dry (Acros Organics,  $\geq 99.8\%$ ), and tetrachloroethylene anhydrous (TCE, Sigma Aldrich,  $\geq 99\%$ ) were used as received from the manufacturer and handled in the glovebox. Zinc acetate dihydrate ( $\text{Zn}(\text{OAc})_2 \cdot 2\text{H}_2\text{O}$ , Sigma-Aldrich,  $\geq 99.5\%$ ), myristic acid (MA, Sigma,  $\geq 99\%$ ), and 1-octadecene (ODE, Sigma-Aldrich, 90%) were handled in standard laboratory conditions without any extra precautions. *N*-dodecanethiol (*n*-DDT, Aldrich,  $\geq 98\%$ ) was stored and handled in an  $\text{N}_2$ -filled glovebox after  $\text{N}_2$  was bubbled through for more than 24 hours. All the phosphorus precursors were stored in an  $\text{N}_2$ -filled glovebox.

**Synthesis of the acylphosphines** involved in this work is reported elsewhere, as well as their characterization.

**Preparation of TOP-S and TOP-Se 2.2 M solution.** Solutions of TOP-S and TOP-Se 2.2 M were prepared by loading into a vial 44 mmol of S and Se, respectively, along with 20 mL TOP in an  $\text{N}_2$ -filled glovebox. The mixture was stirred at 80 °C, typically overnight, until the solution became transparent and all the S and Se, respectively, were solubilized.

**Preparation of zinc oleate 0.4 M solution in ODE.** Zinc acetate dihydrate (12 mmol) along with oleic acid (36 mmol) in 1-octadecene (18.6 mL) were charged into a 3-neck flask and heated up to 150 °C under Ar until the zinc acetate dihydrate solubilized completely. The temperature was lowered to 125 °C, and the reaction mixture was degassed for 2 hours 30 minutes under vacuum, after which it was switched back on Ar and cooled down. A white precipitate appeared from the clear light yellow solution during cooling down to room temperature. The solution was kept under argon pressure and heated up to redissolve the zinc oleate precipitate whenever the solution was used.



### **One-pot synthesis of In(Zn)P QDs and In(Zn)P/ZnS core/shell QDs with <sup>Ph</sup>BAPH as the phosphorous source**

**Acetate approach.** Indium acetate (0.4 mmol) along with zinc acetate dihydrate (1.5 mmol) were loaded into a 25 mL 3-neck flask inside an N<sub>2</sub>-filed glovebox. Myristic acid (1.5 mmol) and 1-octadecene (5 mL) were added to indium and zinc acetates just before connecting the reaction flask to the Schlenk line and vigorously stirred under vacuum for 1 hour at 120 °C. The clear colorless solution was cooled down at room temperature (RT). <sup>Ph</sup>BAPH (0.4 mmol), solubilized in ODE (2 mL), was added, and the reaction mixture was heated up to 200 °C for 30 minutes.

After 30 minutes at 200 °C, 1-dodecanethiol (1.5 mmol) was injected slowly (10 minutes injection) into the reaction mixture. After 1 hour at 200 °C, the reaction was stopped, and the product was washed several times with toluene and a 1:1 (v:v) methanol and isopropanol. The final product was stored in toluene.

**Halide approach.** Indium chloride (0.4 mmol), zinc chloride (1 mmol) and OLAH (5 mL) were loaded into a 3-neck flask inside an N<sub>2</sub>-filed glovebox. The reaction mixture was connected to the Schlenk line and degassed for 1 hour at 120 °C. The reaction mixture was switched on an N<sub>2</sub> atmosphere, and the temperature was increased to 200 °C. <sup>Ph</sup>TAP (0.3 mmol), solubilized in ODE (2 mL), was swiftly injected and the mixture was allowed to react for 10 minutes at 200°C.

The temperature was decreased to 150 °C, and 1-dodecanethiol (2.3 mmol) was injected slowly (10 minutes injection) into the reaction mixture. After 30 minutes at 150 °C, the temperature was raised to 200 °C. The reaction was stopped after 30 minutes at 200 °C, and the product was washed several times with toluene and a 1:1 (v:v) methanol and isopropanol. The final product was stored in toluene.

### **One-pot synthesis of In(Zn)P/GaP core/shell QDs and In(Zn)P/GaP/ZnS core/shell/shell QDs with <sup>Ph</sup>BAPH as the phosphorous source**

**Acetate approach.** Indium acetate (0.4 mmol) along with zinc acetate dihydrate (1.5 mmol) were loaded into a 25 mL 3-neck flask inside an N<sub>2</sub>-filed glovebox. Myristic acid (1.5 mmol) and 1-octadecene (5 mL) were added to indium and zinc acetates just before connecting the reaction flask to the Schlenk line and vigorously stirred under vacuum for 1 hour at 120 °C. The clear colorless solution was cooled down at room temperature (RT). GaCl<sub>3</sub> (0.25 mmol)

and <sup>Ph</sup>BAPH (0.4 mmol), each solubilized in ODE (2 mL), were added, and the reaction mixture was heated up to 200 °C for 30 minutes.

After 30 minutes at 200 °C, 1-dodecanethiol (1 mmol) was injected slowly (10 minutes injection) into the reaction mixture. After 1 hour at 200 °C, the reaction was stopped, and the product was washed several times with toluene and a 1:1 (v:v) methanol and isopropanol. The final product was stored in toluene.

### **One-pot synthesis of In(Zn)P QDs and In(Zn)P/ZnS core/shell QDs with <sup>Ph</sup>TAP as the phosphorous source**

**Acetate approach.** Indium acetate (0.4 mmol) along with zinc acetate dihydrate (1 mmol) were loaded into a 25 mL 3-neck flask inside an N<sub>2</sub>-filed glovebox. Myristic acid (2.5 mmol) and 1-octadecene (5 mL) were added to indium and zinc acetates just before connecting the reaction flask to the Schlenk line and vigorously stirred under vacuum for 90 minutes at 120 °C. The clear colorless solution was cooled down at room temperature (RT). <sup>Ph</sup>TAP (0.4 mmol), solubilized in OLAH (2 mL), was added, and the reaction mixture was heated up to 200 °C for 30 minutes.

After 30 minutes at 200 °C, 1-dodecanethiol (1 mmol) was injected slowly (10 minutes injection) into the reaction mixture at 200 °C. After 1 hour at 200 °C, the reaction was stopped, and the product was washed several times with toluene and a 1:1 (v:v) methanol and isopropanol. The final product was stored in toluene.

**Halide approach.** Indium chloride (0.4 mmol), zinc chloride (1 mmol) and OLAH (5 mL) were loaded into a 3-neck flask inside an N<sub>2</sub>-filled glovebox. The reaction mixture was connected to the Schlenk line and degassed for 1 hour at 120 °C. The clear colorless solution was cooled down at room temperature (RT). <sup>Ph</sup>TAP (0.4 mmol), solubilized in OLAH (2 mL), was added, and the reaction mixture was heated up to 200 °C for 30 minutes.

After 30 minutes at 200 °C, 1-dodecanethiol (1 mmol) was injected slowly (10 minutes injection) into the reaction mixture at 200 °C. After 1 hour at 200 °C, the reaction was stopped, and the product was washed several times with toluene and a 1:1 (v:v) methanol and isopropanol. The final product was stored in toluene.

### **Synthesis of In(Zn)P QDs with <sup>Me</sup>TAP as the phosphorous source**

**Halide approach.** Indium chloride (0.25 mmol), zinc chloride (1 mmol) and OLAH (5 mL) were loaded into a 3-neck flask inside an N<sub>2</sub>-filed glovebox. The reaction mixture was connected to the Schlenk line and degassed for 1 hour at 120 °C, after which the temperature was raised to 200 °C and a specific amount of <sup>Me</sup>TAP (0.4 or 0.8 mmol) solubilized in OLAH (1 mL) was swiftly injected. The reaction was stopped after 30 minutes at 200 °C and the product purified by washing several times with toluene and a 1:1 (v:v) methanol and isopropanol. The final product was stored in toluene.

**One-pot synthesis of In(Zn)P/ZnX (X = Se, S) core/shell QDs and In(Zn)P/ZnSe/ZnS core/shell/shell QDs with <sup>Me</sup>TAP as the phosphorous source**

- (i) The In(Zn)P QDs were synthesized according to the above procedure by using 0.4 mmol <sup>Me</sup>TAP. A protective shell of ZnS was overgrown at 200 °C, by adding dropwise (10 minutes injection), 1-dodecanethiol (1 mmol) and vigorously stirred for 1 hour. The final product was washed several times with toluene and a 1:1 (v:v) methanol and isopropanol. The final product was stored in toluene.
- (ii) The In(Zn)P QDs were synthesized according to the above procedure by using 0.8 mmol <sup>Me</sup>TAP. After 30 minutes (at 200 °C) growing time, 1 mmol TOP-X 2.2 M was injected slowly (6 minutes injection) and reacted for another 30 minutes at 200 °C. Further, 1.3 mmol Zn-oleate in ODE 0.5 M was added dropwise followed by another 30 minutes of vigorous stirring at 200 °C. Another round of TOP-X 2.2 M (1.5 mmol) was added dropwise followed by another 30 minutes of vigorous stirring, and finished by another dropwise injection of Zn-oleate in ODE 0.5 M (1.5 mmol) and let to react for 30 minutes at 200 °C. The final product was washed several times with toluene and a 1:1 (v:v) methanol and isopropanol. The final product was stored in toluene.
- (iii) In the case of overgrowing the mixed ZnSe/ZnS shells, 0.8 mmol <sup>Me</sup>TAP were injected for the synthesis of the cores. After 30 minutes at 200 °C, 1 mmol TOP-Se 2.2 M was injected slowly (6 minutes injection) and reacted for another 30 minutes at 200 °C. Further, 1.3 mmol Zn-oleate in ODE 0.5 M was added dropwise followed by another 30 minutes of vigorous stirring at 200 °C. Further, TOP-S 2.2 M (1.5 mmol) was added dropwise followed by another 30 minutes of vigorous stirring, and finished by a final dropwise injection of Zn-oleate in ODE 0.5 M (1.5 mmol). After 30 minutes at 200 °C, the reaction was stopped

and the final product was washed several times with toluene and a 1:1 (v:v) methanol and isopropanol. The final product was stored in toluene.

### Characterization

**Absorbance** measurements were carried out using a Jasco V670 spectrometer in transmission mode.

**Photoluminescence (PL) and absolute quantum yield (QY) measurements.** Fluorolog iHR 320 Horiba Jobin Yvon spectrofluorimeter equipped with a PMT detector was used to acquire steady-state PL spectra from solutions and films. PL QYs were estimated according to standard procedure using rhodamine 6G.<sup>315</sup>

## 3.3. Results and discussion

To the best of my knowledge, this is the first time when compounds of acylphosphine type are used for the synthesis of metal phosphide nanoparticles, especially In(Zn)P QDs. In this study, nine acylphosphines (**Figure 3.1**) were selected for testing their capabilities in different synthetic protocols, with the goal of achieving the facile synthesis of luminescent In(Zn)P QDs. All nine precursors were tested in various conditions, and each of them showed good reactivity generating In(Zn)P QDs, which, in most cases, showed PL emission without requiring a protective shell to overcoat the QDs. It is expected that these acylphosphines will decompose by losing, one-by-one, the acyl substituents on phosphorous, generating in-situ active and reactive phosphorous species, such as phosphine gas. Moreover, the acyl groups can act as oxygen scavengers for the oxygen species that might exist as a residue in the reaction mixture. Two general synthetic approaches were used, referred to as the acetate approach and the halide approach. In both situations, a zinc source (acetate or chloride, respectively) was used to generate zinc-doped InP QDs. As shown by Pietra *et al.*, the zinc has here a dual role. The Zn<sup>2+</sup> ions will be incorporated into the structure of InP QDs as substitutional dopants on In<sup>3+</sup> sites, modifying in this manner the lattice constant and encouraging the overgrowth of a protective zinc-based shell.

Hereafter the results from the most promising three compounds are focused on, namely bis(benzoyl)phosphine – <sup>Ph</sup>BAPH, tris(benzoyl)phosphine – <sup>Ph</sup>TAP, and tris(acetyl)phosphine – <sup>Me</sup>TAP.

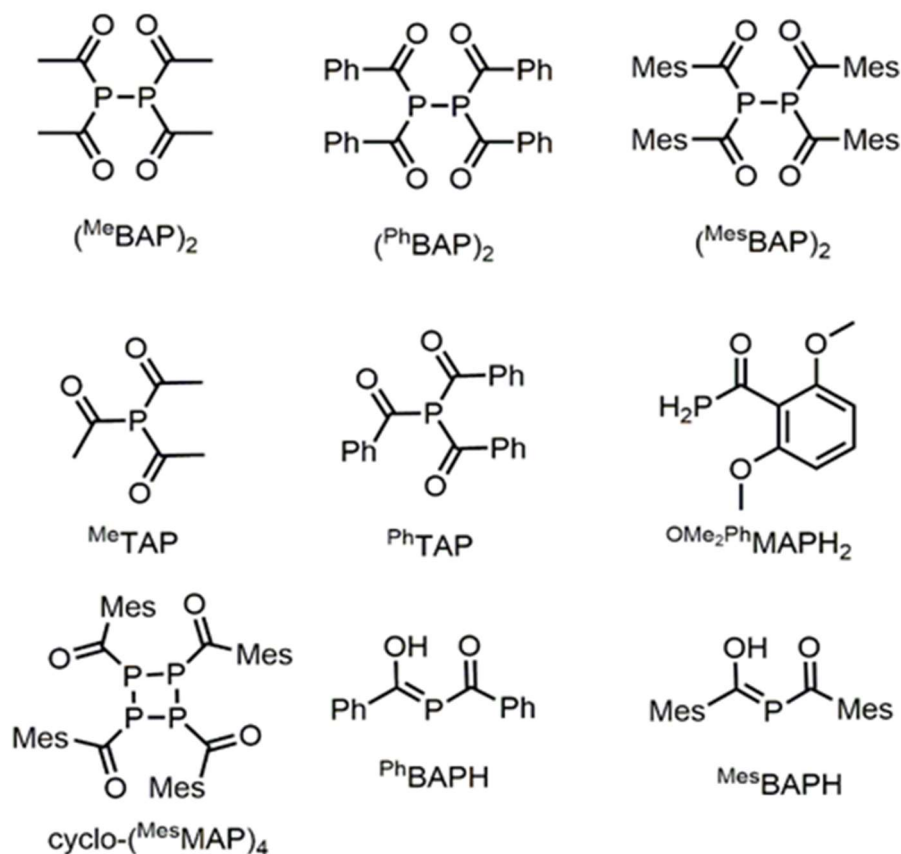


**Figure 3.1.** Simplified structural representation of the acylphosphines tested for the synthesis of  $\text{In}(\text{Zn})\text{P}$  QDs:  $(^{\text{Me}}\text{BAP})_2$  = tetrakis(acetyl)diphosphine;  $(^{\text{Ph}}\text{BAP})_2$  = tetrakis(benzoyl)diphosphine;  $(^{\text{Mes}}\text{BAP})_2$  = tetrakis(mesityl)diphosphine;  $^{\text{Me}}\text{TAP}$  = tris(acetyl)phosphine;  $^{\text{Ph}}\text{TAP}$  = tris(benzoyl)phosphine;  $^{\text{OMe}_2\text{Ph}}\text{MAPH}_2$  = mono(2,6-dimethoxybenzoyl)phosphine;  $\text{cyclo-}(^{\text{Mes}}\text{MAP})_4$  = tetrakis(mesityl)cyclotetraphosphine;  $^{\text{Ph}}\text{BAPH}$  = bis(benzoyl)phosphine;  $^{\text{Mes}}\text{BAPH}$  = bis(mesityl)phosphine.

Bis(benzoyl)phosphine –  $^{\text{Ph}}\text{BAPH}$  – revealed to be a very efficient phosphorus source when used in the acetate approach and less efficient in the halide approach (**Figure 3.2**). As described in the **Experimental Section**, in the case of acetate approach, the  $^{\text{Ph}}\text{BAPH}$  was solubilized in ODE and injected into the reaction mixture at room temperature after which the temperature was increased to 200 °C. The reaction was stopped after 30 minutes and the weakly green-emitting  $\text{In}(\text{Zn})\text{P}$  QDs (**Figure 3.2. a**) were purified, showing PL QYs in the range of 1-2%. In the case of halide approach, the hot-injection model was applied, and the  $^{\text{Ph}}\text{BAPH}$  was injected directly at 200 °C. The reaction was stopped after 30 minutes, as in the case of acetate approach, but the obtained cores did not show any PL emission (**Figure 3.2. b**). In order to increase the PL QYs of the obtained  $\text{In}(\text{Zn})\text{P}$  QDs, in both cases, a shell of ZnS was overgrown. In the case of acetate approach, 1-dodecanethiol was slowly injected directly at 200 °C,

followed by a growth time of one hour at the same temperature, while in the case of halide approach, the 1-dodecanethiol was slowly added to the In(Zn)P cores at 150 °C after which the temperature was raised again to 200 °C and stopped after one hour. As can be observed from **Figure 3.2**, in the acetate approach the overgrowth of a ZnS shell improved the PL QY tremendously, reaching values as high as 62% at 565 nm, while in the halide approach, the final In(Zn)P/ZnS heterostructures displayed poor optical properties with PL QYs around 2% at 625 nm.

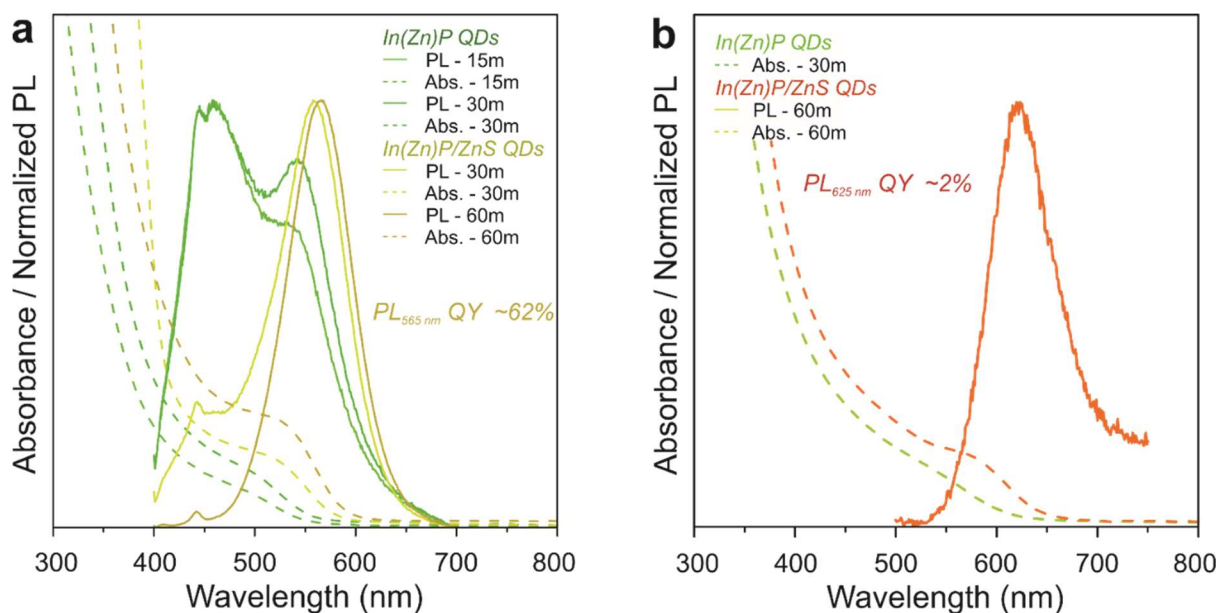


**Figure 3.2.** Typical absorbance and photoluminescence spectra of the obtained InP QDs using <sup>Ph</sup>BAPH as a phosphorous source in (a) the acetate method and (b) the halide method. The <sup>Ph</sup>BAPH proved to be very efficient when injected in the acetate method (a), generating luminescent InP QDs which increased their PL QYs up to 62% after overcoating them with ZnS, in contrast to the halide method (b) where the formed QDs showed a weak emission only after overgrowing a shell of ZnS.

In order to further enhance the PL QYs of In(Zn)P QDs, different amounts of GaCl<sub>3</sub> (0.2 – 0.4 mmol) solubilized in ODE were added to the reaction just before the injection of <sup>Ph</sup>BAPH. After 30 minutes at 200 °C, emissive heterostructures of In(Zn)P/GaP core/shell QDs were obtained, showing minor redshifts of 5-10 nm for the case when 0.2 and 0.25 mmol GaCl<sub>3</sub> were used and a larger one (~40 nm) for 0.4 mmol GaCl<sub>3</sub> in comparison with the In(Zn)P QDs that show an emission at 545 nm (**Figure 3.3. a**). The PL QYs of these heterostructures were rather modest, showing only a small increase (3-4%), but they were substantially increased by overgrowing a ZnS shell. The In(Zn)P/GaP/ZnS QDs showed PL emission in the range of 580-585 nm with QYs of 41.4% and 56% after one-hour growth of ZnS for the cases when 0.2 mmol and 0.25 mmol GaCl<sub>3</sub>, respectively, were used (**Figure 3.3. b**). Also, by allowing the

ZnS shell to grow for an extended period (3 hours), the PL QYs increased up to 72.3% approaching the state-of-the-art.<sup>103</sup> Moreover, as can be observed from **Figure 3.2.** and **3.3,** the emission of the In(Zn)P QDs can be easily tuned by adjusting the amounts of Ga, and the PL QYs can be enhanced even further by allowing the shell to grow for more extended periods.

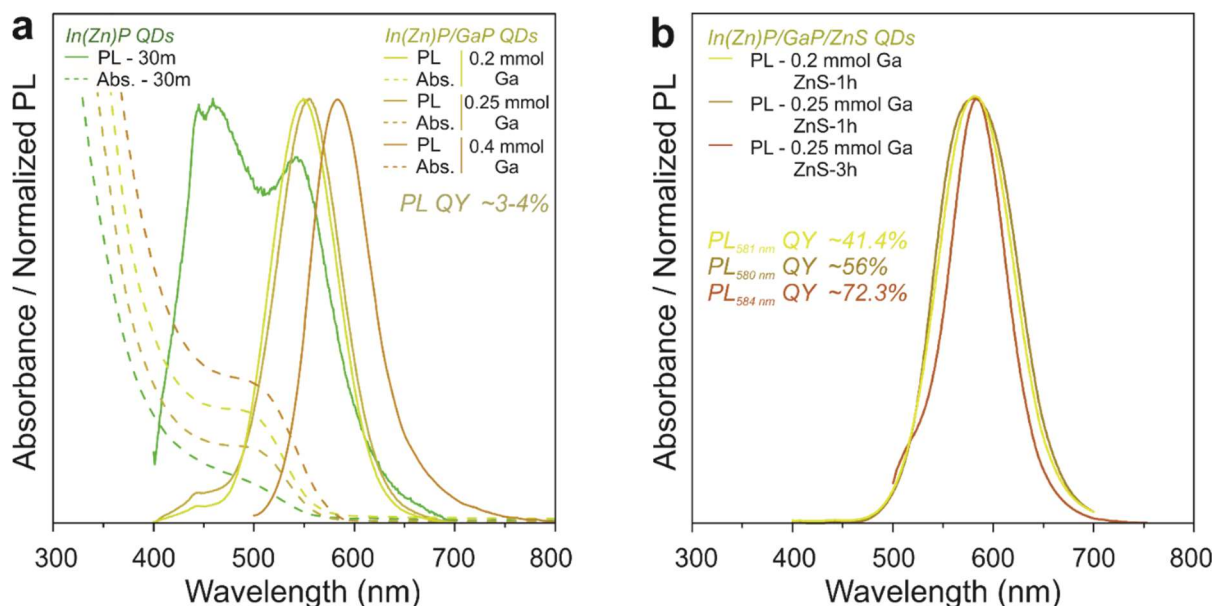


**Figure 3.3.** Variation of the synthesis of In(Zn)P QDs obtained via the acetate method using <sup>Ph</sup>BAPH as a phosphorus source. Evolution of absorbance and photoluminescence spectra of In(Zn)P after adding Ga<sup>3+</sup> to the synthesis for the formation of a passivating shell of GaP. Minor red-shifts can be observed as the amount of Ga<sup>3+</sup> is increased while the PL QYs are remaining modest around 3-4 %. (b) Normalized photoluminescence spectra of In(Zn)P/GaP/ZnS QDs and their corresponding PL QYs, displaying a maximum of PL QY of 72.3% for the case when the outer-shell of ZnS was grown for 3 hours.

Tris(phenyl)phosphine – <sup>Ph</sup>TAP – revealed a good reactivity in both approaches (acetate and halide), but as in the case of <sup>Ph</sup>BAPH, superior performance was observed when the acetate approach was used (**Figure 3.4**), facilitating the synthesis of red-emitting (600 nm) In(Zn)P QDs. Both approaches for the <sup>Ph</sup>TAP precursor followed the model of the heat-up method. The phosphorous precursor was solubilized in OLAH and injected into the reaction mixture at room temperature, followed by an increase of the reaction temperature to 200 °C. The reaction was stopped after 30 minutes of vigorous stirring at 200 °C, revealing luminescent In(Zn)P QDs with PL QYs of about 1-2% but only in the case of the acetate approach. The PL QYs could be improved by overgrowing a ZnS shell in one-pot synthesis, as in the previous case, by adding to the In(Zn)P cores specific amounts of 1-dodecanethiol (see **Experimental Section** for details). The ZnS shells were allowed to grow for one hour at 200 °C and showed, in the end, red emission at 610 nm and PL QYs of 49% for the In(Zn)P/ZnS QDs synthesized by the

acetate approach (**Figure 3.4. a**), while the halide approach generated QD heterostructures with emission at 565 nm and lower PL QYs of about 21.5% (**Figure 3.4. b**).

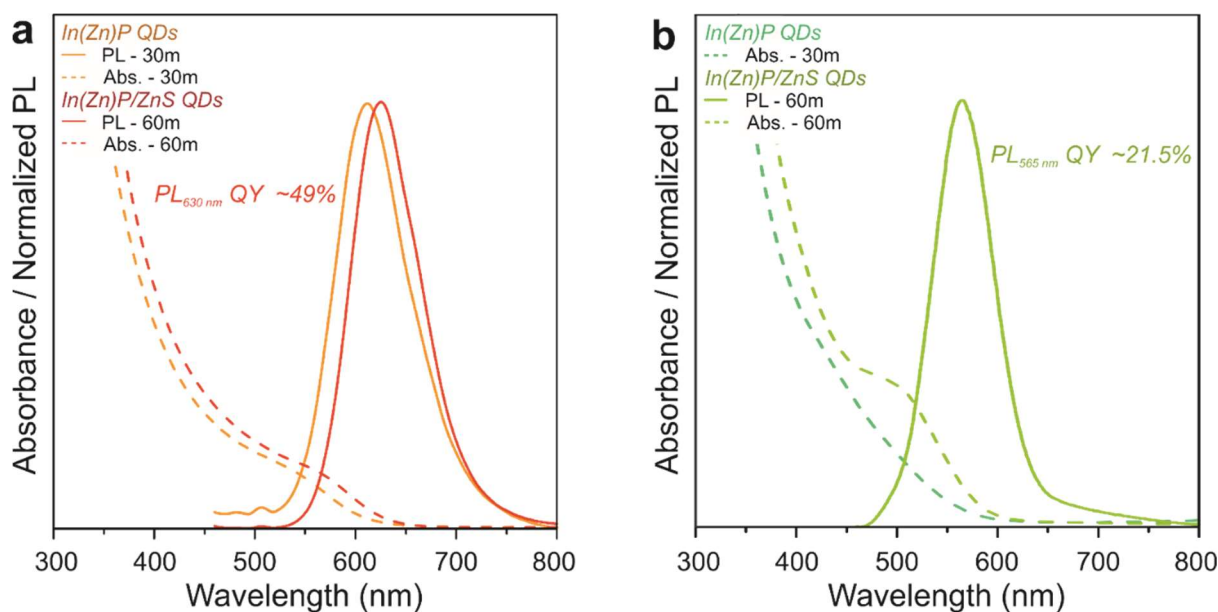


**Figure 3.4.** Absorbance and photoluminescence spectra of In(Zn)P QDs and In(Zn)P/ZnS core/shell QDs synthesized by using  $^{Ph}TAP$  as a phosphorous precursor in the acetate approach (**a**) and the halide approach (**b**), respectively.

The results presented in **Figure 3.4**, clearly prove that  $^{Ph}TAP$  can generate high quality In(Zn)P QDs that can emit in both green and red spectral regimes. Their PL emission can be further tuned over a broader spectral range by simply adjusting the ratio between the reactants and the reaction conditions. Different core/shell systems, for instance, GaP/ZnS as shown for the  $^{Ph}BAPH$  case, can be used as well for further enhancement of the PL QYs but also for fine tuning the emission of the In(Zn)P QDs.

Tris(acetyl)phosphine –  $^{Me}TAP$  – was tested as well in both approaches but showed positive results only in the case of the halide approach following the model of the hot-injection method. For this particular compound, two different ratios between In and P were tested, namely 1:1.6 and 1:3.2 In:P. As can be observed in **Figure 3.5. a** the PL optical properties of the In(Zn)P QDs can be tuned from the green to red spectral regimes by using different ratios between In and P precursors. After overgrowing a protective shell of ZnS on the In(Zn)P cores synthesized by using 0.4 mmol  $^{Me}TAP$  (ration In:P = 1:1.6), emission at 515 nm could be revealed. The PL spectrum shows a tail in the red spectral regime, most likely because of the intrinsic defects or not well passivated QDs. By using higher amounts of  $^{Me}TAP$  (0.8 mmol, ratio In:P = 1:3.2), the PL emission is redshifted at 600 nm, and the PL spectrum shows a



Gaussian shape meaning that the QDs have minimal amounts of defects and the overgrowing of ZnS shell is successfully passivating their surface. Further, for the case of In:P = 1:3.2, thicker passivating shells of ZnSe, ZnS and double ZnSe/ZnS, were applied. The shells were overgrown by sequential additions of the chalcogenide (TOP-S and TOP-Se) and zinc (Zn-oleate) precursors at 200 °C with growing periods of 30 minutes between the additions. After a total time of two hours for the overgrowth of the protective shells, In(Zn)P/ZnS, In(Zn)P/ZnSe and In(Zn)P/ZnSe/ZnS heterostructures were obtained with emission at 600, 630 and 660 nm, respectively (**Figure 3.5. a**). The PL QYs of the QDs synthesized with <sup>Me</sup>TAP were considerably lower (about 15%) than the values revealed in the previously presented cases. Despite the preferential reactivity for the halide approach only and the lower PL QYs, this phosphorous precursor presents great potential for the synthesis of In(Zn)P QDs with easily tunable optical properties over a broad spectral range.

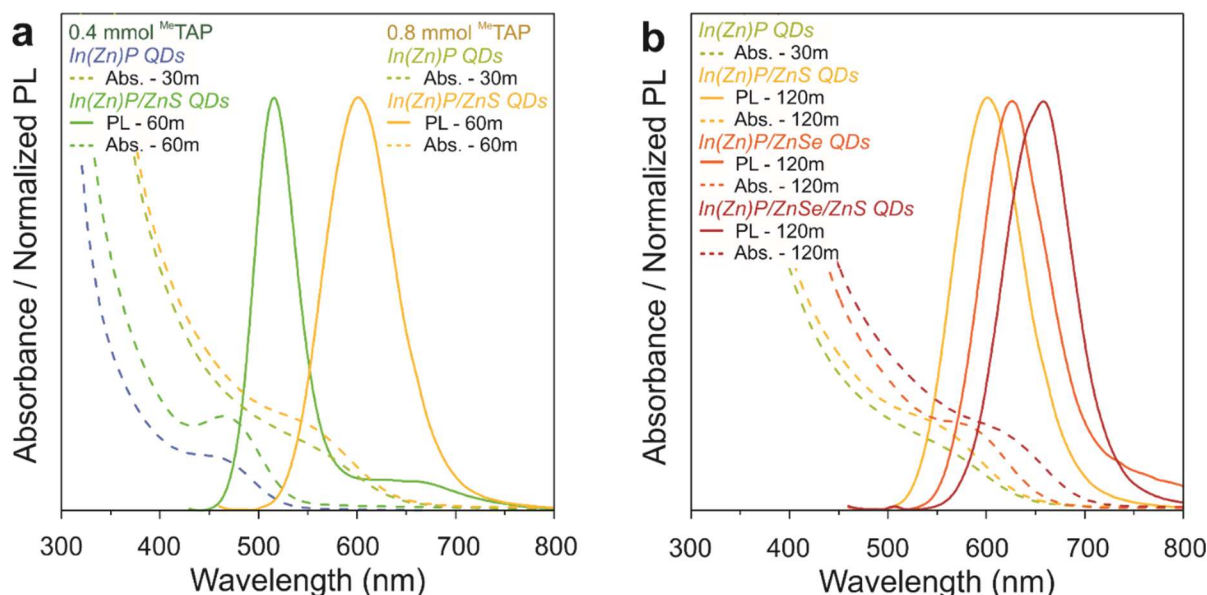


**Figure 3.5.** (a) Absorbance and photoluminescence spectra of In(Zn)P QDs and In(Zn)P/ZnS core/shell QDs synthesized using different amounts of <sup>Me</sup>TAP, showing green and red, respectively, emission. (b) Absorbance spectrum of typical In(Zn)P cores and absorbance and photoluminescence spectra of In(Zn)P/ZnSe, In(Zn)P/ZnS and In(Zn)P/ZnSe/ZnS cores, core/shell and core/shell/shell heterostructures showing emission maxima at 600, 630 and 660 nm, respectively.

### 3.4. Conclusions

The use of acylphosphines as potential precursors for the facile and safer synthesis of In(Zn)P QDs is reported. A series of nine acylphosphines has been tested in two different approaches, the acetate and the halide approach, respectively. All the precursors have

facilitated the synthesis of In(Zn)P QDs characterized by optical properties spanning a broad spectral range from 500 up to 660 nm. It was found for the case of <sup>Ph</sup>BAPH that has a higher reactivity when used in the acetate approach facilitating the synthesis of emissive In(Zn)P QDs. The emission could be further tuned either by overgrowing a protective shell of ZnS or by overgrowing a double protective shell of GaP/ZnS. Moreover, PL QYs of 62% and 72.3%, respectively, could be observed for In(Zn)P/ZnS and In(Zn)P/GaP/ZnS QD heterostructures. The <sup>Ph</sup>TAP precursor behaved similarly to <sup>Ph</sup>BAPH, showing higher performance in the acetate approach, affording the synthesis of In(Zn)P QDs with PL at 600 nm. The PL was slightly redshifted to 610 nm by overgrowing a protective shell of ZnS, and the obtained core/shell QDs showed a PL QY of 49%, while by using the halide approach, emission at 565 nm and PL QYs of about 21.5% could be revealed only after the ZnS shelling. <sup>Me</sup>TAP proved to be reactive only in the halide method showing, nice tunability of the PL spectra by using different ratios between the In and P precursors. Extra tunability could be attained by overcoating the QDs with different shells, such as ZnSe, ZnS, and ZnSe/ZnS. Therefore, judging from the presented results, it can be concluded that acylphosphines are efficient and safer phosphorous precursors for the synthesis of luminescent In(Zn)P QDs, and by careful investigation of the synthetic parameters and wise selection of the shelling strategy, record PL QYs can be revealed. Moreover, acylphosphines have great potential for the facile synthesis of other metal phosphide QDs, such as GaP.

## Chapter 4. Aluminum-tris(bismesitoylarsine), $Al^{(Mes)BAAs}_3$ – inexpensive, air-stable, and versatile arsenic-precursor for the synthesis of metal-arsenide quantum dots

### 4.1. Introduction

Colloidal metal-arsenide quantum dots (QDs) are of great interest for a broad range of applications, such as telecommunications, bioimaging, photovoltaics, photodetectors, and lasers, due to their ability to absorb and to emit in the near-infrared (NIR) spectral range.<sup>31, 61, 105, 291-292, 307-313, 327</sup> The metal-arsenide QDs are characterized by broad absorption spectra, narrow emission profiles, and high resistance toward photobleaching in contrast to organic dyes.<sup>10, 328</sup> Moreover, their optoelectronic properties can be finely tuned over broad spectral range via quantum confinement effect.<sup>62-63, 105, 329-330</sup> The synthesis of metal-arsenide QDs is somewhat challenging and more difficult in contrast to other more conventional NCs, such as II-VI (CdE, E = S, Se, Te) or IV-VI (PbE, E = S, Se, Te) NCs. Metal-arsenide QDs present stronger covalent character in the crystal lattice, which means that higher reaction temperatures are needed to overcome the activation barriers for the formation of their crystal structure.<sup>131, 331</sup>

Despite the recent improvements of arsenide-based QDs regarding their photoluminescence (PL) quantum yields (QYs), narrow full-width at half-maximum (FWHM), photostability, serious drawbacks still exist when it comes to the synthetic procedures and the available precursors. Nowadays, the most commonly used As-precursors are the very-much-expensive, highly pyrophoric, toxic, moisture and air sensitive tris(trimethylsilyl)arsine,  $As(SiMe_3)_3$ <sup>63, 66, 229</sup> besides the less reactive tris(trimethylgermyl)arsine,  $As(GeMe_3)_3$ <sup>105, 131</sup> or the highly toxic arsine gas ( $AsH_3$ )<sup>101, 332</sup>. Recently, hexaalkylarsenic triamide ( $As(NR_2)_3$ , R = Me, Et), has been proposed as commercially available and less expensive precursors.<sup>138</sup> It was reported for both precursors,  $As(NMe_2)_3$  and  $As(NEt_2)_3$ , that they undergo a transamination reaction with oleylamine, which is used as solvent and ligand in order to stabilize the newly formed InAs QDs, generating three equivalents of flammable and corrosive dialkylamines in order to provide trioilylaminearsenide,  $As(OLA)_3$ , for the reaction. Moreover, subsequent

addition of a reducing agent is necessary in order to obtain InAs from the reaction of  $InX_3$  ( $X = Cl, Br, I$ ) with  $As(OLA)_3$ . Typically, diisobutylaluminum hydride (DIBAL-H)<sup>138</sup> is used but, nowadays, also *N, N*-dimethylethylamine complex ( $DMEA-AlH_3$ )<sup>25</sup> and trioctylphosphine ( $P(OLA)_3$ )<sup>139</sup>. More recently, tri(pyrazolyl)arsine,  $As(pyr)_3$ , has been reported as a less toxic and much safer to handle precursors for the synthesis of InAs QDs.<sup>140</sup> Even this compound is available on a gram-scale synthesis, and it is safer to work with, has the inconvenience of being needed to first prepare a stock solution of  $As(OLA)_3$  by reacting the  $As(pyr)_3$  with oleylamine (OLA), which would make it inconvenient for the scale-up synthesis. Also, in this situation, the addition of a reducing agent is needed in order to react  $As(OLA)_3$  with  $InX_3$ .

Herein, aluminum-tris (bismesitoylarsine),  $Al^{(Mes)BAAs}_3$ , is introduced as a versatile arsenic precursor for the synthesis of metal-arsenide QDs.  $Al^{(Mes)BAAs}_3$  was successfully tested for the synthesis of the most important metal-arsenide QDs, namely InAs, GaAs,  $Cd_3As_2$ , and  $Zn_3As_2$  QDs, yielding emissive InAs and  $Cd_3As_2$  QDs. For the case of GaAs and  $Zn_3As_2$  QDs, the synthetic procedure was less successful than in the case of the other two, InAs and  $Cd_3As_2$  QDs, generating non-emissive nanoparticles in the preliminary tests.  $Al^{(Mes)BAAs}_3$  complex has a good air and moisture stability (minor decomposition of the aluminum complex was observed after the compound was exposed for 4 weeks to air), is highly reactive and can be easy, fast, and economically produced on a large scale – about 20 g of pure compound is obtained per batch on a lab-scale synthesis.

## 4.2. Experimental section

**Materials and chemicals.** Indium acetate ( $In(OAc)_3$ , Aldrich, 99.99%), cadmium chloride anhydrous ( $CdCl_2$ , ABCR, 99.99%), cadmium acetate dihydrate ( $Cd(OAc)_2 \cdot 2H_2O$ , Fluka,  $\geq 98\%$ ), oleylamine (OLAH, Acros Organics, 80-90), di-isobutylaluminum hydride solution 1.0 M in toluene (DIBAL-H, Aldrich), hexane anhydrous (Sigma-Aldrich, 95%), acetone extra dry (Acros Organics,  $\geq 99.8\%$ ), and tetrachloroethylene anhydrous (TCE, Sigma Aldrich,  $\geq 99\%$ ) were used as received from the manufacturer and handled in the glovebox. Zinc acetate dihydrate ( $Zn(OAc)_2 \cdot 2H_2O$ , Sigma-Aldrich,  $\geq 99.5\%$ ), myristic acid (MA, Sigma,  $\geq 99\%$ ), and 1-octadecene (ODE, Sigma-Aldrich, 90%) were handled in standard laboratory conditions without any extra precautions. Diphyl (Dowtherm@A, eutectic mixture of 26.5% diphenyl + 73.5% diphenyl oxide, Aldrich) was stored and handled in an  $N_2$ -filled glovebox

after was degassed for 2 hours at 100 °C. *n*-dodecanethiol (*n*-DDT, Aldrich,  $\geq 98\%$ ) was stored and handled in an  $N_2$ -filled glovebox after  $N_2$  was bubbled through for more than 24 hours.

**Synthesis of Aluminium-tris[bis(mesitoyl)arsine] –  $Al^{(Mes)BAAs}_3$ .** Aluminium-tris[bis(mesitoyl)arsine] –  $Al^{(Mes)BAAs}_3$  – was synthesized by the reaction between aluminum chloride, 2,4,6-trimethyl benzoyl chloride, and arsine, by the group of Prof. Dr. Matthias Driess (Berlin University of Technology) after an adaptation of the synthesis of phosphorous analog developed by the group of Prof. Dr. Hansjörg Grützmacher (ETH Zürich) and the detailed procedure will be published elsewhere.

**Synthesis of InAs QDs.** Indium acetate (0.18 mmol) was loaded into a 25 mL 3-neck flask inside a glovebox. Myristic acid (0.75 mmol) and 1-octadecene (5 mL) were added to indium acetate just before connecting the reaction flask to the Schlenk line and vigorously stirred under vacuum for 2 hours at 125 °C. Next, the clear colorless solution was brought to the desired reaction temperature (90, 120, 150, 180, 210, 240 or 270 °C) and  $Al^{(Mes)BAAs}_3$  (0.04 mmol) solubilized in diphyl (0.5 mL) was swiftly injected. The reaction was stopped after 30 minutes by rapidly immersing the reaction flask into a water-bath. The obtained product was purified in an  $N_2$ -filled glovebox by using dried hexane and dried acetone as a solvent-antisolvent couple. The turbid solution was centrifuged, and the precipitated product was redispersed in hexane. The cycle was repeated three times, and at the end, the nanoparticles were stored in anhydrous TCE.

**Synthesis of In(Zn)As QDs.** For the synthesis of In(Zn)As, zinc acetate dihydrate (0.225 mmol) was added at the beginning of the reaction along with indium acetate, myristic acid, and 1-octadecene, and the same protocol as described above for InAs was followed.

**Synthesis of In(Zn)As QDs – two-step-injection approach.** Indium acetate (0.18 mmol), zinc acetate dihydrate (0.225 mmol), myristic acid (0.75 mmol), and 1-octadecene (5 mL) were loaded into a 3-neck flask and degassed for 2 hours at 125 °C. Next, the temperature was raised at 270 °C under  $N_2$  atmosphere and 0.02 mmol of  $Al^{(Mes)BAAs}_3$  solubilized in diphyl (0.3 mL) was swiftly injected. After 15 minutes of vigorous stirring at 270 °C, the second addition of  $Al^{(Mes)BAAs}_3$  (0.04 mmol solubilized in 0.5 mL diphyl) was injected dropwise over 15 minutes, and the reaction was left to run for 24 hours at 270 °C.

**Synthesis of In(Zn)As/ZnS core/shell QDs.** Zinc acetate dihydrate (1 mmol) was added in a 25 mL 3-neck flask along with *n*-dodecanethiol (5 mL) and heated up to 150 °C

under  $N_2$  atmosphere for few minutes in order to solubilize the Zn precursor. After the zinc acetate dihydrate was solubilized, the temperature was lowered to 80 °C and applied vacuum for 2 hours. Next, the reaction mixture was switched again on  $N_2$  for the addition of InAs cores (10 mg/mL) dispersed in the minimum amount of hexane. The flask was switched slowly on the vacuum and kept for about 5-10 minutes at 80 °C in order to remove the hexane. When no bubbling was observed, the flask was switched on  $N_2$ , and the temperature was raised to 230 °C and kept for 3 hours. The purification of the core/shell NPs was similar to that one described above for the InAs cores.

### Synthesis of $Cd_3As_2$ QDs

**Acetate method I.** Cadmium acetate dihydrate (0.18 mmol), myristic acid (0.75 mmol), and 1-octadecene (5 mL) were loaded into a 25 mL 3-neck flask and connected to a Schlenk line. The reaction mixture was vigorously stirred for 2 hours at 125 °C under vacuum. Next, the reaction mixture was switched on an  $N_2$  atmosphere, and the temperature was raised to 250 °C.  $Al^{(Mes)BAAs}_3$  (0.04 mmol) solubilized in diphenyl (0.5 mL) was swiftly injected and the reaction was stopped after 5 minutes by cooling down the reaction flask first with an air flow (to bring the flask temperature below 200 °C), and after by rapidly immersing the flask into a water bath. The  $Cd_3As_2$  NPs were purified in an  $N_2$  filled glovebox in the same manner as the InAs NCs.

**Acetate method II.** Cadmium acetate dihydrate (0.18 mmol), myristic acid (0.75 mmol), and 1-octadecene (5 mL) were loaded into a 25 mL 3-neck flask and connected to a Schlenk line. The reaction mixture was vigorously stirred for 2 hours at 125 °C under vacuum. Next, the reaction mixture was switched on an  $N_2$  atmosphere, the temperature was raised to  $t$  °C ( $t = 150, 160$  or  $180$  °C) and  $Al^{(Mes)BAAs}_3$  (0.04 mmol) solubilized in diphenyl (0.5 mL) followed by DIBAL-H 0.1 M in toluene (0.3 mL) were swiftly injected. The reaction was stopped after 5 minutes by cooling down the reaction flask using a water bath. The  $Cd_3As_2$  NPs were purified in an  $N_2$  filled glovebox in the same manner as the InAs NCs.

**Halide method.** Cadmium chloride (0.18 mmol) and oleylamine (3 mL) were loaded into a 25 mL 3-neck flask inside of an  $N_2$ -filled glovebox and transferred to a Schlenk line. The reaction mixture was evacuated for 1 hour under vacuum at 125 °C, after which was switched on  $N_2$  and the temperature was raised to  $t$  °C ( $t = 140, 160, 180$  °C). Next,  $Al^{(Mes)BAAs}_3$  (0.04 mmol) solubilized in diphenyl (0.5 mL) and DIBAL-H 0.1 M in toluene (0.3 mL) were swiftly injected one after another. The reaction was stopped after 5 minutes by immersing the flask

rapidly into a water bath. The Cd<sub>3</sub>As<sub>2</sub> NPs were purified in an N<sub>2</sub> filled glovebox in the same manner as the InAs NCs.

### **Synthesis of GaAs QDs**

**Acetate method I.** Gallium acetylacetonate (0.18 mmol), myristic acid (0.75 mmol), and 1-octadecene (5 mL) were loaded into a 25 mL 3-neck flask and connected to a Schlenk line. The reaction mixture was vigorously stirred for 2 hours at 125 °C under vacuum. Next, the reaction mixture was switched on an N<sub>2</sub> atmosphere, and the temperature was raised to 250 °C. Al<sup>(Mes)BAAs</sup><sub>3</sub> (0.04 mmol) solubilized in diphenyl (0.5 mL) was swiftly injected followed by the injection of DIBAL-H 0.1 M in toluene (0.3 mL). The reaction was stopped after a certain period (5, 30, 60 minutes) by cooling down the reaction flask first with air flow (to bring the flask temperature below 200 °C), and after by rapidly immersing the flask into a water bath. The GaAs QDs were purified in an N<sub>2</sub> filled glovebox in the same manner as the InAs NCs.

**Halide method.** Gallium chloride (0.18 mmol) and oleylamine (5 mL) were loaded into a 25 mL 3-neck flask inside of an N<sub>2</sub>-filled glovebox and transferred to a Schlenk line. The reaction mixture was evacuated for 1 hour under vacuum at 125 °C after which was switched on N<sub>2</sub> and the temperature was raised to 250 °C. Next, Al<sup>(Mes)BAAs</sup><sub>3</sub> (0.04 mmol) solubilized in diphenyl (0.5 mL) and DIBAL-H 0.1 M in toluene (0.3 mL) were swiftly injected one after another. The reaction was stopped after a certain period (5, 30, 60 minutes) by cooling down the reaction flask first with air flow (to bring the flask temperature below 200 °C), and after by rapidly immersing the flask into a water bath. The GaAs QDs were purified in an N<sub>2</sub> filled glovebox in the same manner as the InAs NCs.

### **Synthesis of Zn<sub>3</sub>As<sub>2</sub> QDs**

**Acetate method I.** Zinc acetate dihydrate (0.18 mmol), myristic acid (0.75 mmol), and 1-octadecene (3 mL) were loaded into a 25 mL 3-neck flask and connected to a Schlenk line. The reaction mixture was vigorously stirred for 2 hours at 125 °C under vacuum. Next, the reaction mixture was switched on an N<sub>2</sub> atmosphere, and the temperature was raised to 180 °C. Al<sup>(Mes)BAAs</sup><sub>3</sub> (0.04 mmol) solubilized in diphenyl (0.5 mL) was swiftly injected followed by the injection of DIBAL-H 0.1 M in toluene (0.3 mL or 1 mL). The reaction was stopped after a certain period (30 minutes or 1 minute, depending on the volume of injected DIBAL-H) by rapidly immersing the flask into a water bath. The Zn<sub>3</sub>As<sub>2</sub> QDs were purified in an N<sub>2</sub> filled glovebox in the same manner as the InAs NCs.

**Halide method.** Gallium chloride (0.18 mmol) and oleylamine (3 mL) were loaded into a 25 mL 3-neck flask inside of an  $N_2$ -filled glovebox and transferred to a Schlenk line. The reaction mixture was evacuated for 1 hour under vacuum at 125 °C after which was switched on  $N_2$  and the temperature was raised to 180 °C. Next,  $Al^{(Mes)BAAs}_3$  (0.04 mmol) solubilized in diphyl (0.5 mL) and the reaction was stopped after 30 minutes by rapidly immersing the flask into a water bath. The  $Zn_3As_2$  QDs were purified in an  $N_2$  filled glovebox in the same manner as the InAs NCs. It was also tried the fast addition of DIBAL-H 0.1 M in toluene (0.3 mL) immediately after the  $Al^{(Mes)BAAs}_3$  precursor letting the reaction to run for 30 minutes.

**Growth of ZnS outer shell onto InAs QDs.** Zinc acetate dihydrate (1 mmol) was loaded in a 25 mL 3-neck flask along n-dodecanethiol (5 mL) and degassed for 2 hours at 80 °C. Next, the reaction mixture was switched on an  $N_2$  atmosphere and the temperature raised and maintained for 30 minutes at 150 °C to assure that the Zn salt was completely solubilized. The temperature was lowered again at 80 °C, and about 10 mg of In(Zn)As QDs dispersed in a minimum volume of hexane was injected to the reaction mixture. The reaction flask was kept under vacuum for about 5 minutes in order to evaporate the hexane after which the temperature was raised to 230 °C and kept for 3 hours.

**Characterization.** For optical measurements, small volumes of each sample were diluted in dry TCE, and the  $O_2$  exposure was minimized. Absorbance measurements were effectuated using a Jasco V670 spectrometer in transmission mode. The photoluminescence spectra of InAs QDs and  $Cd_3As_2$  QDs emitting bellow 1000 nm were measured with a CCD fiber spectrometer (LR1, Aseq Instruments) with a 532 nm excitation source (frequency-doubled, CW Nd:YAG diode-pumped solid-state laser ). PL emission from the samples passed through a long-pass optical filter with an edge at 550 nm in order to reject the excitation laser line. For the samples emitting above 1000 nm, a Fluorolog iHR 320 Horiba Jobin Yvon spectrofluorimeter equipped with an 808 nm laser diode as an excitation source and liquid-nitrogen-cooled InGaAs and InSb photodetectors. Absolute PL quantum yields (QY) of the QDs (dispersed in TCE) were measured using a Quantaaurus QY (C11347-0X) from Hamamatsu equipped with a 150W Xenon light source and a 3.3 inches integrating sphere covered with highly reflective Spectralon. The detailed procedure for the PLQY measurement has been reported elsewhere.<sup>333</sup> Transmission electron microscopy images were recorded using a Hitachi HT7700 EXALENS microscope operated at 100 kV. For the X-ray diffraction measurements, a film of NPs was deposited on Mylar foils by evaporating the solvent out and sandwiched with another Mylar foil. The XRD patterns were collected with an STOE STADI



P powder diffractometer, operating in transmission mode. A germanium monochromator, Cu K $\alpha_1$  irradiation, and Dectris Mythen silicon strip detector were used.

### 4.3. Results and discussion

A general synthetic procedure has been designed for the efficient synthesis of InAs, GaAs, Cd<sub>3</sub>As<sub>2</sub>, and Zn<sub>3</sub>As<sub>2</sub> QDs. In this general procedure, the metal salts (In<sup>3+</sup>, Ga<sup>3+</sup>, Cd<sup>2+</sup>, and Zn<sup>2+</sup>) along with a ligand (MA or OLAH) in a non-coordinating solvent (ODE), or coordinating OLAH used both as ligand and solvent, for the particular case of II-V QDs (see Halide method); were degassed at 125 °C. The air-stable Al<sup>(Mes)BAAs</sup><sub>3</sub> precursor solubilized in diphyl was swiftly injected, and luminescent InAs and Cd<sub>3</sub>As<sub>2</sub> QDs were obtained. GaAs and Zn<sub>3</sub>As<sub>2</sub> nanoparticles were obtained as well by following the general synthetic procedure, but they presented reduced colloidal stability and showed no PL. The primary objective was to test the capabilities of Al<sup>(Mes)BAAs</sup><sub>3</sub> as an arsenic precursor for the synthesis of metal-arsenide QDs, the reason for which only the InAs and Cd<sub>3</sub>As<sub>2</sub> systems were explored in greater detail.

#### **Indium Arsenide Quantum Dots (InAs QDs)**

The InAs QDs were synthesized following the synthetic scheme depicted in **Figure 4.1a** (details in **Experimental Section**). The In(OAc)<sub>3</sub> and MA in ODE were degassed for 2 hours at 125 °C, after which the reaction mixture was switched on N<sub>2</sub> atmosphere. The temperature was adjusted in the range of 90 to 300 °C and the air-stable Al<sup>(Mes)BAAs</sup><sub>3</sub> precursor solubilized in diphyl was swiftly injected. Depending on the injection temperature, a slower or rapid change of color was noticed. In the case of the reaction at 90 °C, the change of color was slow – minimum of 3 hours to notice an almost black coloration of the solution; less slower for the reaction at 120 °C – about 5 minutes – and very fast – less than 1 minute – for the reactions done at temperatures higher than 200 °C. As can be observed in **Figure 4.1b**, after a general reaction time of 30 minutes (except for the reaction at 90 °C which was left to run for 28 hours), luminescent InAs QDs cores were obtained.

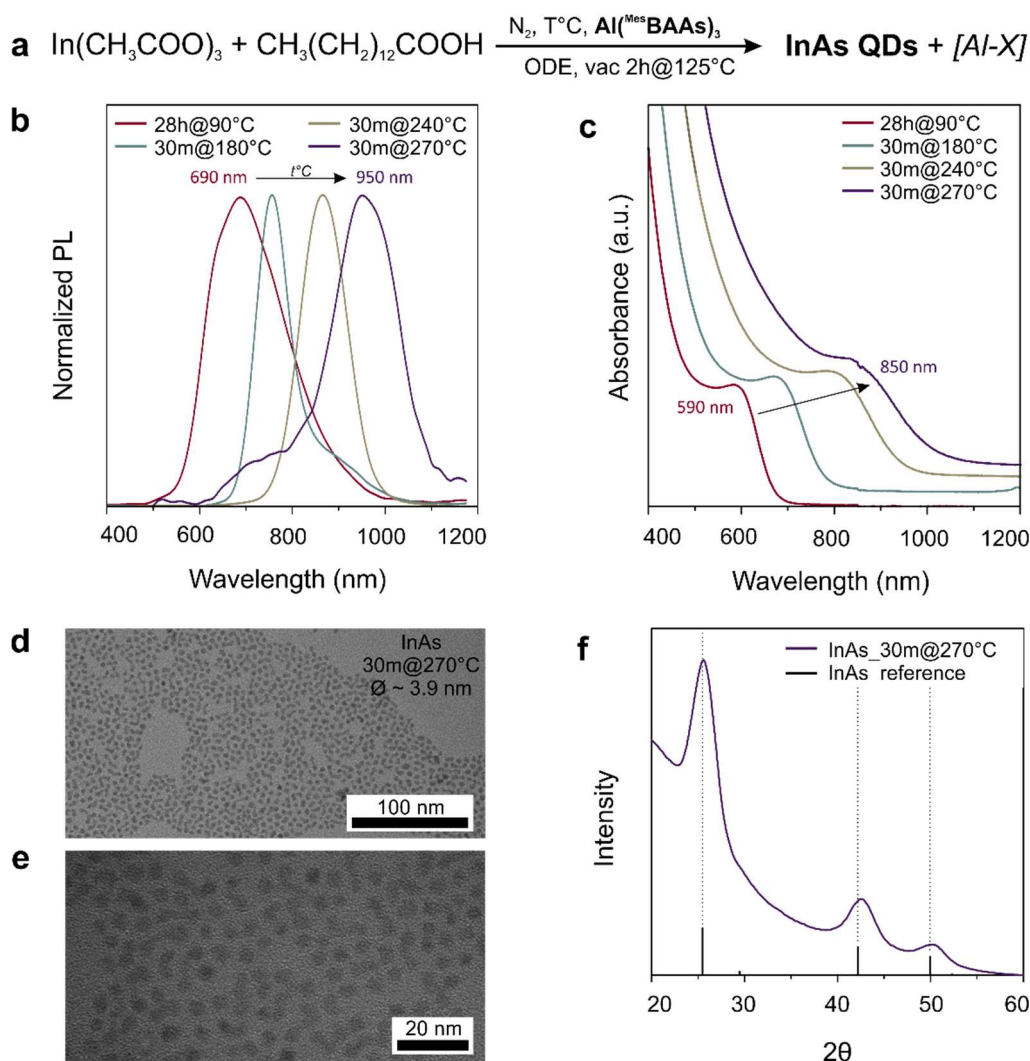


**Figure 4.1.** (a) Schematic representation of the synthetic protocol used to synthesize the emissive InAs QDs. (b) Typical photoluminescence emission of the InAs QDs synthesized at 90, 180, 240, and 270 °C. (c) Corresponding absorption spectra of the InAs QDs obtained after 28 hours at 90 °C and 30 minutes at 180, 240, and 270 °C showing a redshift into the NIR by increasing the reaction temperature. (d) and (e) Transmission electron micrographs at low and high magnification, respectively, of the InAs QDs, synthesized at 270 °C showing monodisperse nanocrystals with an average size of 4 nm. (f) X-ray diffraction pattern corresponding to the InAs QDs synthesized at 270 °C.

The synthesized QDs have photoluminescence emission covering the spectral regime from 690 nm up to 950 nm with typical PLQYs of 1-2%. The tuning of the PL was achieved in this case by running the synthesis over a broad range of temperatures (90 – 270 °C). When the reaction was done at 90 °C, the resultant PL was broad and showing a tail in the second part of the spectrum most likely due to the defective surface of the QDs. Opposite to the broad and asymmetric PL spectrum, as can be observed in **Figure 4.1c**, the corresponding absorption

spectrum is showing a sharp peak around 590 nm, suggesting that the QDs are quite small and nicely monodisperse. When the reaction temperature was increased above 180 °C, the absorption peaks started to broaden while red shifting further in the NIR, as can be noticed in **Figure 4.1c**, but still maintaining a monodisperse size distribution as confirmed by the TEM images. For instance, in the case of the InAs QDs prepared at 270 °C which shows the broadest absorption spectrum with a maximum around 850 nm, the average size of the QDs is about 4 nm (**Figures 4.1d** and **4.1e**). In **Figure 4.1f**, it is displayed a typical XRD pattern of the synthesized InAs QDs matching the cubic crystal structure. The evolution of the size of InAs QDs and their optical properties were monitored by collecting aliquots at specific periods. For instance, in **Figure 4.2** are presented the PL and absorption spectra, and the size evolution of the InAs QDs synthesized at 270 °C over two hours. The PL is red shifted during the first 45 minutes of the reaction but later is stopping at 985 nm and does not show any further evolution (**Figure 4.2a**) even though the absorption spectra show further shifting after 2 hours at 270 °C (**Figure 4.2b**). Also, it can be observed by comparing **Figures 4.2c**, **4.2d**, and **4.2e** that after 15 minutes of reaction the QDs are monodisperse and have an average size of ~3.4 nm and stop increasing in size already at ~4 nm after 45 minutes of reaction at 270 °C.

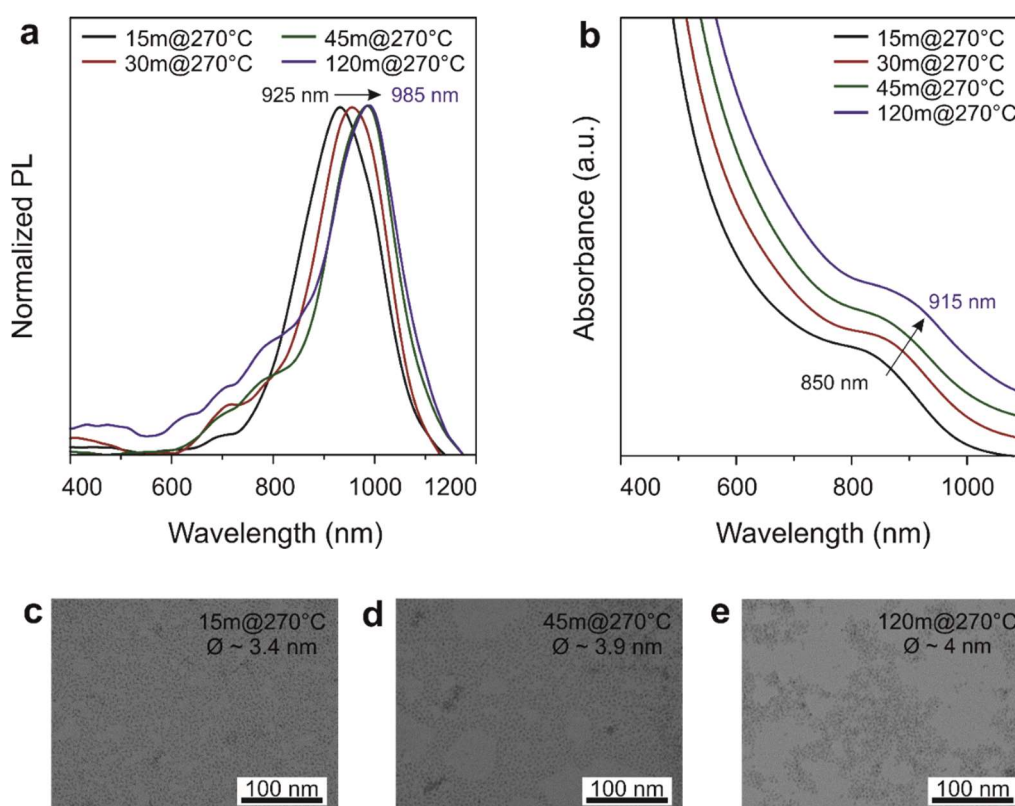


**Figure 4.2.** Normalized photoluminescence emission (a) and absorption spectra (b) of InAs QDs synthesized at 270 °C for 120 minutes. The PL spectra show no red-shift after 45 minutes

at 270 °C while the absorption spectra still red-shift over 120 minutes. Transmission electronic micrographs of InAs QDs after 15 (c), 45 (d), and 120 (e) minutes showing that the size stops increasing after 45 minutes at 270 °C.

### Indium (Zinc) Arsenide Quantum Dots (In(Zn)As QDs)

Recently, few studies on InP QDs focused on proving that by introducing  $Zn^{2+}$  ions into the QDs is curing the structural defects responsible for the self-trapped excitons. Besides this, by introducing  $Zn^{2+}$  into the InAs QDs will also facilitate later the growth of a Zn-based shell since the  $Zn^{2+}$  will not be only inside the crystal structure but also on the surface.<sup>128, 334-335</sup> The reaction was realized as schematically represented in **Figure 4.3a**, following the same procedure as described for the synthesis of InAs QDs having zinc acetate dihydrate added extra from the beginning of the reaction (see the **Experimental Section**). It was observed that in the case of the reactions having Zn-precursor from the beginning, it would take a longer time for the change of color to occur (slower reaction) or the reaction would not take place at all at temperatures as low as 90 °C. The profile of the PL spectra shows a considerable improvement (**Figure 4.3b**) for the QDs synthesized at temperatures higher than 150 °C and lower than 270 °C when Zn-ions were present in the reaction mixture. For the QDs synthesized at 150 °C, a tail still can be observed in the PL spectrum, most likely, because longer reaction time is needed in order to improve the quality of the QDs. In the case of the QDs synthesized at 270 °C, was observed the apparition of traces of black-grey precipitate into the reaction flask but it was easily separated during the purification procedure. This observation suggests that it would be desirable a shorter reaction time at temperatures as high as 270 °C. Also, by addition of  $Zn^{2+}$  to the synthesis the PL emission of the In(Zn)As QDs is covering a smaller spectral regime, namely from 745 to 925 nm (**Figure 4.1b**), in comparison with the emission capabilities of InAs QDs (**Figure 4.1a**); also, narrower emission line widths can be observed. These observations can be explained as the results of  $Zn^{2+}$  incorporation into the InAs crystal lattice as noticed in previous studies for the case of In(Zn)P QDs.<sup>334-335</sup> The absorption response of In(Zn)As QDs seems to be very similar with the response of InAs QDs showing distinct absorption peaks starting from 660 nm up to 870 nm depending on the reaction temperature (**Figure 4.3b**). The size of the QDs was maintained in the same range after the introduction of  $Zn^{2+}$  ions. The smallest size was found to be about 2.4 nm for the In(Zn)As QDs synthesized at 150 °C (**Figure 4.3c**), and the largest size about 4 nm for the QDs synthesized at 270 °C (**Figure 4.3d**). By comparing the case of the QDs synthesized with and without  $Zn^{2+}$  at 270 °C (**Figures 4.1d, 4.1e and Figure 4.3d**), one can notice that the size of the QDs after 30 minutes

of reaction is almost the same in both situations. The QY of the newly synthesized In(Zn)As QDs was measured as well and was found to be in the same range of 1-2 % as for the InAs QDs.

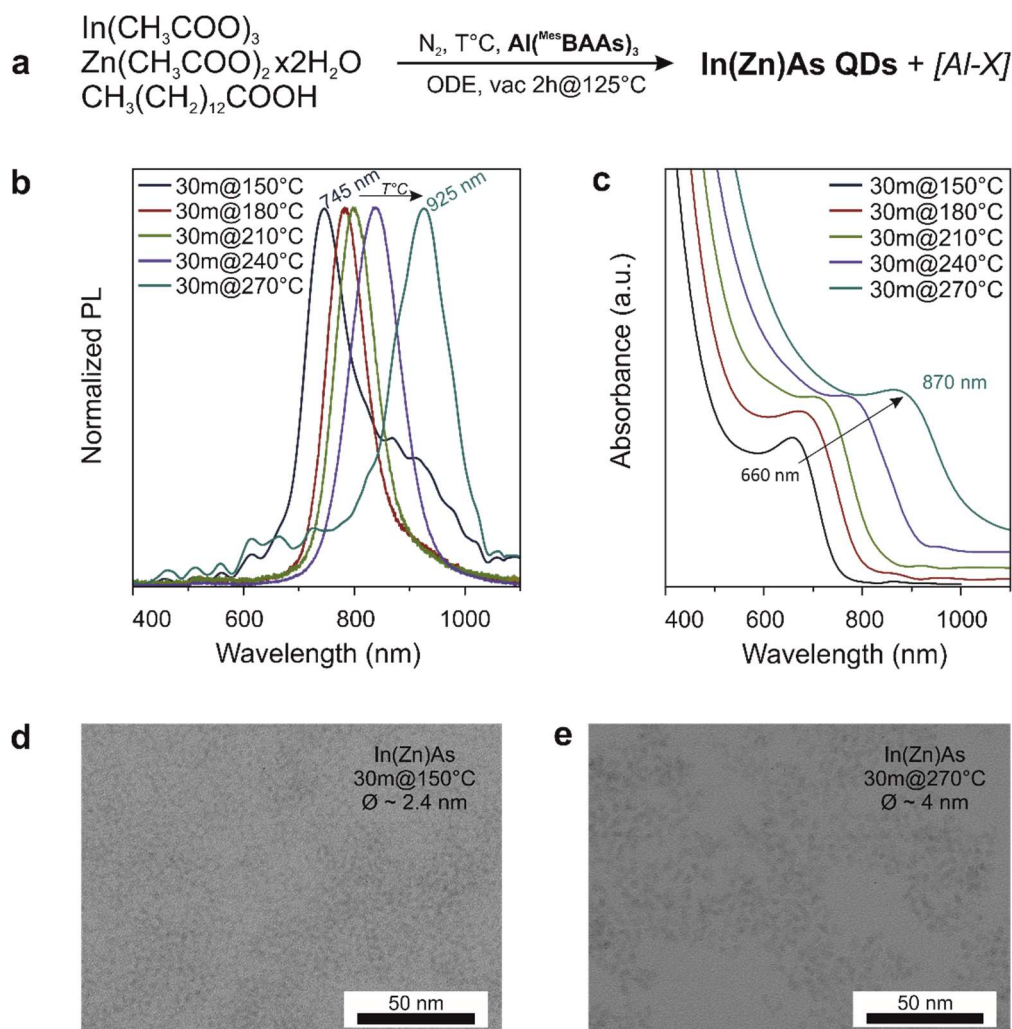


**Figure 4.3.** (a) Schematic representation of the synthetic protocol used to synthesize the emissive In(Zn)As QDs. (b) Normalized photoluminescence emission of the In(Zn)As QDs synthesized at different reaction temperatures ranging from 150 °C up to 270 °C. (c) Absorbance spectra of the In(Zn)As QDs obtained after 30 minutes reaction time at 150, 180, 210, 240, and 270 °C showing a redshift from 660 nm to 845 nm by increasing the reaction temperature. (d) and (e) Transmission electron micrographs of the In(Zn)As QDs synthesized at 150 °C and 270 °C showing monodisperse nanocrystals with an average size of 2.4 nm and 4 nm, respectively.

Similar to the case of InAs QDs, the evolution of size and optical properties of In(Zn)As QDs were monitored, and a minor redshift of the PL emission was observed for the In(Zn)As QDs, from 915 nm up to 940 nm, during 3 hours of reaction at 270 °C ( **Figure 4.4a**), in comparison with InAs QDs. In **Figure 4.4b** can be observed the corresponding absorption

spectra of In(Zn)As QDs monitored over 3 hours of reaction at 270 °C which display a similar redshift as noticed for InAs QDs, but with better and more notable features. In contrast to InAs QDs, the In(Zn)As QDs are showing a tendency to cluster if the reaction is left to run for longer times (**Figures 4.4c, 4.4d, and 4.4e**) and also to increase their size up to ~4.6 nm after 3 hours at 270 °C.

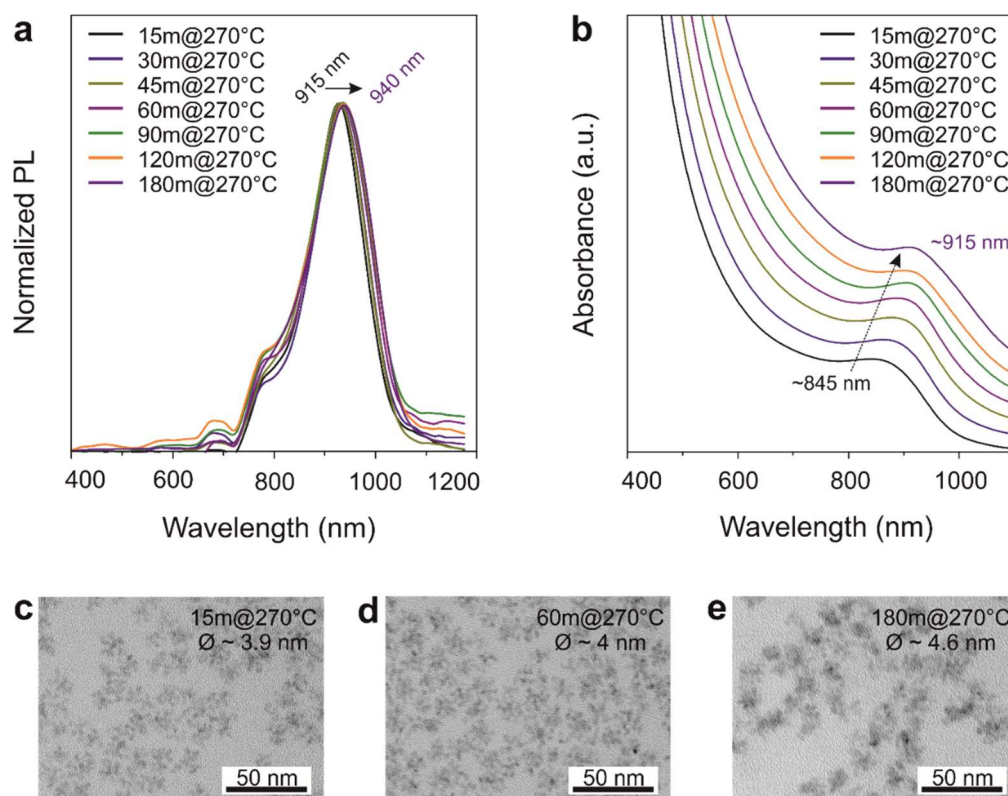


**Figure 4.4.** Normalized photoluminescence emission (**a**) and absorption (**b**) spectra of In(Zn)As QDs monitoring their red-shift over a period of 180 minutes while vigorously steering at 270 °C; Transmission electron micrographs of the In(Zn)As QDs synthesized at 270 °C after 15 (**c**), 60 (**d**), and 180 (**e**) minutes of reaction.

Moreover, inspired by the work of Franke *et al.*, a two-step-injection of the As-precursor was used in order to verify how far in IR can be obtained PL emission from the naked In(Zn)As QDs.<sup>105</sup> In order to achieve this, the standard synthetic protocol was modified and a second injection step was introduced. First, at 270 °C, a small fraction of 0.02 mmol of  $Al^{(Mes)BAAs}_3$  solubilized in diphyl (0.3 mL), and emission and absorption maximum at 880 nm and 815 nm, respectively, (**Figure 4.5a and 4.5b**) were recorded for the naked In(Zn)As QDs having an average size of 2.6 nm (**Figure 4.5c**). After 15 minutes, the second injection of 0.04 mmol of  $Al^{(Mes)BAAs}_3$  solubilized in diphyl (0.5 mL) was slowly added manually over 15 minutes. As a result, after the slow injection was finished, an emission band centered at 975

nm was recorded and can be observed in **Figure 4.5** that the PL emission is reaching a maximum of emission of 1000 nm after 24 hours of reaction. The same trend can be observed as well in **Figure 4.5b** where the absorption spectra are showing a red-shift starting from 910 nm (15 minutes after the second injection was finished) up to 930 nm after the reaction was stopped after 24 hours at 270 °C. The In(Zn)As QDs showed a stronger tendency of clustering after the second injection was finished and also an increase in size to ~3.9 nm after 15 minutes at 270 °C (**Figure 4.5d**), and stopping at ~4.5 nm after 24 hours of reaction at 270 °C (**Figure 4.5e**).

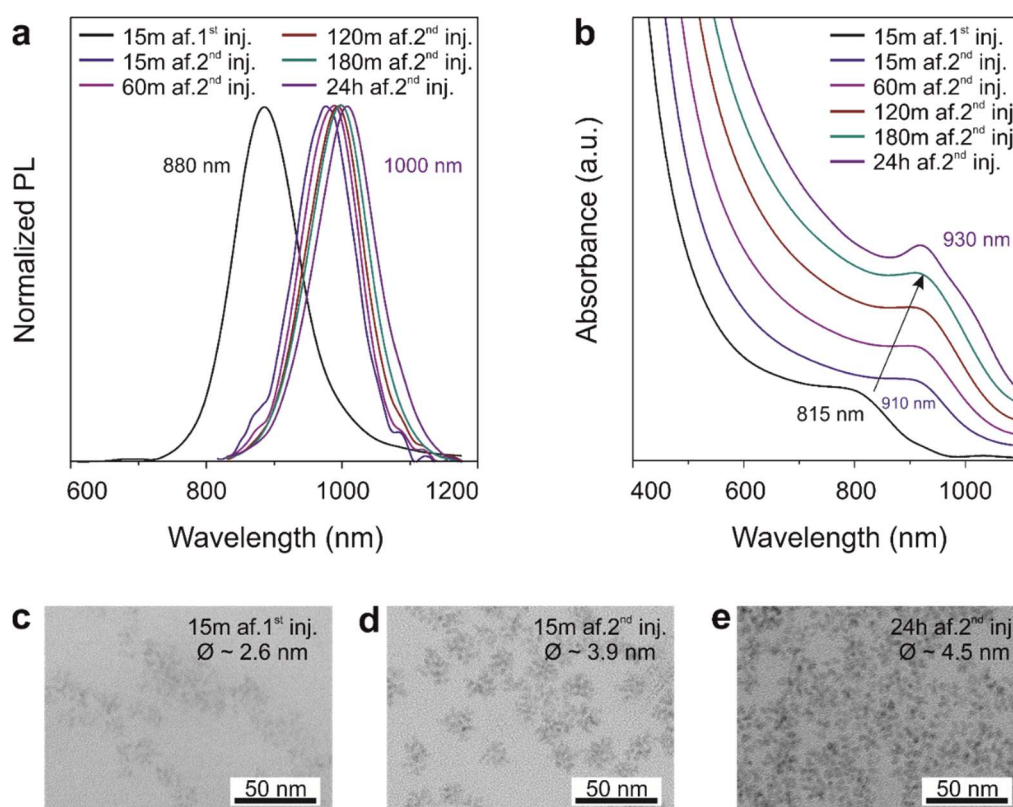


**Figure 4.5.** (a) Normalized photoluminescence spectra of In(Zn)As QDs synthesized by a two-step-injection approach showing a significant red-shift immediately after the second injection and displaying a maximum of emission centered at 1000 nm after 24 hours of reaction at 270 °C; (b) Evolution of the absorption spectra of In(Zn)As QDs during 24 hours reaction at 270 °C obtained by a two-step-injection approach; (c) Observation of the size evolution of In(Zn)As QDs synthesized by a two-step-injection approach over 24 hours of reaction at 270 °C.

In order to improve the photostability and the PL QY, an outer layer of a robust wide-band-gap of ZnS was grown onto the In(Zn)As QDs. In **Figure 4.6** can be seen the preliminary results of our attempts of growing a shell of ZnS onto In(Zn)As QDs synthesized at three different temperatures. Briefly, about 10 mg In(Zn)As QDs dispersed in a minimum volume of

hexane was injected into a mixture of zinc acetate dihydrate and n-DDT and kept under vigorous stirring for 3 hours at 230 °C (see the detailed procedure in **Experimental Section**). Small redshifts of the emission spectra can be observed in **Figures 4.6a, 4.6d, and 4.6g** as evidence of the formation of In(Zn)As/ZnS core/shell QDs. Also, the PL QY was boosted from 1-2%, the initial value for the In(Zn)As QDs cores, up to 21%, for the case of the covered cores synthesized at 240 °C, and in the range of 10-15% for the other cases. As can be noticed from the TEM images shown in **Figure 4.6**, also the size of the QDs increased after the shelling procedure (**Figures 4.6c, 4.6f, and 4.6i**) in comparison with the size of the initial QDs (**Figures 4.6b, 4.6e, and 4.6h**).

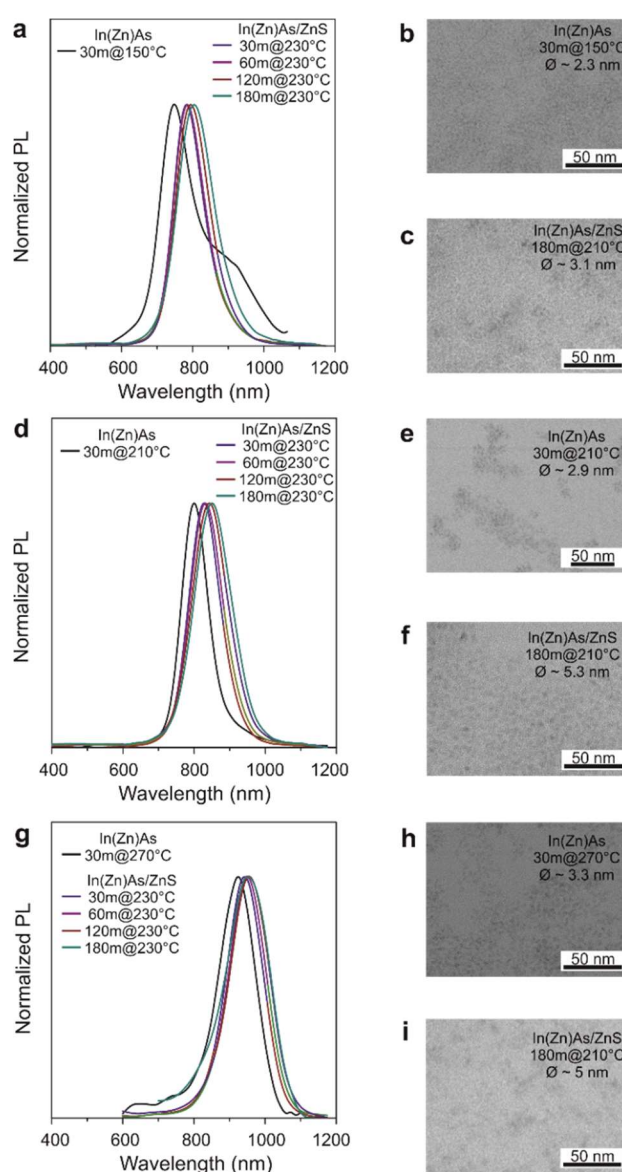


**Figure 4.6.** (a, d, g) Normalized photoluminescence emission spectra of In(Zn)As QDs cores synthesized at 3 different temperatures (150, 210, and 270 °C) and In(Zn)As/ZnS core/shell QDs evolution during the growing of a ZnS shell at 210 °C. Transmission electron micrographs



of the starting  $In(Zn)As$  QDs cores (**b, e, h**) and the final  $In(Zn)As/ZnS$  core/shell QDs (**c, f, i**) showing an increase in size due to the growing of ZnS shell.

### Cadmium Arsenide Quantum Dots ( $Cd_3As_2$ QDs)

The  $Al^{(Mes)3}BAAs_3$  was also tested as As-precursor for the synthesis of  $Cd_3As_2$  QDs. As can be noticed in **Figure 4.7**, the As-precursor was tested in two main-different synthetic approaches.

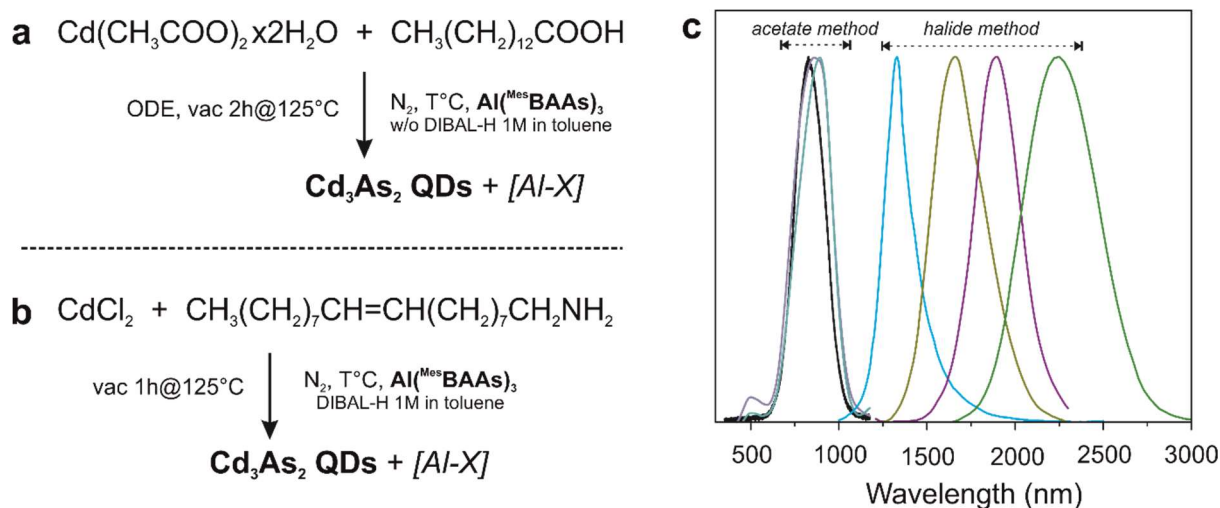


**Figure 4.7.** Schematic representation of the synthetic protocol employed for the synthesis of  $Cd_3As_2$  QDs using as starting materials **(a)** cadmium acetate dihydrate and myristic acid (acetate method), and **(b)** cadmium chloride and oleylamine (halide method), respectively; **(c)** Normalized photoluminescence spectra of the  $Cd_3As_2$  QDs obtained by using the two methods showing the tunability of the optical properties.

The first approach is similar to the procedure for the synthesis of  $InAs$  QDs and involves the use of cadmium acetate dihydrate along with myristic acid in ODE (**Figure 4.7a**). First, the precursor and ligand along with the solvent were degassed for 2 hours at 125 °C in a 3-neck round bottom flask. Then the reaction mixture was switched on an  $N_2$  atmosphere, and the temperature was raised at the desired injection temperature as described in the **Experimental section (Acetate method I and II)**. In the first situation – **Acetate method I** – when the conditions for synthesizing  $InAs$  QDs were mimicked, the reaction temperature was set at 250 °C, and the QDs were allowed to grow for 5 minutes before the reaction was stopped by rapid cooling down to room temperature. As a result,  $Cd_3As_2$  QDs were obtained showing in TEM images two size-populations: the main population with an average size of 6 nm and a second small population of about 2 nm (**Figure 4.8a**), showing an emission peak centered at 825 nm

(**Figure 4.7c**). In the second situation, namely **Acetate method II**, the reaction temperature was in the range of 150 – 180 °C and, additionally, DIBAL-H was used as a reducing agent. This second approach generated  $Cd_3As_2$  QDs with an average size in the range of 3.8 – 4.8 nm, depending on the reaction temperature and having PL emission in the range of 865 – 895 nm (**Figure 4.7c**). More than that, when the DIBAL-H was used, besides the shrinkage of the QDs' size as well the size disparity improved tremendously having one single population of QDs (**Figure 4.8b**) instead of two as noticed when no DIBAL-H was used.

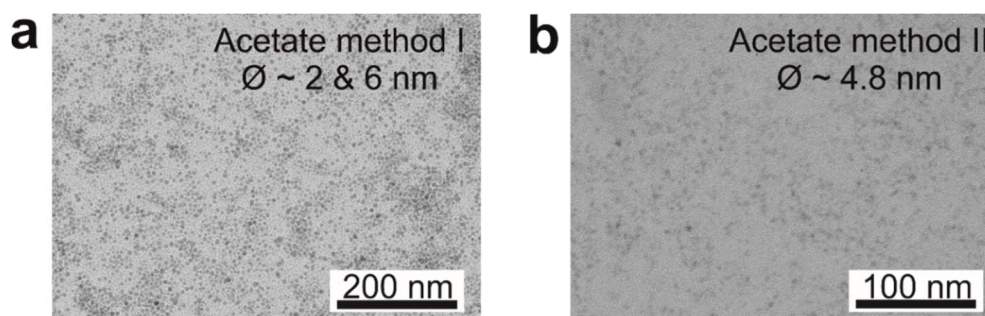


**Figure 4.8.** Transmission electronic micrographs of  $Cd_3As_2$  QDs synthesized by Acetate method I (**a**) and Acetate method II (**b**), respectively.

In the case of the second approach – **Halide method** – the operating reaction temperature was in the range of 120 – 180 °C and a reducing agent, namely DIBAL-H, was added immediately after the injection of  $Al^{(Mes)BAAs}_3$  (**Figure 4.7b**). The obtained  $Cd_3As_2$  QDs have a diameter in the range of 4.7 – 5.5 nm, depending on the reaction temperature (**Figure 4.9**). When the reaction was done at 120 °C, the resultant QDs showed high polydispersity and the largest size (5.5 nm, **Figure 4.9a**), most likely due of the slow release of reactive As species. By increasing the reaction temperature, the size of the obtained  $Cd_3As_2$  QDs is decreasing, and their size dispersity is improved as well, as can be observed in **Figures 4.9b** and **4.9c**. Moreover, by adjusting the reaction temperature, the PL emission can be tuned over a wide range, 1300 – 2250 nm (**Figure 4.7.c**). Further fine tuning of the PL emission can be done in the mentioned range by adjusting the injected volume (0.05 – 0.6 mL) of the reducing agent.

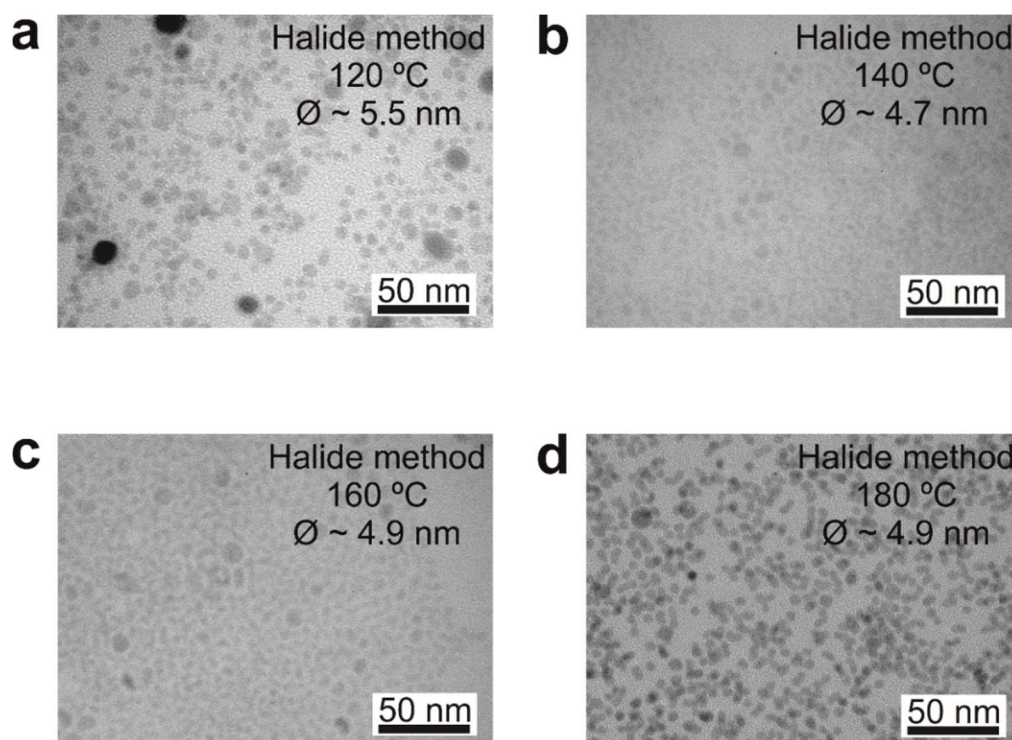


**Figure 4.9.** Transmission electron micrographs showing the size and size distribution of  $Cd_3As_2$  QDs synthesized at 120 °C (a), 140 °C (b), 160 °C (c), and 180 °C (d) while keeping all the other parameters constant.

#### Gallium Arsenide and Zinc Arsenide Quantum Dots (GaAs and $Zn_3As_2$ QDs)

The  $Al^{(Mes)BAAs}_3$  precursor was also tested for the synthesis of GaAs and  $Zn_3As_2$  QDs, but those preliminary trials will not be discussed here. Briefly, in the preliminary trials, I used the synthetic protocols described for the synthesis of  $Cd_3As_2$  QDs, both Acetate, and Halide method (see the details in the **Experimental Section**), using gallium acetylacetonate and zinc acetate dihydrate for the Acetate method, and gallium chloride and zinc chloride for the Halide method, respectively, respecting all the previously reported parameters for  $Cd_3As_2$  QDs.

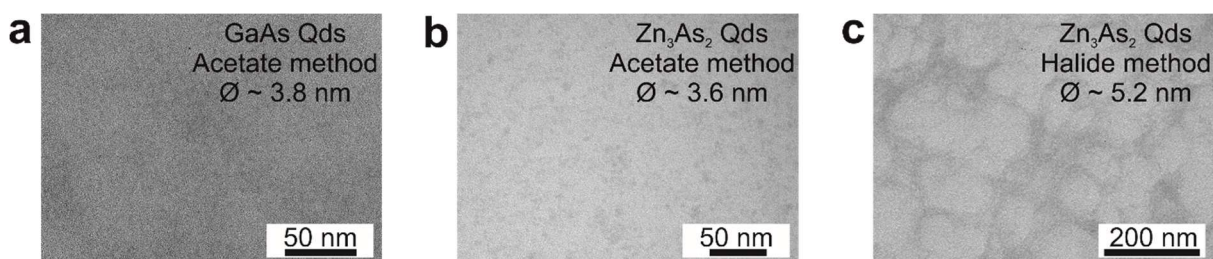


**Figure 4.10.** Transmission electron micrographs showing the results for the synthesis of GaAs QDs via the Halide method (a), and the  $Zn_3As_2$  QDs via the Acetate (b) and the Halide method (c).

In the case of GaAs QDs synthesis, after the first trials, only the Halide method proved to be efficient and to generate QDs. As shown in **Figure 4.10a**, QDs with an average size of  $\sim 3.8$  nm were obtained, but they did not show any photoluminescence capabilities. Whereas for the synthesis of  $Zn_3As_2$  QDs, both Acetate and Halide methods favored the generation of QDs as can be noticed in **Figures 4.10b** and **4.10c**. In the case of Acetate method, QDs with an average size of  $\sim 3.6$  nm were obtained (**Figure 4.10b**), whereas, by using the Halide method, larger QDs with an average size of  $\sim 5.2$  nm were obtained. The obtained  $Zn_3As_2$  nanoparticles presented the lowest colloidal stability and no photoluminescence activity, as observed for the GaAs QDs. No further experiments were conducted in order to improve the synthesis of GaAs and  $Zn_3As_2$  QDs.

## 4.4. Conclusions

This work demonstrates that  $Al^{(Mes)BAAs}_3$  is a potent As-precursor for the synthesis of metal-arsenide QDs. A generalized synthetic protocol favored the fast synthesis of InAs, GaAs,  $Cd_3As_2$ , and  $Zn_3As_2$  QDs. In the case of InAs and  $Cd_3As_2$  QDs, the  $Al^{(Mes)BAAs}_3$  precursor proved to be very efficient, generating luminescent QDs without growing a protective shell or applying additional post-synthetic treatments. Very mild reaction conditions such as relatively low reaction temperature ( $90$  °C for InAs QDs), short reaction time (5 minutes for  $Cd_3As_2$  QDs and 30 minutes for InAs QDs), and optional employment of reducing agents, are used in order to obtain QDs. In a preliminary attempt of improving the QY for the InAs QDs, a boost from 1-2 % up to 20 % was accomplished by the growth of a shell of ZnS. The PL QYs can be increased tremendously by a more detailed investigation of the necessary conditions for growing a protective shell. GaAs and  $Zn_3As_2$  QDs were obtained as well using  $Al^{(Mes)BAAs}_3$  as an As-source but showing less remarkable properties.

## Chapter 5. Fast anion-exchange in highly luminescent nanocrystals of cesium lead halide perovskites (CsPbX<sub>3</sub>, X = Cl, Br, I)

### 5.1. Introduction

Rational synthesis of colloidal nanocrystals (NCs) is of paramount importance in NC research due to the growing demand for compositional diversity, shape engineering and new optical, electronic, magnetic or catalytic functionalities of NCs.<sup>336-337</sup> In this regard, post-synthetic chemical transformations of metallic, semiconducting and magnetic NCs are increasingly useful, such as by galvanic replacement,<sup>338-339</sup> cation-exchange reactions,<sup>340-345</sup> or the nanoscale Kirkendall effect.<sup>346-348</sup> These transformation routes, particularly suited to NCs due to their high surface-to-volume ratios and short diffusion path lengths, give access to a myriad of structures that are difficult or impossible to synthesize directly. The initial (parent) NC serves as a template whose size, shape, and composition can be independently modified.

For semiconductor NCs, typically metal chalcogenides, cation-exchange reactions are particularly powerful, resulting in a partial or complete replacement of cations while maintaining an uninterrupted anionic sub-lattice and often preserving the pre-existing shape as well.<sup>340-342</sup> A partial list of notable examples includes (with the parent NC in parentheses): the first report on cation exchange leading to Ag<sub>2</sub>Se (from CdSe NCs),<sup>234</sup> CdS-Ag<sub>2</sub>S nanorod superlattices (from CdS nanorods),<sup>235</sup> core-shell PbTe/CdTe, PbSe/CdSe and PbS/CdS NCs (from PbTe, PbSe and PbS NCs),<sup>29, 240</sup> PbSe/PbS core-shell and dot-in-rod NCs (from respective CdSe/CdS nanomorphologies),<sup>236</sup> PbS nanorods (from CdS nanorods),<sup>239</sup> disk-shaped CdTe NCs (from Cu<sub>2</sub>Te nanodisks),<sup>349</sup> CuInS<sub>2</sub> NCs (from Cu<sub>2-x</sub>S NCs),<sup>238</sup> InP nanoplatelets (from Cu<sub>3-x</sub>P nanoplatelets)<sup>350</sup> and sequential multiple cation exchanges for obtaining metastable phases.<sup>340</sup> In contrast to the facile extraction and replacement of cations, anion-exchange in NCs has remained elusive. Taking CdSe as an example, where Cd<sup>2+</sup> has at most half the radius of Se<sup>2-</sup>, cations are much easier to manipulate within the voids of the anionic sub-lattice than vice-versa. The scarcity of reported examples of successful anion-

exchange post-treatments in NCs is reflective of both the typical difficulties encountered (e.g., substantial restructuring or fracturing) and the demanding reaction conditions necessary (e.g., high reaction temperatures of 160-450 °C for ZnO to ZnS(Se) conversions) or the incomplete nature of the process (e.g., partial or limited to only a few surface atomic layers).<sup>100, 231, 248-251, 351</sup> In this work, a shift in the status quo is reported; halide anions in metal halide semiconductor NCs can be easily extracted and replaced with another halide, owing to their single ionic charge, the rigid nature of the cationic sublattice and an efficient vacancy-assisted diffusion mechanism.

Recently, Protesescu *et al.* reported a simple one-step synthesis of cesium lead halide perovskites (CsPbX<sub>3</sub>, X=Cl, Br, I) in the form of monodisperse colloidal nanocubes (4-15 nm edge lengths).<sup>352</sup> Through compositional modulations and quantum size-effects, the bandgap energies, and photoluminescence (PL) spectra are readily tunable over the entire visible spectral region of 410-700 nm. A peculiar feature of CsPbX<sub>3</sub> NCs is that, contrary to uncoated chalcogenide NCs, dangling bonds on the surface do not impart severe mid-gap trap states and the as-synthesized NCs exhibit bright emission with quantum efficiencies of up to 90% in the green-to-red spectral region. The fact that metal halides are significantly different from metal chalcogenides (e.g., from a structural standpoint, they consist of singly-charged anions and exhibit highly ionic bonding) led us to explore post-synthetic chemical transformations of CsPbX<sub>3</sub> NCs, the subject of this work. Cation- and anion-exchange reactions of ABX<sub>3</sub> perovskite structures offer a very promising avenue to a plethora of optoelectronic materials.

With this motivation in mind, various attempts to exchange either Cs<sup>+</sup> cations (with Rb<sup>+</sup>, Ag<sup>+</sup>, Cu<sup>+</sup> or Ba<sup>2+</sup>) or Pb<sup>2+</sup> cations (with Sn<sup>2+</sup>, Ge<sup>2+</sup> or Bi<sup>3+</sup>) in CsPbX<sub>3</sub> NCs were undertaken, though unfortunately leading to the decomposition of the parent CsPbX<sub>3</sub> NCs in every case. To this end, the most common outcome was the formation of a new halide such as AgX. In stark contrast, fast (e.g., in several seconds), low-temperature, deliberately partial or complete anion-exchange (**Figure 5.1a**) could easily be performed in the cases of Cl-to-Br, Br-to-Cl, Br-to-I, and I-to-Br anion-exchange, *via* the formation of homogeneous solid solutions. Due to the large difference in ionic radii between Cl<sup>-</sup> and I<sup>-</sup> causing the instability of Cl/I solid solutions, no mixed-halide solid solutions could be obtained in CsPbCl<sub>3</sub> + I<sup>-</sup> or CsPbI<sub>3</sub> + Cl<sup>-</sup> systems, but rather slow and complete exchange occurred.

## 5.2. Experimental section

**Preparation of Cs-oleate.** Cs<sub>2</sub>CO<sub>3</sub> (0.814 g, Aldrich, 99.9%), OA (2.5 mL, Sigma-Aldrich, 90%) and ODE (40 mL, Sigma-Aldrich, 90%) were added into a 100 mL 3-neck flask, dried for 1h at 120 °C and then heated under N<sub>2</sub> to 150 °C until all Cs<sub>2</sub>CO<sub>3</sub> reacted with OA. Since Cs-oleate precipitates out of ODE at room-temperature, it must be preheated to 100 °C before injection.

**Preparation of oleylammonium halides (OAmX).** Ethanol (100 mL, Aldrich) and OAm (0.038 mol, Acros Organics 80-90%) were combined in a 250 mL 2-neck flask and vigorously stirred. The reaction mixture was cooled in an ice-water bath and HX (0.076mol, HCl ≥37%, Aldrich; HBr 48%, Aldrich; HI 57%, Aldrich) was added. The reaction mixture was left to react overnight under N<sub>2</sub> flow. Then the solvent was evaporated under vacuum and the obtained product was purified by rinsing multiple times with diethyl ether. The product was left under vacuum overnight in a vacuum oven at 80 °C resulting in a white powder for OAmCl and OAmBr and a dark orange waxy-powder for OAmI.

**Synthesis of CsPbX<sub>3</sub> NCs.** ODE (5 mL) and 0.188 mmol of PbX<sub>2</sub> (PbCl<sub>2</sub> – 0.052 g, ABCR, 99.999%; PbBr<sub>2</sub> – 0.069 g, ABCR, 98%; PbI<sub>2</sub> – 0.086 g, ABCR, 99.999%) were loaded into a 25 mL 3-neck flask and dried under vacuum at 120 °C for 1h. Dried OA (0.5 mL) and OAm (0.5 mL) were injected at 120 °C under N<sub>2</sub> flow. After complete solubilization of a PbX<sub>2</sub> salt, the temperature was raised to 180-190 °C, and Cs-oleate solution (0.4 mL of a stock solution prepared as described above) was swiftly injected and 1 minute later the reaction mixture was cooled down by a water bath. For obtaining CsPbCl<sub>3</sub> NCs, a higher temperature of 170 °C and 1 mL of n-Trioctylphosphine (TOP, Strem, 97%) are necessary to solubilize PbCl<sub>2</sub>. After the reaction, the aggregated NCs were separated by centrifugation. After centrifugation, the supernatant was discarded, and the precipitate was redispersed in dry toluene for further use in anion-exchange reactions.

**Anion-exchange reactions (Table 5.1).** The anion exchange reactions were conducted using a Schlenk line. PbBr<sub>2</sub>, PbI<sub>2</sub>, and OAmX as anion sources were mixed with ODE (5 mL) in a 25 mL 3-neck flask and kept under vacuum at 120 °C for 10 minutes. Dried OA and OAm (0.2 mL each) were injected at 120 °C under N<sub>2</sub> flow. After complete solubilization of the anion source, the temperature was lowered to 40 °C and CsPbX<sub>3</sub> NCs (20-25 mg) dispersed in toluene were injected to initiate the anion-exchange. When using PbCl<sub>2</sub> as the anion source, 1mL TOP

was added, and it was necessary to raise the temperature to 150-170 °C for a short time in order to solubilize PbCl<sub>2</sub>. When using MeMgX as the anion source, it should be injected after the solvent and ligands are dried, just before the addition of NCs. After the reaction, the NCs were isolated by centrifugation. The supernatant was discarded, and the precipitate was dispersed in hexane (0.3) and centrifuged again. The supernatant was mixed with toluene (0.9 mL). NCs were precipitated by adding 0.3 mL acetonitrile, followed by centrifuging. The obtained precipitated NCs were redispersed in toluene for further analysis.

**Table 5.1.** All Cl↔Br and Br↔I anion exchange reactions were conducted in dry ODE (5 mL) at 40 °C. 1 mL TOP was added in all experiments where PbCl<sub>2</sub> used as halide source. The evolution of the PL peak maxima as a result of anion exchange has been completed within several seconds to several minutes (faster for Cl/Br systems).

Starting NCs [mmol] in 1 mL toluene	Halide precursor [mmol]	Resulting PL peak [nm]	OA [mL]	OAm [mL]
CsPbCl <sub>3</sub> – 0.047	PbBr <sub>2</sub> – 0.0188	470	0.1	0.1
CsPbCl <sub>3</sub> – 0.098	PbBr <sub>2</sub> – 0.098	494	0.4	0.4
CsPbCl <sub>3</sub> – 0.035	OAmBr – 0.035	467	0.2	0.2
CsPbCl <sub>3</sub> – 0.05	OAmBr -0.15	508	0.6	0.6
CsPbCl <sub>3</sub> – 0.058	MeMgBr – 0.058	467	0.2	0.2
CsPbCl <sub>3</sub> – 0.055	MeMgBr -0.165	508	0.4	0.4
CsPbBr <sub>3</sub> – 0.044	PbCl <sub>2</sub> – 0.025	468	0.3	0.3
CsPbBr <sub>3</sub> – 0.044	PbCl <sub>2</sub> – 0.132	410	0.8	0.8
CsPbBr <sub>3</sub> – 0.05	PbCl <sub>2</sub> – 0.05	432	0.7	0.7
CsPbBr <sub>3</sub> – 0.025	OAmCl – 0.025	484	0.2	0.2
CsPbBr <sub>3</sub> – 0.034	OAmCl – 0.062	456	0.3	0.3
CsPbBr <sub>3</sub> – 0.034	OAmCl – 0.1	404	0.4	0.4
CsPbBr <sub>3</sub> – 0.046	MeMgCl – 0.023	465	0.1	0.1
CsPbBr <sub>3</sub> – 0.046	MeMgCl – 0.046	443	0.2	0.2
CsPbBr <sub>3</sub> – 0.046	MeMgCl – 0.139	419	0.4	0.4
CsPbBr <sub>3</sub> – 0.0479	PbI <sub>2</sub> – 0.0137	550	0.2	0.2
CsPbBr <sub>3</sub> – 0.0567	PbI <sub>2</sub> – 0.022	584	0.2	0.2
CsPbBr <sub>3</sub> – 0.0431	PbI <sub>2</sub> – 0.0246	604	0.2	0.2
CsPbBr <sub>3</sub> – 0.05	PbI <sub>2</sub> – 0.038	632	0.2	0.2
CsPbBr <sub>3</sub> – 0.06	PbI <sub>2</sub> – 0.06	650	0.4	0.4
CsPbBr <sub>3</sub> – 0.037	PbI <sub>2</sub> – 0.112	680	0.6	0.6
CsPbBr <sub>3</sub> – 0.025	OAmI – 0.025	610	0.1	0.1
CsPbBr <sub>3</sub> – 0.034	OAmI – 0.1	675	0.3	0.3
CsPbBr <sub>3</sub> – 0.027	MeMgI – 0.027	570	0.1	0.1
CsPbBr <sub>3</sub> – 0.031	MeMgI – 0.077	628	0.2	0.2
CsPbBr <sub>3</sub> – 0.035	MeMgI – 0.122	688	0.3	0.3
CsPbI <sub>3</sub> – 0.058	PbBr <sub>2</sub> – 0.0166	658	0.1	0.1
CsPbI <sub>3</sub> – 0.031	PbBr <sub>2</sub> – 0.0158	636	0.1	0.1
CsPbI <sub>3</sub> – 0.049	PbBr <sub>2</sub> – 0.049	578	0.2	0.2



CsPbI <sub>3</sub> – 0.0479	PbBr <sub>2</sub> – 0.0638	548	0.3	0.3
CsPbI <sub>3</sub> – 0.033	OAmBr – 0.033	628	0.1	0.1
CsPbI <sub>3</sub> – 0.034	OAmBr – 0.069	545	0.2	0.2
CsPbI <sub>3</sub> – 0.035	OAmBr – 0.105	516	0.2	0.2
CsPbI <sub>3</sub> – 0.043	MeMgBr – 0.043	628	0.1	0.1
CsPbI <sub>3</sub> – 0.045	MeMgBr – 0.090	543	0.2	0.2
CsPbI <sub>3</sub> – 0.040	MeMgBr – 0.120	508	0.3	0.3

**Absorbance measurements.** UV-VIS absorption spectra were collected using a Jasco V670 spectrometer in transmission mode.

**Photoluminescence (PL) and absolute quantum yield (QY) measurements.** Fluorolog iHR 320 Horiba Jobin Yvon spectrofluorimeter equipped with a PMT detector was used to acquire steady-state PL spectra from solutions and films. PL QYs were estimated according to standard procedure using appropriate dye molecules for blue, green and red spectral regions (coumarine 343, fluorescein, and rhodamine 6G).<sup>315</sup>

**In-situ photoluminescence measurements** were performed with excitation light from a CW laser ( $\lambda=405$  nm, P= 300 mW) delivered through one branch of a Y-shaped fiber optic bundle to the flask during the anion-exchange. The emission light was collected with the second branch of the fiber optic bundle. PL spectra were recorded with a compact CCD spectrometer (LR1, Aseq-Instruments)

**Powder X-ray diffraction (XRD) patterns** were collected with an STOE STADI P powder diffractometer, operating in transmission mode. A germanium monochromator, Cu K $\alpha_1$  irradiation, and Dectris Mythen silicon strip detector were used.

**Transmission electron microscopy (TEM)** images were recorded using a JEOL JEM-2200FS microscope operated at 200 kV.

**Energy dispersive X-ray (EDX).** Elemental analysis was performed with two scanning electron microscopes (Zeiss Gemini 1530 and Hitachi, S-4800).

**Rutherford backscattering spectrometry (RBS)** was performed at the ETH Laboratory of Ion Beam Physics. Measurements were conducted using a 2 MeV 4He beam and a silicon PIN diode detector under an angle of 168°. The collected RBS data was analyzed using simulations by the RUMP code.<sup>316</sup>

### 5.3. Results and discussion

The anion-exchange reactions reported herein were conducted in dry 1-octadecene (ODE) as a solvent by mixing a specific ratio of the desired halide source and CsPbX<sub>3</sub> NCs (Table 5.1). The concentrations of capping ligands (oleylamine and oleic acid) were adjusted to be similar to those used for the synthesis of the parent CsPbX<sub>3</sub> NCs. All tested halide sources, from organometallic Grignard reagents (MeMgX) to oleylammonium halides (OAmX) and simple PbX<sub>2</sub> salts, afforded fast anion-exchange at 40 °C; at this temperature the solubility of all reagents and NCs could be maintained.

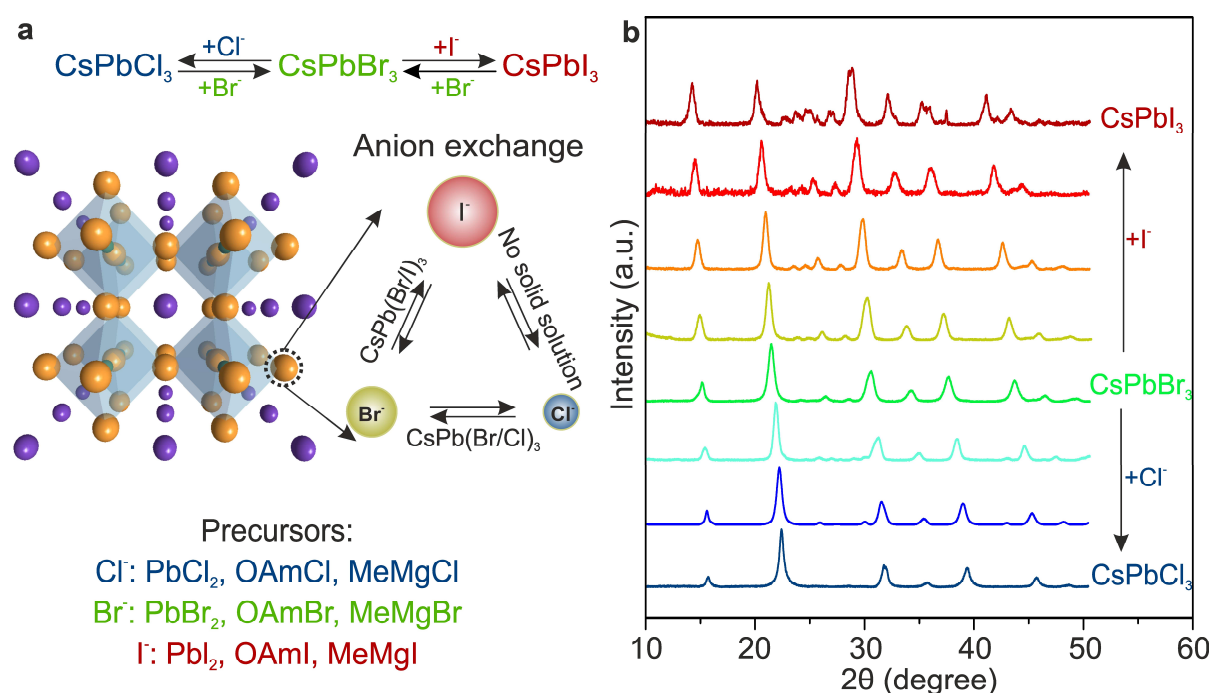


**Figure 5.1.** (a) Schematic of the anion-exchange within the cubic perovskite crystal structure of CsPbX<sub>3</sub>, along with a list of suitable reagents for each reaction when performed in organic media. Corner-sharing PbX<sub>6</sub> octahedra form a three-dimensional network with Cs<sup>+</sup> (purple spheres) occupying the interstitial voids. Ionic radii: Cs<sup>+</sup>-1.88 Å, Pb<sup>2+</sup>-1.16 Å, Cl<sup>-</sup>-1.81 Å, Br<sup>-</sup>-1.96 Å and I<sup>-</sup>-2.2 Å.<sup>357-359</sup> (b) Powder X-ray diffraction (XRD) patterns of the parent CsPbBr<sub>3</sub> NCs and anion-exchanged samples (using PbCl<sub>2</sub> and PbI<sub>2</sub> as halide sources), showing the retention of phase-pure cubic perovskite structure and an average (Scherrer) crystallite size of 8-10 nm. The shift of the XRD reflections is linearly dependent on the composition (Vegard's law), indicating the formation of uniform solid solutions. Equivalent behaviors were also observed for CsPbCl<sub>3</sub> + Br<sup>-</sup> and CsPbI<sub>3</sub> + Br<sup>-</sup> systems. Formation of solid solutions has also been confirmed by Energy Dispersive X-ray spectroscopy (EDX) and Rutherford backscattering spectrometry (RBS).

It is well known that bulk  $\text{CsPbX}_3$  phases crystallize in orthorhombic, tetragonal and cubic polymorphs of the perovskite lattice, with the cubic phase being the high-temperature state for all compounds.<sup>353-355</sup> By direct synthesis at 160-200 °C,  $\text{CsPbX}_3$  NCs are formed in the cubic phase.<sup>352</sup> Interestingly, the subsequent anion-exchange manipulations of the halide ions do not seem to affect the cationic sub-lattice, and the cubic perovskite crystal structure is maintained (**Figure 5.1.**) despite the low temperature of the anion-exchange reaction. The size and shape of the parent NCs are also preserved in the course of the anion-exchange (**Figure 5.2.**) The direct synthesis of single- or mixed-halide  $\text{CsPbX}_3$  at such low temperatures yields either exclusively large and polydisperse crystallites of poorly or non-luminescent, wider-bandgap orthorhombic phases or simply no crystalline products at all.  $\text{CsPbI}_3$ , for example, is highly luminescent and red in its three-dimensional cubic phase, yet yellow and non-luminescent upon conversion into its orthorhombic polymorph.<sup>353-356</sup>

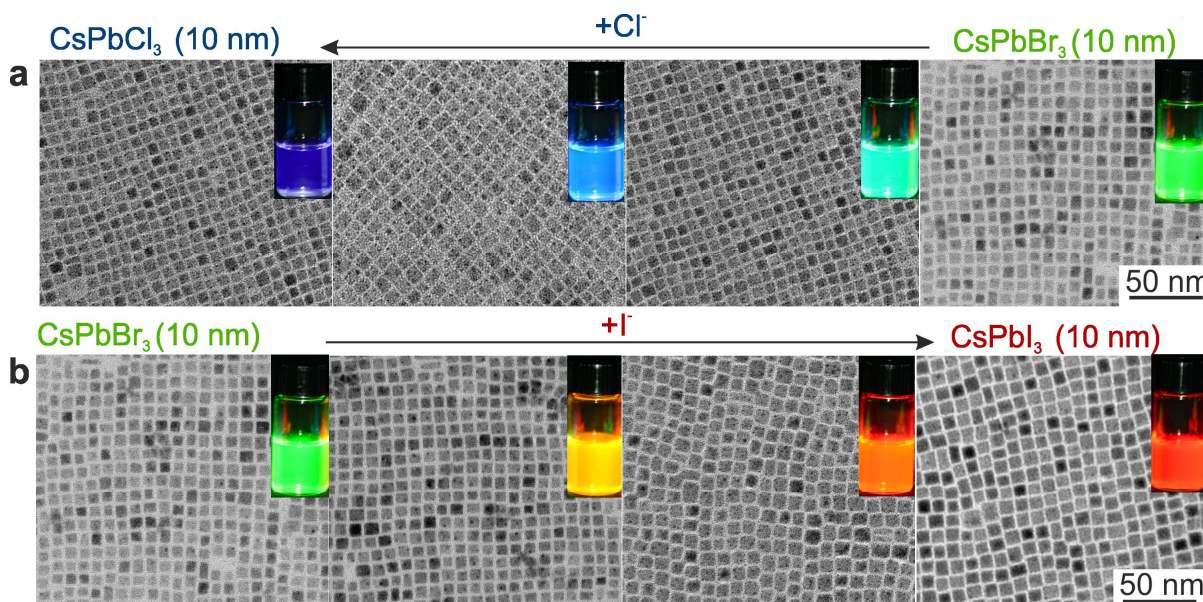


**Figure 5.2.** Transmission electron microscopy (TEM) images of  $\sim 10$  nm  $\text{CsPbX}_3$  NCs after treatment with various quantities of (a) chloride and (b) iodide anions. The insets show the evolution of emission colors (under a UV lamp,  $\lambda = 365$  nm) upon forming mixed-halide  $\text{CsPb}(\text{Br}/\text{Cl})_3$  and  $\text{CsPb}(\text{Br}/\text{I})_3$  to fully exchanged  $\text{CsPbCl}_3$  and  $\text{CsPbI}_3$  NCs.

Along with the cubic crystal structure, bright PL (with quantum yields of 10-80%, the lowest values for  $\text{CsPbCl}_3$ ) is retained in anion-exchanged  $\text{CsPbX}_3$  NCs, with FWHM peak widths ranging from 12 nm for  $\text{CsPbCl}_3$  to 40 nm for  $\text{CsPbI}_3$  (**Figure 5.3**), comparable to directly synthesized  $\text{CsPbX}_3$  NCs.<sup>352</sup> The PL spectra of such exchanged NCs are Stokes-shifted with respect to the optical absorption spectra. As previously reported on the direct synthesis of

mixed-halide NCs,<sup>352</sup> the resulting composition of anion-exchanged NCs follows the overall halide ratio in the system, which is  $[\text{X}]_{\text{parent}}:[\text{X}]_{\text{incoming}}$  for anion-exchange or simply the precursor ratio in direct synthesis. The  $[\text{X}]_{\text{parent}}:[\text{X}]_{\text{incoming}}$  ratio in Cl-to-Br, Br-to-Cl, Br-to-I, and I-to-Br anion-exchanges was varied continuously from 3:1 to 1:3 for three tested halide sources to cover the entire visible spectral region (Table 5.1 and Figure 5.4).

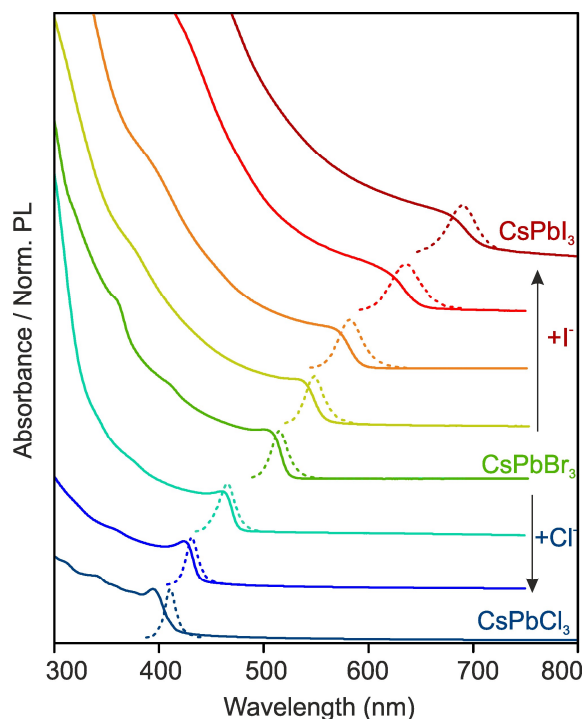


**Figure 5.3.** Evolution of the optical absorption (solid lines) and PL (dashed lines) spectra of  $\text{CsPbBr}_3$  NCs with increasing quantities of  $\text{PbCl}_2$  or  $\text{PbI}_2$  (halide sources).

In general, the distribution of two halide ions between the solution and the crystal is governed by the balance of the crystal energies of the mixed solid-solution and single-halide perovskites on the one side and the solvation energies of halide ions in solution on the other side. The lack of a strong preference towards one of the halides either indicates that the crystal energies are similar for different ions, or that the preferred halide is also preferably solvated, thereby maintaining balance. Eventually, also an entropy of mixing should favor the formation of solid-solutions in the absence of strong enthalpic factors (crystal energy). A different picture is found for I-to-Cl or Cl-to-I exchanges. Treatment of  $\text{CsPbCl}_3$  NCs with a large excess of  $\text{PbI}_2$  (or OAmI and MeMgI) transforms the PL color from blue (410 nm) directly to red (690 nm) in ca. 30-60 s. The rate for backward transition is similar, also lacking any intermediate color. This can be explained by the larger difference in ionic radii between  $\text{Cl}^-$  and  $\text{I}^-$ , leading to the higher stability of the single-halide crystals as compared to the solid-solutions.

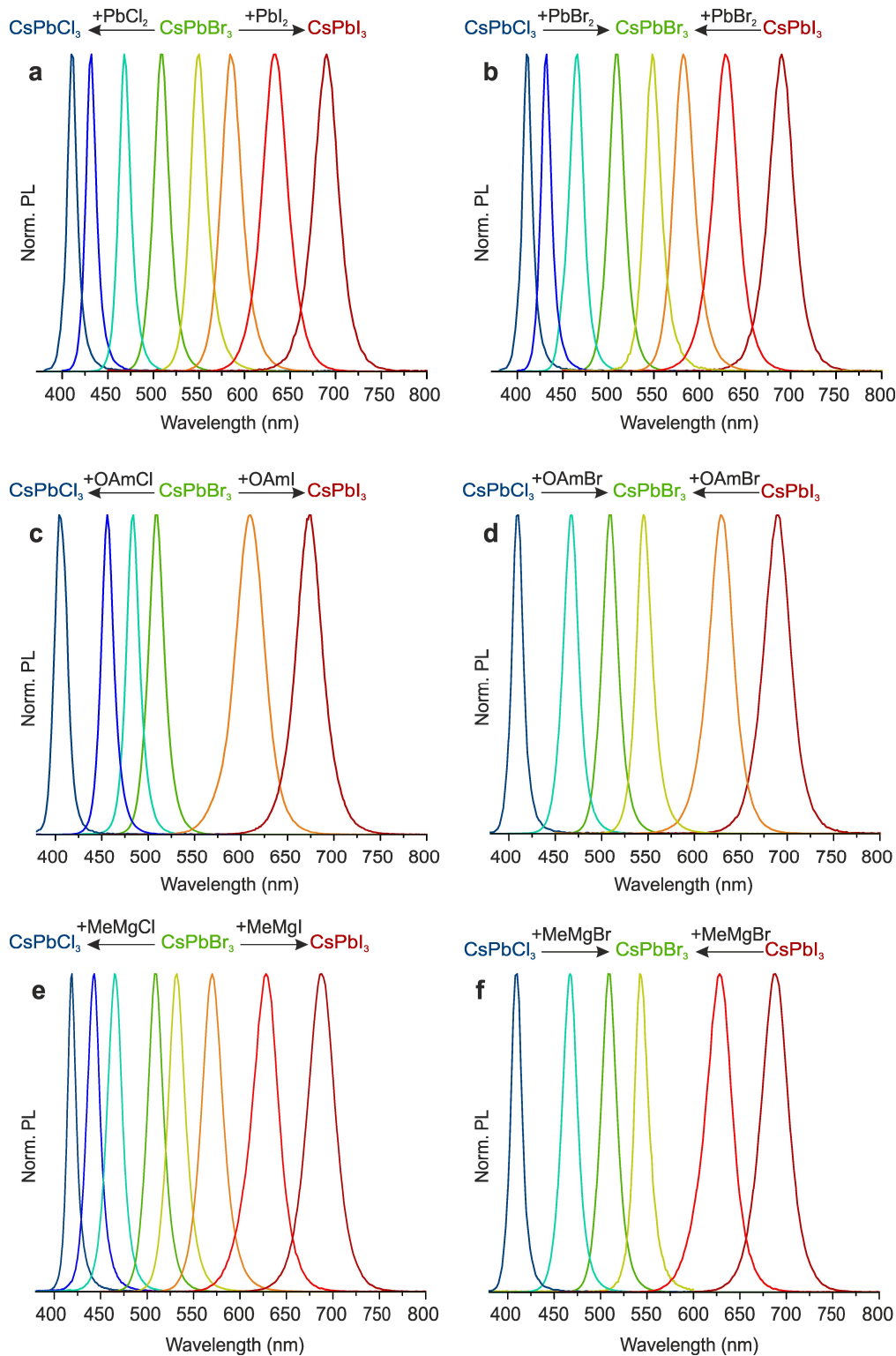


**Figure 5.4.** PL spectra for anion-exchange reactions in  $\text{CsPbX}_3$  NCs using various halide sources. The gradual change in the PL peak wavelengths reflects the ease of halide mixing within the perovskite lattice for Cl/Br and Br/I systems.

The fast anion-exchange in perovskite NCs is rooted in the ionic properties of perovskite metal halide crystals. The high ionic conductivity of halides in bulk CsPbX<sub>3</sub> has been known for 30 years.<sup>360</sup> The primary conduction mechanism is the diffusion of halide vacancies, V<sub>X</sub><sup>\*</sup> (X = Br, Cl), where the activation energy is 0.29 eV for CsPbCl<sub>3</sub> and 0.25 eV for CsPbBr<sub>3</sub>. Recently, methyl ammonium hybrid organic-inorganic perovskite analogues (CH<sub>3</sub>NH<sub>3</sub>PbI<sub>3</sub> and CH<sub>3</sub>NH<sub>3</sub>PbBr<sub>3</sub>) have been the subject of numerous studies due to their unprecedented (for solution-processed absorber materials) photovoltaic power conversion efficiencies of up to 20%.<sup>361-366</sup> Also here understanding the ionics of perovskite halides holds a potential key to explaining a range of important observations such as the hysteresis of current-voltage characteristics<sup>367</sup> or the self-compensating mechanism of electrical conductivity.<sup>368</sup> DFT calculations point to a prevalence of the ionic vs. electronic disorder, with the charged vacancy concentration exceeding 0.4% at room temperature,<sup>368</sup> and electron and hole traps being rather shallow with respect to the hole and conduction bands.<sup>160, 369-370</sup> In an elegant study using specially designed ion-selective galvanic cells, Maier *et al.* have confirmed that, of the three ions in the lattice (CH<sub>3</sub>NH<sub>3</sub><sup>+</sup>, Pb<sup>2+</sup>, and I<sup>-</sup>), only the latter I<sup>-</sup> is responsible for ionic conductivity, via the vacancy diffusion mechanism.<sup>371</sup>

An *in-situ* PL study of the Br-to-I exchange in CsPbBr<sub>3</sub> is presented in **Figure 5.5**. Most of the anion-exchange occurs within the first several seconds. The gradual shift of the PL color is consistent with the continuous formation of homogeneous CsPbBr<sub>x</sub>I<sub>3-x</sub> solid solutions since compositional inhomogeneities or preferred compositions within the NC ensemble would lead to broad or multiple peaks. Importantly, the integrated intensities of the PL spectra of each exchanged sample remain comparable to that of the parent sample, indicating high PL quantum yields throughout the process. In the course of this work, rapid anion-exchange in thin films of hybrid perovskites of CH<sub>3</sub>NH<sub>3</sub>PbX<sub>3</sub> was reported,<sup>260</sup> along with *in-situ* optical measurements. In such 2D extended films, CH<sub>3</sub>NH<sub>3</sub>PbBr<sub>3</sub>-to-CH<sub>3</sub>NH<sub>3</sub>PbI<sub>3</sub> conversion was determined to progress via the formation of iodine-rich domains within the first seconds, with the immediate appearance of red-emission closer to the PL of pure CH<sub>3</sub>NH<sub>3</sub>PbI<sub>3</sub> followed by a slower homogenization of the composition over the entire sample. In accord with our study, CH<sub>3</sub>NH<sub>3</sub>PbCl<sub>3</sub>↔CH<sub>3</sub>NH<sub>3</sub>PbI<sub>3</sub> conversions do not involve solid solutions due to the lattice mismatch between the parent and fully exchanged phases. Another study on the anion-exchange in the films of plate-type CH<sub>3</sub>NH<sub>3</sub>PbX<sub>3</sub> NCs has appeared during the revision of our manuscript,<sup>372</sup> where again Br-Cl and Br-I systems showed tunable solid solutions, while mixed Cl-I systems were not obtained.

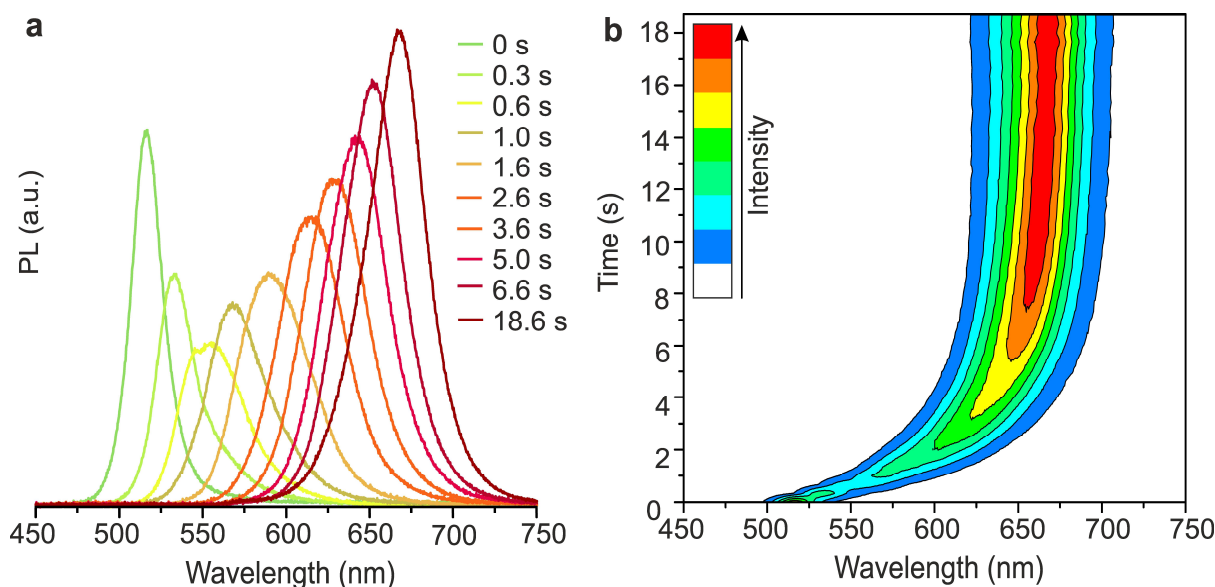


**Figure 5.5.** *In-situ* PL measurements during a  $\text{CsPbBr}_3$  to  $\text{CsPbI}_3$  NC conversion at  $40^\circ\text{C}$  with  $[\text{Br}]_{\text{parent}}:[\text{I}]_{\text{incoming}} = 1:3$ , (a) plotted at specific times during conversion and (b) throughout the complete process (with three spectra acquired per second).

In addition to fast halide motion within the perovskite lattice, the ease of anion-exchange in  $\text{CsPbX}_3$  NCs is in part also due to fast exchange dynamics of the halide ions in solution. Even in the absence of added halide source, the NCs themselves can serve as halide sources for each other (**Figure 5.6a**). For example, the mixing of  $\text{CsPbBr}_3$  and  $\text{CsPbI}_3$  in colloidal solution is followed by fast cross-exchange and homogenization of their compositions, forming  $\text{CsPb}(\text{Br/I})_3$  solid solutions. Shuttling of halide ions between NCs is facilitated by the small concentration of the solvated halide ions in the colloidal dispersion, present as  $\text{OAmX}$  or similar species after the isolation of NCs or due to desorption from the NC surface. Consequently, only one PL peak is measured after the completion of the ionic exchange. The time taken to reach full homogeneity, in this case, is 10-20 minutes, much longer than for direct anion-exchange. Investigations of intermediate stages of this process indicate that exchange occurs simultaneously in both kinds of particles; the  $\text{CsPbBr}_3$  PL peaks shift to longer wavelengths, and the  $\text{CsPbI}_3$  PL moves to shorter wavelengths (**Figure 5.6b** and detailed *in-situ* PL study in **Figure 5.7**). The tunability of the PL peaks, emission linewidths and quantum yields after full homogenization are equivalent to those obtained from direct synthesis or via direct ion-exchange as discussed above.

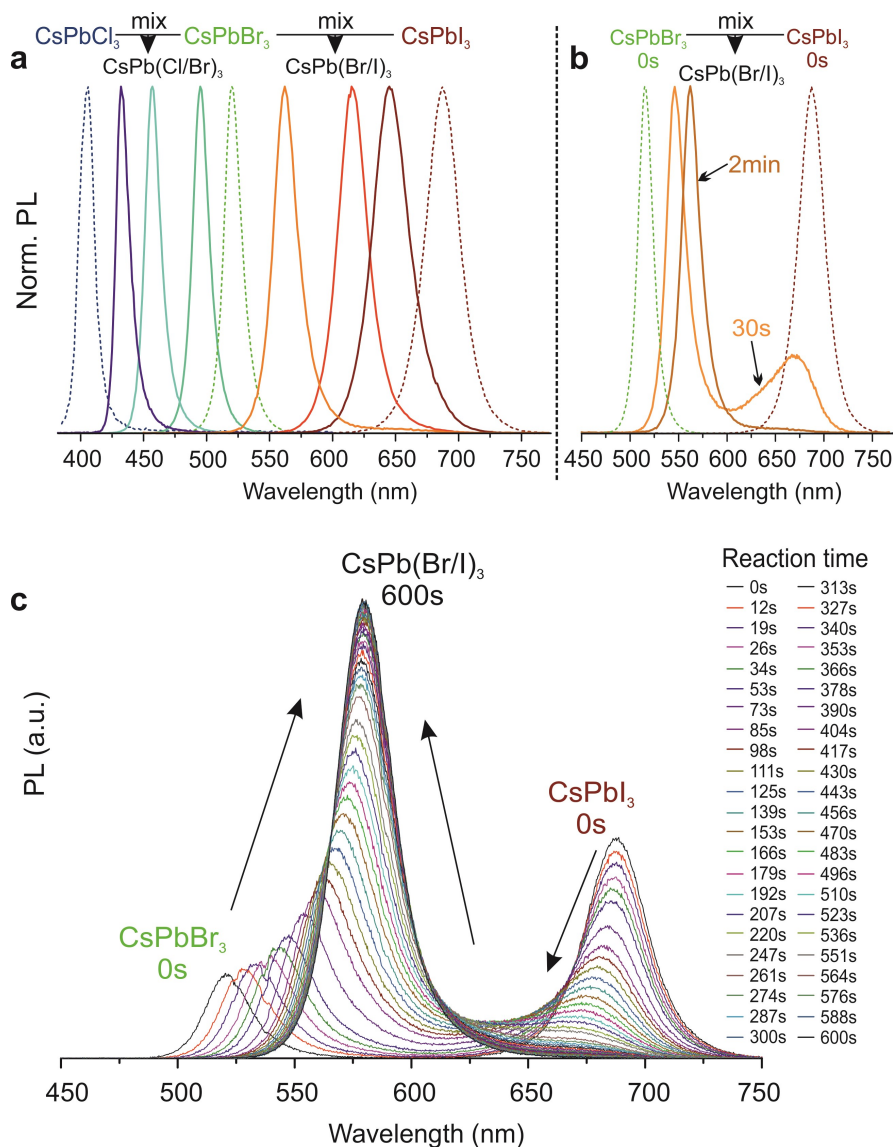


**Figure 5.6.** Inter-NC anion-exchange reactions in  $\text{CsPbX}_3$  NC systems. **(a)** An overview of the PL spectra of samples obtained by mixing  $\text{CsPbBr}_3$  NCs with either  $\text{CsPbCl}_3$  or  $\text{CsPbI}_3$  NCs in various ratios. **(b)** Time-dependent PL spectra showing an intermediate stage formed during inter-NC anion-exchange between  $\text{CsPbBr}_3$  and  $\text{CsPbI}_3$ , in which two distinct NC species co-exist with altered compositions. **(c)** In-situ PL study of the anion-exchange between  $\text{CsPbBr}_3$  and  $\text{CsPbI}_3$  NCs in toluene.

## 5.4. Conclusions

In summary, remarkably fast anion-exchange was observed in perovskite  $\text{CsPbX}_3$  NCs. Overall, the behavior of perovskite halides with respect to anion-exchange is orthogonal to common metal chalcogenide NCs, namely since the cationic sub-lattice is substantially rigid and the singly-charged halide ions are highly mobile. In metal chalcogenides, ion-exchange



has been observed with such ease only for cations. Semiconducting properties of lead halide perovskites are highly defect-tolerant, maintaining bright excitonic emission throughout and upon completion of the anion-exchange. Of practical note, the herein demonstrated fine-tuning of the spectrally narrow and bright PL of anion-exchanged CsPbX<sub>3</sub> NCs over the entire visible spectral region can be conveniently accomplished from numerous halide sources at low temperatures. In addition, fast anion-exchange between CsPbX<sub>3</sub> NCs of different compositions can also be readily achieved. Future investigations of halide-exchange reactions in other nanoscale metal halide systems are clearly warranted, as high ionic conductivity may not be strictly necessary due to the short diffusion paths within the NCs and the low charges of halide ions.

**Reproduced with modifications from:**

Georgian Nedelcu, Loredana Protesescu, Sergii Yakunin, Maryna I. Bodnarchuk, Matthias J. Grotevent, and Maksym V. Kovalenko, *Fast Anion-Exchange in Highly Luminescent Nanocrystals of Cesium Lead Halide Perovskites (CsPbX<sub>3</sub>, X = Cl, Br, I)*, *Nano Lett.* **2015**, *15*, 5635–5640 (<https://pubs.acs.org/doi/abs/10.1021/acs.nanolett.5b02404>).

*Notice to readers: Further permissions related to the material excerpted should be directed to the ACS.*

## Chapter 6. Cesium lead bromide nanoplatelets ( $\text{CsPbBr}_3$ NPLs) with stable emission at 492 nm

### 6.1. Introduction

Entirely inorganic highly monodisperse cesium lead halide colloiddally-stabilized nanocrystals (NCs) with a perovskite crystal structure and cubic shape were recently synthesized by Protesescu *et al.*<sup>373</sup> Due to their outstanding optical properties in emission and absorption, they have recently gained much interest, and a tremendous number of reports emerged in a short period. Their robust synthesis allows precise control of the emission and absorption properties of the NCs through compositional modulations. Moreover, fine-tuning of these properties can be obtained via anion exchange which proved to lead to bright and narrowband photoluminescence (PL) covering the entire visible spectrum while preserving the size and shape of the parent NCs.<sup>64, 300, 374</sup> Despite no surface passivation treatments, high quantum yields of up to 80-90% have been reported, enabling the opportunity for highly-efficient tunable light sources.<sup>64, 300, 373, 375-379</sup> Their ability for single-photon emission at room-temperature and cryogenic temperatures facilitates the usage also for secure quantum cryptography in addition to the optoelectronic applications (light emitting diodes (LEDs), low-threshold lasers).<sup>379-381</sup> With anisotropic nanocrystals, where one length is reduced compared to the others, it is even possible to tune the emission further and absorption properties as it was recently demonstrated for cadmium selenide/cadmium sulfide nanoplatelets (NPLs).<sup>382</sup> Such nanoparticles have shown improved optical properties enabling, for example, the observation of ultrafast energy transfer in the multiexciton regime and the realization of continuous wave (CW) optically-pumped lasing. Pivotal to these observations was the dipolar character excitons experienced in such high-aspect ratio nanoparticles.<sup>383-385</sup>

By varying different parameters (reaction temperature, ligand ratio or using long and short ligands at the same time) in the synthetic protocol, the shape and size of the  $\text{CsPbBr}_3$  nanocubes were varied to zero-dimensional quantum dots (QDs), one-dimensional nanowires (NWs) and two-dimensional NPLs and nanosheets (NSs).<sup>197, 386-391</sup> As already remarked by

Ravi *et al.*, all these new morphologies suffer from a stability point of view disabling any further processing for device applications.<sup>392</sup> More importantly, in almost all the cases, the final product consists of a mixture of at least two different morphologies or different thicknesses of the NPLs.<sup>197, 392-393</sup> Because of the poor stability and difficulty to process these newly shaped  $\text{CsPbBr}_3$  nanomaterials, no attempts were reported regarding their use in devices.

Organic-inorganic lead halide perovskites were reported as well in the form of NWs, nanorods (NRs), NPLs and NSs. They were obtained either by the classical method of incorporating one of the precursors in a porous scaffold (nanoporous titania, mesoporous silica, fluorine-doped tin oxide, self-organized conducting polymers, and much more) or by expensive vapor methods such as chemical vapor deposition, van der Waals epitaxy and so on.<sup>393-404</sup> The results consisted of different architectures in the form of a deposited film. Colloidally-capped organic-inorganic NPLs were reported as well, either as a mixture of NPLs with different thickness or only one thickness characterized by poor stability.<sup>405-407</sup>

Here, it is reported the synthesis of highly stable (more than two years) and monodisperse  $\text{CsPbBr}_3$  NPLs with a thickness of  $\sim 4\frac{1}{2}$  perovskite unit cells and characteristic emission in blue spectral regime (492 nm). High quantum yields (QY) up to 75% are retained in deposited films, a prerequisite for efficient light emitting devices employing NPLs as the active medium. While preserving the particular size and shape of the NPLs, the emission and absorption spectra can be tuned from 492 nm to 398 nm in the blue region and 632 nm in the red region via fast anion exchange at room temperature in air. Besides the synthesis of these new blue-emitting  $\text{CsPbBr}_3$  NPLs, a comprehensive optical characterization, and for the first time, a blue LED containing  $\text{CsPbBr}_3$  perovskite NPLs as an emissive layer are reported. Ultrafast spectroscopy (transient absorption and time-resolved PL) unveiled the exciton dynamics with the specific Auger relaxation time and exciton radiative decay. Single NPL spectroscopy performed at cryogenic and RT attest single NPLs emit a stream of single photons, making them a good candidate for single photon LEDs. For the first time, a light emitting diode architecture having blue-emissive (492 nm)  $\text{CsPbBr}_3$  NPLs as the emissive layer was realized. The preliminary results have shown a maximum luminance of  $22.1 \text{ cd m}^{-2}$  and high external quantum efficiency (EQE) of 0.19%.

## 6.2. Experimental section

**Materials and chemicals.** Cesium carbonate ( $\text{Cs}_2\text{CO}_3$ , Aldrich, 99.9%), Oleic Acid (OA, Sigma-Aldrich, 90%), 1-octadecene (ODE, Sigma-Aldrich, 90%), oleylamine (OAm, Acros Organics, 80-90%), lead bromide ( $\text{PbBr}_2$ , ABCR, 98%), mesitylene (Aldrich, 97%), diphenyl (Dowtherm@A, eutectic mixture of 26.5% diphenyl + 73.5% diphenyl oxide, Aldrich), ethanol (EtOH, Aldrich,  $\geq 99.8\%$  (GC)), hydrochloric acid (HCl, Aldrich,  $\geq 37\%$ ), hydroiodic acid (HI, Aldrich, 57%), toluene (Fischer Scientific, HPLC grade), hexane (Sigma-Aldrich,  $\geq 95\%$ ), poly(methyl methacrylate). The indium tin oxide (ITO) coated glass substrates with a sheet resistance of  $15 \Omega/\square$  were purchased from Lumtech Corp. The hole injection material poly(3,4-ethylene-dioxythiophene)-poly(styrene sulfonate) (PEDOT: PSS) was purchased from Heraeus (Clevios P VPCH 8000). High quality 99.95% pure sublimed grade hole transporting material poly[*N,N'*-bis(4-butylphenyl)-*N,N'*-bis(phenyl)-benzidine] (Poly-TPD) and electron transporting material 2,2',2''-(1,3,5-benzinetriyl)-*tris*(1-phenyl-1-*H*-benzimidazole) (TPBi) was purchased from Lumtech Corp. and e-Ray Optoelectronic, respectively. The electron injection material lithium fluoride (LiF) with a purity of 99.98% was purchased from Acros Organics. Aluminum (Al) pellets (99.999%) were purchased from Kurt J. Lesker Co. Ltd. All the materials were used without any further purification.

**Preparation of Cs-oleate.**  $\text{Cs}_2\text{CO}_3$  (0.4075 g, Aldrich, 99.9%), OA (1.25 mL, Sigma-Aldrich, 90%) and ODE (20 mL, Sigma-Aldrich, 90%) were added into a 50 mL 3-neck flask, dried for 1h at 120 °C. Since Cs-oleate precipitates out of ODE at room-temperature, it must be preheated to 100 °C before injection.

**Preparation of oleylammonium halides (OAmX).** Ethanol (100 mL, Aldrich) and OAm (0.038 mol, Acros Organics 80-90%) were combined in a 250 mL 2-neck flask and vigorously stirred. The reaction mixture was cooled in an ice-water bath and HX (0.076 mol, HCl  $\geq 37\%$ , Aldrich; HI 57%, Aldrich) was added. The reaction mixture was left to react overnight under  $\text{N}_2$  flow. Then the solvent was evaporated under vacuum, and the obtained product was purified by rinsing multiple times with diethyl ether. The product was left under vacuum overnight in a vacuum oven at 80 °C resulting in a white powder.

**Synthesis of  $\text{CsPbX}_3$  NPLs.** 138 mg  $\text{PbBr}_2$ , 1 mL dried OA, and 1 mL dried OAm were loaded into a 25 mL 3-neck flask in the glovebox. Mesitylene (5 mL) was added to the reaction mixture, and the flask was connected to the Schlenk line. The entire system was

flushed three times at room temperature by quickly changing from vacuum to N<sub>2</sub>, and left on N<sub>2</sub>. The reaction mixture was heated up to 130 °C, and Cs-oleate (0.8 mL of a stock solution prepared as described above) was swiftly injected. In the next second from the injection, the flask is immersed in a water-ice bath to stop the reaction. After the reaction, 1 mL of crude solution was centrifuged for 3 minutes at 5000 rpm. The resulted precipitate was dispersed in 1 mL toluene, centrifuged again for 10 minutes at a maximum speed of centrifuge (13400 rpm) and after this, the supernatant was filtrated and used further for different experiments. The typical concentration of the 492 nm emissive NPLs was about 8-10 mg/mL.

**Anion-exchange reactions (Table 6.1).** The anion exchange reactions were conducted in air at room temperature and are summarized in **Table 6.1**. 0.2 mL CsPbBr<sub>3</sub> NPLs in toluene (5 mg/mL) were added in a vial and different volumes of a solution of OAmX (X = Cl, I) 1.5 mM in toluene was added to obtain different mixed halide compositions with PL emission at different wavelengths.

**Table 6.1.** Summary of anion exchange reactions.

CsPbBr <sub>3</sub> NPLs (5 mg/mL in toluene)	OAmCl 1.5 mM (mL)	OAmI 1.5 mM (mL)	PL emission (nm)	FWHM (nm)
0.2 mL	3.7	-	398	12.37
0.2 mL	3.1	-	406	14.02
0.2 mL	2.5	-	416	14.85
0.2 mL	1.5	-	430	15.97
0.2 mL	0.7	-	452	16.37
0.2 mL	0.3	-	472	17.71
0.2 mL	-	-	492	18.33
0.2 mL	-	0.1	515	22.13
0.2 mL	-	0.35	550	24.71
0.2 mL	-	0.6	575	27.9
0.2 mL	-	0.85	600	31.87
0.2 mL	-	1.6	632	32.78

**Device fabrication.** Firstly, patterned ITO-coated glass substrates were rinsed with Extran MA02 neutral detergent and deionized (DI) water mixture (1:3). Subsequently, substrates were sonicated in DI water, acetone, and isopropanol, respectively, each for 10

minutes. Then the substrates were treated with oxygen plasma for 10 min. The aqueous solution of PEDOT: PSS was spin-coated on the pre-cleaned ITO glass at a speed of 4000 rpm for 20 s and then annealed at 125 °C for 20 min in the ambient conditions. All the annealed substrates were transferred into a nitrogen atmosphere glove box for the deposition of successive layers. A Poly-TPD solution (2 mg ml<sup>-1</sup> in chlorobenzene) was then spin-coated at 3000 rpm for 20 s. Subsequently, the colloidal suspension of  $\text{CsPbBr}_3$  NPLs (in toluene) was spin-coated at 2500 rpm for 20 s under a nitrogen atmosphere. Then the ETL was deposited by the sequential thermal evaporation of TPBi in a vacuum chamber at  $7.5 \times 10^{-8}$  Torr. Finally, a 1 nm LiF electron injection layer and a 100 nm Al cathode layer were also deposited in a high vacuum chamber using a shadow mask. The active area of LED was 37.5 mm<sup>2</sup>. Before measurement, all the devices were stored in the glove box and tested in the ambient atmosphere without encapsulation.

**Absorbance measurements.** UV-VIS absorption spectra were collected using a Jasco V670 spectrometer in transmission mode.

**Photoluminescence (PL), photoluminescence excitation (PLE).** Fluorolog iHR 320 Horiba Jobin Yvon spectrofluorimeter equipped with a PMT detector was used to acquire steady-state PL spectra from solutions and films.

**PL quantum yields (QYs) in films.** The absolute value of the PL QY was measured at room temperature on a Quantaurus QY (C11347-11, Hamamatsu) equipped with an integrated sphere.

**Time-resolved photoluminescence (TR PL) spectroscopy.** PL lifetime measurements were performed using a time-correlated single photon counting (TCSPC) setup, equipped with SPC-130-EM counting module (Becker & Hickl GmbH) and an IDQ-ID-100-20-ULN avalanche photodiode (Quantique) for recording the decay traces. The emission of the perovskite NCs was excited by a BDL-488-SMN laser (Becker & Hickl) with a pulse duration of 50 ps and a wavelength of 488 nm, CW power equivalent of ~0.5 mW, externally triggered at a 1 MHz repetition rate or with 10 ps pulses of frequency-tripled (355 nm) irradiation of a Duetto laser (Time-Bandwidth) triggered at 200 kHz. The intensity of the pumping laser beam was varied over two orders of magnitude by a neutral density optical attenuator (NDC-100C-2M, Thorlabs). PL emission from the samples passed through a long-pass optical filter with an

edge at 500 nm in order to reject the excitation laser line. The PL emission was attenuated with optical density filters in order to prevent the avalanche detector from saturation effects.

**Powder X-ray diffraction (XRD) patterns** were collected with an STOE STADI P powder diffractometer, operating in transmission mode. A germanium monochromator, Cu  $K\alpha_1$  irradiation, and Dectris Mythen silicon strip detector were used.

**Transmission electron microscopy (TEM)** images were recorded using a Philips CM 12 and Hitachi HT7700 EXALENS microscope operated at 100 kV (low-resolution TEM) and a JEOL JEM-2200FS microscope operated at 200 kV (high-resolution TEM).

**Micro-photoluminescence measurements on single NPL.** All single NPL PL measurements were performed on samples mounted inside a liquid helium flow cryostat (CryoVac) at 5 Kelvin on a micro-photoluminescence setup with a fiber-coupled pulsed excitation laser at a wavelength of  $\lambda = 405$  nm and a repetition rate of 40 MHz. For focusing (excitation and detection), a 100x microscope objective (Mitutoyo Plan Apo NIR HR) was utilized, with a resulting spot size  $1/e^2$ -radius of 1.4  $\mu\text{m}$ . The PL emission was dispersed by either an 1800 lines/mm or an 300 lines/mm grating, respectively in a monochromator with an optical length of 0.75 m and detected by a back-illuminated cooled EMCCD camera (Princeton Instruments ProEM). For lifetime and photon-correlation measurements, a time-correlated single photon counting system was used (PicoQuant PicoHarp 300 with PDM, MPD avalanche photodiodes with a nominal time resolution of 30 ps).

**Device measurement.** The electroluminescence (EL) spectrum and current density-voltage-luminance ( $J$ - $V$ - $L$ ) characteristics of the perovskite LED were measured by using a Photo Research Spectrascan PR 655 spectrometer and a Keithley 2400 source meter. All the measurements were performed under the atmospheric conditions. The emission area of the devices was 15  $\text{mm}^2$ , and only a luminance in the forward direction was measured. The EQE was calculated from current density, luminance, and EL spectrum by assuming a Lambertian-like pattern due to the surface light source.

### 6.3. Results and discussion

The  $\text{CsPbBr}_3$  NPLs were synthesized via a low-temperature injection reaction. By some specific modifications of the synthesis reported by Protesescu *et al.*, the typical highly

monodisperse colloidally stabilized nanocubes were converted into highly monodisperse self-assembled superstructures of colloidally stable nanoplatelets of  $\text{CsPbBr}_3$  perovskite with a rectangular shape. As described in **Figure 6.1a**, the synthesis of  $\text{CsPbBr}_3$  NPLs has simple underlying chemistry based on the swift metathesis reaction between very much inexpensive and commercially available  $\text{PbBr}_2$  and  $\text{Cs}_2\text{CO}_3$ . The  $\text{CsPbBr}_3$  NPLs are formed in less than 3 seconds due to the fast nucleation and growth kinetics.  $\text{PbBr}_2$  along with dried oleic acid (OA) and dried oleylamine (OAm) were loaded in a three-neck flask in the glovebox and transferred to the schlenk line. Mesitylene was added to the reaction mixture, and the entire system was flushed at room temperature with  $\text{N}_2$  three times by quickly switching between vacuum and  $\text{N}_2$  flow. The reaction mixture was heated up to 130 °C under  $\text{N}_2$  atmosphere, and Cs-oleate was swiftly injected (see **Experimental Section** for detailed procedure). Rectangular-shaped  $\text{CsPbBr}_3$  NPLs (**Figure 6.1b**) formed in less than 3 seconds, and the reaction was stopped by cooling down the reaction mixture with a water-ice bath. The bright blue-emitting material was easily separated from the reaction mixture by centrifugation. The precipitate is further dispersed in toluene, and highly monodisperse self-assembled superstructures can be obtained, as is presented in the transmission electron microscopy (TEM) images in **Figures 6.1c** and **6.1e**. Similar quality of the material was obtained when 1-octadecene or Dowtherm@A were used as solvents. As can be observed in **Figure 6.1c**, the  $\text{CsPbBr}_3$  NPLs expose two possible arrangements: “flat” side up, when the NPLs are forming a single layer exposing the two long sides; and in stacking, when one of the longest sides is exposed along with the shortest side, the last one describing the thickness of the NPLs. Lateral dimensions of 12 – 14 nm along one side and 10 – 11 nm along the second-long edge can be identified when the “flat” side is exposed. Short dimensions of ~3.8 nm can be observed when the stacking arrangement is exposed (**Figure 6.1e**). These NPLs exhibit a bright blue emission under UV light ( $\lambda = 366$  nm), as shown in **Figure 6.1d**, having a sharp absorption peak at 482 nm and narrow PL peak at 492 nm with a full width at half maximum (FWHM) about 18 nm (**Figure 6.1f**). A small Stokes shift of 10 nm can be identified between the absorption edge and the emission peak maximum this being consistent with direct exciton recombination.



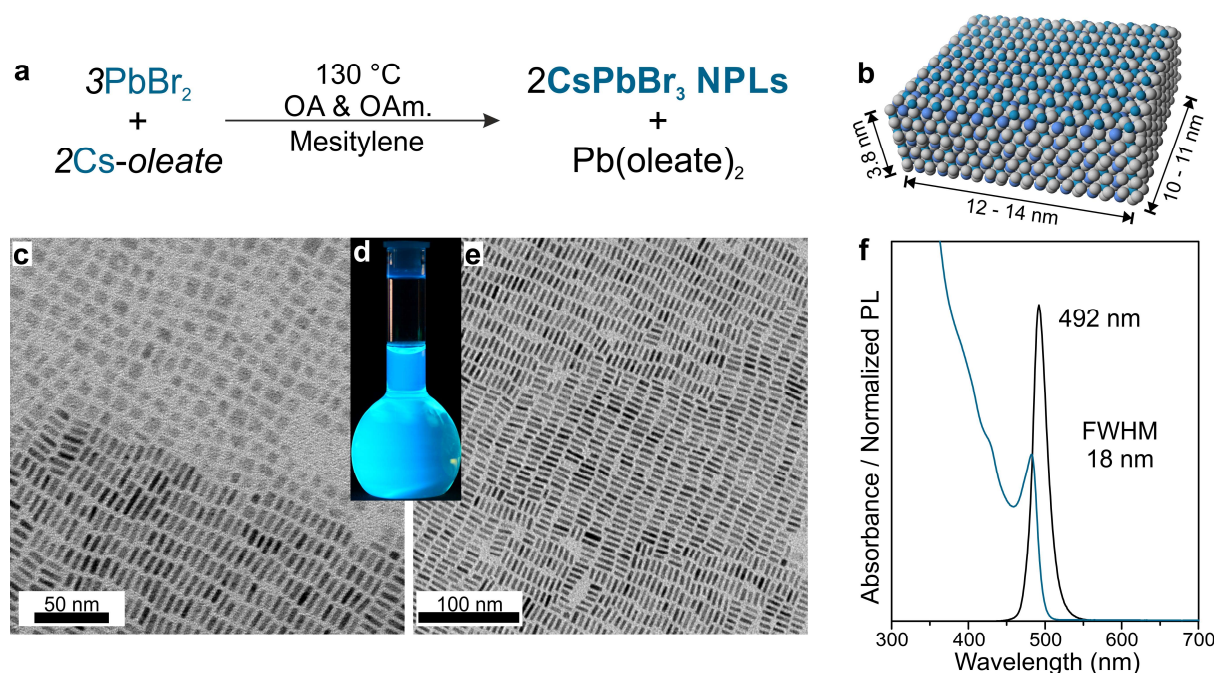


**Figure 6.1.** (a) Reaction scheme for the formation of  $\text{CsPbBr}_3$  NPLs at 130 °C in Mesitylene in the presence of OA and OAm.; (b) Representation of a typical 3D NPL; (c) Low-resolution TEM micrograph of  $\text{CsPbBr}_3$  NPLs arranged in stacking and with the “flat” side up; (d) Photograph of  $\text{CsPbBr}_3$  NPLs solution in toluene (under a UV lamp,  $\lambda = 365$  nm) showing the bright blue-cyan emission; (e) Low-resolution TEM micrograph of  $\text{CsPbBr}_3$  NPLs displaying an arrangement in stacking exposing their uniform thickness; (f) Typical absorbance and PL spectra of  $\text{CsPbBr}_3$  NPLs with a characteristic emission at 492 nm.

The NPLs obtained by our method have high stability preserving their features for more than 21 months. As can be observed in **Figures 6.2a** and **6.2b**, the absorbance, and PL spectra of 11 months aged and 21 months aged, respectively, are unchanged. Also, the morphology of the NPLs was preserved in time as can be observed in **Figures 6.2c** and **6.2d**. The QY of the NPLs embedded in polymer films was re-checked as well and was found to be around 41% for the 11 months aged, and around 28% for the 21 months aged NPLs, respectively. A certain instability towards the formation of traces of yellowish precipitate was observed and identified as being the insulating  $\text{Cs}_4\text{PbBr}_6$  phase, as witnessed by other authors.<sup>206, 408</sup> The quantification of this phase, possessing a well distinguishable structure with respect to LHPs, was carefully performed by monitoring both  $\text{CsPbBr}_3$  colloidal solutions and films upon aging with conventional XRD characterization (**Figures 6.2e** and **6.2f**): the impurity amount remains very low if the LHPs are stored as colloidal suspensions (ca. 5% w/w), and slightly increases after deposition in a film (up to a max 11% w/w, measured after 15 days and ca. 1 month later).

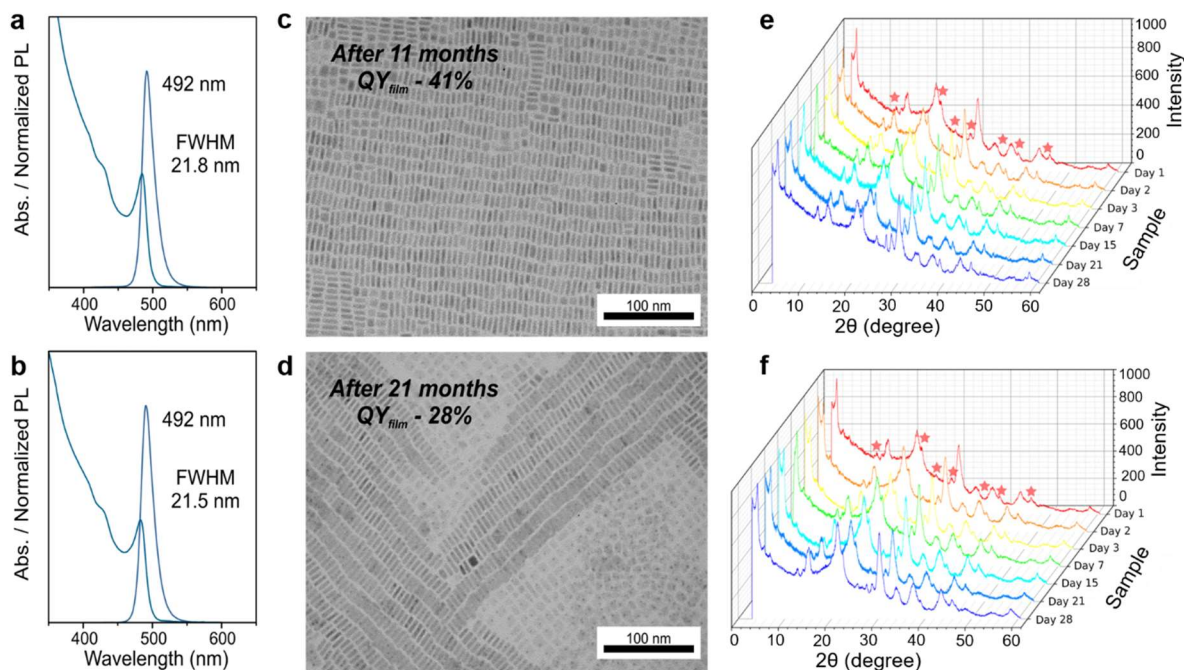


**Figure 6.2.** Absorbance and PL spectra of  $\text{CsPbBr}_3$  NPLs aged for 11 months (a) and 21 months (b), respectively, showing the preservation of the absorbance and PL peak position in time; Low-resolution TEM micrographs of the aged  $\text{CsPbBr}_3$  NPLs proving the conservation of the morphology after (c) 11 months and (d) 21 months. Monitoring the time evolution of  $\text{Cs}_4\text{PbBr}_6$  (impurity phase) with laboratory X-ray diffraction (XRD) data of (e) a  $\text{CsPbBr}_3$  NPLs film deposited immediately after synthesis and (f)  $\text{CsPbBr}_3$  NPLs films deposited each time just before the measurement from the same solution. The peaks of  $\text{Cs}_4\text{PbBr}_6$  are highlighted by red stars. As shown in (e), after  $\text{CsPbBr}_3$  deposition the impurity amount increases from 5% w/w (day 1) up to 11% w/w (day 15), and it appears to be stable from then on. On the other hand, the solution in (f) shows approximately the same amount of  $\text{Cs}_4\text{PbBr}_6$  after each deposition, suggesting that the  $\text{CsPbBr}_3$  NPLs suspensions are quite stable in their colloidal state.

Moreover, with this protocol, by lowering the injection temperature, the absorption and PL emission band edge can be gradually blue shifted. By injecting the Cs-oleate precursor at 120 °C, 110 °C, 100 °C, or 90 °C, emission peaks at 488, 474, 461, and 449 nm, respectively, are obtained as presented in **Figure 6.3**. These deeper-blue emissions correspond to thinner nanoplatelets and are described by Bekestein *et al.* as having 5, 4, 3, and two perovskite unit cell with cubic symmetry.<sup>197</sup>

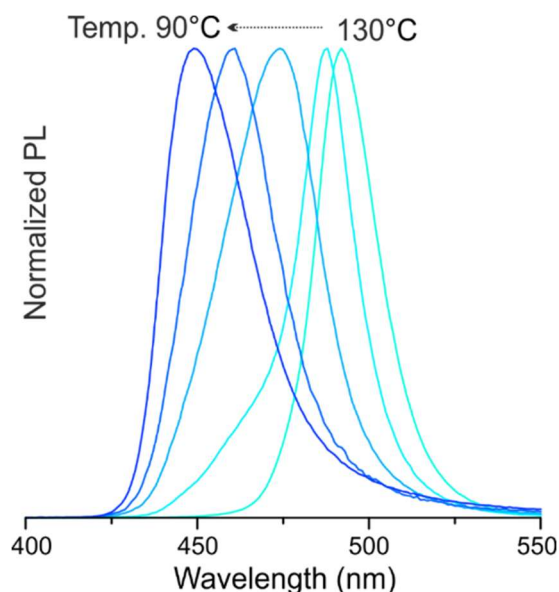


**Figure 6.3.** Normalized PL spectra of  $\text{CsPbBr}_3$  NPLs with emission at 492, 488, 474, 461 and 449 obtained by injecting Cs-oleate at 130, 120, 110, 100 and 90 °C (from right to left)

The 488 nm, 474 nm, 461 nm, and 449 nm emissive NPLs proved to be impossible to purify and isolate from the crude solution without affecting their integrity. Different strategies (solvent/antisolvent couples, centrifugation speeds, etc.) for separation and purification were tested. Each time, multiple red-shifted emission peaks, most likely due to the rapid merging of the NPLs, could be observed. Since the lower wavelength emissive NPLs proved to be challenging to process and stable for a short time just in crude solution after synthesis, the study focused only on the new synthesized 492 nm emissive  $\text{CsPbBr}_3$  NPLs.

Instead of tuning the emission energy via quantum size effect, fast anion exchange reactions performed by using the 492 nm emissive  $\text{CsPbBr}_3$  NPLs as parent-emitters, enabled the coverage of a broad spectral range from 398 nm to 632 nm (**Table 6.1** and **Figure 6.4**). The anion exchange experiments were conducted in air at room temperature without any special precautions (for the detailed procedure see **Experimental Section**).

Assuming that NPLs are colloiddally stabilized with oleylammonium oleate and oleylammonium bromide, as reported for  $\text{CsPbBr}_3$  NCs by De Roo *et al.*,<sup>409</sup> oleylammonium chloride (OAmCl) and oleylammonium iodide (OAmI) were selected as halide sources for anion exchange reactions in order to not affect the stabilization of the NPLs. In **Table 6.1** are presented the results of the anion exchange reactions with OAmCl and OAmI. As can be observed in **Figure 6.4**, the PL peak position is gradually blue or redshifted, with respect to the 492 nm PL emission of the parent  $\text{CsPbBr}_3$  NPLs, maintaining a narrow FWHM.

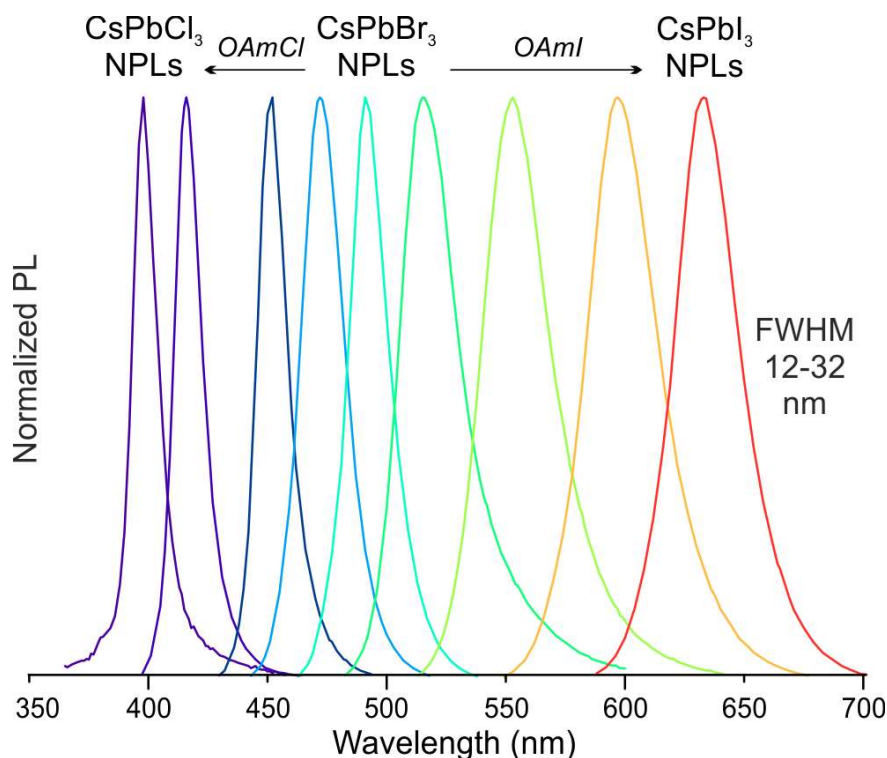


**Figure 6.4.** Normalized PL spectra for anion-exchange reactions in  $\text{CsPbBr}_3$  NPLs ( $PL = 492$  nm) using various halide sources. The tunability of the PL peak can be easily achieved over the entire UV-VIS spectral region by modulating the ratio between the parent NPLs and the halide source.

As observed in our previous work,<sup>64</sup> a trend in variation of the FWHM value is present as in the case of nanocubes. The FWHM values are decreasing from 18 nm (97.16 meV, for the parent-NPLs) to 12 nm (93.5 meV), for the chloride-enriched compositions, and increasing from 18 nm to 32 nm (95.53 meV) for the maximum red emission obtained for the iodide-enriched compositions. By modulating the ratio between the parent-NPLs and the  $\text{OAmX}$  ( $X = \text{Cl}, \text{I}$ ), mixed  $\text{CsPb}(\text{ClBr})_3$  or  $\text{CsPb}(\text{BrI})_3$  compositions can be obtained, as well as  $\text{CsPbCl}_3$  and  $\text{CsPbI}_3$  NPLs. As expected from previous experience, the size, shape, and the special self-assembled arrangement of the NPLs are preserved after the anion exchange process as can be seen in **Figure 6.5**. This has indeed enabled broad range tunability of emission energy in high aspect/ratio NPLs, which are robust against the washing procedures used for further encapsulation in devices.

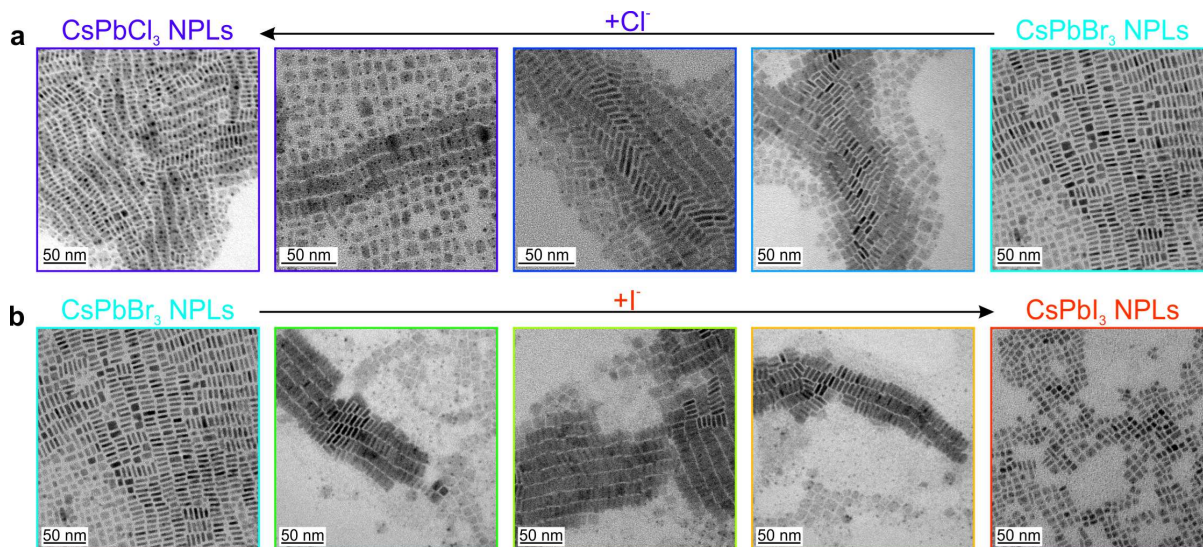


**Figure 6.5.** Transmission electron microscopy (TEM) images of  $\text{CsPbX}_3$  NPLs after treatment with different amounts of (a) chloride and (b) iodide anions showing the size and shape preservation upon forming mixed-halide  $\text{CsPbBr}_{3-x}\text{Cl}_x$  and  $\text{CsPbBr}_{3-x}\text{I}_x$ , to fully exchanged  $\text{CsPbCl}_3$  and  $\text{CsPbI}_3$  NPLs.

**Figure 6.6** presents low and high angle region X-ray diffraction (XRD) patterns (a and b) typical for the  $\text{CsPbBr}_3$  NPLs. In **Figure 6.6a**, a first diffraction peak at  $2\theta = 1.36$  degrees is identified. This reflection corresponds to an interlayer  $d$  – spacing of 64.79 Å, coming from the self-assembled superstructure of the NPLs, and it is matching with the thickness of one NPL stabilized by a ligand shell in the value of  $\sim 6.5$  nm, as it is shown in **Figure 6.6c**. The next peak in the lower angle region XRD is at  $2\theta = 2.75$  degrees, corresponding to a  $d$  – spacing of 32.11 Å, being nearly half of the first XRD peak. The third peak in the lower angle region XRD from  $2\theta = 4.13$  degree is identical with the first peak from the high angle region XRD pattern (due of the  $2\theta$  overlapping range of the measurements), showing a  $d$  – spacing of 21.36 Å corresponding to  $\frac{1}{3}$  from the value of the self-assembled superstructure. The XRD peaks corresponding to the stacking of the NPLs are dropping gradually in intensity, and they are precisely positioned in the XRD pattern in the range  $2\theta = 1.36 - 15$  degree. This family of diffraction peaks demonstrates the long-range ordering of the NPLs being also a consequence of the relatively high electron density of the NPLs.

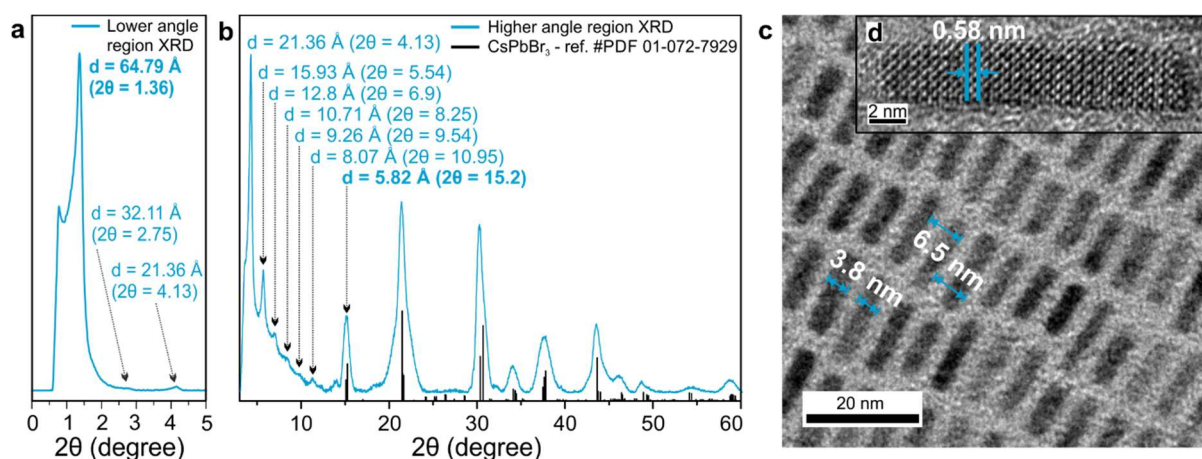


**Figure 6.6.** (a) Low angle region powder X-ray diffraction pattern of  $\text{CsPbBr}_3$  NPLs displaying a first peak at  $d = 64.79 \text{ \AA}$  ( $2\theta = 1.36$ ) corresponding to the thickness of the NPL (3.8 nm) surrounded by a shell of organic ligands; (b) High angle region powder X-ray diffraction pattern of  $\text{CsPbBr}_3$  NPLs showing the diffraction peaks corresponding to the stacking of the NPLs (3 – 15 degree) and the typical diffraction peaks matching to the orthorhombic perovskite crystal structure (ref. JCPDF #01-072-7929); (c) Low-resolution TEM micrograph showing stacked NPLs exposing a thickness of  $\sim 6.5 \text{ nm}$  (NPL + ligand shell) corresponding with the first diffraction peak ( $d = 64.79 \text{ \AA}$ ); (d) High-resolution TEM micrograph presenting an interplanar distance of  $0.58 \text{ nm}$  corresponding to the cell parameters.

According to Bekenstein *et al.*, these new NPLs with emission at 492 nm should consist of 6 perovskite unit cells and a cubic symmetry.<sup>197</sup> By correlating the thickness of the NPLs obtained from TEM images and XRD data with the value of the cubic perovskite unit cell, a value of  $\sim 6\frac{1}{2}$  perovskite unit cell is obtained for the 492 nm emissive NPLs, which would be consistent with most of the previous reports. Recently, it was reported that  $\text{CsPbBr}_3$  NCs and also NSs exhibit orthorhombic crystal structure.<sup>388, 390, 410</sup> More recently, was identified by Bertolotti *et al.* that the crystal structure of  $\text{CsPbX}_3$  NCs consists of subdomains with different symmetry.<sup>411</sup> By standard XRD measurements, the average crystal symmetry was identified to be predominantly orthorhombic, consistent with the orthorhombic phase (reference pattern: JCPDF #01-072-7929), as can be observed in **Figure 6.6b**. This means that they contain about  $4\frac{1}{2}$  perovskite unit cells. In the high angle region XRD pattern of the 492 nm emissive NPLs (**Figure 6.6b**), the peaks at  $2\theta = 15.1, 21.5, 30.4, 34.2,$  and  $37.6^\circ$  correspond to the reflections from  $\{001\}, \{110\}, \{002\}, \{210\}$  and  $\{211\}$  planes of  $\text{CsPbBr}_3$  orthorhombic phase which is also consistent with JCPDF #01-072-7929.<sup>388</sup> **Figure 6.6d** depicts a high-resolution TEM image of  $\text{CsPbBr}_3$  NPLs, from side-view, confirming their high crystallinity. From the side

view of the NPLs interplanar distances of 5.8 Å, between the {001} planes was easily identified.

### 6.3.1. Optical characterization

In order to retrieve a comprehensive picture of the underlying optical properties of these newly synthesized NPLs, ultrafast spectroscopy and single dot spectroscopy at either cryogenic temperature and RT were performed. Investigation of the time-resolved PL dynamics for NPLs emitting at 492 nm, as shown in **Figure 6.7a**, reveals a short fluorescence lifetime, with a typical decay time of 3.5 ns. It can be seen how short this lifetime is when compared to perovskite materials such as  $\text{MAPbBr}_{3-x}\text{Cl}_x$  ( $x = 1.2 - 1$ ), which has decay lifetimes between 116 and 172 ns.<sup>412</sup> The lifetime found for the 492 nm NPLs produced here are comparable to PL lifetimes found by Akkerman *et al.* for thin (5 monolayers thick)  $\text{CsPbBr}_3$  NPLs synthesized via a room-temperature growth scheme that utilizes acetone to initiate nucleation.<sup>413</sup> Such short radiative lifetime could be related to the diminished dielectric screening or an enhanced electron-hole Coulomb interaction in NPLs.<sup>414</sup>

Ultrafast TA spectroscopy maps, shown in **Figure 6.7b**, allow for the investigation of essential processes and their characteristic time constants involved in the absorption of light. The relevant constants that are being analyzed here are intraband relaxation lifetime, Auger recombination lifetime, and absorption cross-section. By finding the dynamics of the bleach, the intense negative signal found here around 481 nm, at many different powers, each of these photophysical constants can be determined. The intraband relaxation lifetime, which is the lifetime of the electron relaxing from the state in the conduction band to which the electron was initially excited to the conduction band edge, is derived from an exponential fit of the initial rise of the bleach signal, shown for  $\text{CsPbBr}_3$  NPLs at low power in **Figure 6.7c**.  $\text{CsPbBr}_3$  NPLs with emission at 492 nm show a very short lifetime, with typical relaxation lifetime of  $188.2 \pm 13.3$  fs.  $\text{CsPbBr}_3$  QDs, which have higher degrees of quantum confinement compared to NPLs, exhibited an intraband relaxation lifetime of 320 fs, for comparison.<sup>415</sup> The faster intraband relaxation lifetime of the NPLs indicates a high efficiency in the relaxation of the electron through the conduction band, which could be related to the coupling of the higher energy state in the conduction band to phonon states, a typical process for intraband relaxation.<sup>416</sup> This greater efficiency follows from the higher density of states in the nanoplatelets.<sup>417-418</sup>

The absorption cross section and Auger recombination lifetime were obtained via power-dependent bleach dynamics, shown normalized to long decay time signal in **Figure 6.7d**. Auger recombination lifetimes are derived from these power-dependent bleach dynamics by comparing the dynamics for low power scans, where single excitons are the predominant contributor to signal dynamics, to the dynamics for higher power scans, where contributions from biexciton recombination appear. Exponential fits to the difference between these bleach dynamics allow the determination of the biexciton lifetime. By averaging the lifetimes obtained from the difference spectra of each high power scan and the low power scan, the Auger recombination lifetime was shown to be  $10 \pm 2$  ps, an extremely short lifetime. The lifetime of  $\text{CsPbBr}_3$  nanocubes has been recently found by Makarov et al. to range from 20-40 ps, so the change in morphology for these NPLs leads to an even shorter lifetime.<sup>419</sup> This highly efficient Auger recombination might be detrimental for efficient laser devices, as the recombination stands in the way of achieving population inversion.<sup>420</sup> However, highly efficient non-radiative multiexciton recombination makes the material an excellent single-photon emitter.<sup>380, 421</sup>

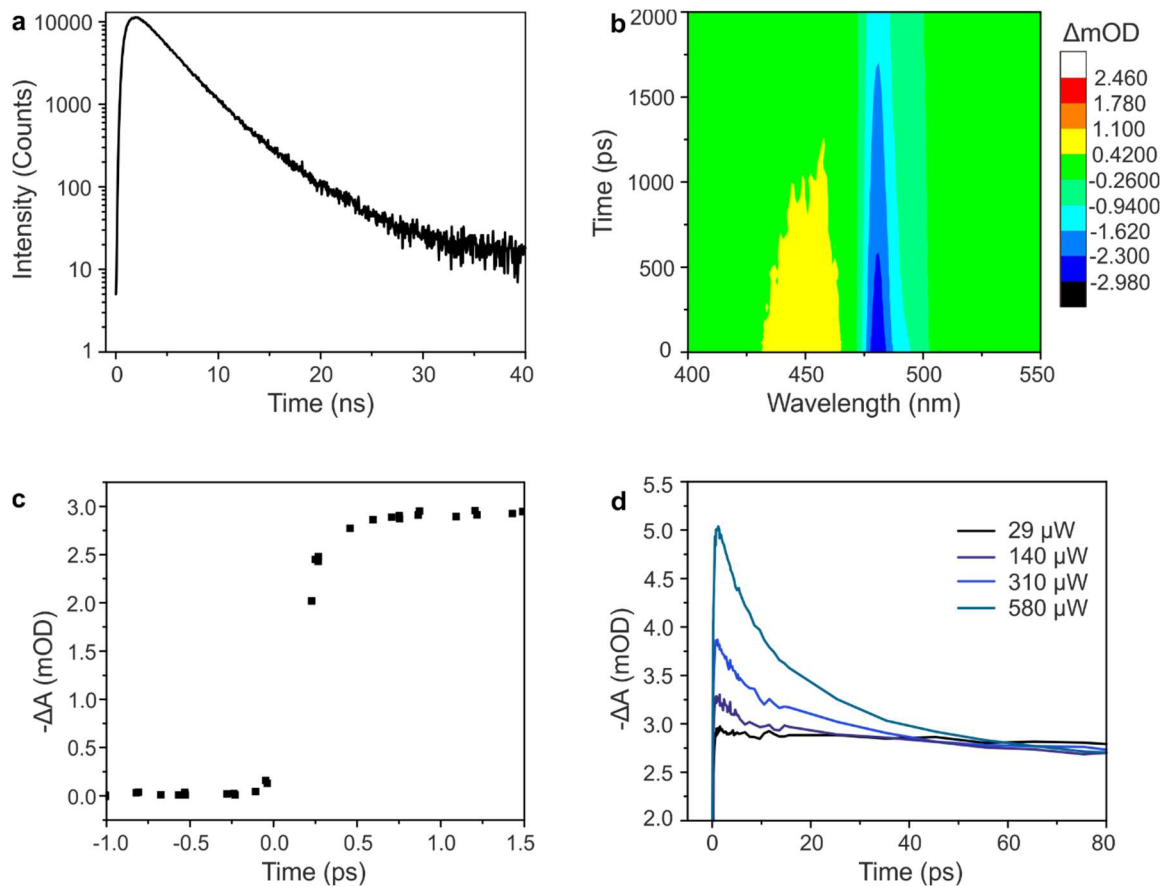


**Figure 6.7.** (a) Transient photoluminescence spectrum of  $\text{CsPbBr}_3$  NPLs taken at the 492 nm PL peak. This spectrum shows a very short PL lifetime for  $\text{CsPbBr}_3$  NPL. (b) Transient absorption map of the  $\text{CsPbBr}_3$  NPLs taken at  $29 \mu\text{W}$ , low power at which single exciton dynamics are the sole contributors



to the TA signal. (c) Early-time bleach dynamics of the 29 μW TA scan. The initial rise of the signal gives the intraband relaxation lifetime. (d) Power-dependent bleach dynamics of the CsPbBr<sub>3</sub> NPLs normalized to signal at long decay time. Increasing power causes biexciton recombination to contribute a fast feature to the bleach. The difference between the high power scans and the low power scan allows for the derivation of Auger recombination lifetime.

Finally, absorption cross-section is derived from fitting power-dependent signal at long decay time to an equation of the following form:

$$A(j, \lambda_{pump}) = B(1 - e^{-\sigma j})$$

where A is the amplitude of the bleach signal, j is the pump fluence in photons/cm<sup>2</sup>, B is a bleach amplitude scaling factor, and σ is the absorption cross section at λ<sub>pump</sub>, here 400 nm.<sup>422-</sup>

<sup>423</sup> Fitting is done at long decay times in order to remove the influence of biexcitons from the bleach signal, so the fitting depends solely on the effect of higher pump fluences on single exciton saturation. The absorption cross section of the material, derived from power-dependent TA scans, is 1.498×10<sup>-12</sup> ± 3.557×10<sup>-14</sup> cm<sup>2</sup>. By comparing this value to that of more traditional nanomaterials, it can be seen that the value of the absorption cross section for the CsPbBr<sub>3</sub> NPLs is a similar order of magnitude to the absorption cross section of thin CdSe NPLs.<sup>424</sup> The summary of the optical characterization that was done here can be seen in Error! Reference source not found..

**Table 6.2.** Photophysical constants for CsPbBr<sub>3</sub> NPLs derived from TRPL and TA data.

Photoluminescence Lifetime	3.334 ns ± 0.0066 ns
Intraband Relaxation Time	188.2 fs ± 13.3 fs
Absorption Cross Section	1.498×10 <sup>-12</sup> cm <sup>2</sup> ± 3.557×10 <sup>-14</sup> cm <sup>2</sup>
Auger Time	10.7 ps ± 2.15 ps

The behavior of 492 nm emissive CsPbBr<sub>3</sub> NPLs was also investigated in thin films since in most of the applications; it is necessary to deposit the material on a substrate. By simply casting the solution of NPLs in a solvent, typically toluene, on a glass substrate, after a very short time (1-2 hours) can be observed a red-shift of the PL emission up to 520 nm (**Figure 6.8**).

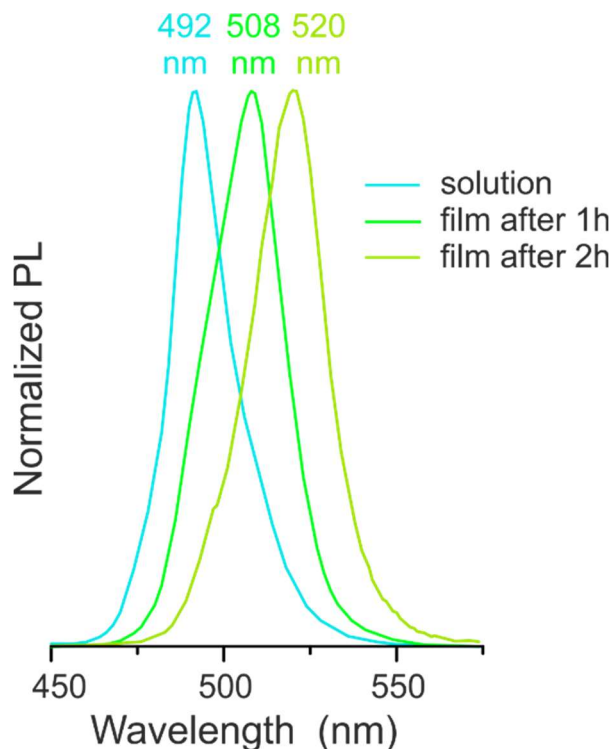


**Figure 6.8.** Evolution of PL peak position of  $\text{CsPbBr}_3$  NPLs cast in films on a glass substrate without being embedded in a polymer.

This red-shift can be attributed to the merging of the NPLs organized in self-assembled superstructures which can easily favor their merging by desorption of the ligands with solvent evaporation. The preservation of the integrity of the self-assembled superstructures was possible by mixing the NPLs solution with a solution of the polymer. Poly(bisphenol A carbonate) and poly(methyl methacrylate) (with two different molecular weights MW = 50.000 – PMMA50K; and MW = 495.000 – PMMA495K) were used as scaffolds for preserving the emission at 492 nm of  $\text{CsPbBr}_3$  NPLs. The best results in terms of film morphology were obtained when  $\text{CsPbBr}_3$  NPLs dispersed in toluene ( $\sim 10$  mg/mL) were mixed with a solution of PMMA495K (4% in anisole). As presented in **Figure 6.9a**, the PL emission was preserved at 492 nm after mixing the  $\text{CsPbBr}_3$  NPLs with polymer and cast in a film on a glass substrate. By mixing 0.1 mL  $\text{CsPbBr}_3$  NPLs with 0.1 mL PMMA495K and casting on a glass slide, a smooth film with bright blue emission (under a UV lamp,  $\lambda = 365$  nm) and high quantum yield (QY > 75%) are obtained, as can be observed in **Figure 6.9b – inset**. The normalized PLE spectrum of the film of  $\text{CsPbBr}_3$  NPLs embed in PMMA495K is presented as well in **Figure 6.9a**, and features a sharp absorption band edge at a similar position to the absorption band edge presented in **Figure 6.1f**. Moreover, due to the absence of scattering losses and probably

due to an increased exciton binding energy in a low dielectric constant polymer matrix,<sup>425</sup> the second and third excitonic peak is better resolved by the PLE measurement than absorbance presented in **Figure 6.1f**.

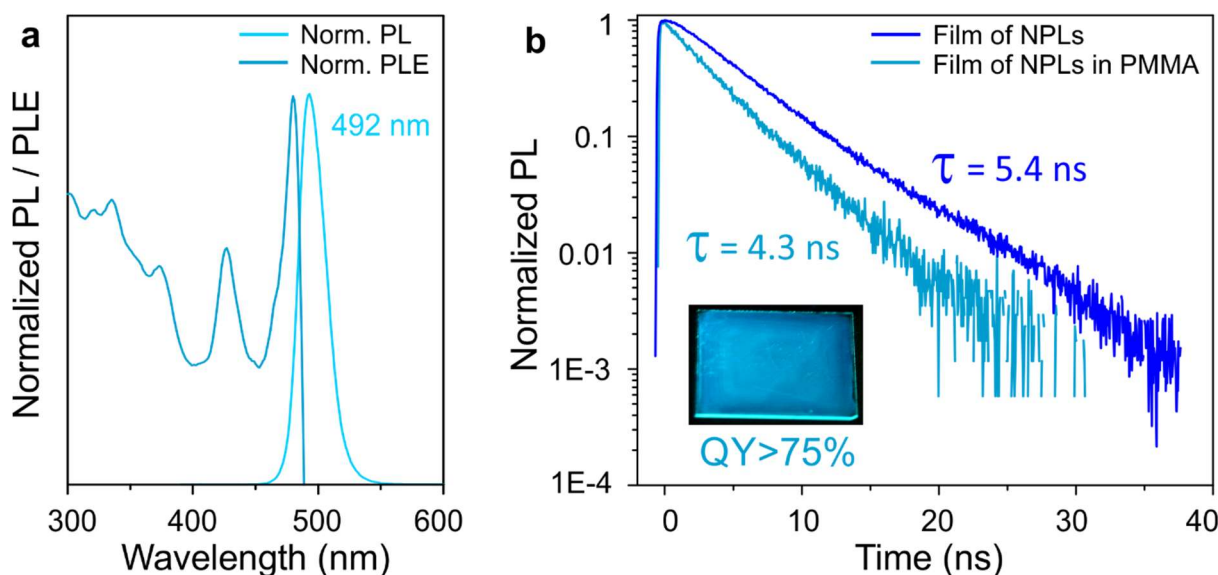


**Figure 6.9.** (a) Normalized PLE and PL spectra of CsPbBr<sub>3</sub> NPLs embedded in a polymeric film of PMMA495K; (b) Time-resolved PL of CsPbBr<sub>3</sub> NPLs in film prepared by casting the NPLs in toluene (blue trace) and NPLs mixed with PMMA 495K solution (cyan trace) on glass slide; inset – Photograph of deposited film (QY>75%) of CsPbBr<sub>3</sub> NPLs embedded in polymeric film (PMMA 495K, 4% solution in anisole) cast on glass slide.

Judging from the PL and PLE spectra, it can be concluded that, by mixing the CsPbBr<sub>3</sub> NPLs with a PMMA495K solution, the merging of the NPLs is prevented ensuring stable emission at 492 nm and sharp absorption band edge at 480-482 nm. The absence of direct contact in-between CsPbBr<sub>3</sub> NPLs in PMMA matrix is confirmed by the power-independent time-resolved PL decay (in contrast to pure CsPbBr<sub>3</sub> NPLs, in which PL lifetime accelerates by increasing the excitation density, as shown in **Figure 6.10a**) while the pump intensity was varied in 2 orders of magnitude from 30 nJ cm<sup>-2</sup> to 3 μJ cm<sup>-2</sup> (**Figure 6.10b**). This disproves the possibility of exciton delocalization and exciton-exciton interaction in the aggregates of NPLs, as it was observed for methylammonium lead bromide nanoplatelets.<sup>407</sup> Thus, it can be concluded that in the PMMA matrix, the individual CsPbBr<sub>3</sub> NPLs are well isolated. Time-resolved photoluminescence (TRPL) – **Figure 6.9b** – was performed on films obtained by drop casting dispersions of CsPbBr<sub>3</sub> NPLs in toluene (blue trace) and CsPbBr<sub>3</sub> NPLs mixed with a PMMA495K solution (cyan trace). A longer exciton lifetime (5.4 ns) was found for the NPLs directly drop cast from the toluene solution, while the exciton lifetime for NPLs embedded in

PMMA polymer is found to be 4.3 ns. In both cases, time-resolved traces have a mono-exponential decay, the moderate lifetime shortening of  $\text{CsPbBr}_3$  NPLs in PMMA matrix can be explained by the increased exciton binding energy in low dielectric constant polymer matrix.<sup>425</sup>

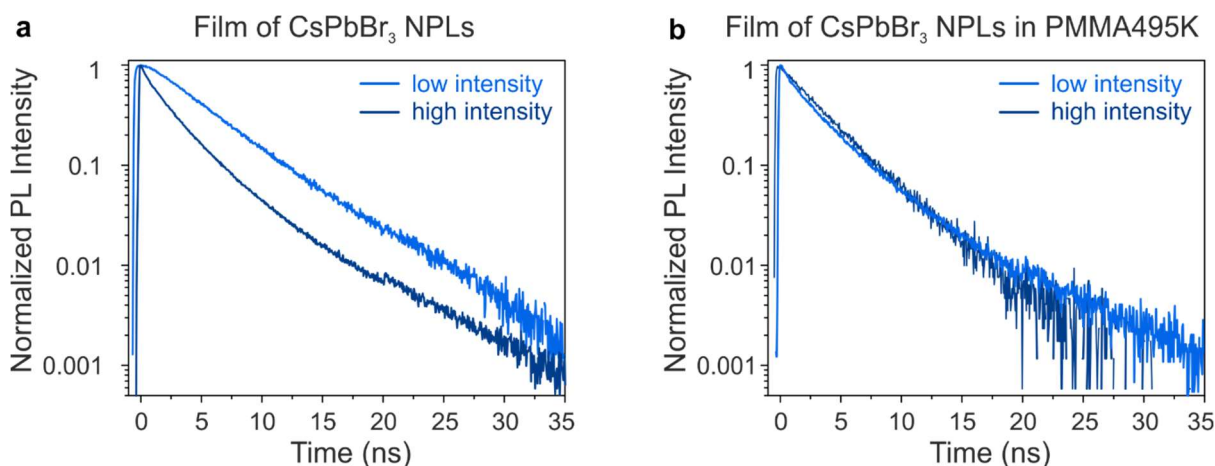


**Figure 6.10.** Time resolved PL at low and high intensity for film of  $\text{CsPbBr}_3$  NPLs (a); and  $\text{CsPbBr}_3$  NPLs embed in PMMA495K (b).

Single NC spectroscopy has been widely used to further get inside into the optical properties of nanomaterial. Here, single dot spectroscopy at room and cryogenic temperature were performed. Room temperature single NPL PL spectrum is reported in **Figure 6.11a**. For comparison, the ensemble PL has also been reported. Due to the very narrow size distribution in the ensemble, PL broadening is almost the same as for the single NPL, attesting the robustness of the newly developed synthetic protocol. Time-resolved PL experiments, as shown in **Figure 6.11b**, confirm the results described previously, with the typical radiative decay of about 4.5 ns. As already reported for cubic-shaped NCs, single NPLs still suffer from PL intermittency or blinking (**Figure 6.11c**), a detrimental feature that has been subjected to intense research. Similar to previous reports, blinking in NPLs can be described considering the formation of charged excitons, which experience strong Auger relaxation with strongly reduced PL intensity. This is well supported by the plot of PL intensity versus lifetime (**Figure 6.11d**), where low-intensity events are characterized by shorter lifetime (non-radiative, Auger-mediated triions decay). In addition to blinking, perovskite cubic-shaped NCs are also subject to fast photo-degradation.<sup>380</sup> Due to interaction with moisture, the physical dimension of NC is reduced, and a dynamical blue shift is usually observed in single PL spectroscopy.<sup>426</sup> It is remarkable that the newly developed NPLs show strongly reduced blueshift in the PL spectra

series (**Figure 6.11d**) making them much more robust than similar  $\text{CsPbBr}_3$  nanocubes dispersed in the same polymer matrix (PMMA). While the origin of such enhanced stability has to be fully unveiled, it shows the potential of such nanomaterials as the active medium in single-photon devices.

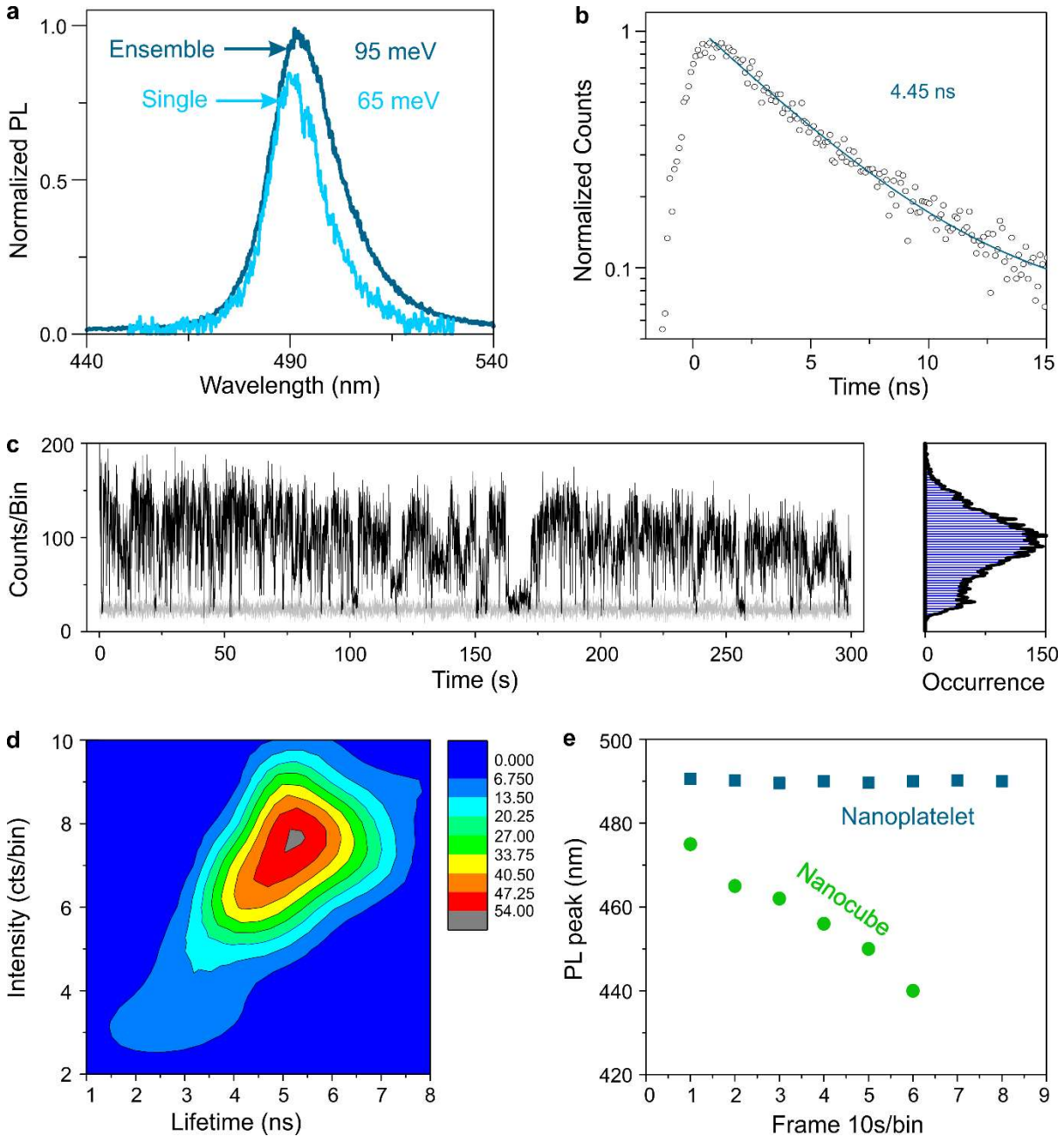


**Figure 6.11.** (a) RT PL spectrum of an ensemble of  $\text{CsPbBr}_3$  NPLs (FWHM=95 meV) together with the PL spectrum obtained at a single NPL level (FWHM=65 meV). (b) Single NPL time-resolved PL at RT. By fitting the experimental data (black squares) to an exponential decay function (solid line), a decay time of 4.5 ns has been obtained. (c) PL blinking trace and the relative intensity histogram. (d) 2D-colour plot of PL intensity versus lifetime showing “A-type” blinking behavior. (e) Comparison of PL peak emission as a function of time in cubic  $\text{CsPbBr}_3$  NCs and NPLs. While nanocubes experience a

---

*blueshift (shorter emission wavelength) in the emission energy, NPLs are more robust against photo-degradation, resulting in a more stable emission wavelength.*

Single NPL spectroscopy was also performed at cryogenic temperatures ( $T = 5$  K). Typical PL spectrum is reported in **Figure 6.12a**. Similarly to fully inorganic CsPbBr<sub>3</sub> nanocubes, the emission peak energy redshifts by decreasing temperatures.<sup>381</sup> PL measurements on single CsPbBr<sub>3</sub> NPLs show narrow, sub-nanometer Lorentzian-shaped emission line at a wavelength of  $\lambda = 512.2$  nm (2.421 eV) with an FWHM of 0.385 nm (1.82 meV) while exciting with low optical excitation power  $P_{\text{exc}} = 0.04$   $\mu$ W (**Figure 6.12a**). As often reported in different quantum systems, trapped charges or polarization of the host material leads to spectral diffusion of the PL signal. **Figure 6.12b** displays a typical PL time series, also at low excitation powers with 1 s integration time, where the spectral diffusion is less than the FWHM of the emission line.

Additionally, statistics on the intensity of the emitted light with a 10 ms time bin (**Figure 6.12b inset**) reveal that blinking events, associated with dark states or intensity flickering are not present at low excitation powers.<sup>381</sup> The newly developed NPLs have long-time optical stability and behave very similar to the best-reported cubic CsPbBr<sub>3</sub> NCs.<sup>427-428</sup>

The PL lifetime, measured at low excitation power, revealed a single-exponential decay over almost three orders of magnitude (**Figure 6.12c**), which is a clear indication for a single exciton transition. The measured decay time is  $\tau = 195$  ps. Such ultrafast decay was very recently reported to be connected to the peculiar energy level ordering of the fine structure states and the giant oscillator character of triplet states in CsPbX<sub>3</sub> compounds. The measured decay time is faster than the calculated one for CsPbBr<sub>3</sub> NCs and is comparable to the observed decay times of cubic-shaped CsPb(Br/Cl)<sub>3</sub> NCs.<sup>381</sup> This increased oscillator strength of excitons confined in high aspect ratio nanoparticles can be associated with the diminished dielectric screening in asymmetrically-shaped NCs.<sup>414</sup> Furthermore, a second-order photon-correlation measurement in an Hanbury-Brown-Twiss setup was performed, and it was observed a clear anti-bunching with  $g^{(2)}(\tau=0) = 0.27$ , which is irrefutable proof for the single-photon emission character of NC (**Figure 6.12d**). Hence, it is possible to engineer the shape of cesium lead halide perovskites and thereby further tune the electron-hole coupling strength as demonstrated in II-VI NCs, enabling the development of novel quantum devices based on CsPbBr<sub>3</sub> NPLs.

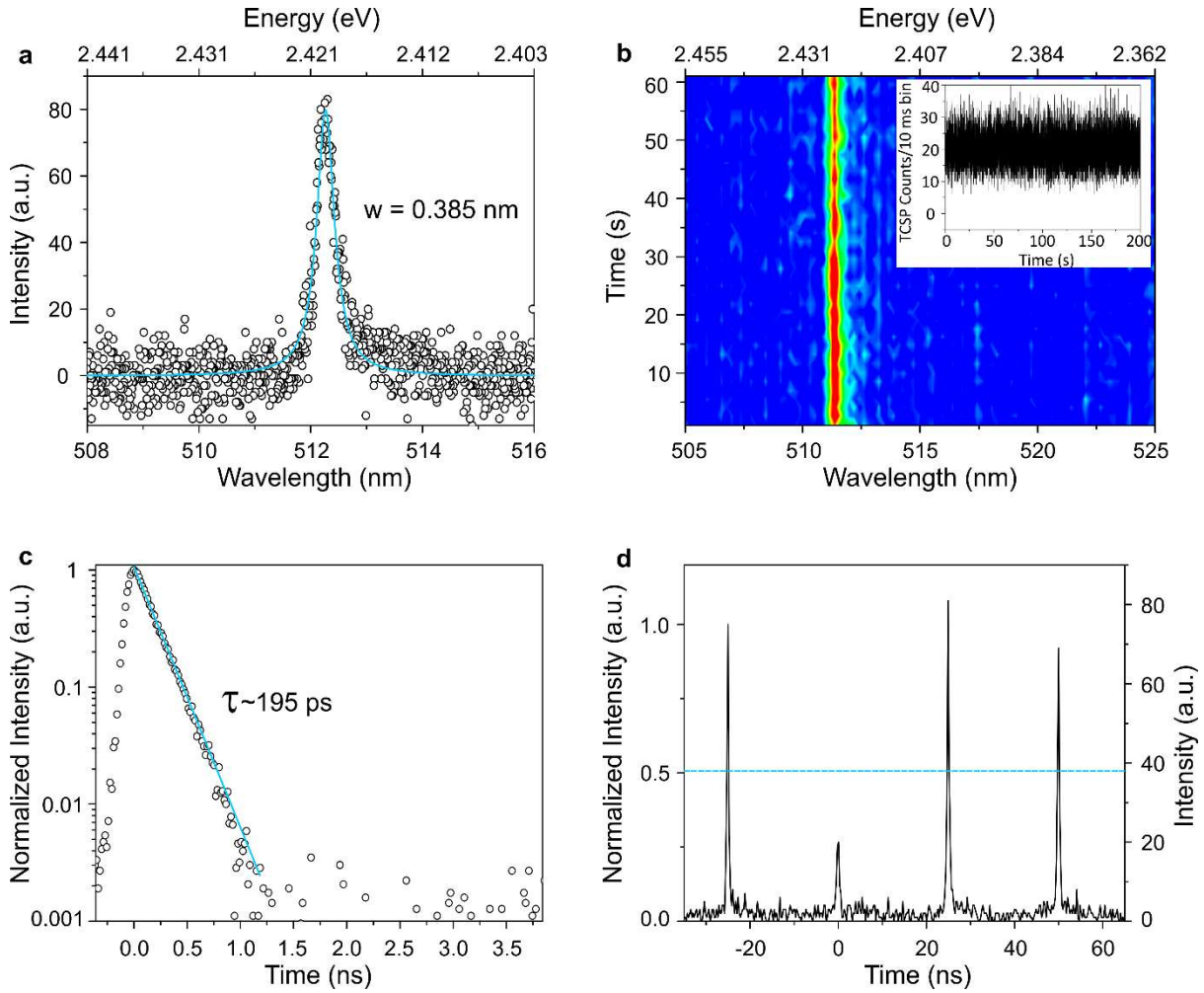


**Figure 6.12.** (a) High-resolution PL spectrum of a single NPLs, collected at 5K with an integration time of 10 s at low excitation powers  $P_{exc}=0.04 \mu\text{W}$ . (b) PL spectral time series at low excitation power reveals blinking-free emission with low spectral diffusion. **Inset:** Intensity of the emitted light with a binning time of 10 ms over a timescale of 200s. (c) Time-resolved photon emission with background subtraction evinces single-exponential decay over almost three decades with a decay time of 195 ps. (d) Second-order photon-correlation measurement of the PL emission from a single NPLs showing anti-bunching behavior ( $g^{(2)}(\tau = 0) < 0.5$ ), manifesting its single-photon character. The NPLs was excited with a 400 nm laser with a repetition rate of 40 MHz at low excitation power in a Hanbury-Brown-Twiss setup.

### 6.3.2. Light-emitting diode

A high solid-state PLQY, rationally excited state lifetime, narrow FWHM and ultimate stability and dispersity in the colloidal solution of the  $\text{CsPbBr}_3$  NPLs stimulated to investigate their light-emitting characteristics in LEDs. **Figure 6.13a** shows the schematic multi-layer device architecture. Briefly, on a glass substrate pre-patterned with a thin film of indium tin oxide (ITO,  $\sim 120$  nm) a 32 nm hole injection layer of PEDOT:PSS was spin-coated and

annealed in ambient conditions. The annealed substrate was transferred into a nitrogen atmosphere glovebox for the deposition of successive layers. A 20±4 nm hole transporting layer of Poly-TPD was deposited by spin coating and, subsequently, the emissive layer (EML) of a colloidal suspension of CsPbBr<sub>3</sub> NPLs (36±2 nm). Further, the electron transport layer of TPBi (35 nm) was deposited by sequential thermal evaporation under vacuum, followed by a 1 nm thick layer of electron injection layer of LiF. Finally, a 100 nm Al cathode layer was deposited in a high vacuum chamber using a shadow mask. **Figure 6.13b** exhibits the energy levels of each material. As shown in **Figure 6.13c**, the electroluminescence spectrum of the blue LED demonstrates a strong blue emission peak at the wavelength of 492 nm with FWHM of 25 nm. **Figure 6.13d** presents a photograph of the device illuminated at 5 V, while a weak emission is also observed at 429 nm from Poly-TPD layer. This undesirable feeble peak can be abolished by further optimizations of the thicknesses of the carrier (hole and electron) transporting layers and also the EML.<sup>429</sup> The current density-voltage-luminance (*J-V-L*) characteristics of perovskite LED are demonstrated in **Figure 6.13e**. The resultant device shows a turn-on voltage of 3.8 V at an initial luminance of 0.5 cd m<sup>-2</sup>. The maximum luminance of 22.1 cd m<sup>-2</sup> was achieved at an operating voltage of 10.5 V and a current density of 73.43 mA cm<sup>2</sup>. As shown in **Figure 6.13f**, the record high external quantum efficiency (EQE) of 0.19 % and the maximum current efficiency of 0.26 cd A<sup>-1</sup> are achieved. Moreover, the resultant device also exhibits a maximum power efficiency of 0.21 lm W<sup>-1</sup> (**Figure 6.13g**). These preliminary results indicate that the performance of the blue LED can be further improved by carefully optimizing the device architecture.



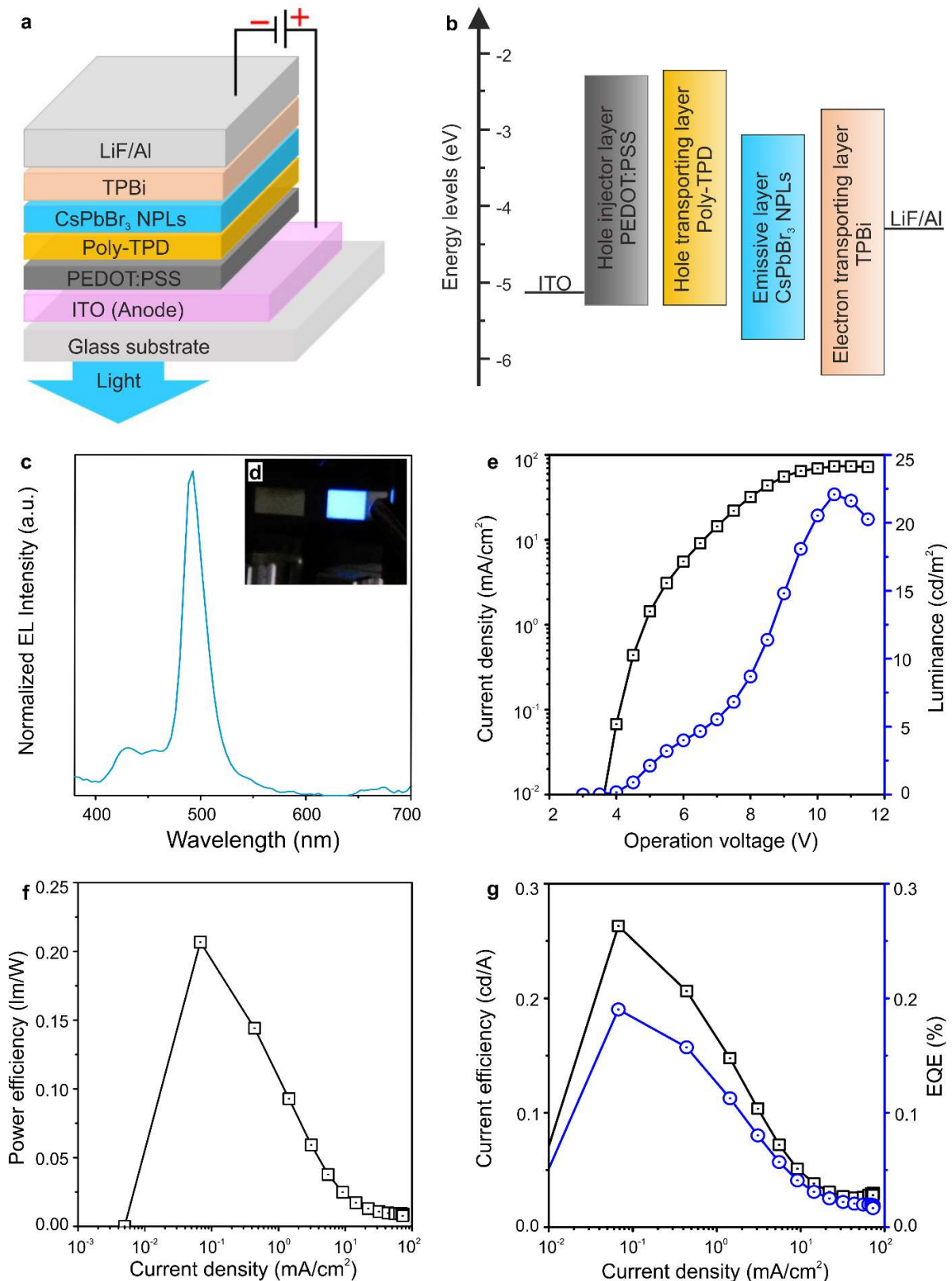


**Figure 6.13.** (a) Graphical representation of LED architecture. (b) Energy levels diagram of the LED components. (c) Normalized EL spectrum of the device under an applied voltage of 5V. (d) Photograph of the device with an active area of  $37.5 \text{ mm}^2$  that illuminated at 5V. (e) Current density-voltage-

---

luminescence (*J-V-L*) characteristics of the device. **(f)** Current efficiency and EQE of the device as a function of current density. **(g)** The power efficiency of LED as a function of current density.

## 6.4. Conclusions

In conclusion, it has been presented a fast synthesis of  $\text{CsPbBr}_3$  NPLs with the perovskite crystal structure, which has a stable PL emission in the blue spectral region at 492 nm. The emission and absorption spectra can be easily tuned via fast anion exchange over a broad spectral range (398 – 632 nm) while the size, shape, and distinctive self-assembled superstructure are preserved. Due to the high stability of the NPLs and their bright emission (PLQYs in films >75%), they proved to be viable candidates for blue LED showing in the preliminary results a maximum luminance of 22.1 cd m<sup>-2</sup>. Moreover, it has been demonstrated that  $\text{CsPbBr}_3$  perovskite NPLs serve as optically stable quantum light sources with ultrafast decay times and subnanometer spectral emission width at low temperatures. The sharp absorption peak and a fast radiative lifetime of nanocrystal NPLs, besides the use in LEDs, might open a path towards integration into high-quality microcavities for lasing devices, or for exploring the strong coupling regime.

### **Reproduced with modifications from:**

Georgian Nedelcu, Michael Wagner, Michael A. Becker, Gabriele Rainò, Sudhir Kumar, Thilo Stöferle, Rainer F. Mahrt, Victor I. Klimov, Sergii Yakunin, Chih-Jen Shih, Richard Schaller and Maksym V. Kovalenko, *Cesium lead bromide nanoplatelets ( $\text{CsPbBr}_3$  NPLs) with stable emission at 492 nm.*

*In preparation.*

## Chapter 7. Conclusions and Outlook

### 7.1. Conclusions

This dissertation encompassed four projects, which all attained their initial targets. Two of them contributed to finding safer alternative pnictide precursors for the facile, fast, and less expensive synthesis of luminescent metal pnictide semiconductor QDs. A third project had as its objective the development of a fast and facile method for tuning the optical properties of CsPbX<sub>3</sub> NCs by deliberately altering their composition while preserving their size, morphology, and crystal structure. The fourth project targeted the synthesis of CsPbBr<sub>3</sub> NPLs with stable emission in the blue spectral range and high PL QYs that can be further processed for various applications such as blue-emitting LEDs. The specific scientific findings of these four projects can be summarised as follows:

1. The outstanding capabilities of a new type of phosphorous precursors from the class of acylphosphines are demonstrated for the synthesis of In(Zn)P QDs. Several air-stable acylphosphine compounds were successfully utilized in two different synthetic approaches: (i) the acetate approach, and (ii) the halide approach, following both the heat-up and hot-injection methods. The synthesis of luminescent In(Zn)P QDs was achieved using <sup>Ph</sup>BAPH and <sup>Ph</sup>TAP as the phosphorous precursor in the acetate method, in contrast to previous studies that report luminescent InP QDs only after surface passivation. The PL tunability over a relatively broad spectral range was also possible for each of the tested precursors for the synthesis of InP QDs. PL QYs reaching values higher than 70% were recorded after effective surface passivation with a GaP/ZnS double shell. Based on their demonstrated performance for In(Zn)P QDs, these new precursors present exceptional potential for the synthesis of other metal phosphide NCs, opening new venues for fundamental studies as well as safer, scalable, economical, and facile syntheses for practical applications like LEDs or LCD TV displays.

2. It has been demonstrated that the air-stable Al(<sup>Mes</sup>BAAs)<sub>3</sub> can successfully afford luminescent InAs QDs by reacting quickly at various temperatures (90 – 270 °C) with In(OAc)<sub>3</sub> and myristic acid in 1-octadecene. Furthermore, the synthetic protocol can be generalized to enable the efficient synthesis of other metal arsenide QDs such as Cd<sub>3</sub>As<sub>2</sub>, GaAs, or Zn<sub>3</sub>As<sub>2</sub>. For the synthesis of InAs QDs, introducing Zn(OAc)<sub>2</sub> into the synthesis afforded less surface defective QDs, as proved by the quality of the PL spectra. Moreover, the PL QYs

of the InAs cores could be increased from 1-2% up to 20% after a preliminary trial of overcoating the cores with a ZnS shell. Remarkably luminescent Cd<sub>3</sub>As<sub>2</sub> QDs could be afforded as well after very short reaction time (5 minutes), by using Al(<sup>Mes</sup>BAAs)<sub>3</sub> in the generalized synthetic protocol. Additionally, tunability of the PL emission can be achieved either by varying the reaction temperature or by altering the procedure and using also reducing agents. GaAs and Zn<sub>3</sub>As<sub>2</sub> QDs were obtained as well using Al(<sup>Mes</sup>BAAs)<sub>3</sub> as an As-source but showed less remarkable properties.

3. A remarkably fast and efficient anion-exchange process was observed for the first time in perovskite CsPbX<sub>3</sub> NCs, in contrast to all known studies that describe this process as a prolonged and inefficient one in metal chalcogenide NCs. Overall, the behavior of perovskite halides with respect to anion-exchange is orthogonal to common metal chalcogenide NCs, namely since the cationic sub-lattice is quite rigid and the singly-charged halide ions are highly mobile. Semiconducting properties of lead halide perovskites are highly defect-tolerant, maintaining bright excitonic emission throughout and upon completion of the anion-exchange. Of practical note, the herein demonstrated fine-tuning of the spectrally narrow and bright PL of anion-exchanged CsPbX<sub>3</sub> NCs over the entire visible spectral region can be conveniently accomplished from numerous halide sources at low temperatures. In addition, fast anion-exchange between CsPbX<sub>3</sub> NCs of different compositions can also be readily achieved. Future investigations of halide-exchange reactions in other nanoscale metal halide systems are warranted, as high ionic conductivity may not be strictly necessary due to the short diffusion paths within the NCs and the low charges of halide ions.

4. A fast, inexpensive and facile synthesis was developed for CsPbBr<sub>3</sub> NPLs with the perovskite crystal structure, stable PL emission in the blue spectral region at 492 nm, and high PL QYs. It has been demonstrated that the emission and absorption spectra can be easily tuned via fast anion exchange over a broad spectral range (398 – 632 nm) while the size, shape, and distinctive self-assembled superstructure are preserved. Due to the high stability of the NPLs and their bright emission (PLQYs in films >75%), they proved to be viable candidates for blue LEDs showing in the preliminary results a maximum luminance of 22.1 cd m<sup>-2</sup>. Moreover, it has been demonstrated that CsPbBr<sub>3</sub> perovskite NPLs serve as optically stable quantum light sources with ultrafast decay times and subnanometer spectral emission width at low temperatures. The sharp absorption peak and a fast radiative lifetime of nanocrystal NPLs, besides the use in LEDs, might open a path towards integration into high-quality microcavities for lasing devices, or for exploring the strong coupling regime.

## 7.2 Outlook

The results presented in Chapter 3 and 4 reveal the performance of safer, inexpensive, and efficient pnictogen precursors for the synthesis of high-quality metal pnictide emitters covering the visible and infrared spectral regimes, which are excellent candidates for devices operating in these spectral windows.

In Chapter 3, several compounds belonging to the Acylphophines class were systematically tested for the synthesis of InP QDs. <sup>Ph</sup>BAPH, <sup>Ph</sup>TAP, and <sup>Me</sup>TAP were selected for more in-depth investigations. These friendly-to-work-with phosphorus precursors have the great advantage of a facile and fast synthesis (few grams of pure product per batch). Based on the findings presented in this chapter, many aspects can be studied for improvement. In order to obtain In(Zn)P QDs at its highest quality, the proposed synthetic protocol would need fine optimization, such as determining whether the hot-injection or the heat-up method would be better suited for their synthesis. An improvement of the PL QYs is presented as well and should be further investigated in greater depth to find the perfect conditions for this particular system of overgrowing, preferably in a one-pot synthesis, a protective shell using high throughput laboratory and learning machines, as well as microfluidic screening. Since the ultimate purpose is to produce, ideally falling under the principles of green chemistry, high-quality environmentally-friendly emitters with tunable emission characterized by high QYs and narrow line widths, it would be desirable to overcoat the InP QDs with an environmentally-friendly protective shell of either GaP/ZnS or ZnSeS. Also, the reaction mechanism involving this particular class of compounds should be studied for a better understanding of the underlying chemistry to identify similarly promising systems.

The second project, presented in Chapter 4, focused on testing the capabilities of Al(<sup>Mes</sup>BAAs)<sub>3</sub> as an As-source for the synthesis of metal arsenide emitters, in particular, InAs QDs with emission in the NIR spectral regime. As presented in this chapter, Al(<sup>Mes</sup>BAAs)<sub>3</sub> proved to be a versatile precursor enabling the fast and facile synthesis of luminescent Cd<sub>3</sub>As<sub>2</sub> QDs, and also of GaAs and Zn<sub>3</sub>As<sub>2</sub> NCs. Further studies of the reaction mechanism are necessary in order to design a better synthetic protocol which can enable the synthesis of luminescent GaAs and Zn<sub>3</sub>As<sub>2</sub> QDs. Another point that should be investigated in greater depth is the overgrowing of a protective shell, such as ZnSeS. Based on these findings, Al(<sup>Mes</sup>BAAs)<sub>3</sub> may be suitable for the synthesis of other arsenide-based NCs as well and should be tested accordingly. Ultimately, the performance of the infrared emitters synthesized with

$\text{Al}(\text{MesBAAs})_3$  should be tested in devices, such as photodetectors or photovoltaics, but also biomedical applications.

In the third project, presented in Chapter 5, the anion-exchange reaction in fully inorganic perovskite NCs is presented as an extremely fast and facile process, showing a great utility in tuning the emission PL of the NCs by merely changing the halide composition while preserving the morphology of the parent NCs. While this can be a great advantage, as proved in this chapter, it is also a drawback when it comes to the use of two different compositions of these perovskite NCs (i.e.,  $\text{CsPbBr}_3$  and  $\text{CsPbI}_3$ ) in applications, such as LEDs. Therefore, studies should focus on the direction of finding an efficient method to prevent the anion exchange when it is not necessary. One approach is to embed the perovskite NCs into a polymeric matrix; however, this approach proved to be challenging and the results were highly dependent on the chosen polymer. One way of overcoming this is to overcoat the perovskite NCs with an appropriate shell material which should be optically transparent and very robust. Candidate materials include  $\text{SiO}_2$ ,  $\text{TiO}_2$  or  $\text{ZrO}_2$  and this field is ripe for exploration as few attempts have been reported with rather unsuccessful or at least doubtful results to date. The overgrowth of such a shell on  $\text{CsPbX}_3$  NCs is very challenging in general, because, for instance, for the overgrowth of a  $\text{SiO}_2$  shell one needs either basic conditions (typically in the presence of  $\text{NH}_3$ ) or the presence of  $\text{H}_2\text{O}$  to which the  $\text{CsPbX}_3$  perovskite NCs are highly sensitive.

Even though the synthesized  $\text{CsPbBr}_3$  NPLs, presented in Chapter 6, present steady PL emission and unchanged morphology for more than two years, they still show minor degradation in time, which leads to a drop in PL QYs while still preserving the initial size and shape. A significant disadvantage of these NPLs is that even though they can be synthesized in various sizes with PL emission deeper in the blue spectral range, they cannot be stabilized after the synthesis and, therefore, they cannot be purified for further use in devices. Thus, special attention should be given on trying to find the right parameters which would afford increased stability, preventing in this way, the redshift of the PL emission towards the value corresponding to the bulk. In this situation, two directions might be worth attention: (i) overgrowing a protective shell, or (ii) manipulating the stabilizing ligands. Another major point here would be a more in-depth investigation of these materials as the emissive layer in various oriented lighting applications.

---

## Bibliography

1. Efros, A. L.; Rosen, M.; Kuno, M.; Nirmal, M.; Norris, D. J.; Bawendi, M., Band-edge exciton in quantum dots of semiconductors with a degenerate valence band: Dark and bright exciton states. *Physical Review B* **1996**, *54*, 4843-4856.
2. Bawendi, M. G.; Steigerwald, M. L.; Brus, L. E., The Quantum Mechanics of Larger Semiconductor Clusters ("Quantum Dots"). *Annual Review of Physical Chemistry* **1990**, *41*, 477-496.
3. Leonhardt, U., Invisibility cup. *Nature Photonics* **2007**, *1*.
4. Daniel, M.-C.; Astruc, D., Gold Nanoparticles: Assembly, Supramolecular Chemistry, Quantum-Size-Related Properties, and Applications toward Biology, Catalysis, and Nanotechnology. *Chem. Rev.* **2004**, *104*, 293-346.
5. Das, G.; Coluccio, M. L.; Alrasheed, S.; Giugni, A.; Allione, M.; Torre, B.; Perozziello, G.; P.Candeloro; Fabrizio, E. D., Plasmonic nanostructures for the ultrasensitive detection of biomolecules. *RIVISTA DEL NUOVO CIMENTO* **2016**, *39*, 547-586.
6. Schaming, D.; Remita, H., Nanotechnology: from the ancient time to nowadays. *Foundations of Chemistry* **2015**, *17*, 187-205.
7. Faraday, M., The Bakerian Lecture - Experimental Relations of Gold (and other Metals) to Light. *Phil. Trans. R. Soc. A* **1857**, *147*, 145-181.
8. Feynman, R., There's Plenty of Room at the Bottom. *Engineering and Science* **1960**, 22-36.
9. Ekimov, A.-I.; Onushchenko, A.-A., Quantum Size Effect in Three-Dimensional Microscopic Semiconductor Crystals. *Sov. Phys. JETP* **1981**, *34*, 345-349.
10. Brus, L., Electronic Wave Functions in Semiconductor Clusters: Experiment and Theory. *J. Phys. Chem.* **1986**, *90*, 2555.
11. Efros, A. L., Interband Light Absorption in Semiconductor Spheres. *Sov. Phys. Semicond.* **1982**, *16*, 772-775.
12. Rossetti, R.; Nakahara, S.; Brus, L. E., Quantum size effects in the redox potentials, resonance Raman spectra, and electronic spectra of CdS crystallites in aqueous solution. *The Journal of Chemical Physics* **1983**, *79*, 1086-1088.
13. Murray, C. B.; Norris, D. J.; Bawendi, M. G., Synthesis and Characterization of Nearly Monodisperse CdE (E = Sulfur, Selenium, Tellurium) Semiconductor Nanocrystallites. *J. Am. Chem. Soc.* **1993**, *115*, 8706.
14. Hines, M. A.; Guyot-Sionnest, P., Synthesis and Characterization of Strongly Luminescing ZnS-Capped CdSe Nanocrystals. *The Journal of Physical Chemistry* **1996**, *100*, 468-471.
15. Yu, W. W.; Peng, X., Formation of high-quality CdS and other II-VI semiconductor nanocrystals in noncoordinating solvents: tunable reactivity of monomers. *Angew Chem Int Ed* **2002**, *41*, 2368-2371.
16. Zhang, C.; O'Brien, S.; Balogh, L., Comparison and Stability of CdSe Nanocrystals Covered with Amphiphilic Poly(amidoamine) Dendrimers. *J. Phys. Chem. B* **2002**, *106*, 10316.
17. Micic, O. I.; Curtis, C. J.; Jones, K. M.; Sprague, J. R.; Nozik, A. J., Synthesis and characterization of InP quantum dots. *J Phys Chem* **1994**, *98*, 4966-4969.
18. Guzelian, A. A.; Katari, J. E. B.; Kadavanich, A. V.; Banin, U.; Hamad, K.; Juban, E.; Alivisatos, A. P.; Wolters, R. H.; Arnold, C. C.; Heath, J. R., Synthesis of Size-Selected, Surface-Passivated InP Nanocrystals. *The Journal of Physical Chemistry* **1996**, *100*, 7212-7219.

19. Battaglia, D.; Peng, X., Formation of High Quality InP and InAs Nanocrystals in a Noncoordinating Solvent. *Nano Letters* **2002**, *2*, 1027-1030.
20. Jun, K. W.; Khanna, P. K.; Hong, K. B.; Baeg, J. O.; Suh, Y. D., Synthesis of InP nanocrystals from indium chloride and sodium phosphide by solution route. *Mater Chem Phys* **2006**, *96*.
21. Xu, S.; Kumar, S.; Nann, T., Rapid synthesis of high-quality InP nanocrystals. *J Am Chem Soc* **2006**, *128*.
22. Li, L.; Protiere, M.; Reiss, P., Economic synthesis of high quality InP nanocrystals using calcium phosphide as the phosphorus precursor. *Chem Mater* **2008**, *20*.
23. Stein, J. L.; Mader, E. A.; Cossairt, B. M., Luminescent InP Quantum Dots with Tunable Emission by Post-Synthetic Modification with Lewis Acids. *J Phys Chem Lett* **2016**, *7*, 1315-20.
24. Guzelian, A. A.; Banin, U.; Kadavanich, A. V.; Peng, X.; Alivisatos, A. P., Colloidal chemical synthesis and characterization of InAs nanocrystal quantum dots. *Applied Physics Letters* **1996**, *69*, 1432-1434.
25. Srivastava, V.; Dunitz, E.; Kamysbayev, V.; Anderson, J. S.; Talapin, D. V., Monodisperse InAs Quantum Dots from Aminoarsine Precursors: Understanding the Role of Reducing Agent. *Chemistry of Materials* **2018**, *30*, 3623-3627.
26. Yarema, M.; Kovalenko, M. V., Colloidal Synthesis of InSb Nanocrystals with Controlled Polymorphism Using Indium and Antimony Amides. *Chemistry of Materials* **2013**, *25*, 1788-1792.
27. Schaller, R. D.; Klimov, V. I., High Efficiency Carrier Multiplication in PbSe Nanocrystals: Implications for Solar Energy Conversion. *Phys. Rev. Lett.* **2004**, *92*, 186601.
28. Cademartiri, L.; Bertolotti, J.; Sapienza, R.; Wiersma, D. S.; von Freymann, G.; Ozin, G. A., Multigram Scale, Solventless, and Diffusion-Controlled Route to Highly Monodisperse PbS Nanocrystals. *J. Phys. Chem. B* **2005**, *110*, 671.
29. Lambert, K.; Geyter, B. D.; Moreels, I.; Hens, Z., PbTe|CdTe Core|Shell Particles by Cation Exchange, a HR-TEM study. *Chemistry of Materials* **2009**, *21*, 778-780.
30. Cho, K. S.; Talapin, D. V.; Gaschler, W.; Murray, C. B., Designing PbSe Nanowires and Nanorings through Oriented Attachment of Nanoparticles. *J. Am. Chem. Soc.* **2005**, *127*, 7140.
31. Hsing, J. Y.; Tzeng, T. E.; Chuang, K. Y.; Lay, T. S.; Kuo, M. Y.; Tsai, Y. Y.; Hsu, K. S.; Shih, M. H., Lasing in compact microdisks with InAs quantum dots in a well structure. *Journal of Crystal Growth* **2011**, *323*, 457-459.
32. Li, H.; Brescia, R.; Povia, M.; Prato, M.; Bertoni, G.; Manna, L.; Moreels, I., Synthesis of Uniform Disk-Shaped Copper Telluride Nanocrystals and Cation Exchange to Cadmium Telluride Quantum Disks with Stable Red Emission. *Journal of the American Chemical Society* **2013**, *135*, 12270-12278.
33. Manna, L.; Scher, E. C.; Alivisatos, A. P., Synthesis of Soluble and Processable Rod-, Arrow-, Teardrop-, and Tetrapod-Shaped CdSe Nanocrystals. *J. Am. Chem. Soc.* **2000**, *122*, 12700.
34. Christodoulou, S.; Climente, J. I.; Planelles, J.; Brescia, R.; Prato, M.; Martín-García, B.; Khan, A. H.; Moreels, I., Chloride-Induced Thickness Control in CdSe Nanoplatelets. *Nano Letters* **2018**, *18*, 6248-6254.
35. Bouet, C.; Mahler, B.; Nadal, B.; Abecassis, B.; Tessier, M. D.; Ithurria, S.; Xu, X.; Dubertret, B., Two-Dimensional Growth of CdSe Nanocrystals, from Nanoplatelets to Nanosheets. *Chemistry of Materials* **2013**, *25*, 639-645.
36. LaMer, V. K.; Dinigar, R. H., Theory, Production and Mechanism of Formation of Monodispersed Hydrosols. *Journal of the American Chemical Society* **1950**, *72*, 4847-4854.



37. Reiss, P.; Carriere, M.; Lincheneau, C.; Vaure, L.; Tamang, S., Synthesis of Semiconductor Nanocrystals, Focusing on Nontoxic and Earth-Abundant Materials. *Chem Rev* **2016**, *116*, 10731-819.
38. Zsigmondy, R., Über Mikroskopische Goldkeime. *Z. Physik. Chem.* **1906**, *56*, 77.
39. Carbone, L.; Nobile, C.; De Giorgi, M.; Sala, F. D.; Morello, G.; Pompa, P.; Hytch, M.; Snoeck, E.; Fiore, A.; Franchini, I. R.; Nadasan, M.; Silvestre, A. F.; Chiodo, L.; Kudera, S.; Cingolani, R.; Krahne, R.; Manna, L., Synthesis and Micrometer-Scale Assembly of Colloidal CdSe/CdS Nanorods Prepared by a Seeded Growth Approach. *Nano Letters* **2007**, *7*, 2942-2950.
40. Talapin, D. V.; Nelson, J. H.; Shevchenko, E. V.; Aloni, S.; Sadtler, B.; Alivisatos, A. P., Seeded Growth of Highly Luminescent CdSe/CdS Nanoheterostructures with Rod and Tetrapod Morphologies. *Nano Letters* **2007**, *7*, 2951-2959.
41. Shweky, I.; Aharoni, A.; Mokari, T.; Rothenberg, E.; Nadler, M.; Popov, I.; Banin, U., Seeded growth of InP and InAs quantum rods using indium acetate and myristic acid. *Materials Science and Engineering: C* **2006**, *26*, 788-794.
42. Kwon, S. G.; Hyeon, T., Formation mechanisms of uniform nanocrystals via hot-injection and heat-up methods. *Small* **2011**, *7*, 2685-702.
43. van Embden, J.; Chesman, A. S. R.; Jasieniak, J. J., The Heat-Up Synthesis of Colloidal Nanocrystals. *Chemistry of Materials* **2015**, *27*, 2246-2285.
44. Nicolis, G.; Maes, D., *Kinetics and Thermodynamics of Multistep Nucleation and Self-Assemble in Nanoscale Materials*. 2012; Vol. 151.
45. Lee, J.; Yang, J.; Kwon, S. G.; Hyeon, T., Nonclassical nucleation and growth of inorganic nanoparticles. *Nature Reviews Materials* **2016**, *1*, 16034.
46. Cossairt, B. M., Shining Light on Indium Phosphide Quantum Dots: Understanding the Interplay among Precursor Conversion, Nucleation, and Growth. *Chemistry of Materials* **2016**, *28*, 7181-7189.
47. Gary, D. C.; Terban, M. W.; Billinge, S. J. L.; Cossairt, B. M., Two-Step Nucleation and Growth of InP Quantum Dots via Magic-Sized Cluster Intermediates. *Chemistry of Materials* **2015**, *27*, 1432-1441.
48. McBride, J. R.; Dukes, A. D.; Schreuder, M. A.; Rosenthal, S. J., On ultrasmall nanocrystals. *Chemical Physics Letters* **2010**, *498*, 1-9.
49. Evans, C. M.; Guo, L.; Peterson, J. J.; Maccagnano-Zacher, S.; Krauss, T. D., Ultrabright PbSe Magic-sized Clusters. *Nano Letters* **2008**, *8*, 2896-2899.
50. Kudera, S.; Zanella, M.; Giannini, C.; Rizzo, A.; Li, Y.; Gigli, G.; Cingolani, R.; Ciccarella, G.; Spahl, W.; Parak, W. J.; Manna, L., Sequential Growth of Magic-Size CdSe Nanocrystals. *Advanced Materials* **2007**, *19*, 548-552.
51. Jin, R., Quantum sized, thiolate-protected gold nanoclusters. *Nanoscale* **2010**, *2*, 343-362.
52. Qian, H.; Zhu, M.; Wu, Z.; Jin, R., Quantum Sized Gold Nanoclusters with Atomic Precision. *Accounts of Chemical Research* **2012**, *45*, 1470-1479.
53. Wall, M. A.; Cossairt, B. M.; Liu, J. T. C., Reaction-Driven Nucleation Theory. *The Journal of Physical Chemistry C* **2018**, *122*, 9671-9679.
54. Gary, D. C.; Glassy, B. A.; Cossairt, B. M., Investigation of Indium Phosphide Quantum Dot Nucleation and Growth Utilizing Triarylsilylphosphine Precursors. *Chemistry of Materials* **2014**, *26*, 1734-1744.
55. and, C. B. M.; Kagan, C. R.; Bawendi, M. G., Synthesis and Characterization of Monodisperse Nanocrystals and Close-Packed Nanocrystal Assemblies. *Annual Review of Materials Science* **2000**, *30*, 545-610.
56. Ozbay, E., Plasmonics: Merging Photonics and Electronics at Nanoscale Dimensions. *Science* **2006**, *311*, 189-193.

57. Bell, A. T., The Impact of Nanoscience on Heterogeneous Catalysis. *Science* **2003**, *299*, 1688-1691.
58. Phan, C. M.; Nguyen, H. M., Role of Capping Agent in Wet Synthesis of Nanoparticles. *The Journal of Physical Chemistry A* **2017**, *121*, 3213-3219.
59. Micic, O. I.; Sprague, J. R.; Curtis, C. J.; Jones, K. M.; Machol, J. L.; Nozik, A. J.; Giessen, H.; Fluegel, B.; Mohs, G.; Peyghambarian, N., Synthesis and Characterization of InP, GaP, and GaInP<sub>2</sub> Quantum Dots. *The Journal of Physical Chemistry* **1995**, *99*, 7754-7759.
60. Wells, R. L.; Aubuchon, S. R.; Kher, S. S.; Lube, M. S.; White, P. S., Synthesis of Nanocrystalline Indium Arsenide and Indium Phosphide from Indium(III) Halides and Tris(trimethylsilyl)pnictogens. Synthesis, Characterization, and Decomposition Behavior of I<sub>3</sub>In-P(SiMe<sub>3</sub>)<sub>3</sub>. *Chemistry of Materials* **1995**, *7*, 793-800.
61. Kim, S. W.; Zimmer, J. P.; Ohnishi, S.; Tracy, J. B.; Frangioni, J. V.; Bawendi, M. G., Engineering InAs P1- /InP/ZnSe III-V Alloyed Core/Shell Quantum Dots for the Near-Infrared. *J. Am. Chem. Soc.* **2005**, *127*, 10526.
62. Harris, D. K.; Allen, P. M.; Han, H.-S.; Walker, B. J.; Lee, J.; Bawendi, M. G., Synthesis of Cadmium Arsenide Quantum Dots Luminescent in the Infrared. *Journal of the American Chemical Society* **2011**, *133*, 4676-4679.
63. Glassy, B. A.; Lai, N. L.; Cossairt, B. M., Synthesis of Zn<sub>3</sub>As<sub>2</sub> and (Cd<sub>y</sub>Zn<sub>1-y</sub>)<sub>3</sub>As<sub>2</sub> Colloidal Quantum Dots. *Chemistry of Materials* **2017**, *29*, 6195-6199.
64. Nedelcu, G.; Protesescu, L.; Yakunin, S.; Bodnarchuk, M. I.; Grotevent, M. J.; Kovalenko, M. V., Fast Anion-Exchange in Highly Luminescent Nanocrystals of Cesium Lead Halide Perovskites (CsPbX<sub>3</sub>, X = Cl, Br, I). *Nano Letters* **2015**, *15*, 5635-5640.
65. Jiang, C.; Lee, J. S.; Talapin, D. V., Soluble Precursors for CuInSe<sub>2</sub>, CuIn<sub>1-x</sub>Ga<sub>x</sub>Se<sub>2</sub>, and Cu<sub>2</sub>ZnSn(S,Se)<sub>4</sub> Based on Colloidal Nanocrystals and Molecular Metal Chalcogenide Surface Ligands. *J. Am. Chem. Soc.* **2012**, *134*, 5010.
66. Enright, M. J.; Cossairt, B. M., Synthesis of tailor-made colloidal semiconductor heterostructures. *Chem Commun (Camb)* **2018**, *54*, 7109-7122.
67. Hu, H.; Wu, L.; Tan, Y.; Zhong, Q.; Chen, M.; Qiu, Y.; Yang, D.; Sun, B.; Zhang, Q.; Yin, Y., Interfacial Synthesis of Highly Stable CsPbX<sub>3</sub>/Oxide Janus Nanoparticles. *J. Am. Chem. Soc.* **2018**, *140*, 406.
68. Lim, J.; Bae, W. K.; Lee, D.; Nam, M. K.; Jung, J.; Lee, C.; Char, K.; Lee, S., InP@ZnSeS, Core@Composition Gradient Shell Quantum Dots with Enhanced Stability. *Chemistry of Materials* **2011**, *23*, 4459-4463.
69. Li, L.; Reiss, P., One-pot synthesis of highly luminescent InP/ZnS nanocrystals without precursor injection. *J Am Chem Soc* **2008**, *130*.
70. Zherebetsky, D.; Scheele, M.; Zhang, Y.; Bronstein, N.; Thompson, C.; Britt, D.; Salmeron, M.; Alivisatos, P.; Wang, L.-W., Hydroxylation of the surface of PbS nanocrystals passivated with oleic acid. *Science* **2014**, *344*, 1380-1384.
71. Song, W.-S.; Lee, H.-S.; Lee, J. C.; Jang, D. S.; Choi, Y.; Choi, M.; Yang, H., Amine-derived synthetic approach to color-tunable InP/ZnS quantum dots with high fluorescent qualities. *Journal of Nanoparticle Research* **2013**, *15*, 1750.
72. Tessier, M. D.; Dupont, D.; De Nolf, K.; De Roo, J.; Hens, Z., Economic and Size-Tunable Synthesis of InP/ZnE (E = S, Se) Colloidal Quantum Dots. *Chemistry of Materials* **2015**, *27*, 4893-4898.
73. Green, M. L. H., A new approach to the formal classification of covalent compounds of the elements. *Journal of Organometallic Chemistry* **1995**, *500*, 127-148.
74. Owen, J., The coordination chemistry of nanocrystal surfaces. *Science* **2015**, *347*, 615-616.
75. Boles, M. A.; Ling, D.; Hyeon, T.; Talapin, D. V., The surface science of nanocrystals. *Nature Materials* **2016**, *15*, 141.

76. Aldana, J.; Wang, Y. A.; Peng, X., Photochemical Instability of CdSe Nanocrystals Coated by Hydrophilic Thiols. *Journal of the American Chemical Society* **2001**, *123*, 8844-8850.
77. Brown, P. R.; Kim, D.; Lunt, R. R.; Zhao, N.; Bawendi, M. G.; Grossman, J. C.; Bulović, V., Energy Level Modification in Lead Sulfide Quantum Dot Thin Films through Ligand Exchange. *ACS Nano* **2014**, *8*, 5863-5872.
78. Frederick, M. T.; Weiss, E. A., Relaxation of Exciton Confinement in CdSe Quantum Dots by Modification with a Conjugated Dithiocarbamate Ligand. *ACS Nano* **2010**, *4*, 3195-3200.
79. Dirin, D. N.; Dreyfuss, S.; Bodnarchuk, M. I.; Nedelcu, G.; Papagiorgis, P.; Itskos, G.; Kovalenko, M. V., Lead Halide Perovskites and Other Metal Halide Complexes as Inorganic Capping Ligands for Colloidal Nanocrystals. *J. Am. Chem. Soc.* **2014**, *136*, 6550.
80. Kovalenko, M. V.; Scheele, M.; Talapin, D. V., Colloidal Nanocrystals with Molecular Metal Chalcogenide Surface Ligands. *Science* **2009**, *324*, 1417.
81. Kovalenko, M. V.; Schaller, R. D.; Jarzab, D.; Loi, M. A.; Talapin, D. V., Inorganically Functionalized PbS–CdS Colloidal Nanocrystals: Integration into Amorphous Chalcogenide Glass and Luminescent Properties. *J. Am. Chem. Soc.* **2012**, *134*, 2457.
82. Kim, D. K.; Lai, Y.; Diroll, B. T.; Murray, C. B.; Kagan, C. R., Flexible and low-voltage integrated circuits constructed from high-performance nanocrystal transistors. *Nature Communications* **2012**, *3*, 1216.
83. Koh, W.-k.; Saudari, S. R.; Fafarman, A. T.; Kagan, C. R.; Murray, C. B., Thiocyanate-Capped PbS Nanocubes: Ambipolar Transport Enables Quantum Dot Based Circuits on a Flexible Substrate. *Nano Letters* **2011**, *11*, 4764-4767.
84. Kovalenko, M. V.; Bodnarchuk, M. I.; Zaumseil, J.; Lee, J.-S.; Talapin, D. V., Expanding the Chemical Versatility of Colloidal Nanocrystals Capped with Molecular Metal Chalcogenide Ligands. *Journal of the American Chemical Society* **2010**, *132*, 10085-10092.
85. Lee, J.-S.; Kovalenko, M. V.; Huang, J.; Chung, D. S.; Talapin, D. V., Band-like transport, high electron mobility and high photoconductivity in all-inorganic nanocrystal arrays. *Nature Nanotechnology* **2011**, *6*, 348.
86. Llordés, A.; Hammack, A. T.; Buonsanti, R.; Tangirala, R.; Aloni, S.; Helms, B. A.; Milliron, D. J., Polyoxometalates and colloidal nanocrystals as building blocks for metal oxide nanocomposite films. *Journal of Materials Chemistry* **2011**, *21*, 11631-11638.
87. Llordés, A.; Garcia, G.; Gazquez, J.; Milliron, D. J., Tunable near-infrared and visible-light transmittance in nanocrystal-in-glass composites. *Nature* **2013**, *500*, 323.
88. Nag, A.; Kovalenko, M. V.; Lee, J.-S.; Liu, W.; Spokoyny, B.; Talapin, D. V., Metal-free Inorganic Ligands for Colloidal Nanocrystals: S<sup>2-</sup>, HS<sup>-</sup>, Se<sup>2-</sup>, HSe<sup>-</sup>, Te<sup>2-</sup>, HTe<sup>-</sup>, TeS<sub>3</sub><sup>2-</sup>, OH<sup>-</sup>, and NH<sub>2</sub><sup>-</sup> as Surface Ligands. *Journal of the American Chemical Society* **2011**, *133*, 10612-10620.
89. Ashrafi, A. A., Quantum Confinement: An Ultimate Physics of Nanostructures. In *Encyclopedia of Semiconductor Nanotechnology*, Umar, A., Ed. American Scientific Publishers: USA, 2011; Vol. 5.
90. Gaponenko, S. V., *Optical properties of semiconductor nanocrystals*. Cambridge University Press: Cambridge UK, 1998.
91. Talapin, D. V.; Rogach, A. L.; Kornowski, A.; Haase, M.; Weller, H., Highly Luminescent Monodisperse CdSe and CdSe/ZnS Nanocrystals Synthesized in a Hexadecylamine–Trioctylphosphine Oxide–Trioctylphosphine Mixture. *Nano Letters* **2001**, *1*, 207-211.
92. Rogach, A. L., Semiconductor Nanocrystal Quantum Dots - Synthesis, Assembly, Spectroscopy, and Applications. *SpringerWienNewYork* **2008**.

93. Nirmal, M.; Norris, D. J.; Kuno, M.; Bawendi, M. G.; Efros, A. L.; Rosen, M., Observation of the "Dark Exciton" in CdSe Quantum Dots. *Physical Review Letters* **1995**, *75*, 3728-3731.
94. Ekimov, A. I.; Hache, F.; Schanne-Klein, M. C.; Ricard, D.; Flytzanis, C.; Kudryavtsev, I. A.; Yazeva, T. V.; Rodina, A. V.; Efros, A. L., Absorption and intensity-dependent photoluminescence measurements on CdSe quantum dots: assignment of the first electronic transitions. *J. Opt. Soc. Am. B* **1993**, *10*, 100-107.
95. Talapin, D. V.; Gaponik, N.; Borchert, H.; Rogach, A. L.; Haase, M.; Weller, H., Etching of Colloidal InP Nanocrystals with Fluorides: Photochemical Nature of the Process Resulting in High Photoluminescence Efficiency. *The Journal of Physical Chemistry B* **2002**, *106*, 12659-12663.
96. Micic, O. I.; Cheong, H. M.; Fu, H.; Zunger, A.; Sprague, R. J.; Mascarenhas, A.; Nozik, A. J., Size-dependent spectroscopy of InP quantum dots. *J Phys Chem B* **1997**, *101*.
97. Reiss, P.; Protière, M.; Li, L., Core/Shell Semiconductor Nanocrystals. *Small* **2009**, *5*, 154-168.
98. Wei, S.-H.; Zunger, A.; G., V. d. W. C., Calculated natural band offsets of all II–VI and III–V semiconductors: Chemical trends and the role of cation d orbitals. *Applied Physics Letters* **1998**, *72*, 2011-2013.
99. Kim, S.; Fisher, B.; Eisler, H.-J.; Bawendi, M., Type-II Quantum Dots: CdTe/CdSe(Core/Shell) and CdSe/ZnTe(Core/Shell) Heterostructures. *Journal of the American Chemical Society* **2003**, *125*, 11466-11467.
100. Saruyama, M.; So, Y.-G.; Kimoto, K.; Taguchi, S.; Kanemitsu, Y.; Teranishi, T., Spontaneous Formation of Wurzite-CdS/Zinc Blende-CdTe Heterodimers through a Partial Anion Exchange Reaction. *Journal of the American Chemical Society* **2011**, *133*, 17598-17601.
101. Allen, P. M.; Liu, W.; Chauhan, V. P.; Lee, J.; Ting, A. Y.; Fukumura, D.; Jain, R. K.; Bawendi, M. G., InAs(ZnCdS) Quantum Dots Optimized for Biological Imaging in the Near-Infrared. *Journal of the American Chemical Society* **2010**, *132*, 470-471.
102. Kim, Y.; Ham, S.; Jang, H.; Min, J. H.; Chung, H.; Lee, J.; Kim, D.; Jang, E., Bright and Uniform Green Light Emitting InP/ZnSe/ZnS Quantum Dots for Wide Color Gamut Displays. *Acs Applied Nano Materials* **2019**, *2*, 1496-1504.
103. Kim, S.; Kim, T.; Kang, M.; Kwak, S. K.; Yoo, T. W.; Park, L. S.; Yang, I.; Hwang, S.; Lee, J. E.; Kim, S. K.; Kim, S.-W., Highly Luminescent InP/GaP/ZnS Nanocrystals and Their Application to White Light-Emitting Diodes. *Journal of the American Chemical Society* **2012**, *134*, 3804-3809.
104. Aharoni, A.; Mokari, T.; Popov, I.; Banin, U., Synthesis of InAs--CdSe--ZnSe Core--Shell1--Shell2 Structures with Bright and Stable Near-IR Fluorescence. **2005**.
105. Franke, D.; Harris, D. K.; Chen, O.; Bruns, O. T.; Carr, J. A.; Wilson, M. W.; Bawendi, M. G., Continuous injection synthesis of indium arsenide quantum dots emissive in the short-wavelength infrared. *Nat Commun* **2016**, *7*, 12749.
106. Lim, J.; Park, M.; Bae, W. K.; Lee, D.; Lee, S.; Lee, C.; Char, K., Highly Efficient Cadmium-Free Quantum Dot Light-Emitting Diodes Enabled by the Direct Formation of Excitons within InP@ZnSeS Quantum Dots. *ACS Nano* **2013**, *7*, 9019-9026.
107. Jiang, W.; Lin, S. J.; Chang, C. H.; Ji, Z. X.; Sun, B. B.; Wang, X.; Li, R. B.; Pon, N.; Xia, T.; Nel, A. E., Implications of the Differential Toxicological Effects of III-V Ionic and Particulate Materials for Hazard Assessment of Semiconductor Slurries. *Acs Nano* **2015**, *9*, 12011-12025.
108. Brunetti, V.; Chibli, H.; Fiammengo, R.; Galeone, A.; Malvindi, M. A.; Vecchio, G.; Cingolani, R.; Nadeau, J. L.; Pompa, P. P., InP/ZnS as a safer alternative to CdSe/ZnS core/shell quantum dots: in vitro and in vivo toxicity assessment. *Nanoscale* **2013**, *5*, 307-17.

109. Heath, J. R.; Shiang, J. J., Covalency in semiconductor quantum dots. *Chem Soc Rev* **1998**, *27*, 65-71.
110. Xie, R.; Battaglia, D.; Peng, X., Colloidal InP Nanocrystals as Efficient Emitters Covering Blue to Near-Infrared. *Journal of the American Chemical Society* **2007**, *129*, 15432-15433.
111. Zhang, J.; Zhang, D., Synthesis and growth kinetics of high quality InAs nanocrystals using in situ generated AsH<sub>3</sub> as the arsenic source. *CrystEngComm* **2010**, *12*, 591-594.
112. Maurice, A.; Haro, M. L.; Hyot, B.; Reiss, P., Synthesis of Colloidal Indium Antimonide Nanocrystals Using Stibine. *Part Part Syst Char* **2013**, *30*, 828-831.
113. Tamang, S.; Kim, K.; Choi, H.; Kim, Y.; Jeong, S., Synthesis of colloidal InSb nanocrystals via in situ activation of InCl<sub>3</sub>. *Dalton Transactions* **2015**, *44*, 16923-16928.
114. Liu, W.; Chang, A. Y.; Schaller, R. D.; Talapin, D. V., Colloidal InSb Nanocrystals. *Journal of the American Chemical Society* **2012**, *134*, 20258-20261.
115. Evans, C. M.; Castro, S. L.; Worman, J. J.; Raffaele, R. P., Synthesis and Use of Tris(trimethylsilyl)antimony for the Preparation of InSb Quantum Dots. *Chemistry of Materials* **2008**, *20*, 5727-5730.
116. Lucovsky, G.; Martin, R. M.; Burstein, E., Localized Effective Charges in Diatomic Crystals. *Physical Review B* **1971**, *4*, 1367-1374.
117. Kuno, M., *Introductory nanoscience: physical and chemical concepts*. Garland Science: London, 2011.
118. Tamang, S.; Lincheneau, C.; Hermans, Y.; Jeong, S.; Reiss, P., Chemistry of InP Nanocrystal Syntheses. *Chemistry of Materials* **2016**, *28*, 2491-2506.
119. Carenco, S.; Demange, M.; Shi, J.; Boissière, C.; Sanchez, C.; Le Floch, P.; Mézailles, N., White phosphorus and metal nanoparticles: a versatile route to metal phosphide nanoparticles. *Chemical Communications* **2010**, *46*, 5578-5580.
120. Carenco, S.; Hu, Y.; Florea, I.; Ersen, O.; Boissière, C.; Mézailles, N.; Sanchez, C., Metal-Dependent Interplay between Crystallization and Phosphorus Diffusion during the Synthesis of Metal Phosphide Nanoparticles. *Chemistry of Materials* **2012**, *24*, 4134-4145.
121. Yang, S. J.; Oh, J. H.; Kim, S.; Yang, H.; Do, Y. R., Realization of InP/ZnS quantum dots for green, amber and red down-converted LEDs and their color-tunable, four-package white LEDs. *Journal of Materials Chemistry C* **2015**, *3*, 3582-3591.
122. Ning, J. J.; Banin, U., Magic size InP and InAs clusters: synthesis, characterization and shell growth. *Chemical Communications* **2017**, *53*, 2626-2629.
123. Wall, M. A.; Cossairt, B. M.; Liu, J. T. C., Reaction-Driven Nucleation Theory. *Journal of Physical Chemistry C* **2018**, *122*, 9671-9679.
124. Micić, O. I.; Sprague, J.; Lu, Z.; Nozik, A. J., Highly efficient band-edge emission from InP quantum dots. *Applied Physics Letters* **1996**, *68*, 3150-3152.
125. Adam, S.; Talapin, D. V.; Borchert, H.; Lobo, A.; McGinley, C.; Castro, A. R. B. d.; Haase, M.; Weller, H.; Möller, T., The effect of nanocrystal surface structure on the luminescence properties: Photoemission study of HF-etched InP nanocrystals. *The Journal of Chemical Physics* **2005**, *123*, 084706.
126. Micić, O. I.; Smith, B. B.; Nozik, A. J., Core-Shell Quantum Dots of Lattice-Matched ZnCdSe<sub>2</sub> Shells on InP Cores: Experiment and Theory. *The Journal of Physical Chemistry B* **2000**, *104*, 12149-12156.
127. Haubold, S.; Haase, M.; Kornowski, A.; Weller, H., Strongly Luminescent InP/ZnS Core-Shell Nanoparticles. *ChemPhysChem* **2001**, *2*, 331-334.
128. Thuy, U. T. D.; Reiss, P.; Liem, N. Q., Luminescence properties of In(Zn)P alloy core/ZnS shell quantum dots. *Applied Physics Letters* **2010**, *97*, 193104.
129. Thuy, U. T. D.; Maurice, A.; Liem, N. Q.; Reiss, P., Europium doped In(Zn)P/ZnS colloidal quantum dots. *Dalton Transactions* **2013**, *42*, 12606-12610.

130. Allen, P. M.; Walker, B. J.; Bawendi, M. G., Mechanistic Insights into the Formation of InP Quantum Dots. *Angewandte Chemie International Edition* **2010**, *49*, 760-762.
131. Harris, D. K.; Bawendi, M. G., Improved Precursor Chemistry for the Synthesis of III–V Quantum Dots. *Journal of the American Chemical Society* **2012**, *134*, 20211-20213.
132. Jang, E.-P.; Jo, J.-H.; Lim, S.-W.; Lim, H.-B.; Kim, H.-J.; Han, C.-Y.; Yang, H., Unconventional formation of dual-colored InP quantum dot-embedded silica composites for an operation-stable white light-emitting diode. *Journal of Materials Chemistry C* **2018**, *6*, 11749-11756.
133. Glassy, B. A.; Cossairt, B. M., Ternary synthesis of colloidal Zn<sub>3</sub>P<sub>2</sub> quantum dots. *Chemical Communications* **2015**, *51*, 5283-5286.
134. Clark, M. D.; Kumar, S. K.; Owen, J. S.; Chan, E. M., Focusing Nanocrystal Size Distributions via Production Control. *Nano Letters* **2011**, *11*, 1976-1980.
135. Xie, R.; Peng, X., Synthetic Scheme for High-Quality InAs Nanocrystals Based on Self-Focusing and One-Pot Synthesis of InAs-Based Core–Shell Nanocrystals. *Angewandte Chemie* **2008**, *120*, 7791-7794.
136. Thessing, J.; Qian, J.; Chen, H.; Pradhan, N.; Peng, X., Interparticle Influence on Size/Size Distribution Evolution of Nanocrystals. *Journal of the American Chemical Society* **2007**, *129*, 2736-2737.
137. Cao; Banin, U., Growth and Properties of Semiconductor Core/Shell Nanocrystals with InAs Cores. *Journal of the American Chemical Society* **2000**, *122*, 9692-9702.
138. Srivastava, V.; Janke, E. M.; Diroll, B. T.; Schaller, R. D.; Talapin, D. V., Facile, Economic and Size-Tunable Synthesis of Metal Arsenide Nanocrystals. *Chemistry of Materials* **2016**, *28*, 6797-6802.
139. Grigel, V.; Dupont, D.; De Nolf, K.; Hens, Z.; Tessier, M. D., InAs Colloidal Quantum Dots Synthesis via Aminopnictogen Precursor Chemistry. *J Am Chem Soc* **2016**, *138*, 13485-13488.
140. Tietze, R.; Panzer, R.; Starzynski, T.; Guhrenz, C.; Frenzel, F.; Wurth, C.; Resch-Genger, U.; Weigand, J. J.; Eychmuller, A., Synthesis of NIR-Emitting InAs-Based Core/Shell Quantum Dots with the Use of Tripyrazolylarsane as Arsenic Precursor. *Part Part Syst Char* **2018**, *35*, 1800175.
141. Wells, H. L., Über die Cäsium- und Kalium-Bleihalogenide. *Zeitschrift für anorganische Chemie* **1893**, *3*, 195-210.
142. Moller, C. K., A Phase Transition in Caesium Plumbochloride. *Nature* **1957**, *180*, 981-982.
143. Moller, C. K., Crystal Structure and Photoconductivity of Caesium Plumbohalides. *Nature* **1958**, *182*, 1436-1436.
144. Nikl, M.; Nitsch, K.; Polák, K.; Mihókova, E.; Zazubovich, S.; Pazzi, G. P.; Fabeni, P.; Salvini, L.; Aceves, R.; Barbosa-Flores, M.; Salas, R. P.; Gurioli, M.; Scacco, A., Quantum size effect in the excitonic luminescence of CsPbX<sub>3</sub>-like quantum dots in CsX (X = Cl, Br) single crystal host. *Journal of Luminescence* **1997**, *72-74*, 377-379.
145. Protesescu, L.; Yakunin, S.; Bodnarchuk, M. I.; Krieg, F.; Caputo, R.; Hendon, C. H.; Yang, R. X.; Walsh, A.; Kovalenko, M. V., Nanocrystals of Cesium Lead Halide Perovskites (CsPbX<sub>3</sub>, X = Cl, Br, and I): Novel Optoelectronic Materials Showing Bright Emission with Wide Color Gamut. *Nano Lett.* **2015**, *15*, 3692.
146. He, X.; Qiu, Y.; Yang, S., Fully-Inorganic Trihalide Perovskite Nanocrystals: A New Research Frontier of Optoelectronic Materials. *Advanced Materials* **2017**, *29*, 1700775.
147. Zhao, Y.; Zhu, K., Organic–inorganic hybrid lead halide perovskites for optoelectronic and electronic applications. *Chemical Society Reviews* **2016**, *45*, 655-689.
148. Protesescu, L.; Yakunin, S.; Kumar, S.; Bar, J.; Bertolotti, F.; Masciocchi, N.; Guagliardi, A.; Grotevent, M.; Shorubalko, I.; Bodnarchuk, M. I., Dismantling the "Red Wall"

- of Colloidal Perovskites: Highly Luminescent Formamidinium and Formamidinium-Cesium Lead Iodide Nanocrystals. *ACS Nano* **2017**, *11*, 3119.
149. Manser, J. S.; Christians, J. A.; Kamat, P. V., Intriguing Optoelectronic Properties of Metal Halide Perovskites. *Chem. Rev.* **2016**, *116*, 12956.
150. Travis, W.; Glover, E. N. K.; Bronstein, H.; Scanlon, D. O.; Palgrave, R. G., On the application of the tolerance factor to inorganic and hybrid halide perovskites: a revised system. *Chem. Sci.* **2016**, *7*, 4548.
151. Li, W.; Wang, Z.; Deschler, F.; Gao, S.; Friend, R. H.; Cheetham, A. K., Chemically diverse and multifunctional hybrid organic–inorganic perovskites. *Nature Reviews Materials* **2017**, *2*, 16099.
152. Correa-Baena, J.-P.; Saliba, M.; Buonassisi, T.; Grätzel, M.; Abate, A.; Tress, W.; Hagfeldt, A., Promises and challenges of perovskite solar cells. *Science* **2017**, *358*, 739-744.
153. Huang, H.; Bodnarchuk, M.; Kershaw, S. V.; Kovalenko, M. V.; Rogach, A. L., Lead Halide Perovskite Nanocrystals in the Research Spotlight: Stability and Defect-Tolerance. *ACS Energy Lett.* **2017**, *2*, 2071.
154. Dirin, D. N.; Protesescu, L.; Trummer, D.; Kochetygov, I. V.; Yakunin, S.; Krumeich, F.; Stadie, N. P.; Kovalenko, M. V., Harnessing Defect-Tolerance at the Nanoscale: Highly Luminescent Lead Halide Perovskite Nanocrystals in Mesoporous Silica Matrixes. *Nano Lett.* **2016**, *16*, 5866.
155. Kang, J.; Wang, L. W., High Defect Tolerance in Lead Halide Perovskite CsPbBr<sub>3</sub>. *J. Phys. Chem. Lett.* **2017**, *8*, 489.
156. Guo, Y.; Wang, Q.; Saidi, W. A., Structural Stabilities and Electronic Properties of High-Angle Grain Boundaries in Perovskite Cesium Lead Halides. *The Journal of Physical Chemistry C* **2017**, *121*, 1715-1722.
157. Akkerman, Q. A.; Raino, G.; Kovalenko, M. V.; Manna, L., Genesis, challenges and opportunities for colloidal lead halide perovskite nanocrystals. *Nat. Mater.* **2018**, *17*, 394.
158. Shamsi, J.; Urban, A. S.; Imran, M.; De Trizio, L.; Manna, L., Metal Halide Perovskite Nanocrystals: Synthesis, Post-Synthesis Modifications, and Their Optical Properties. *Chemical Reviews* **2019**, *119*, 3296-3348.
159. Du, M. H., Efficient carrier transport in halide perovskites: theoretical perspectives. *Journal of Materials Chemistry A* **2014**, *2*, 9091-9098.
160. Buin, A.; Pietsch, P.; Xu, J.; Voznyy, O.; Ip, A. H.; Comin, R.; Sargent, E. H., Materials Processing Routes to Trap-Free Halide Perovskites. *Nano Letters* **2014**, *14*, 6281-6286.
161. Liu, F.; Zhang, Y.; Ding, C.; Kobayashi, S.; Izuishi, T.; Nakazawa, N.; Toyoda, T.; Ohta, T.; Hayase, S.; Minemoto, T., Highly Luminescent Phase-Stable CsPbI<sub>3</sub> Perovskite Quantum Dots Achieving Near 100% Absolute Photoluminescence Quantum Yield. *ACS Nano* **2017**, *11*, 10373.
162. Koscher, B. A.; Swabeck, J. K.; Bronstein, N. D.; Alivisatos, A. P., Essentially Trap-Free CsPbBr<sub>3</sub> Colloidal Nanocrystals by Postsynthetic Thiocyanate Surface Treatment. *Journal of the American Chemical Society* **2017**, *139*, 6566-6569.
163. Zhu, H.; Miyata, K.; Fu, Y.; Wang, J.; Joshi, P. P.; Niesner, D.; Williams, K. W.; Jin, S.; Zhu, X.-Y., Screening in crystalline liquids protects energetic carriers in hybrid perovskites. *Science* **2016**, *353*, 1409-1413.
164. Bakulin, A. A.; Selig, O.; Bakker, H. J.; Rezus, Y. L. A.; Müller, C.; Glaser, T.; Lovrincic, R.; Sun, Z.; Chen, Z.; Walsh, A.; Frost, J. M.; Jansen, T. L. C., Real-Time Observation of Organic Cation Reorientation in Methylammonium Lead Iodide Perovskites. *The Journal of Physical Chemistry Letters* **2015**, *6*, 3663-3669.
165. Lignos, I.; Stavrakis, S.; Nedelcu, G.; Protesescu, L.; deMello, A. J.; Kovalenko, M. V., Synthesis of Cesium Lead Halide Perovskite Nanocrystals in a Droplet-Based Microfluidic Platform: Fast Parametric Space Mapping. *Nano Lett.* **2016**, *16*, 1869.

166. Kovalenko, M. V.; Protesescu, L.; Bodnarchuk, M. I., Properties and potential optoelectronic applications of lead halide perovskite nanocrystals. *Science* **2017**, *358*, 745.
167. Protesescu, L.; Yakunin, S.; Nazarenko, O.; Dirin, D. N.; Kovalenko, M. V., Low-Cost Synthesis of Highly Luminescent Colloidal Lead Halide Perovskite Nanocrystals by Wet Ball Milling. *ACS Appl. Nano Mater.* **2018**, *1*, 1300.
168. Huang, H.; Polavarapu, L.; Sichert, J. A.; Susha, A. S.; Urban, A. S.; Rogach, A. L., Colloidal lead halide perovskite nanocrystals: synthesis, optical properties and applications. *NPG Asia Materials* **2016**, *8*, e328-e328.
169. Zhang, Q.; Yin, Y., All-Inorganic Metal Halide Perovskite Nanocrystals: Opportunities and Challenges. *ACS Cent. Sci.* **2018**, *4*, 668.
170. Akkerman, Q. A.; Motti, S. G.; Srimath Kandada, A. R.; Mosconi, E.; D’Innocenzo, V.; Bertoni, G.; Marras, S.; Kamino, B. A.; Miranda, L.; De Angelis, F., Solution Synthesis Approach to Colloidal Cesium Lead Halide Perovskite Nanoplatelets with Monolayer-Level Thickness Control. *J. Am. Chem. Soc.* **2016**, *138*, 1010.
171. Creutz, S. E.; Crites, E. N.; De Siena, M. C.; Gamelin, D. R., Colloidal Nanocrystals of Lead-Free Double-Perovskite (Elpasolite) Semiconductors: Synthesis and Anion Exchange To Access New Materials. *Nano Lett.* **2018**, *18*, 1118.
172. Tong, Y.; Ehrat, F.; Vanderlinden, W.; Cardenas-Daw, C.; Stolarczyk, J. K.; Polavarapu, L.; Urban, A. S., Dilution-Induced Formation of Hybrid Perovskite Nanoplatelets. *ACS Nano* **2016**, *10*, 10936.
173. Tong, Y.; Bladt, E.; Aygüler, M. F.; Manzi, A.; Milowska, K. Z.; Hintermayr, V. A.; Docampo, P.; Bals, S.; Urban, A. S.; Polavarapu, L.; Feldmann, J., Highly Luminescent Cesium Lead Halide Perovskite Nanocrystals with Tunable Composition and Thickness by Ultrasonication. *Angewandte Chemie International Edition* **2016**, *55*, 13887-13892.
174. Chen, M.; Zou, Y.; Wu, L.; Pan, Q.; Yang, D.; Hu, H.; Tan, Y.; Zhong, Q.; Xu, Y.; Liu, H.; Sun, B.; Zhang, Q., Solvothermal Synthesis of High-Quality All-Inorganic Cesium Lead Halide Perovskite Nanocrystals: From Nanocube to Ultrathin Nanowire. *Advanced Functional Materials* **2017**, *27*, 1701121.
175. Tong, Y.; Bohn, B. J.; Bladt, E.; Wang, K.; Müller-Buschbaum, P.; Bals, S.; Urban, A. S.; Polavarapu, L.; Feldmann, J., From Precursor Powders to CsPbX<sub>3</sub> Perovskite Nanowires: One-Pot Synthesis, Growth Mechanism, and Oriented Self-Assembly. *Angewandte Chemie International Edition* **2017**, *56*, 13887-13892.
176. Pan, Q.; Hu, H.; Zou, Y.; Chen, M.; Wu, L.; Yang, D.; Yuan, X.; Fan, J.; Sun, B.; Zhang, Q., Microwave-assisted synthesis of high-quality “all-inorganic” CsPbX<sub>3</sub> (X = Cl, Br, I) perovskite nanocrystals and their application in light emitting diodes. *Journal of Materials Chemistry C* **2017**, *5*, 10947-10954.
177. Shamsi, J.; Rastogi, P.; Caligiuri, V.; Abdelhady, A. L.; Spirito, D.; Manna, L.; Krahn, R., Bright-Emitting Perovskite Films by Large-Scale Synthesis and Photoinduced Solid-State Transformation of CsPbBr<sub>3</sub> Nanoplatelets. *ACS Nano* **2017**, *11*, 10206-10213.
178. Liu, H.; Wu, Z.; Gao, H.; Shao, J.; Zou, H.; Yao, D.; Liu, Y.; Zhang, H.; Yang, B., One-Step Preparation of Cesium Lead Halide CsPbX<sub>3</sub> (X = Cl, Br, and I) Perovskite Nanocrystals by Microwave Irradiation. *ACS Appl. Mater. Interfaces* **2017**, *9*, 42919.
179. Long, Z.; Ren, H.; Sun, J.; Ouyang, J.; Na, N., High-throughput and tunable synthesis of colloidal CsPbX<sub>3</sub> perovskite nanocrystals in a heterogeneous system by microwave irradiation. *Chemical Communications* **2017**, *53*, 9914-9917.
180. Yang, D.; Zou, Y.; Li, P.; Liu, Q.; Wu, L.; Hu, H.; Xu, Y.; Sun, B.; Zhang, Q.; Lee, S.-T., Large-scale synthesis of ultrathin cesium lead bromide perovskite nanoplates with precisely tunable dimensions and their application in blue light-emitting diodes. **2018**, *47*, 235-242.



181. Wei, S.; Yang, Y.; Kang, X.; Wang, L.; Huang, L.; Pan, D., Room-temperature and gram-scale synthesis of CsPbX<sub>3</sub> (X = Cl, Br, I) perovskite nanocrystals with 50–85% photoluminescence quantum yields. *Chemical Communications* **2016**, *52*, 7265-7268.
182. Wang, K.-H.; Wu, L.; Li, L.; Yao, H.-B.; Qian, H.-S.; Yu, S.-H., Large-Scale Synthesis of Highly Luminescent Perovskite-Related CsPb<sub>2</sub>Br<sub>5</sub> Nanoplatelets and Their Fast Anion Exchange. *Angewandte Chemie International Edition* **2016**, *55*, 8328-8332.
183. Veldhuis, S. A.; Tay, Y. K. E.; Bruno, A.; Dintakurti, S. S. H.; Bhaumik, S.; Muduli, S.; Li, M.; Mathews, N.; Sum, T. C.; Mhaisalkar, S. G., Benzyl Alcohol-treated CH<sub>3</sub>NH<sub>3</sub>PbBr<sub>3</sub> Nanocrystals Exhibiting High Luminescence, Stability and Ultralow Amplified Spontaneous Emission Thresholds. *Nano Lett.* **2017**, *17*, 7424.
184. Shamsi, J.; Abdelhady, A. L.; Accornero, S.; Arciniegas, M.; Goldoni, L.; Kandada, A. R.; Petrozza, A.; Manna, L., N-Methylformamide as a Source of Methylammonium Ions in the Synthesis of Lead Halide Perovskite Nanocrystals and Bulk Crystals. *ACS Energy Lett.* **2016**, *1*, 1042.
185. Dai, S.-W.; Hsu, B.-W.; Chen, C.-Y.; Lee, C.-A.; Liu, H.-Y.; Wang, H.-F.; Huang, Y.-C.; Wu, T.-L.; Manikandan, A.; Ho, R.-M.; Tsao, C.-S.; Cheng, C.-H.; Chueh, Y.-L.; Lin, H.-W., Perovskite Quantum Dots with Near Unity Solution and Neat-Film Photoluminescent Quantum Yield by Novel Spray Synthesis. *Advanced Materials* **2018**, *30*, 1705532.
186. Levchuk, I.; Osvet, A.; Tang, X.; Brandl, M.; Perea, J. D.; Hoegl, F.; Matt, G. J.; Hock, R.; Batentschuk, M.; Brabec, C. J., Brightly Luminescent and Color-Tunable Formamidinium Lead Halide Perovskite FAPbX<sub>3</sub> (X = Cl, Br, I) Colloidal Nanocrystals. *Nano Lett.* **2017**, *17*, 2765.
187. Zhang, F.; Huang, S.; Wang, P.; Chen, X.; Zhao, S.; Dong, Y.; Zhong, H., Colloidal Synthesis of Air-Stable CH<sub>3</sub>NH<sub>3</sub>PbI<sub>3</sub> Quantum Dots by Gaining Chemical Insight into the Solvent Effects. *Chemistry of Materials* **2017**, *29*, 3793-3799.
188. Sun, S.; Yuan, D.; Xu, Y.; Wang, A.; Deng, Z., Ligand-Mediated Synthesis of Shape-Controlled Cesium Lead Halide Perovskite Nanocrystals via Reprecipitation Process at Room Temperature. *ACS Nano* **2016**, *10*, 3648.
189. Teunis, M. B.; Lawrence, K. N.; Dutta, P.; Siegel, A. P.; Sardar, R., Pure white-light emitting ultrasmall organic-inorganic hybrid perovskite nanoclusters. *Nanoscale* **2016**, *8*, 17433.
190. Teunis, M. B.; Johnson, M. A.; Muhoberac, B. B.; Seifert, S.; Sardar, R., Programmable Colloidal Approach to Hierarchical Structures of Methylammonium Lead Bromide Perovskite Nanocrystals with Bright Photoluminescent Properties. *Chemistry of Materials* **2017**, *29*, 3526-3537.
191. Locardi, F.; Cirignano, M.; Baranov, D.; Dang, Z.; Prato, M.; Drago, F.; Ferretti, M.; Pinchetti, V.; Fanciulli, M.; Brovelli, S., Colloidal Synthesis of Double Perovskite Cs<sub>2</sub>AgInCl<sub>6</sub> and Mn-Doped Cs<sub>2</sub>AgInCl<sub>6</sub> Nanocrystals. *J. Am. Chem. Soc.* **2018**, *140*, 12989.
192. Song, J.; Li, J.; Li, X.; Xu, L.; Dong, Y.; Zeng, H., Quantum Dot Light-Emitting Diodes Based on Inorganic Perovskite Cesium Lead Halides (CsPbX<sub>3</sub>). *Adv. Mater.* **2015**, *27*, 7162.
193. Woo, J. Y.; Kim, Y.; Bae, J.; Kim, T. G.; Kim, J. W.; Lee, D. C.; Jeong, S., Highly Stable Cesium Lead Halide Perovskite Nanocrystals through in Situ Lead Halide Inorganic Passivation. *Chemistry of Materials* **2017**, *29*, 7088-7092.
194. Su, Y.; Chen, X.; Ji, W.; Zeng, Q.; Ren, Z.; Su, Z.; Liu, L., Highly Controllable and Efficient Synthesis of Mixed-Halide CsPbX<sub>3</sub> (X = Cl, Br, I) Perovskite QDs toward the Tunability of Entire Visible Light. *ACS Appl. Mater. Interfaces* **2017**, *9*, 33020.
195. Liu, P.; Chen, W.; Wang, W.; Xu, B.; Wu, D.; Hao, J.; Cao, W.; Fang, F.; Li, Y.; Zeng, Y.; Pan, R.; Chen, S.; Cao, W.; Sun, X. W.; Wang, K., Halide-Rich Synthesized Cesium Lead Bromide Perovskite Nanocrystals for Light-Emitting Diodes with Improved Performance. *Chemistry of Materials* **2017**, *29*, 5168-5173.

196. Imran, M.; Caligiuri, V.; Wang, M.; Goldoni, L.; Prato, M.; Krahne, R.; De Trizio, L.; Manna, L., Benzoyl Halides as Alternative Precursors for the Colloidal Synthesis of Lead-Based Halide Perovskite Nanocrystals. *J. Am. Chem. Soc.* **2018**, *140*, 2656.
197. Bekenstein, Y.; Koscher, B. A.; Eaton, S. W.; Yang, P.; Alivisatos, A. P., Highly Luminescent Colloidal Nanoplates of Perovskite Cesium Lead Halide and Their Oriented Assemblies. *Journal of the American Chemical Society* **2015**, *137*, 16008-16011.
198. Zhang, D.; Eaton, S. W.; Yu, Y.; Dou, L.; Yang, P., Solution-Phase Synthesis of Cesium Lead Halide Perovskite Nanowires. *J. Am. Chem. Soc.* **2015**, *137*, 9230.
199. Pan, A.; He, B.; Fan, X.; Liu, Z.; Urban, J. J.; Alivisatos, A. P.; He, L.; Liu, Y., Insight into the Ligand-Mediated Synthesis of Colloidal CsPbBr<sub>3</sub> Perovskite Nanocrystals: The Role of Organic Acid, Base, and Cesium Precursors. *ACS Nano* **2016**, *10*, 7943-7954.
200. Song, J.; Xu, L.; Li, J.; Xue, J.; Dong, Y.; Li, X.; Zeng, H., Monolayer and Few-Layer All-Inorganic Perovskites as a New Family of Two-Dimensional Semiconductors for Printable Optoelectronic Devices. *Adv. Mater.* **2016**, *28*, 4861.
201. Shamsi, J.; Dang, Z.; Bianchini, P.; Canale, C.; Di Stasio, F.; Brescia, R.; Prato, M.; Manna, L., Colloidal Synthesis of Quantum Confined Single Crystal CsPbBr<sub>3</sub> Nanosheets with Lateral Size Control up to the Micrometer Range. *J. Am. Chem. Soc.* **2016**, *138*, 7240.
202. Tang, X.; Zu, Z.; Shao, H.; Hu, W.; Zhou, M.; Deng, M.; Chen, W.; Zang, Z.; Zhu, T.; Xue, J., All-inorganic perovskite CsPb(Br/I)<sub>3</sub> nanorods for optoelectronic application. *Nanoscale* **2016**, *8*, 15158.
203. Shamsi, J.; Rastogi, P.; Caligiuri, V.; Abdelhady, A. L.; Spirito, D.; Manna, L.; Krahne, R., Bright-Emitting Perovskite Films by Large-Scale Synthesis and Photoinduced Solid-State Transformation of CsPbBr<sub>3</sub> Nanoplatelets. *ACS Nano* **2017**, *11*, 10206.
204. Liu, W.; Lin, Q.; Li, H.; Wu, K.; Robel, I.; Pietryga, J. M.; Klimov, V. I., Mn<sup>2+</sup>-Doped Lead Halide Perovskite Nanocrystals with Dual-Color Emission Controlled by Halide Content. *J. Am. Chem. Soc.* **2016**, *138*, 14954.
205. Jang, D. M.; Kim, D. H.; Park, K.; Park, J.; Lee, J. W.; Song, J. K., Ultrasound synthesis of lead halide perovskite nanocrystals. *Journal of Materials Chemistry C* **2016**, *4*, 10625-10629.
206. Zhai, W.; Lin, J.; Li, Q.; Zheng, K.; Huang, Y.; Yao, Y.; He, X.; Li, L.; Yu, C.; Liu, C.; Fang, Y.; Liu, Z.; Tang, C., Solvothermal Synthesis of Ultrathin Cesium Lead Halide Perovskite Nanoplatelets with Tunable Lateral Sizes and Their Reversible Transformation into Cs<sub>4</sub>PbBr<sub>6</sub> Nanocrystals. *Chemistry of Materials* **2018**, *30*, 3714-3721.
207. Papavassiliou, G. C.; Pagona, G.; Karousis, N.; Mousdis, G. A.; Koutselas, I.; Vassilakopoulou, A., Nanocrystalline/microcrystalline materials based on lead-halide units. *Journal of Materials Chemistry* **2012**, *22*, 8271-8280.
208. Zhang, F.; Zhong, H.; Chen, C.; Wu, X. G.; Hu, X.; Huang, H.; Han, J.; Zou, B.; Dong, Y., Brightly Luminescent and Color-Tunable Colloidal CH<sub>3</sub>NH<sub>3</sub>PbX<sub>3</sub> (X = Br, I, Cl) Quantum Dots: Potential Alternatives for Display Technology. *ACS Nano* **2015**, *9*, 4533.
209. Wang, A.; Guo, Y.; Muhammad, F.; Deng, Z., Controlled Synthesis of Lead-Free Cesium Tin Halide Perovskite Cubic Nanocages with High Stability. *Chemistry of Materials* **2017**, *29*, 6493-6501.
210. Pal, J.; Manna, S.; Mondal, A.; Das, S.; Adarsh, K. V.; Nag, A., Colloidal Synthesis and Photophysics of M<sub>3</sub>Sb<sub>2</sub>I<sub>9</sub> (M=Cs and Rb) Nanocrystals: Lead-Free Perovskites. *Angewandte Chemie International Edition* **2017**, *56*, 14187-14191.
211. Pal, J.; Bhunia, A.; Chakraborty, S.; Manna, S.; Das, S.; Dewan, A.; Datta, S.; Nag, A., Synthesis and Optical Properties of Colloidal M<sub>3</sub>Bi<sub>2</sub>I<sub>9</sub> (M = Cs, Rb) Perovskite Nanocrystals. *The Journal of Physical Chemistry C* **2018**, *122*, 10643-10649.

212. Wu, X.; Song, W.; Li, Q.; Zhao, X.; He, D.; Quan, Z., Synthesis of Lead-free CsGeI<sub>3</sub> Perovskite Colloidal Nanocrystals and Electron Beam-induced Transformations. *Chemistry – An Asian Journal* **2018**, *13*, 1654-1659.
213. Leng, M.; Yang, Y.; Zeng, K.; Chen, Z.; Tan, Z.; Li, S.; Li, J.; Xu, B.; Li, D.; Hautzinger, M. P.; Fu, Y.; Zhai, T.; Xu, L.; Niu, G.; Jin, S.; Tang, J., All-Inorganic Bismuth-Based Perovskite Quantum Dots with Bright Blue Photoluminescence and Excellent Stability. *Advanced Functional Materials* **2018**, *28*, 1704446.
214. Yang, B.; Chen, J.; Hong, F.; Mao, X.; Zheng, K.; Yang, S.; Li, Y.; Pullerits, T.; Deng, W.; Han, K., Lead-Free, Air-Stable All-Inorganic Cesium Bismuth Halide Perovskite Nanocrystals. *Angewandte Chemie International Edition* **2017**, *56*, 12471-12475.
215. Ruan, L.; Shen, W.; Wang, A.; Xiang, A.; Deng, Z., Alkyl-Thiol Ligand-Induced Shape- and Crystalline Phase-Controlled Synthesis of Stable Perovskite-Related CsPb<sub>2</sub>Br<sub>5</sub> Nanocrystals at Room Temperature. *J. Phys. Chem. Lett.* **2017**, *8*, 3853.
216. Ruan, L.; Lin, J.; Shen, W.; Deng, Z., Ligand-mediated synthesis of compositionally related cesium lead halide CsPb<sub>2</sub>X<sub>5</sub> nanowires with improved stability. *Nanoscale* **2018**, *10*, 7658.
217. Leng, M.; Chen, Z.; Yang, Y.; Li, Z.; Zeng, K.; Li, K.; Niu, G.; He, Y.; Zhou, Q.; Tang, J., Lead-Free, Blue Emitting Bismuth Halide Perovskite Quantum Dots. *Angewandte Chemie International Edition* **2016**, *55*, 15012-15016.
218. Li, X.; Yu, D.; Cao, F.; Gu, Y.; Wei, Y.; Wu, Y.; Song, J.; Zeng, H., Healing All-Inorganic Perovskite Films via Recyclable Dissolution–Recrystallization for Compact and Smooth Carrier Channels of Optoelectronic Devices with High Stability. *Advanced Functional Materials* **2016**, *26*, 5903-5912.
219. Schmidt, L. C.; Pertegas, A.; Gonzalez-Carrero, S.; Malinkiewicz, O.; Agouram, S.; Espallargas, G. M.; Bolink, H. J.; Galian, R. E.; Perez-Prieto, J., Nontemplate Synthesis of CH<sub>3</sub>NH<sub>3</sub>PbBr<sub>3</sub> Perovskite Nanoparticles. *J. Am. Chem. Soc.* **2014**, *136*, 850.
220. Huang, H.; Zhao, F.; Liu, L.; Zhang, F.; Wu, X. G.; Shi, L.; Zou, B.; Pei, Q.; Zhong, H., Emulsion Synthesis of Size-Tunable CH<sub>3</sub>NH<sub>3</sub>PbBr<sub>3</sub> Quantum Dots: An Alternative Route toward Efficient Light-Emitting Diodes. *ACS Appl. Mater. Interfaces* **2015**, *7*, 28128.
221. Tyagi, P.; Arveson, S. M.; Tisdale, W. A., Colloidal Organohalide Perovskite Nanoplatelets Exhibiting Quantum Confinement. *J. Phys. Chem. Lett.* **2015**, *6*, 1911.
222. Cho, J.; Choi, Y.-H.; O’Loughlin, T. E.; De Jesus, L.; Banerjee, S., Ligand-Mediated Modulation of Layer Thicknesses of Perovskite Methylammonium Lead Bromide Nanoplatelets. *Chemistry of Materials* **2016**, *28*, 6909-6916.
223. Li, X.; Wu, Y.; Zhang, S.; Cai, B.; Gu, Y.; Song, J.; Zeng, H., CsPbX<sub>3</sub> Quantum Dots for Lighting and Displays: Room-Temperature Synthesis, Photoluminescence Superiorities, Underlying Origins and White Light-Emitting Diodes. *Advanced Functional Materials* **2016**, *26*, 2435-2445.
224. Gonzalez-Carrero, S.; Francés-Soriano, L.; González-Béjar, M.; Agouram, S.; Galian, R. E.; Pérez-Prieto, J., The Luminescence of CH<sub>3</sub>NH<sub>3</sub>PbBr<sub>3</sub> Perovskite Nanoparticles Crests the Summit and Their Photostability under Wet Conditions is Enhanced. *Small* **2016**, *12*, 5245.
225. Yuan, Z.; Shu, Y.; Xin, Y.; Ma, B., Highly luminescent nanoscale quasi-2D layered lead bromide perovskites with tunable emissions. *Chemical Communications* **2016**, *52*, 3887-3890.
226. Teunis, M. B.; Jana, A.; Dutta, P.; Johnson, M. A.; Mandal, M.; Muhoberac, B. B.; Sardar, R., Mesoscale Growth and Assembly of Bright Luminescent Organolead Halide Perovskite Quantum Wires. *Chemistry of Materials* **2016**, *28*, 5043-5054.
227. Bodnarchuk, M. I.; Boehme, S. C.; ten Brinck, S.; Bernasconi, C.; Shynkarenko, Y.; Krieg, F.; Widmer, R.; Aeschlimann, B.; Günther, D.; Kovalenko, M. V., Rationalizing and

- Controlling the Surface Structure and Electronic Passivation of Cesium Lead Halide Nanocrystals. *ACS Energy Lett.* **2018**, *4*, 63.
228. De Roo, J.; Ibanez, M.; Geiregat, P.; Nedelcu, G.; Walravens, W.; Maes, J.; Martins, J. C.; Van Driessche, I.; Kovalenko, M. V.; Hens, Z., Highly Dynamic Ligand Binding and Light Absorption Coefficient of Cesium Lead Bromide Perovskite Nanocrystals. *ACS Nano* **2016**, *10*, 2071.
229. Beberwyck, B. J.; Alivisatos, A. P., Ion exchange synthesis of III-V nanocrystals. *J Am Chem Soc* **2012**, *134*, 19977-80.
230. Mews, A.; Eychmuller, A.; Giersig, M.; Schooss, D.; Weller, H., Preparation, characterization, and photophysics of the quantum dot quantum well system cadmium sulfide-mercury sulfide-cadmium sulfide. *J. Phys. Chem.* **1994**, *98*, 934-941.
231. Dloczik, L.; Könenkamp, R., Nanostructure Transfer in Semiconductors by Ion Exchange. *Nano Letters* **2003**, *3*, 651-653.
232. Li, H.; Zanella, M.; Genovese, A.; Povia, M.; Falqui, A.; Giannini, C.; Manna, L., Sequential Cation Exchange in Nanocrystals: Preservation of Crystal Phase and Formation of Metastable Phases. *Nano Letters* **2011**, *11*, 4964-4970.
233. Hodges, J. M.; Kletetschka, K.; Fenton, J. L.; Read, C. G.; Schaak, R. E., Sequential Anion and Cation Exchange Reactions for Complete Material Transformations of Nanoparticles with Morphological Retention. *Angew Chem Int Ed Engl* **2015**, *54*, 8669-72.
234. Son, D. H.; Hughes, S. M.; Yin, Y.; Paul Alivisatos, A., Cation Exchange Reactions in Ionic Nanocrystals. *Science* **2004**, *306*, 1009-1012.
235. Robinson, R. D.; Sadtler, B.; Demchenko, D. O.; Erdonmez, C. K.; Wang, L.-W.; Alivisatos, A. P., Spontaneous Superlattice Formation in Nanorods Through Partial Cation Exchange. *Science* **2007**, *317*, 355-358.
236. Jain, P. K.; Amirav, L.; Aloni, S.; Alivisatos, A. P., Nanoheterostructure Cation Exchange: Anionic Framework Conservation. *Journal of the American Chemical Society* **2010**, *132*, 9997-9999.
237. De Trizio, L.; Gaspari, R.; Bertoni, G.; Kriegel, I.; Moretti, L.; Scotognella, F.; Maserati, L.; Zhang, Y.; Messina, G. C.; Prato, M.; Marras, S.; Cavalli, A.; Manna, L., Cu<sub>3-x</sub>P Nanocrystals as a Material Platform for Near-Infrared Plasmonics and Cation Exchange Reactions. *Chemistry of Materials* **2015**, *27*, 1120-1128.
238. van der Stam, W.; Berends, A. C.; Rabouw, F. T.; Willhammar, T.; Ke, X.; Meeldijk, J. D.; Bals, S.; de Mello Donega, C., Luminescent CuInS<sub>2</sub> Quantum Dots by Partial Cation Exchange in Cu<sub>2-x</sub>S Nanocrystals. *Chemistry of Materials* **2015**, *27*, 621-628.
239. Rivest, J. B.; Swisher, S. L.; Fong, L.-K.; Zheng, H.; Alivisatos, A. P., Assembled Monolayer Nanorod Heterojunctions. *ACS Nano* **2011**, *5*, 3811-3816.
240. Pietryga, J. M.; Werder, D. J.; Williams, D. J.; Casson, J. L.; Schaller, R. D.; Klimov, V. I.; Hollingsworth, J. A., Utilizing the Lability of Lead Selenide to Produce Heterostructured Nanocrystals with Bright, Stable Infrared Emission. *Journal of the American Chemical Society* **2008**, *130*, 4879-4885.
241. van der Stam, W.; Geuchies, J. J.; Altantzis, T.; van den Bos, K. H.; Meeldijk, J. D.; Van Aert, S.; Bals, S.; Vanmaekelbergh, D.; de Mello Donega, C., Highly Emissive Divalent-Ion-Doped Colloidal CsPb<sub>1-x</sub>M<sub>x</sub>Br<sub>3</sub> Perovskite Nanocrystals through Cation Exchange. *J. Am. Chem. Soc.* **2017**, *139*, 4087.
242. Hills-Kimball, K.; Nagaoka, Y.; Cao, C.; Chaykovsky, E.; Chen, O., Synthesis of formamidinium lead halide perovskite nanocrystals through solid-liquid-solid cation exchange. *Journal of Materials Chemistry C* **2017**, *5*, 5680-5684.
243. Yu, D.; Cai, B.; Cao, F.; Li, X.; Liu, X.; Zhu, Y.; Ji, J.; Gu, Y.; Zeng, H., Cation Exchange-Induced Dimensionality Construction: From Monolayered to Multilayered 2D Single Crystal Halide Perovskites. *Advanced Materials Interfaces* **2017**, *4*, 1700441.

244. Gao, D.; Qiao, B.; Xu, Z.; Song, D.; Song, P.; Liang, Z.; Shen, Z.; Cao, J.; Zhang, J.; Zhao, S., Postsynthetic, Reversible Cation Exchange between  $\text{Pb}^{2+}$  and  $\text{Mn}^{2+}$  in Cesium Lead Chloride Perovskite Nanocrystals. *The Journal of Physical Chemistry C* **2017**, *121*, 20387-20395.
245. Xu, W.; Li, F.; Lin, F.; Chen, Y.; Cai, Z.; Wang, Y.; Chen, X., Synthesis of  $\text{CsPbCl}_3$ -Mn Nanocrystals via Cation Exchange. *Advanced Optical Materials* **2017**, *5*, 1700520.
246. Li, F.; Xia, Z.; Gong, Y.; Gu, L.; Liu, Q., Optical properties of  $\text{Mn}^{2+}$  doped cesium lead halide perovskite nanocrystals via a cation-anion co-substitution exchange reaction. *Journal of Materials Chemistry C* **2017**, *5*, 9281-9287.
247. Li, F.; Xia, Z.; Pan, C.; Gong, Y.; Gu, L.; Liu, Q.; Zhang, J. Z., High Br- content  $\text{CsPb}(\text{Cl}_y\text{Br}_{1-y})_3$  perovskite nanocrystals with strong  $\text{Mn}^{2+}$  emission through diverse cation/anion exchange engineering. *ACS Appl. Mater. Interfaces* **2018**, *10*, 11739.
248. Park, J.; Zheng, H.; Jun, Y.-w.; Alivisatos, A. P., Hetero-Epitaxial Anion Exchange Yields Single-Crystalline Hollow Nanoparticles. *Journal of the American Chemical Society* **2009**, *131*, 13943-13945.
249. Choi, D.; Lee, S.; Lee, J.; Cho, K.-S.; Kim, S.-W., Disodium diselenide in colloidal nanocrystals: acting as an anion exchange precursor, a metal selenide precursor, and a chalcogenide ligand. *Chemical Communications* **2015**, *51*, 899-902.
250. Brumer, M.; Kigel, A.; Amirav, L.; Sashchiuk, A.; Solomesch, O.; Tessler, N.; Lifshitz, E.,  $\text{PbSe/PbS}$  and  $\text{PbSe/PbSe}_x\text{S}_{1-x}$  Core/Shell Nanocrystals. *Advanced Functional Materials* **2005**, *15*, 1111-1116.
251. Bailey, R. E.; Nie, S., Alloyed Semiconductor Quantum Dots: Tuning the Optical Properties without Changing the Particle Size. *Journal of the American Chemical Society* **2003**, *125*, 7100-7106.
252. Akkerman, Q. A.; D'Innocenzo, V.; Accornero, S.; Scarpellini, A.; Petrozza, A.; Prato, M.; Manna, L., Tuning the Optical Properties of Cesium Lead Halide Perovskite Nanocrystals by Anion Exchange Reactions. *J. Am. Chem. Soc.* **2015**, *137*, 10276.
253. Guhrenz, C.; Benad, A.; Ziegler, C.; Haubold, D.; Gaponik, N.; Eychmüller, A., Solid-State Anion Exchange Reactions for Color Tuning of  $\text{CsPbX}_3$  Perovskite Nanocrystals. *Chemistry of Materials* **2016**, *28*, 9033-9040.
254. Koscher, B. A.; Bronstein, N. D.; Olshansky, J. H.; Bekenstein, Y.; Alivisatos, A. P., Surface- vs Diffusion-Limited Mechanisms of Anion Exchange in  $\text{CsPbBr}_3$  Nanocrystal Cubes Revealed through Kinetic Studies. *J. Am. Chem. Soc.* **2016**, *138*, 12065.
255. Dou, L.; Lai, M.; Kley, C. S.; Yang, Y.; Bischak, C. G.; Zhang, D.; Eaton, S. W.; Ginsberg, N. S.; Yang, P., Spatially resolved multicolor  $\text{CsPbX}_3$  nanowire heterojunctions via anion exchange. *Proc. Natl. Acad. Sci. U. S. A.* **2017**, *114*, 7216.
256. Parobek, D.; Dong, Y.; Qiao, T.; Rossi, D.; Son, D. H., Photoinduced Anion Exchange in Cesium Lead Halide Perovskite Nanocrystals. *J. Am. Chem. Soc.* **2017**, *139*, 4358.
257. Fang, S.; Li, G.; Lu, Y.; Li, L., Highly Luminescent  $\text{CsPbX}_3$  (X = Cl, Br, I) Nanocrystals Achieved by a Novel Rapid Anion Exchange at Room Temperature. *Chem. - Eur. J.* **2018**, *24*, 1898.
258. Yan, A.; Guo, Y.; Liu, C.; Deng, Z.; Guo, Y.; Zhao, X., Tuning the Optical Properties of  $\text{CsPbBr}_3$  Nanocrystals by Anion Exchange Reactions with  $\text{CsX}$  Aqueous Solution. *Nanoscale Res Lett* **2018**, *13*, 185.
259. Noh, J. H.; Im, S. H.; Heo, J. H.; Mandal, T. N.; Seok, S. I., Chemical management for colorful, efficient, and stable inorganic-organic hybrid nanostructured solar cells. *Nano Lett.* **2013**, *13*, 1764.
260. Pellet, N.; Teuscher, J.; Maier, J.; Grätzel, M., Transforming Hybrid Organic Inorganic Perovskites by Rapid Halide Exchange. *Chemistry of Materials* **2015**, *27*, 2181-2188.

261. Frost, J. M.; Walsh, A., What Is Moving in Hybrid Halide Perovskite Solar Cells? *Acc. Chem. Res.* **2016**, *49*, 528.
262. Haruyama, J.; Sodeyama, K.; Han, L.; Tateyama, Y., First-Principles Study of Ion Diffusion in Perovskite Solar Cell Sensitizers. *J. Am. Chem. Soc.* **2015**, *137*, 10048.
263. Mokari, T.; Rothenberg, E.; Popov, I.; Costi, R.; Banin, U., Selective Growth of Metal Tips onto Semiconductor Quantum Rods and Tetrapods. *Science* **2004**, *304*, 1787.
264. Petrus, M. L.; Schlipf, J.; Li, C.; Gujar, T. P.; Giesbrecht, N.; Müller-Buschbaum, P.; Thelakkat, M.; Bein, T.; Hüttner, S.; Docampo, P., Capturing the Sun: A Review of the Challenges and Perspectives of Perovskite Solar Cells. *Advanced Energy Materials* **2017**, *7*, 1700264.
265. De Bastiani, M.; Dell'Erba, G.; Gandini, M.; D'Innocenzo, V.; Neutzner, S.; Kandada, A. R. S.; Grancini, G.; Binda, M.; Prato, M.; Ball, J. M.; Caironi, M.; Petrozza, A., Solar Cells: Ion Migration and the Role of Preconditioning Cycles in the Stabilization of the J–V Characteristics of Inverted Hybrid Perovskite Solar Cells (Adv. Energy Mater. 2/2016). *Advanced Energy Materials* **2016**, *6*.
266. Azpiroz, J. M.; Mosconi, E.; Bisquert, J.; De Angelis, F., Defect migration in methylammonium lead iodide and its role in perovskite solar cell operation. *Energy & Environmental Science* **2015**, *8*, 2118-2127.
267. Ball, J. M.; Petrozza, A., Defects in perovskite-halides and their effects in solar cells. *Nature Energy* **2016**, *1*, 16149.
268. Mosconi, E.; De Angelis, F., Mobile Ions in Organohalide Perovskites: Interplay of Electronic Structure and Dynamics. *ACS Energy Letters* **2016**, *1*, 182-188.
269. Ning, C.-Z.; Dou, L.; Yang, P., Bandgap engineering in semiconductor alloy nanomaterials with widely tunable compositions. *Nature Reviews Materials* **2017**, *2*, 17070.
270. Shan, Q.; Song, J.; Zou, Y.; Li, J.; Xu, L.; Xue, J.; Dong, Y.; Han, B.; Chen, J.; Zeng, H., High Performance Metal Halide Perovskite Light-Emitting Diode: From Material Design to Device Optimization. *Small* **2017**, *13*, 1701770.
271. Li, M.; Zhang, X.; Lu, S.; Yang, P., Phase transformation, morphology control, and luminescence evolution of cesium lead halide nanocrystals in the anion exchange process. *RSC Advances* **2016**, *6*, 103382-103389.
272. Wang, P.; Dong, B.; Cui, Z.; Gao, R.; Su, G.; Wang, W.; Cao, L., Environmentally-friendly synthesis of highly luminescent cesium lead halide perovskite nanocrystals using Sn-based halide precursors. *Inorganica Chimica Acta* **2017**, *467*, 251-255.
273. Haque, A.; Ravi, V. K.; Shanker, G. S.; Sarkar, I.; Nag, A.; Santra, P. K., Internal Heterostructure of Anion-Exchanged Cesium Lead Halide Nanocubes. *The Journal of Physical Chemistry C* **2018**, *122*, 13399-13406.
274. Hoffman, J. B.; Schleper, A. L.; Kamat, P. V., Transformation of Sintered CsPbBr<sub>3</sub> Nanocrystals to Cubic CsPbI<sub>3</sub> and Gradient CsPbBr<sub>x</sub>I<sub>3-x</sub> through Halide Exchange. *J. Am. Chem. Soc.* **2016**, *138*, 8603.
275. Fu, Y.; Zhu, H.; Stoumpos, C. C.; Ding, Q.; Wang, J.; Kanatzidis, M. G.; Zhu, X.; Jin, S., Broad Wavelength Tunable Robust Lasing from Single-Crystal Nanowires of Cesium Lead Halide Perovskites (CsPbX<sub>3</sub>, X = Cl, Br, I). *ACS Nano* **2016**, *10*, 7963.
276. Ravi, V. K.; Markad, G. B.; Nag, A., Band Edge Energies and Excitonic Transition Probabilities of Colloidal CsPbX<sub>3</sub> (X = Cl, Br, I) Perovskite Nanocrystals. *ACS Energy Letters* **2016**, *1*, 665-671.
277. Sony announces 2013 BRAVIA TVs.
278. CES 2015: Placing Bets on the New TV Technologies.
279. DIRECTIVE 2002/95/EC OF THE EUROPEAN PARLIAMENT AND OF THE COUNCIL of 27 January 2003 on the restriction of the use of certain hazardous substances in electrical and electronic equipment. Official Journal of the European Union: 2003.

280. Ramasamy, P.; Ko, K. J.; Kang, J. W.; Lee, J. S., Two-Step "Seed-Mediated" Synthetic Approach to Colloidal Indium Phosphide Quantum Dots with High-Purity Photo- and Electroluminescence. *Chemistry of Materials* **2018**, *30*, 3643-3647.
281. Ramasamy, P.; Kim, N.; Kang, Y.-S.; Ramirez, O.; Lee, J.-S., Tunable, Bright, and Narrow-Band Luminescence from Colloidal Indium Phosphide Quantum Dots. *Chemistry of Materials* **2017**, *29*, 6893-6899.
282. Ziegler, J.; Xu, S.; Kucur, E.; Meister, F.; Batentschuk, M.; Gindele, F.; Nann, T., Silica-Coated InP/ZnS Nanocrystals as Converter Material in White LEDs. *Advanced Materials* **2008**, *20*, 4068-4073.
283. Yang, X.; Zhao, D.; Leck, K. S.; Tan, S. T.; Tang, Y. X.; Zhao, J.; Demir, H. V.; Sun, X. W., Full Visible Range Covering InP/ZnS Nanocrystals with High Photometric Performance and Their Application to White Quantum Dot Light-Emitting Diodes. *Advanced Materials* **2012**, *24*, 4180-4185.
284. Wang, H. C.; Zhang, H.; Chen, H. Y.; Yeh, H. C.; Tseng, M. R.; Chung, R. J.; Chen, S.; Liu, R. S., Cadmium-Free InP/ZnSeS/ZnS Heterostructure-Based Quantum Dot Light-Emitting Diodes with a ZnMgO Electron Transport Layer and a Brightness of Over 10 000 cd m<sup>-2</sup>. *Small* **2017**, *13*, 1603962.
285. Shen, W.; Tang, H.; Yang, X.; Cao, Z.; Cheng, T.; Wang, X.; Tan, Z.; You, J.; Deng, Z., Synthesis of highly fluorescent InP/ZnS small-core/thick-shell tetrahedral-shaped quantum dots for blue light-emitting diodes. *Journal of Materials Chemistry C* **2017**, *5*, 8243-8249.
286. Cao, F.; Wang, S.; Wang, F.; Wu, Q.; Zhao, D.; Yang, X., A Layer-by-Layer Growth Strategy for Large-Size InP/ZnSe/ZnS Core-Shell Quantum Dots Enabling High-Efficiency Light-Emitting Diodes. *Chemistry of Materials* **2018**, *30*, 8002-8007.
287. Kang, H.; Kim, S.; Oh, J. H.; Yoon, H. C.; Jo, J.-H.; Yang, H.; Do, Y. R., Color-by-Blue QD-Emissive LCD Enabled by Replacing RGB Color Filters with Narrow-Band GR InP/ZnSeS/ZnS QD Films. *Advanced Optical Materials* **2018**, *6*, 1701239.
288. Li, H.; Jia, C.; Meng, X. W.; Li, H. B., Chemical Synthesis and Applications of Colloidal Metal Phosphide Nanocrystals. *Frontiers in Chemistry* **2019**, *6*, 15.
289. Hong, G.; Diao, S.; Chang, J.; Antaris, A. L.; Chen, C.; Zhang, B.; Zhao, S.; Atochin, D. N.; Huang, P. L.; Andreasson, K. I.; Kuo, C. J.; Dai, H., Through-skull fluorescence imaging of the brain in a new near-infrared window. *Nature Photonics* **2014**, *8*, 723.
290. Diao, S.; Blackburn, J. L.; Hong, G.; Antaris, A. L.; Chang, J.; Wu, J. Z.; Zhang, B.; Cheng, K.; Kuo, C. J.; Dai, H., Fluorescence Imaging In Vivo at Wavelengths beyond 1500 nm. *Angewandte Chemie International Edition* **2015**, *54*, 14758-14762.
291. Loghmari, Z.; Bahriz, M.; Meguekam, A.; Teissier, R.; Baranov, A. N., InAs-based quantum cascade lasers emitting close to 25  $\mu$ m. *Electron. Lett.* **2019**, *55*, 144-145.
292. Karandashev, S. A.; Matveev, B. A.; Remennyi, M. A., Indium Arsenide-Based Spontaneous Emission Sources (Review: a Decade Later). *Semiconductors* **2019**, *53*, 139-149.
293. Marshall, A. R. J.; Ker, P. J.; Krysa, A.; David, J. P. R.; Tan, C. H., High speed InAs electron avalanche photodiodes overcome the conventional gain-bandwidth product limit. *Optics Express* **2011**, *19*, 23341-23349.
294. Swarnkar, A.; Marshall, A. R.; Sanehira, E. M.; Chernomordik, B. D.; Moore, D. T.; Christians, J. A.; Chakrabarti, T.; Luther, J. M., Quantum dot-induced phase stabilization of alpha-CsPbI<sub>3</sub> perovskite for high-efficiency photovoltaics. *Science* **2016**, *354*, 92.
295. Sanehira, E. M.; Marshall, A. R.; Christians, J. A.; Harvey, S. P.; Ciesielski, P. N.; Wheeler, L. M.; Schulz, P.; Lin, L. Y.; Beard, M. C.; Luther, J. M., Enhanced mobility CsPbI<sub>3</sub> quantum dot arrays for record-efficiency, high-voltage photovoltaic cells. *Science Advances* **2017**, *3*, eaao4204.

296. Zhang, T.; Dar, M. I.; Li, G.; Xu, F.; Guo, N.; Grätzel, M.; Zhao, Y., Bication lead iodide 2D perovskite component to stabilize inorganic  $\alpha$ -CsPbI<sub>3</sub> perovskite phase for high-efficiency solar cells. *Science Advances* **2017**, *3*, e1700841.
297. Kulbak, M.; Gupta, S.; Kedem, N.; Levine, I.; Bendikov, T.; Hodes, G.; Cahen, D., Cesium Enhances Long-Term Stability of Lead Bromide Perovskite-Based Solar Cells. *The Journal of Physical Chemistry Letters* **2016**, *7*, 167-172.
298. Li, J.; Xu, L.; Wang, T.; Song, J.; Chen, J.; Xue, J.; Dong, Y.; Cai, B.; Shan, Q.; Han, B.; Zeng, H., 50-Fold EQE Improvement up to 6.27% of Solution-Processed All-Inorganic Perovskite CsPbBr<sub>3</sub> QLEDs via Surface Ligand Density Control. *Advanced Materials* **2017**, *29*, 1603885.
299. Chiba, T.; Hoshi, K.; Pu, Y.-J.; Takeda, Y.; Hayashi, Y.; Ohisa, S.; Kawata, S.; Kido, J., High-Efficiency Perovskite Quantum-Dot Light-Emitting Devices by Effective Washing Process and Interfacial Energy Level Alignment. *ACS Applied Materials & Interfaces* **2017**, *9*, 18054-18060.
300. Ramasamy, P.; Lim, D.-H.; Kim, B.; Lee, S.-H.; Lee, M.-S.; Lee, J.-S., All-inorganic cesium lead halide perovskite nanocrystals for photodetector applications. *Chemical Communications* **2016**, *52*, 2067-2070.
301. Zhang, Q.; Su, R.; Liu, X.; Xing, J.; Sum, T. C.; Xiong, Q., High-Quality Whispering-Gallery-Mode Lasing from Cesium Lead Halide Perovskite Nanoplatelets. *Advanced Functional Materials* **2016**, *26*, 6238-6245.
302. Wang, Y.; Li, X.; Song, J.; Xiao, L.; Zeng, H.; Sun, H., All-Inorganic Colloidal Perovskite Quantum Dots: A New Class of Lasing Materials with Favorable Characteristics. *Advanced Materials* **2015**, *27*, 7101-7108.
303. Zhang, Q.; Su, R.; Du, W.; Liu, X.; Zhao, L.; Ha, S. T.; Xiong, Q., Advances in Small Perovskite-Based Lasers. *Small Methods* **2017**, *1*, 1700163.
304. Fu, Y.; Zhu, H.; Chen, J.; Hautzinger, M. P.; Zhu, X. Y.; Jin, S., Metal halide perovskite nanostructures for optoelectronic applications and the study of physical properties. *Nature Reviews Materials* **2019**, *4*, 169-188.
305. Szkop, K. M.; Geeson, M. B.; Stephan, D. W.; Cummins, C. C., Synthesis of acyl(chloro)phosphines enabled by phosphinidene transfer. *Chemical Science* **2019**, *10*, 3627-3631.
306. Schrader, E. Synthesis and Properties of Acylphosphines. Doctoral Thesis, ETH Zurich, 2018.
307. Maimon, S.; Finkman, E.; Bahir, G.; Schacham, S. E.; Garcia, J. M.; Petroff, P. M., Intersublevel transitions in InAs/GaAs quantum dots infrared photodetectors. *Applied Physics Letters* **1998**, *73*, 2003-2005.
308. Kim, M. D.; Noh, S. K.; Hong, S. C.; Kim, T. W., Formation and optical properties of InAs/GaAs quantum dots for applications as infrared photodetectors operating at room temperature. *Applied Physics Letters* **2003**, *82*, 553-555.
309. Zimmer, J. P.; Kim, S.-W.; Ohnishi, S.; Tanaka, E.; Frangioni, J. V.; Bawendi, M. G., Size Series of Small Indium Arsenide-Zinc Selenide Core-Shell Nanocrystals and Their Application to In Vivo Imaging. *Journal of the American Chemical Society* **2006**, *128*, 2526-2527.
310. Miao, J.; Hu, W.; Guo, N.; Lu, Z.; Liu, X.; Liao, L.; Chen, P.; Jiang, T.; Wu, S.; Ho, J. C.; Wang, L.; Chen, X.; Lu, W., High-Responsivity Graphene/InAs Nanowire Heterojunction Near-Infrared Photodetectors with Distinct Photocurrent On/Off Ratios. *Small* **2015**, *11*, 936-942.
311. Sogabe, T.; Shoji, Y.; Ohba, M.; Yoshida, K.; Tamaki, R.; Hong, H.-F.; Wu, C.-H.; Kuo, C.-T.; Tomić, S.; Okada, Y., Intermediate-band dynamics of quantum dots solar cell in concentrator photovoltaic modules. *Scientific reports* **2014**, *4*, 4792-4792.



312. Tex, D. M.; Kamiya, I.; Kanemitsu, Y., Control of hot-carrier relaxation for realizing ideal quantum-dot intermediate-band solar cells. *Scientific reports* **2014**, *4*, 4125-4125.
313. Gao, J.; Chen, K.; Xie, R.; Xie, J.; Lee, S.; Cheng, Z.; Peng, X.; Chen, X., Ultrasmall near-infrared non-cadmium quantum dots for in vivo tumor imaging. *Small* **2010**, *6*, 256-61.
314. Uesugi, H.; Kita, M.; Omata, T., Synthesis of size-controlled colloidal InAs quantum dots using triphenylarsine as a stable arsenic source. *Journal of Crystal Growth* **2015**, *416*, 134-141.
315. Grabolle, M.; Spieles, M.; Lesnyak, V.; Gaponik, N.; Eychmüller, A.; Resch-Genger, U., Determination of the Fluorescence Quantum Yield of Quantum Dots: Suitable Procedures and Achievable Uncertainties. *Analytical Chemistry* **2009**, *81*, 6285-6294.
316. Doolittle, L. R., A semiautomatic algorithm for rutherford backscattering analysis. *Nuclear Instruments and Methods in Physics Research Section B: Beam Interactions with Materials and Atoms* **1986**, *15*, 227-231.
317. Song, J. H.; Choi, H.; Pham, H. T.; Jeong, S., Energy level tuned indium arsenide colloidal quantum dot films for efficient photovoltaics. *Nature Communications* **2018**, *9*, 9.
318. Crisp, R. W.; Panthani, M. G.; Rance, W. L.; Duenow, J. N.; Parilla, P. A.; Callahan, R.; Dabney, M. S.; Berry, J. J.; Talapin, D. V.; Luther, J. M., Nanocrystal Grain Growth and Device Architectures for High-Efficiency CdTe Ink-Based Photovoltaics. *ACS Nano* **2014**, *8*, 9063.
319. Zhitomirsky, D.; Furukawa, M.; Tang, J.; Stadler, P.; Hoogland, S.; Voznyy, O.; Liu, H.; Sargent, E. H., N-Type Colloidal-Quantum-Dot Solids for Photovoltaics. *Adv. Mater.* **2012**, *24*, 6181.
320. Pickett, N. L.; Gresty, N. C.; Hines, M. A., 34-1: Invited Paper: Heavy Metal-Free Quantum Dots Making Inroads for Consumer Applications. *SID Symposium Digest of Technical Papers* **2016**, *47*, 425-427.
321. Reiss, P.; Protiere, M.; Li, L., Core/Shell Semiconductor Nanocrystals. *Small* **2009**, *5*, 154-168.
322. Brunetti, V.; Chibli, H.; Fiammengo, R.; Galeone, A.; Malvindi, M. A.; Vecchio, G.; Cingolani, R.; Nadeau, J. L.; Pompa, P. P., InP/ZnS as a safer alternative to CdSe/ZnS core/shell quantum dots: in vitro and in vivo toxicity assessment. *Nanoscale* **2013**, *5*, 307-317.
323. Lin, G. M.; Ouyang, Q. L.; Hu, R.; Ding, Z. C.; Tian, J. L.; Yin, F.; Xu, G. X.; Chen, Q.; Wang, X. M.; Yong, K. T., In vivo toxicity assessment of non-cadmium quantum dots in BALB/c mice. *Nanomedicine-Nanotechnology Biology and Medicine* **2015**, *11*, 341-350.
324. Indium Phosphide-Based Semiconductor Nanocrystals and Their Applications. *Journal of Nanomaterials* **2012**, *2012*.
325. Dabbousi, B. O.; RodriguezViejo, J.; Mikulec, F. V.; Heine, J. R.; Mattoussi, H.; Ober, R.; Jensen, K. F.; Bawendi, M. G., (CdSe)ZnS core-shell quantum dots: Synthesis and characterization of a size series of highly luminescent nanocrystallites. *Journal of Physical Chemistry B* **1997**, *101*, 9463-9475.
326. Panzer, R.; Guhrenz, C.; Haubold, D.; Hubner, R.; Gaponik, N.; Eychmüller, A.; Weigand, J. J., Versatile Tri(pyrazolyl)phosphanes as Phosphorus Precursors for the Synthesis of Highly Emitting InP/ZnS Quantum Dots. *Angew Chem Int Ed Engl* **2017**, *56*, 14737-14742.
327. Han, H.-V.; Lin, C.-C.; Tsai, Y.-L.; Chen, H.-C.; Chen, K.-J.; Yeh, Y.-L.; Lin, W.-Y.; Kuo, H.-C.; Yu, P., A Highly Efficient Hybrid GaAs Solar Cell Based on Colloidal-Quantum-Dot-Sensitization. *Scientific Reports* **2014**, *4*, 5734.
328. Bawendi, M. G.; Carroll, P. J.; Wilson, W. L.; Brus, L. E., Luminescence properties of CdSe quantum crystallites: Resonance between interior and surface localized states. *The Journal of Chemical Physics* **1992**, *96*, 946-954.

329. Srivastava, V.; Liu, W.; Janke, E. M.; Kamysbayev, V.; Filatov, A. S.; Sun, C.-J.; Lee, B.; Rajh, T.; Schaller, R. D.; Talapin, D. V., Understanding and Curing Structural Defects in Colloidal GaAs Nanocrystals. *Nano Letters* **2017**, *17*, 2094-2101.
330. Park, J. P., Fabrication of GaAs,  $\text{In}_x\text{Ga}_{1-x}\text{As}$  and Their ZnSe Core/Shell Colloidal Quantum Dots. *Journal of the American Chemical Society* **2016**, *v. 138*, pp. 16568-16571-2016 v.138 no.51.
331. Das, A.; Shamirian, A.; Snee, P. T., Arsenic Silylamide: An Effective Precursor for Arsenide Semiconductor Nanocrystal Synthesis. *Chemistry of Materials* **2016**, *28*, 4058-4064.
332. Zhang, J.; Zhang, D., Photoluminescence and Growth Kinetics of High-Quality Indium Arsenide and InAs-Based Core/Shell Colloidal Nanocrystals Synthesized Using Arsine ( $\text{AsH}_3$ ) Generated via Zinc Arsenide as the Arsenic Source. *Chemistry of Materials* **2010**, *22*, 1579-1584.
333. Kumar, S.; Jagielski, J.; Yakunin, S.; Rice, P.; Chiu, Y. C.; Wang, M.; Nedelcu, G.; Kim, Y.; Lin, S.; Santos, E. J. G., Efficient Blue Electroluminescence Using Quantum-Confinement Two-Dimensional Perovskites. *ACS Nano* **2016**, *10*, 9720.
334. Pietra, F.; De Trizio, L.; Hoekstra, A. W.; Renaud, N.; Prato, M.; Grozema, F. C.; Baesjou, P. J.; Koole, R.; Manna, L.; Houtepen, A. J., Tuning the Lattice Parameter of  $\text{In}_x\text{Zn}_y\text{P}$  for Highly Luminescent Lattice-Matched Core/Shell Quantum Dots. *ACS Nano* **2016**, *10*, 4754-4762.
335. Mordvinova, N. E.; Vinokurov, A. A.; Lebedev, O. I.; Kuznetsova, T. A.; Dorofeev, S. G., Addition of Zn during the phosphine-based synthesis of indium phosphide quantum dots: doping and surface passivation. *Beilstein Journal of Nanotechnology* **2015**, *6*, 1237-1246.
336. Schaak, R. E.; Williams, M. E., Full Disclosure: The Practical Side of Nanoscale Total Synthesis. *ACS Nano* **2012**, *6*, 8492-8497.
337. Kovalenko, M. V.; Manna, L.; Cabot, A.; Hens, Z.; Talapin, D. V.; Kagan, C. R.; Klimov, V. I.; Rogach, A. L.; Reiss, P.; Milliron, D. J.; Guyot-Sionnest, P.; Konstantatos, G.; Parak, W. J.; Hyeon, T.; Korgel, B. A.; Murray, C. B.; Heiss, W., Prospects of Nanoscience with Nanocrystals. *ACS Nano* **2015**, *9*, 1012-1057.
338. Oh, M. H.; Yu, T.; Yu, S.-H.; Lim, B.; Ko, K.-T.; Willinger, M.-G.; Seo, D.-H.; Kim, B. H.; Cho, M. G.; Park, J.-H.; Kang, K.; Sung, Y.-E.; Pinna, N.; Hyeon, T., Galvanic Replacement Reactions in Metal Oxide Nanocrystals. *Science* **2013**, *340*, 964-968.
339. Xia, X.; Wang, Y.; Ruditskiy, A.; Xia, Y., 25th Anniversary Article: Galvanic Replacement: A Simple and Versatile Route to Hollow Nanostructures with Tunable and Well-Controlled Properties. *Advanced Materials* **2013**, *25*, 6313-6333.
340. Li, H. B.; Zanella, M.; Genovese, A.; Povia, M.; Falqui, A.; Giannini, C.; Manna, L., Sequential Cation Exchange in Nanocrystals: Preservation of Crystal Phase and Formation of Metastable Phases. *Nano Letters* **2011**, *11*, 4964-4970.
341. Gupta, S.; Kershaw, S. V.; Rogach, A. L., 25th Anniversary Article: Ion Exchange in Colloidal Nanocrystals. *Advanced Materials* **2013**, *25*, 6923-6944.
342. Rivest, J. B.; Jain, P. K., Cation Exchange On The Nanoscale: An Emerging Technique For New Material Synthesis, Device Fabrication, And Chemical Sensing. *Chemical Society Reviews* **2013**, *42*, 89-96.
343. Sytnyk, M.; Kirchschlager, R.; Bodnarchuk, M. I.; Primetzhofer, D.; Kriegner, D.; Enser, H.; Stangl, J.; Bauer, P.; Voith, M.; Hassel, A. W.; Krumeich, F.; Ludwig, F.; Meingast, A.; Kothleitner, G.; Kovalenko, M. V.; Heiss, W., Tuning the Magnetic Properties of Metal Oxide Nanocrystal Heterostructures by Cation Exchange. *Nano Letters* **2013**, *13*, 586-593.
344. Beberwyck, B. J.; Surendranath, Y.; Alivisatos, A. P., Cation Exchange: A Versatile Tool for Nanomaterials Synthesis. *J. Phys. Chem. C* **2013**, *117*, 19759-19770.
345. Ott, F. D.; Spiegel, L. L.; Norris, D. J.; Erwin, S. C., Microscopic Theory of Cation Exchange in CdSe Nanocrystals. *Physical Review Letters* **2014**, *113*, 156803.

346. Wang, W. S.; Dahl, M.; Yin, Y. D., Hollow Nanocrystals through the Nanoscale Kirkendall Effect. *Chemistry of Materials* **2013**, *25*, 1179-1189.
347. El Mel, A. A.; Buffiere, M.; Tessier, P. Y.; Konstantinidis, S.; Xu, W.; Du, K.; Wathuthanthri, I.; Choi, C. H.; Bittencourt, C.; Snyders, R., Highly Ordered Hollow Oxide Nanostructures: The Kirkendall Effect at the Nanoscale. *Small* **2013**, *9*, 2838-2843.
348. Yin, Y.; Rioux, R. M.; Erdonmez, C. K.; Hughes, S.; Somorjai, G. A.; Alivisatos, A. P., Formation of Hollow Nanocrystals Through the Nanoscale Kirkendall Effect. *Science* **2004**, *304*, 711-714.
349. Li, H. B.; Brescia, R.; Povia, M.; Prato, M.; Bertoni, G.; Manna, L.; Moreels, I., Synthesis of Uniform Disk-Shaped Copper Telluride Nanocrystals and Cation Exchange to Cadmium Telluride Quantum Disks with Stable Red Emission. *Journal of the American Chemical Society* **2013**, *135*, 12270-12278.
350. De Trizio, L.; Gaspari, R.; Bertoni, G.; Kriegel, I.; Moretti, L.; Scotognella, F.; Maserati, L.; Zhang, Y.; Messina, G. C.; Prato, M.; Marras, S.; Cavalli, A.; Manna, L., Cu<sub>3-x</sub>P Nanocrystals as a Material Platform for Near-Infrared Plasmonics and Cation Exchange Reactions. *Chem. Mater.* **2015**, *27*, 1120-1128.
351. Dawood, F.; Schaak, R. E., ZnO-Templated Synthesis of Wurtzite-Type ZnS and ZnSe Nanoparticles. *Journal of the American Chemical Society* **2009**, *131*, 424-425.
352. Protesescu, L.; Yakunin, S.; Bodnarchuk, M. I.; Kriegel, F.; Caputo, R.; Hendon, C. H.; Yang, R. X.; Walsh, A.; Kovalenko, M. V., Nanocrystals of Cesium Lead Halide Perovskites (CsPbX<sub>3</sub>, X = Cl, Br, and I): Novel Optoelectronic Materials Showing Bright Emission with Wide Color Gamut. *Nano Letters* **2015**, *15*, 3692-3696.
353. Sharma, S.; Weiden, N.; Weissen, A., Phase-diagrams of Quasi-Binary Systems of the Type ABX<sub>3</sub>-A'BX<sub>3</sub>, ABX<sub>3</sub>-AB'X<sub>3</sub>, and ABX<sub>3</sub>-ABX'<sub>3</sub>, X = Halogen. *Zeitschrift für Physikalische Chemie* **1992**, *175*, 63-80.
354. Trots, D. M.; Myagkota, S. V., High-temperature structural evolution of caesium and rubidium triiodoplumbates. *Journal of Physics and Chemistry of Solids* **2008**, *69*, 2520-2526.
355. Stoumpos, C. C.; Malliakas, C. D.; Kanatzidis, M. G., Semiconducting Tin and Lead Iodide Perovskites with Organic Cations: Phase Transitions, High Mobilities, and Near-Infrared Photoluminescent Properties. *Inorganic Chemistry* **2013**, *52*, 9019-9038.
356. Babin, V.; Fabeni, P.; Nikl, M.; Nitsch, K.; Pazzi, G. P.; Zazubovich, S., Luminescent CsPbI<sub>3</sub> and Cs<sub>4</sub>PbI<sub>6</sub> aggregates in annealed CsI: Pb crystals. *Phys. Status Solidi B* **2001**, *226*, 419-428.
357. Verma, A. S.; Jindal, V. K., Lattice constant of cubic perovskites. *Journal of Alloys and Compounds* **2009**, *485*, 514-518.
358. Verma, A. S.; Kumar, A.; Bhardwaj, S. R., Correlation between ionic charge and the lattice constant of cubic perovskite solids. *Phys. Status Solidi B* **2008**, *245*, 1520-1526.
359. Ida, Y., Interionic repulsive force and compressibility of ions. *Phys. Earth Planet. Inter.* **1976**, *13*, 97-104.
360. Mizusaki, J.; Arai, K.; Fueki, K., Ionic conduction of the perovskite-type halides. *Solid State Ionics* **1983**, *11*, 203-211.
361. Gratzel, M., The light and shade of perovskite solar cells. *Nature Materials* **2014**, *13*, 838-842.
362. Green, M. A.; Ho-Baillie, A.; Snaith, H. J., The Emergence Of Perovskite Solar Cells. *Nat. Photon.* **2014**, *8*, 506-514.
363. Park, N.-G., Organometal Perovskite Light Absorbers Toward a 20% Efficiency Low-Cost Solid-State Mesoscopic Solar Cell. *J. Phys. Chem. Lett.* **2013**, *4*, 2423-2429.
364. Zhou, H.; Chen, Q.; Li, G.; Luo, S.; Song, T.-b.; Duan, H.-S.; Hong, Z.; You, J.; Liu, Y.; Yang, Y., Interface engineering of highly efficient perovskite solar cells. *Science* **2014**, *345*, 542-546.

365. Chung, I.; Lee, B.; He, J.; Chang, R. P. H.; Kanatzidis, M. G., All-solid-state dye-sensitized solar cells with high efficiency. *Nature* **2012**, *485*, 486-489.
366. Stranks, S. D.; Snaith, H. J., Metal-halide perovskites for photovoltaic and light-emitting devices. *Nature Nanotechnology* **2015**, *10*, 391-402.
367. Xiao, Z.; Yuan, Y.; Shao, Y.; Wang, Q.; Dong, Q.; Bi, C.; Sharma, P.; Gruverman, A.; Huang, J., Giant switchable photovoltaic effect in organometal trihalide perovskite devices. *Nature Materials* **2015**, *14*, 193-198.
368. Walsh, A.; Scanlon, D. O.; Chen, S.; Gong, X. G.; Wei, S.-H., Self-Regulation Mechanism for Charged Point Defects in Hybrid Halide Perovskites. *Angewandte Chemie International Edition* **2015**, *54*, 1791-1794.
369. Agiorgousis, M. L.; Sun, Y.-Y.; Zeng, H.; Zhang, S., Strong Covalency-Induced Recombination Centers in Perovskite Solar Cell Material CH<sub>3</sub>NH<sub>3</sub>PbI<sub>3</sub>. *Journal of the American Chemical Society* **2014**, *136*, 14570-14575.
370. Yin, W.-J.; Shi, T.; Yan, Y., Unusual defect physics in CH<sub>3</sub>NH<sub>3</sub>PbI<sub>3</sub> perovskite solar cell absorber. *Applied Physics Letters* **2014**, *104*, 063903.
371. Yang, T.-Y.; Gregori, G.; Pellet, N.; Grätzel, M.; Maier, J., The Significance of Ion Conduction in a Hybrid Organic–Inorganic Lead-Iodide-Based Perovskite Photosensitizer. *Angewandte Chemie International Edition* **2015**, Early view publication, DOI: 10.1002/anie.201500014.
372. Jang, D. M.; Park, K.; Kim, D. H.; Park, J.; Shojaei, F.; Kang, H. S.; Ahn, J.-P.; Lee, J. W.; Song, J. K., Reversible Halide Exchange Reaction of Organometal Trihalide Perovskite Colloidal Nanocrystals for Full-Range Band Gap Tuning. *Nano Letters* **2015**, 10.1021/acs.nanolett.5b01430.
373. Protesescu, L.; Yakunin, S.; Bodnarchuk, M. I.; Krieg, F.; Caputo, R.; Hendon, C. H.; Yang, R. X.; Walsh, A.; Kovalenko, M. V., Nanocrystals of Cesium Lead Halide Perovskites (CsPbX<sub>3</sub>, X = Cl, Br, and I): Novel Optoelectronic Materials Showing Bright Emission with Wide Color Gamut. *Nano Lett.* **2015**, *15*, 3692.
374. Akkerman, Q. A.; D’Innocenzo, V.; Accornero, S.; Scarpellini, A.; Petrozza, A.; Prato, M.; Manna, L., Tuning the Optical Properties of Cesium Lead Halide Perovskite Nanocrystals by Anion Exchange Reactions. *Journal of the American Chemical Society* **2015**, *137*, 10276-10281.
375. Pathak, S.; Sakai, N.; Wisnivesky Rocca Rivarola, F.; Stranks, S. D.; Liu, J.; Eperon, G. E.; Ducati, C.; Wojciechowski, K.; Griffiths, J. T.; Haghighirad, A. A.; Pellaroque, A.; Friend, R. H.; Snaith, H. J., Perovskite Crystals for Tunable White Light Emission. *Chem. Mater.* **2015**, *27*, 8066.
376. Palazon, F.; Di Stasio, F.; Akkerman, Q. A.; Krahne, R.; Prato, M.; Manna, L., Polymer-Free Films of Inorganic Halide Perovskite Nanocrystals as UV-to-White Color-Conversion Layers in LEDs. *Chemistry of Materials* **2016**, *28*, 2902-2906.
377. Dursun, I.; Shen, C.; Parida, M. R.; Pan, J.; Sarmah, S. P.; Priante, D.; Alyami, N.; Liu, J.; Saidaminov, M. I.; Alias, M. S.; Abdelhady, A. L.; Ng, T. K.; Mohammed, O. F.; Ooi, B. S.; Bakr, O. M., Perovskite Nanocrystals as a Color Converter for Visible Light Communication. *ACS Photonics* **2016**.
378. Li, X.; Wu, Y.; Zhang, S.; Cai, B.; Gu, Y.; Song, J.; Zeng, H., CsPbX<sub>3</sub> Quantum Dots for Lighting and Displays: Room-Temperature Synthesis, Photoluminescence Superiorities, Underlying Origins and White Light-Emitting Diodes. *Adv. Funct. Mater.* **2016**, *26*, 2435.
379. Zhang, X.; Lin, H.; Huang, H.; Reckmeier, C. J.; Zhang, Y.; Choy, W. C.; Rogach, A. L., Enhancing the Brightness of Cesium Lead Halide Perovskite Nanocrystal Based Green Light-Emitting Devices through the Interface Engineering with Perfluorinated Ionomer. *Nano Lett.* **2016**, *16*, 1415.

380. Park, Y. S.; Guo, S. J.; Makarov, N. S.; Klimov, V. I., Room Temperature Single-Photon Emission from Individual Perovskite Quantum Dots. *Acs Nano* **2015**, *9*, 10386-10393.
381. Rainò, G.; Nedelcu, G.; Protesescu, L.; Bodnarchuk, M. I.; Kovalenko, M. V.; Mahrt, R. F.; Stöferle, T., Single Cesium Lead Halide Perovskite Nanocrystals at Low Temperature: Fast Single-Photon Emission, Reduced Blinking, and Exciton Fine Structure. *ACS Nano* **2016**, *10*, 2485-2490.
382. Ithurria, S.; Tessier, M. D.; Mahler, B.; Lobo, R. P. S. M.; Dubertret, B.; Efros, A. L., Colloidal nanoplatelets with two-dimensional electronic structure. *Nat. Mater.* **2011**, *10*, 936.
383. Rowland, C. E.; Fedin, I.; Zhang, H.; Gray, S. K.; Govorov, A. O.; Talapin, D. V.; Schaller, R. D., Picosecond energy transfer and multiexciton transfer outpaces Auger recombination in binary CdSe nanoplatelet solids. *Nat. Mater.* **2015**, *14*, 484.
384. Grim, J. Q.; Christodoulou, S.; Di Stasio, F.; Krahne, R.; Cingolani, R.; Manna, L.; Moreels, I., Continuous-wave biexciton lasing at room temperature using solution-processed quantum wells. *Nat Nanotechnol* **2014**, *9*, 891-5.
385. Scott, R.; Heckmann, J.; Prudnikau, A. V.; Antanovich, A.; Mikhailov, A.; Owschimikow, N.; Artemyev, M.; Climente, J. I.; Woggon, U.; Grosse, N. B.; Achtstein, A. W., Directed emission of CdSe nanoplatelets originating from strongly anisotropic 2D electronic structure. *Nat Nanotechnol* **2017**, *12*, 1155-1160.
386. Zhang, D.; Eaton, S. W.; Yu, Y.; Dou, L.; Yang, P., Solution-Phase Synthesis of Cesium Lead Halide Perovskite Nanowires. *Journal of the American Chemical Society* **2015**, *137*, 9230-9233.
387. Akkerman, Q. A.; D'Innocenzo, V.; Accornero, S.; Scarpellini, A.; Petrozza, A.; Prato, M.; Manna, L., Solution Synthesis Approach to Colloidal Cesium Lead Halide Perovskite Nanoplatelets with Monolayer-Level Thickness Control. *J. Am. Chem. Soc.* **2015**, *137*, 10276.
388. Sun, S.; Yuan, D.; Xu, Y.; Wang, A.; Deng, Z., Ligand-Mediated Synthesis of Shape-Controlled Cesium Lead Halide Perovskite Nanocrystals via Reprecipitation Process at Room Temperature. *ACS Nano* **2016**, *10*, 3648-57.
389. Zhang, D.; Yang, Y.; Bekenstein, Y.; Yu, Y.; Gibson, N. A.; Wong, A. B.; Eaton, S. W.; Kornienko, N.; Kong, Q.; Lai, M.; Alivisatos, A. P.; Leone, S. R.; Yang, P., Synthesis of Composition Tunable and Highly Luminescent Cesium Lead Halide Nanowires through Anion-Exchange Reactions. *Journal of the American Chemical Society* **2016**, *138*, 7236-7239.
390. Shamsi, J.; Dang, Z.; Bianchini, P.; Canale, C.; Stasio, F. D.; Brescia, R.; Prato, M.; Manna, L., Colloidal Synthesis of Quantum Confined Single Crystal CsPbBr<sub>3</sub> Nanosheets with Lateral Size Control up to the Micrometer Range. *Journal of the American Chemical Society* **2016**, *138*, 7240-7243.
391. Eaton, S. W.; Lai, M.; Gibson, N. A.; Wong, A. B.; Dou, L.; Ma, J.; Wang, L.-W.; Leone, S. R.; Yang, P., Lasing in robust cesium lead halide perovskite nanowires. *Proceedings of the National Academy of Sciences of the United States of America* **2016**, *113*, 1993-1998.
392. Vikash Kumar, R.; Abhishek, S.; Rayan, C.; Angshuman, N., Excellent green but less impressive blue luminescence from CsPbBr<sub>3</sub> perovskite nanocubes and nanoplatelets. *Nanotechnology* **2016**, *27*, 325708.
393. Zhang, Q.; Su, R.; Liu, X. F.; Xing, J.; Sum, T. C.; Xiong, Q. H., High-Quality Whispering-Gallery-Mode Lasing from Cesium Lead Halide Perovskite Nanoplatelets. *Advanced Functional Materials* **2016**, *26*, 6238-6245.
394. Burschka, J.; Pellet, N.; Moon, S. J.; Humphry-Baker, R.; Gao, P.; Nazeeruddin, M. K.; Gratzel, M., Sequential deposition as a route to high-performance perovskite-sensitized solar cells. *Nature* **2013**, *499*, 316.
395. Cho, H.; Jeong, S. H.; Park, M. H.; Kim, Y. H.; Wolf, C.; Lee, C. L.; Heo, J. H.; Sadhanala, A.; Myoung, N.; Yoo, S.; Im, S. H.; Friend, R. H.; Lee, T. W., Overcoming the

- electroluminescence efficiency limitations of perovskite light-emitting diodes *Science* **2015**, *350*, 1222.
396. Dou, L.; Wong, A. B.; Yu, Y.; Lai, M.; Kornienko, N.; Eaton, S. W.; Fu, A.; Bischak, C. G.; Ma, J.; Ding, T.; Ginsberg, N. S.; Wang, L. W.; Alivisatos, A. P.; Yang, P., Atomically thin two-dimensional organic-inorganic hybrid perovskites. *Science* **2015**, *349*, 1518.
397. Fu, Y.; Meng, F.; Rowley, M. B.; Thompson, B. J.; Shearer, M. J.; Ma, D.; Hamers, R. J.; Wright, J. C.; Jin, S., Solution Growth of Single Crystal Methylammonium Lead Halide Perovskite Nanostructures for Optoelectronic and Photovoltaic Applications. *J. Am. Chem. Soc.* **2015**, *137*, 5810.
398. Horvath, E.; Spina, M.; Szekrenyes, Z.; Kamaras, K.; Gaal, R.; Gachet, D.; Forro, L., Nanowires of Methylammonium Lead Iodide (CH<sub>3</sub>NH<sub>3</sub>PbI<sub>3</sub>) Prepared by Low Temperature Solution-Mediated Crystallization. *Nano Lett.* **2014**, *14*, 6761.
399. Yuan, M.; Quan, L. N.; Comin, R.; Walters, G.; Sabatini, R.; Voznyy, O.; Hoogland, S.; Zhao, Y.; Beauregard, E. M.; Kanjanaboos, P.; Lu, Z.; Kim, D. H.; Sargent, E. H., Perovskite energy funnels for efficient light-emitting diodes. *Nat Nano* **2016**, *advance online publication*.
400. Dirin, D. N.; Protesescu, L.; Trummer, D.; Kochetygov, I. V.; Yakunin, S.; Krumeich, F.; Stadie, N. P.; Kovalenko, M. V., Harnessing Defect-Tolerance at the Nanoscale: Highly Luminescent Lead Halide Perovskite Nanocrystals in Mesoporous Silica Matrixes. *Nano Lett.* **2016**, 5866-5874.
401. Liu, M.; Johnston, M. B.; Snaith, H. J., Efficient planar heterojunction perovskite solar cells by vapour deposition. *Nature* **2013**, *501*, 395.
402. Ha, S. T.; Liu, X. F.; Zhang, Q.; Giovanni, D.; Sum, T. C.; Xiong, Q. H., Synthesis of Organic-Inorganic Lead Halide Perovskite Nanoplatelets: Towards High-Performance Perovskite Solar Cells and Optoelectronic Devices. *Adv. Opt. Mater.* **2014**, *2*, 838-844.
403. Zhang, Q.; Ha, S. T.; Liu, X. F.; Sum, T. C.; Xiong, Q. H., Room-Temperature Near-Infrared High-Q Perovskite Whispering-Gallery Planar Nano lasers. *Nano Letters* **2014**, *14*, 5995-6001.
404. Niu, L.; Zeng, Q. S.; Shi, J.; Cong, C. X.; Wu, C. Y.; Liu, F. C.; Zhou, J. D.; Fu, W.; Fu, Q. D.; Jin, C. H.; Yu, T.; Liu, X. F.; Liu, Z., Controlled Growth and Reliable Thickness-Dependent Properties of Organic-Inorganic Perovskite Platelet Crystal. *Advanced Functional Materials* **2016**, *26*, 5263-5270.
405. Tyagi, P.; Arveson, S. M.; Tisdale, W. A., Colloidal Organohalide Perovskite Nanoplatelets Exhibiting Quantum Confinement. *J. Phys. Chem. Lett.* **2015**, *6*, 1911.
406. Sichert, J. A.; Tong, Y.; Mutz, N.; Vollmer, M.; Fischer, S.; Milowska, K. Z.; García Cortadella, R.; Nickel, B.; Cardenas-Daw, C.; Stolarczyk, J. K.; Urban, A. S.; Feldmann, J., Quantum Size Effect in Organometal Halide Perovskite Nanoplatelets. *Nano Lett.* **2015**, *15*, 6521.
407. Vybornyi, O.; Yakunin, S.; Kovalenko, M. V., Polar-solvent-free colloidal synthesis of highly luminescent alkylammonium lead halide perovskite nanocrystals. *Nanoscale* **2016**, *8*, 6278-6283.
408. Almeida, G.; Goldoni, L.; Akkerman, Q.; Dang, Z.; Khan, A. H.; Marras, S.; Moreels, I.; Manna, L., Role of Acid-Base Equilibria in the Size, Shape, and Phase Control of Cesium Lead Bromide Nanocrystals. *ACS Nano* **2018**, *12*, 1704.
409. De Roo, J.; Ibáñez, M.; Geiregat, P.; Nedelcu, G.; Walravens, W.; Maes, J.; Martins, J. C.; Van Driessche, I.; Kovalenko, M. V.; Hens, Z., Highly Dynamic Ligand Binding and Light Absorption Coefficient of Cesium Lead Bromide Perovskite Nanocrystals. *ACS Nano* **2016**, *10*, 2071-2081.
410. Cottingham, P.; Brutchey, R. L., On the crystal structure of colloiddally prepared CsPbBr<sub>3</sub> quantum dots. *Chemical Communications* **2016**, *52*, 5246-5249.

411. Bertolotti, F.; Protesescu, L.; Kovalenko, M. V.; Yakunin, S.; Cervellino, A.; Billinge, S. J. L.; Terban, M. W.; Pedersen, J. S.; Masciocchi, N.; Guagliardi, A., Coherent Nanotwins and Dynamic Disorder in Cesium Lead Halide Perovskite Nanocrystals. *ACS Nano* **2017**, *11*, 3819-3831.
412. Zhang, M.; Yu, H.; Lyu, M. Q.; Wang, Q.; Yun, J. H.; Wang, L. Z., Composition-dependent photoluminescence intensity and prolonged recombination lifetime of perovskite  $\text{CH}_3\text{NH}_3\text{PbBr}_{3-x}\text{Cl}_x$  films. *Chemical Communications* **2014**, *50*, 11727-11730.
413. Akkerman, Q. A.; Motti, S. G.; Kandada, A. R. S.; Mosconi, E.; D'Innocenzo, V.; Bertoni, G.; Marras, S.; Kamino, B. A.; Miranda, L.; De Angelis, F.; Petrozza, A.; Prato, M.; Manna, L., Solution Synthesis Approach to Colloidal Cesium Lead Halide Perovskite Nanoplatelets with Monolayer-Level Thickness Control. *Journal of the American Chemical Society* **2016**, *138*, 1010-1016.
414. Becker, M. A.; Vaxenburg, R.; Nedelcu, G.; Sercel, P. C.; Shabaev, A.; Mehl, M. J.; Michopoulos, J. G.; Lambrakos, S. G.; Bernstein, N.; Lyons, J. L.; Stöferle, T.; Mahrt, R. F.; Kovalenko, M. V.; Norris, D. J.; Rainò, G.; Efros, A. L., Bright triplet excitons in caesium lead halide perovskites. *Nature* **2018**, *553*, 189-193.
415. Wu, K. F.; Liang, G. J.; Shane, Q. Y.; Ren, Y. P.; Kong, D. G.; Lian, T. Q., Ultrafast Interfacial Electron and Hole Transfer from  $\text{CsPbBr}_3$  Perovskite Quantum Dots. *Journal of the American Chemical Society* **2015**, *137*, 12792-12795.
416. Guyot-Sionnest, P.; Shim, M.; Matranga, C.; Hines, M., Intraband relaxation in CdSe quantum dots. *Physical Review B* **1999**, *60*, R2181-R2184.
417. Achermann, M.; Bartko, A. P.; Hollingsworth, J. A.; Klimov, V. I., The effect of Auger heating on intraband carrier relaxation in semiconductor quantum rods. *Nat Phys* **2006**, *2*, 557-561.
418. Heitz, R.; Born, H.; Guffarth, F.; Stier, O.; Schliwa, A.; Hoffmann, A.; Bimberg, D., Existence of a phonon bottleneck for excitons in quantum dots. *Physical Review B* **2001**, *64*.
419. Makarov, N. S.; Guo, S. J.; Isaienko, O.; Liu, W. Y.; Robel, I.; Klimov, V. I., Spectral and Dynamical Properties of Single Excitons, Biexcitons, and Trions in Cesium-Lead-Halide Perovskite Quantum Dots. *Nano Letters* **2016**, *16*, 2349-2362.
420. Park, Y. S.; Bae, W. K.; Baker, T.; Lim, J.; Klimov, V. I., Effect of Auger Recombination on Lasing in Heterostructured Quantum Dots with Engineered Core/Shell Interfaces. *Nano Letters* **2015**, *15*, 7319-7328.
421. Rabouw, F. T.; Cogan, N. M. B.; Berends, A. C.; van der Stam, W.; Vanmaekelbergh, D.; Koenderink, A. F.; Krauss, T. D.; Donega, C. D., Non-blinking single-photon emitters in silica. *Sci Rep-Uk* **2016**, *6*.
422. Garcia-Santamaria, F.; Chen, Y. F.; Vela, J.; Schaller, R. D.; Hollingsworth, J. A.; Klimov, V. I., Suppressed Auger Recombination in "Giant" Nanocrystals Boosts Optical Gain Performance. *Nano Letters* **2009**, *9*, 3482-3488.
423. Chang, A. Y.; Liu, W. Y.; Talapin, D. V.; Schaller, R. D., Carrier Dynamics in Highly Quantum-Confined, Colloidal Indium Antimonide Nanocrystals. *ACS Nano* **2014**, *8*, 8513-8519.
424. Yeltik, A.; Delikanli, S.; Olutas, M.; Kelestemur, Y.; Guzelurk, B.; Demir, H. V., Experimental Determination of the Absorption Cross-Section and Molar Extinction Coefficient of Colloidal CdSe Nanoplatelets. *J Phys Chem C* **2015**, *119*, 26768-26775.
425. Kumagai, M.; Takagahara, T., Excitonic and nonlinear-optical properties of dielectric quantum-well structures. *Physical Review B* **1989**, *40*, 12359-12381.
426. Yuan, G.; Ritchie, C.; Ritter, M.; Murphy, S.; Gómez, D. E.; Mulvaney, P., The Degradation and Blinking of Single  $\text{CsPbI}_3$  Perovskite Quantum Dots. *The Journal of Physical Chemistry C* **2018**.

- 
427. Fu, M.; Tamarat, P.; Huang, H.; Even, J.; Rogach, A. L.; Lounis, B., Neutral and Charged Exciton Fine Structure in Single Lead Halide Perovskite Nanocrystals Revealed by Magneto-optical Spectroscopy. *Nano Lett* **2017**, *17*, 2895-2901.
428. Isarov, M.; Tan, L. Z.; Bodnarchuk, M. I.; Kovalenko, M. V.; Rappe, A. M.; Lifshitz, E., Rashba Effect in a Single Colloidal CsPbBr<sub>3</sub> Perovskite Nanocrystal Detected by Magneto-Optical Measurements. *Nano Lett* **2017**, *17*, 5020-5026.
429. Yang, X.; Divayana, Y.; Zhao, D.; Swee Leck, K.; Lu, F.; Tiam Tan, S.; Putu Abiyasa, A.; Zhao, Y.; Volkan Demir, H.; Wei Sun, X., A bright cadmium-free, hybrid organic/quantum dot white light-emitting diode. *Applied Physics Letters* **2012**, *101*, 233110.



## Annex A. List of abbreviations

<i>Abbreviation</i>	<i>Full name</i>
<b>NP(s)</b>	Nanoparticle(s)
<b>NC(s)</b>	Nanocrystal(s)
<b>0D</b>	Zero-dimensional
<b>QD(s)</b>	Quantum Dot(s)
<b>PL</b>	Photoluminescence
<b>QY(s)</b>	Quantum Yield(s)
<b>CNT</b>	Classical Nucleation Theory
<b>MSC(s)</b>	Magic-Sized Cluster(s)
<b>RDNT</b>	Reaction-Driven Nucleation Theory
<b>DFT</b>	Density Functional Theory
<b>UV-Vis</b>	Ultraviolet-Visible
<b>MA</b>	Myristic Acid
<b>OA</b>	Oleic Acid
<b>OLA</b>	Oleylamine
<b>TOP</b>	Trioctylphosphine
<b>TOPO</b>	Trioctylphosphine oxide
<b>ODE</b>	1-octadecene
<b>UPS</b>	Ultraviolet Photoelectron Spectroscopy
<b>1D</b>	One-dimensional
<b>2D</b>	Two-dimensional
<b>3D</b>	Three-dimensional
<b>IR</b>	Infrared
<b>NIR</b>	Near-Infrared
<b>NPLs</b>	Nanoplatelets
<b>NWs</b>	Nanowires
<b>NSs</b>	Nanosheets
<b>LARP</b>	Ligand-assisted reprecipitation
<b>DMF</b>	N,N-dimethylformamide
<b>DMSO</b>	Dimethyl sulfoxide
<b>CE</b>	Cation Exchange
<b>AE</b>	Anion Exchange
<b>LED(s)</b>	Light Emitting Device(s)
<b>QLEDs</b>	Quantum dot-based LEDs
<b>LCDs</b>	Liquid-crystal displays
<b>SWIR</b>	Short-wavelength Infrared
<b>EQE</b>	External Quantum Efficiency
<b>QDEF</b>	Quantum Dot Enhancement Film
<b>EU</b>	European Union
<b>FWHM</b>	Full-Width at Half-Maximum

## Annex B. Curriculum Vitae

Name: Georgian Nedelcu

Date of Birth: November 9<sup>th</sup>, 1989

Nationality: Romanian

### Education

Since 2013	Doctoral studies under the supervision of Prof. Dr. Maksym V. Kovalenko, ETH Zürich (Swiss Federal Institute of Technology), Zürich, Switzerland; and Empa – Swiss Federal Laboratories for Materials Science and Technology), Dübendorf, Switzerland
2011 - 2013	M.Sc. studies in Chemistry of Advanced Materials, Faculty of Chemistry, University of Bucharest, Romania – Master thesis under the supervision of Prof. Dr. Otilia Ludmila Cinteza
2011 - 2013	M.Sc. studies in Science of conservation and restoration of national heritage works by physical and chemical methods, Faculty of Physics, University of Bucharest, Bucharest, Romania – Master thesis under the supervision of Prof. Dr. Otilia Ludmila Cinteza
2008 - 2011	B.Sc. studies in Chemistry, Faculty of Chemistry, University of Bucharest, Romania – Bachelor thesis under the supervision of Prof. Dr. Petre Ionita

Awards: Best Poster Presentation at SCS Fall Meeting 2016  
ACS Nano Poster Award at NaNaX-7 Conference (Marburg 2016)  
Best oral talk at ETH LAC Christmas Symposium 2015

### Scientific and synergistic activities

- More than 15 publications in peer-reviewed journals: Nature (1), Nature Comm. (1), Nano Lett. (4), ACS Nano (3), J. Am. Chem. Soc. (1), J. Phys. Chem. C (2), Adv. Funct. Mater. (1), Arkivoc (1), Struct. Dyn. (1), Appl. Phys. Lett. (1), Adv. Optical Mater. (1).
- Served as reviewer for various peer-reviewed journals from Science, Nature, and Elsevier families.
- Conference participation: 3 oral presentations, 6 poster presentations (PSCO/2017 – Oxford, UK; SCS/2016 – Zurich, Switzerland; NaNaX-7/2016 – Marburg, Germany; E-MRS/2016 – Lille, France; LAC Christmas Symposium/2015 – Zurich, Switzerland; PSCO/2015 – Lausanne, Switzerland; ICSFS X/2013 – Cluj-Napoca, Romania;

XXXIInd National Chemistry Conference/2012 – Ramnicu Valcea, Romania; 2nd International Congress Chemistry for Cultural Heritage/2012 – Istanbul, Turkey).

- 2014-2017 – Mentoring research projects of two master students and two visiting students.
- Teaching assistant for Allgemeine Chemie Praktikum (529-0011-04L, fall 2017); Moodle teacher for Allgemeine Chemie Praktikum (529-0011-02L & 529-0011-04L, 2015 - 2016); Moodle Manager for Allgemeine Chemie Praktikum (529-0011-02L & 529-0011-04L, 2016 - 2017).
- Assistant for public lectures/experiments on Maturandentag (2015).
- Co-organizer of LAC Christmas Symposium 2013 and 2018.

## Annex C. List of publications

### Doctoral publications

19. G. Nedelcu, F. Bertolotti, A. Vivani, A. Cervellino, M.V. Kovalenko, N. Masciocchi, and A. Guagliardi.

*Crystal Structure, Morphology and Surface Termination of Highly Stable Cesium Lead Bromide Nanoplatelets.*

*In preparation.*

18. G. Nedelcu, M. Wagner, M.A. Becker, G. Rainò, S. Kumar, T. Stöferle, R.F. Mahrt, V.I. Klimov, S. Yakunin, C.-J. Shih, R. Schaller, and M.V. Kovalenko.

*Cesium lead bromide nanoplatelets (CsPbBr<sub>3</sub> NPLs) with stable emission at 492 nm.*

*In preparation.*

17. M.A. Becker, L. Scarpelli, G. Nedelcu, G. Rainò, F. Masia, P. Borri, T. Stöferle, M.V. Kovalenko, W. Langbein, R.F. Mahrt.

*Long Exciton Dephasing Time and Coherent Phonon Coupling in CsPbBr<sub>2</sub>Cl Perovskite Nanocrystals.*

Nano Lett., **2018**, 18, 7546–7551.

16. A. Brumberg, B.T. Diroll, G. Nedelcu, M.E. Sykes, Y. Liu, S.M. Harvey, M.R. Wasielewski, M.V. Kovalenko, and R. D. Schaller.

*Material Dimensionality Effects on Electron Transfer Rates Between CsPbBr<sub>3</sub> and CdSe Nanoparticles.*

Nano Lett., **2018**, 18, 4771–4776.

15. A. Perulli, A. Balena, M. Fernandez, G. Nedelcu, A. Cretí, M.V. Kovalenko, M. Lomascolo, and M. Anni.

*Full-color tuning in binary polymer:perovskite nanocrystals organic-inorganic hybrid blends.* Appl. Phys. Lett., **2018**, 112, 171904.

14. A. Balena, A. Perulli, M. Fernandez, M.L. De Giorgi, G. Nedelcu, M.V. Kovalenko, and M. Anni.

---

*Temperature Dependence of the Amplified Spontaneous Emission from CsPbBr<sub>3</sub> Nanocrystal Thin Films.*

J. Phys. Chem. C, **2018**, 122, 5813–5819.

13. M.A. Becker, R. Vaxenburg, G. Nedelcu, P.C. Sercel, A. Shabaev, M.J. Mehl, J.G. Michopoulos, S.G. Lambrakos, N. Bernstein, J.L. Lyons, T. Stöferle, R.F. Mahrt, M.V. Kovalenko, D.J. Norris, G. Rainò, and A.L. Efros.

*Bright triplet excitons in caesium lead halide perovskites.*

Nature, **2018**, 553, 189-193.

12. B.T. Diroll, G. Nedelcu, M.V. Kovalenko, and R.D. Schaller.

*High-Temperature Photoluminescence of CsPbX<sub>3</sub> (X = Cl, Br, I) Nanocrystals.*

Adv. Funct. Mater., **2017**, 1606750.

11. F.G. Santomauro, J. Grilj, L. Mewes, G. Nedelcu, S. Yakunin, T. Rossi, G. Capano, A. Al Haddad, J. Budarz, D. Kinschel, D. S. Ferreira, G. Rossi, M.G. Tovar, D. Grolimund, V. Samson, M. Nachtegaal, G. Smolentsev, M.V. Kovalenko, and M. Chergui.

*Localized holes and delocalized electrons in photoexcited inorganic perovskites: Watching each atomic actor by picosecond X-ray absorption spectroscopy.*

Struct. Dyn., **2017**, 4, 044002.

10. S. Kumar, J. Jagielski, S. Yakunin, P. Rice, Yu-C. Chiu, M. Wang, G. Nedelcu, Y. Kim, S. Lin, E.J.G. Santos, M.V. Kovalenko, and Ch.-J. Shih.

*Efficient Blue Electroluminescence Using Quantum-Confined Two-Dimensional Perovskites.*

ACS Nano, **2016**, 10, 9720–9729.

9. M.V. Pavliuk, D.L.A. Fernandes, A.M. El-Zohry, M. Abdellah, G. Nedelcu, M.V. Kovalenko, and J. Sá.

*Magnetic Manipulation of Spontaneous Emission from Inorganic CsPbBr<sub>3</sub> Perovskites Nanocrystals.*

Adv. Optical Mater., **2016**, 4, 2004-2008

8. C. Weerd, L. Navascues, H. Zhang, W. Buma, G. Nedelcu, M.V. Kovalenko, and T. Gregorkiewicz.

*Energy Transfer Between Inorganic Perovskite Nanocrystals.*

J. Phys. Chem. C, **2016**, 120, 13310-13315.

7. I. Lignos, S. Stavrakis, G. Nedelcu, L. Protesescu, A.J. deMello, and M.V. Kovalenko.

---

*Synthesis of Cesium Lead Halide Perovskite Nanocrystals in a Droplet-Based Microfluidic Platform: Fast Parametric Space Mapping.*

Nano Lett. **2016**, 16, 1869–1877.

6. J. De Roo, M. Ibáñez, P. Geiregat, G. Nedelcu, W. Walravens, J. Maes, J.C. Martins, I. Van Driessche, M.V. Kovalenko, and Z. Hens.

*Highly Dynamic Ligand Binding and Light Absorption Coefficient of Cesium Lead Bromide Perovskite Nanocrystals.*

ACS Nano, **2016**, 10, 2071–2081.

5. G. Raino, G. Nedelcu, L. Protesescu, M.I. Bodnarchuk, M.V. Kovalenko, R.F. Mahrt, and T. Stöferle.

*Single Cesium Lead Halide Perovskite Nanocrystals at Low Temperature: Fast Single-Photon Emission, Reduced Blinking, and Exciton Fine Structure.*

ACS Nano, **2016**, 10, 2485–2490.

4. S. Yakunin, L. Protesescu, F. Krieg, M. I. Bodnarchuk, G. Nedelcu, M. Humer, G. De Luca, M. Fiebig, W. Heiss, and M. V. Kovalenko.

*Low-threshold amplified spontaneous emission and lasing from colloidal nanocrystals of cesium lead halide perovskites  $CsPbX_3$  ( $X=Cl, Br, I$ ).*

Nature Communications, **2015**, 9, 8056.

3. G. Nedelcu, L. Protesescu, S. Yakunin, M.I. Bodnarchuk, M. Grotevent, and M.V. Kovalenko.

*Fast Anion-Exchange in Highly Luminescent Nanocrystals of Cesium Lead Halide Perovskites ( $CsPbX_3$ ,  $X=Cl, Br, I$ ).*

Nano Letters, **2015**, 15, 5635–5640.

2. D. N. Dirin, S. Dreyfuss, M. I. Bodnarchuk, G. Nedelcu, P. Papagiorgis, G. Itskos, and M. V. Kovalenko.

*Lead Halide Perovskites and Other Metal Halide Complexes as Inorganic Capping Ligands for Colloidal Nanocrystals.*

J. Am. Chem. Soc., **2014**, 136, 6550–6553.

## Pre-doctoral publications

1. M. Tudose, M.T. Caproiu, F.D. Badea, G. Nedelcu, P. Ionita, T. Constantinescu, A.T. Balaban.

*New mono- and di-branched derivatives of Kryptofix K22 with N-4-methoxyamino-3, 5-dinitrobenzoyl substituents. Synthesis and properties.*

ARKIVOC, **2011**, 2, 343-354.

## Annex D. List of presentations

### Oral presentations

3. G. Nedelcu, L. Protesescu, S. Yakunin, M.V. Kovalenko.

*Highly luminescent nanocrystals of cesium lead halide perovskites.*

E-MRS, **2016**, Lille, France.

2. G. Nedelcu, L. Protesescu, S. Yakunin, M.V. Kovalenko.

*Highly luminescent nanocrystals of cesium lead halide perovskites.*

LAC Christmas Symposium, **2015**, Zurich, Switzerland.

1. G. Nedelcu, D. Bala, V. Purcar, C. Munteanu, O.L. Cinteza.

*A new approach in the development of porous polymeric matrices with biomedical applications.*

ICSFS X, **2013**, Cluj-Napoca, Romania.

### Poster presentations

6. G. Nedelcu, M. Wagner, M.A. Becker, G. Rainò, R.T. Lechner, S. Kumar, T. Stöferle, R.F.

Mahrt, S. Yakunin, C.-J. Shih, R. Schaller, and M.V. Kovalenko.

*Cesium lead bromide nanoplatelets (CsPbBr<sub>3</sub> NPLs) with unique stable emission at 492 nm: viable nanomaterials for blue light emitting devices.*

PSCO, **2017**, Oxford, United Kingdom.

5. G. Nedelcu, L. Protesescu, S. Yakunin, M.I. Bodnarchuk, M.J. Grotevent, and M.V. Kovalenko.

*Efficient Anion-Exchange in Highly Luminescent Nanocrystals of Cesium Lead Halide Perovskites (CsPbX<sub>3</sub>, X = Cl, Br, I).*

SCS, **2016**, Zurich, Switzerland.

4. G. Nedelcu, L. Protesescu, S. Yakunin, M.V. Kovalenko.

*Highly luminescent nanocrystals of cesium lead halide perovskites.*

NaNax-7, **2016**, Marburg, Germany.

3. G. Nedelcu, L. Protesescu, S. Yakunin, M.V. Kovalenko.



*Synthesis of Highly Luminescent Nanocrystals of Cesium Lead Halide Perovskites (CsPbX<sub>3</sub>, X = Cl, Br, I).*

PSCO, **2015**, Lausanne, Switzerland.

2. G. Nedelcu, D. Bala, M. Florea Spiroiu, L. O. Cinteza.

*Synergistic effects in surfactant – polymer systems at air/water and CO<sub>2</sub>/water interfaces.*

XXXII<sup>nd</sup> National Chemistry Conference, **2012**, Ramnicu Valcea, Romania.

1. G. Nedelcu, T. Miclaus, M. Marinescu, M. Pruna, L.O. Cinteza.

*Novel material for stone protection with water-repellent and antibacterial properties.*

2nd International Congress Chemistry for Cultural Heritage, **2012**, Istanbul, Turkey.